

A Review of Aeronautical Fatigue and
Structural Integrity Research and
Application in China
June 2019-May 2021

SUN Xiasheng, DONG Dengke

Chinese Aeronautical Establishment

sunxiasheng@cae.ac.cn

dongdengke@cae.ac.cn

Table of Contents

1. INTRODUCTION.....	1
2. FUNDAMENTAL RESEARCH ON AERONAUTICAL FATIGUE AND STRUCTURAL INTEGRITY.....	2
2.1 ADDITIVE MANUFACTURING.....	2
2.1.1 Crack Initiation and Evolution Mechanism of Additive Manufactured Titanium Alloys in Very High Cycle Fatigue Regime.....	2
2.1.2 Fatigue Failure Mechanism and Life Model in Additive Manufactured Titanium Alloys.....	3
2.1.3 Study on The Residual Stress Effects and Anisotropic Fatigue Performance of Additive Manufacturing Titanium Alloy.....	5
2.1.4 Research on Influence of Defect and Mechanical Properties of High Strength Aluminum Alloy Based on Selective Laser Melting.....	8
2.1.5 Fatigue Property Evaluation and Creep Crack Growth Simulation of AM Titanium Alloy With Manufactured Defects.....	10
2.1.6 Fracture Performance of Ti-Alloy Made by DED Additive Manufacturing.....	12
2.1.7 Fatigue Evaluation Method of Titanium Alloy Additive Manufacturing.....	14
2.1.8 The Validation Technology of Additive Manufacturing.....	17
2.2 WELDING TECHNOLOGY.....	18
2.2.1 Study on Mechanical Properties and Residual Stress of Friction Stir Welding.....	18
2.2.2 Analysis of Crack Propagation Behaviors in Friction Stir Welding Joint Panels with Stringers.....	20
2.2.3 Fatigue Crack Growth in Welded Joints of 18Ni High-Strength Steel.....	23
2.2.4 Fatigue Property of Friction Stir Welded Butt Joints for 6156-T6 Aluminum Alloy.....	24
2.3 COMPOSITE STRUCTURE.....	26
2.3.1 Research on Low Velocity Impact Behavior and Residual Compressive Strength of Composite Laminate.....	26
2.3.2 Effects of Matrix Cracks on Delamination of Composite Laminates Subjected to Low-Velocity Impact.....	28
2.3.3 Study on Dynamic Mechanical Behavior and Failure Mechanism of Typical Ceramic Matrix Composite Riveted Structures.....	30
2.3.4 Study on Thermal Response and Prediction Method of Fiber Reinforced Polymer Matrix Composites in Aviation Fire.....	33
2.3.5 Fatigue Performance in Fiber Metal Laminates (FMLs).....	35

2.3.6 Experimental Research on Fatigue Threshold Value and Low-Load Cut-Off of Typical Laminates of Composite Fuselage.....	37
2.3.7 Correction of The Large Displacement Effect on Determination of Mode I Interlaminar Fracture Toughness of Composite.....	40
2.3.8 Strength Assessment and Repair for Typical Defects/Damage of Composite Structure	42
2.3.9 Helicopter Composite Material Tail Fin Structure Simulation Analysis and Damage Tolerance Experimental Verification.....	45
2.4 STRENGTHEN TECNOLOGY.....	46
2.4.1 Effect of Shot Peening on Notched Fatigue Performance of Powder Metallurgy Udimet720Li Super Alloy.....	46
2.4.2 Effect of Laser Shock Peening on Structure.....	49
2.5 WIDESPREAD FATIGUE DAMAGE.....	50
2.5.1 Crack Growth Simulation of Lap Joints With MSD Based on 3D Finite Element.....	50
2.5.2 Stiffened Panels With Multiple Collinear Cracks.....	53
2.5.3 Test Research on MSD Structure Containing Multiple Holes.....	55
2.6 FATIGUE AND CRACK GROWTH.....	57
2.6.1 High Cycle and Very High Cycle Fatigue Behavior of a TC17 Titanium Alloy Used for Compressor Blades	57
2.6.2 Cause Analysis and Verification of Stress Corrosion Cracking.....	59
2.6.3 Small Crack Growth Analysis.....	62
2.6.4 Application of 3D Slice Synthesis Weight Function Method.....	64
3. APPLICATION RESEARCH IN FATIGUE AERONAUTICAL AND STRUCTURAL INTEGRITY	66
3.1 FATIGUE AND INTEGRITY DESIGN.....	66
3.1.1 Study on Buckling Fatigue of Thin-Walled Stiffened Structures.....	66
3.1.2 The Design and Analysis of The Composite Material Concentrated Load-Bearing Joint	67
3.1.3 Effect of Surface Roughness on Fatigue Properties of Aluminum Matrix Composite Plywood.....	69
3.2 LOAD AND ENVIRONMENTAL SPECTRUM.....	70
3.2.1 Study on Scatter Factor of Severe Load Spectrum.....	70
3.2.2 Measured Load Analysis of Helicopter.....	73
3.2.3 Study on Service Environment of Aircraft Structure and Compilation Method Of Environment Spectrum of Aviation Aluminum Alloy	74
3.2.4 Equivalent Accelerated Relationship and Numerical Simulation of Corrosion of Aircraft	

Structures.....	77
3.2.5 Research on Corrosion Damage of Aviation Aluminum Alloy in Equivalent Accelerate Corrosion Environment.....	79
3.3 STRUCTURAL INTEGRITY REQUIREMENT AND AIRWORTHINESS COMPLIANCE ASSESSMENT.....	81
3.3.1 Airworthiness Compliance Verification of Hybrid Structure.....	81
3.3.2 Research on Aircraft Seat Dynamic Simulation and Occupant Head Injury Simulation Device	82
3.3.3 Crashworthiness and Numerical Simulation of Civil Aircraft Structure.....	85
3.4 INSPECTION AND MAINTENANCE.....	88
3.4.1 Research on Probability of Detection of Damage and Its Calculation Method.....	88
3.4.2 Application of Cold Spray Reinforcing Material Repairing Technology.....	89
3.4.3 Study on Repair And Fatigue of Super-Strength 300M Steel Structure.....	90
3.4.4 In-situ Nondestructive Testing Approaches for Impact Damage of Honeycomb Sandwich Structures.....	91
3.4.5 Research on The Failure Behavior of Stiffened Composite Repair Structure.....	93
4. AERONAUTICAL FATIGUE WITH DIGITAL TECHNOLOGY.....	97
4.1 NUMERICAL FATIGUE ANALYSIS.....	97
4.1.1 Determination and Analysis of Material Dispersion Coefficient of Aging Aircraft	97
4.1.2 Rapid Stress Analysis With High Accuracy of Complex Structure.....	100
4.1.3 Peridynamics Methods for Fatigue Problems.....	103
4.1.4 Numerical Study on Vibration Fatigue Load of Seaplane Wing During The Taxing on Wavy Surface.....	105
4.1.5 Damage Tolerance Analysis of Mixed-Mode Cracked Structures.....	108
4.2 DAMAGE IDENTIFICATION AND STRUCTURAL HEALTH MONITORING.....	110
4.2.1 Flexible Eddy Current Array Sensor for Monitoring Structural Crack Damage under Varying Temperature Environment.....	110
4.2.2 Individual Aircraft Life Monitoring Based on Artificial Intelligence and Advanced Sensing Technology.....	113
4.2.3 Fatigue Damage Assessment of Structural Critical Locations Based on Flight Parameters.....	115
4.2.4 Strain Monitoring Based Damage Identification in Aircraft Full Scale Fatigue Test... ..	118
4.2.5 Research on Nondestructive Testing Method for Cold Spraying to Repair Structural Defects.....	120
4.2.6 Guided Wave Damage Diagnosis Based on Deep Learning.....	122

4.2.7 Identification of Structural Surface Crack Modeling Characteristics Based on Laser 3D Scanning.....	124
4.2.8 Research on Crack Measurement Method Based on Displacement Field.....	126
4.3 VIRTUAL TEST.....	128
4.3.1 Virtual test case of static strength of aircraft structure.....	128
4.3.2 Evaluation of Residual Stress and Fatigue Life of Large-Diameter Lug with Cold Expanded Bushing.....	130
4.3.3 Research on Typical Structure Corrosion Simulation Technology of Carrier Aircraft	133
5. STRENGTH TESTING AND VERIFICATION ON AERONAUTICAL FATIGUE AND STRUCTURAL INTEGRITY.....	135
5.1 TESTING TECHNOLOGY.....	135
5.1.1 Simulation Analysis Method of Water Load and Key Technology of Special Structure Strength Test for Large Amphibious Aircraft.....	135
5.1.2 A Function Reliability Test Technology of The Dropped Hinge Wing Motion Mechanism.....	138
5.1.3 Deformation Measurement Technology in Complex Environment.....	139
5.1.4 Bidirectional Rigid Loading Technology and Its Application in Full-Scale Aircraft Fatigue Test.....	141
5.2 FULL SCALE STRUCTURE STRENGTH TEST.....	143
5.2.1 J-10 Fighter Full Scale Durability/Damage Tolerance Tests and Sustainment ASIP...	143
5.2.2 Research and Application of C919 Aircraft Static Test Technology.....	152
5.2.3 Static and Damage Tolerance Tests of Full-Scale Composite Fuselage Barrel Sections	154
5.2.4 New Method of Helicopter Large Structure Strength Test Based on Defect Tolerance.....	157

1. INTRODUCTION

This review summarizes the studies on the research of aeronautical fatigue and structural integrity investigations in China during the period June 2019 to May 2021 and is presented at the 37th conference of the International Committee Aeronautical Fatigue and Structural Integrity (ICAF) in Xi'an.

This review includes the research on the structural integrity analysis of additive manufacturing, welding technology, composite structure, strengthen technology, widespread fatigue damage, fatigue and crack growth, fatigue and integrity design, load and environmental spectrum, structural integrity requirement and airworthiness compliance assessment, inspection and maintenance, digital fatigue, etc.

China Delegation ICAF office organizes relevant professional institutions and academics to carry out the research inside China and cooperate with ICAF partners. The China National Review is integrated and compiled by China Delegation ICAF Office based on the recent research progress contributed by the following organizations.

- 1 COMAC Shanghai Aircraft Design & Research Institute
- 2 COMAC Beijing Aircraft Technology Research Institute
- 3 AECC Beijing Institute of Aeronautical Materials
- 4 AVIC Manufacturing Technology Institute
- 5 AVIC Shenyang Aircraft Design & Research Institute
- 6 AVIC Chengdu Aircraft Design & Research Institute
- 7 AVIC China Helicopter Research and Development Institute
- 8 AVIC The First Aircraft Institute
- 9 AVIC Harbin Aviation Industry Group CO.,LTD
- 10 AVIC Aircraft Strength Research Institute
- 11 Beihang University
- 12 Northwestern Polytechnical University
- 13 Nanjing University of Aeronautics and Astronautics
- 14 Civil Aviation University of China
- 15 Shanghai Jiao Tong University
- 16 Air Force Engineering University
- 17 Naval Aeronautical Engineering Institute
- 18 Institute Of Mechanics, Chinese Academy of Sciences

Each item of the report lists the corresponding contributors. The generous contributions provided by these aerospace industries and universities are sincerely acknowledged.

2. FUNDAMENTAL RESEARCH ON AERONAUTICAL FATIGUE AND STRUCTURAL INTEGRITY

2.1 ADDITIVE MANUFACTURING

2.1.1 Crack Initiation and Evolution Mechanism of Additive Manufactured Titanium Alloys in Very High Cycle Fatigue Regime¹

Additively manufactured (AM) titanium alloys have a great prospect for the production of component parts in aerospace. In the potential application of AM titanium alloys, some of the component parts inevitably subject to fatigue loadings during the service time. As a novel technology, the microstructure of AM titanium alloys is different from the conventionally wrought titanium alloys. So, it is very essential to fully understand the fatigue behavior of the AM titanium alloys.

The present study aims at the microstructure characteristic and evolution mechanism in the crack initiation and early growth region for very high cycle fatigue (VHCF) behavior of an AM Ti-6Al-4V by selective laser melting.

The main results of this research are as follows. Discontinuous refined grain regions are observed beneath the fracture surface in the crack initiation and early growth region for interior crack initiation of AM Ti-6Al-4V in VHCF regime. It is proposed that the mechanism of crack initiation and early growth of AM titanium alloys in VHCF regime is attributed to the grain refinement caused by the dislocation interaction followed by cracks combined with the cracks formed at α -phase, interfaces, etc. during cyclic loading.

SEM observation of fatigue fracture surface

Scanning electron microscope (SEM) observation indicates that the fatigue crack of AM Ti-6Al-4V under ultrasonic frequency fatigue test initiates from the surface or the interior of the specimen in VHCF regime, as shown in Figure 2-1. For the interior crack initiation, the fatigue fracture surface presents the fine granular area (FGA) feature, as shown in Figure 2-1 (d).

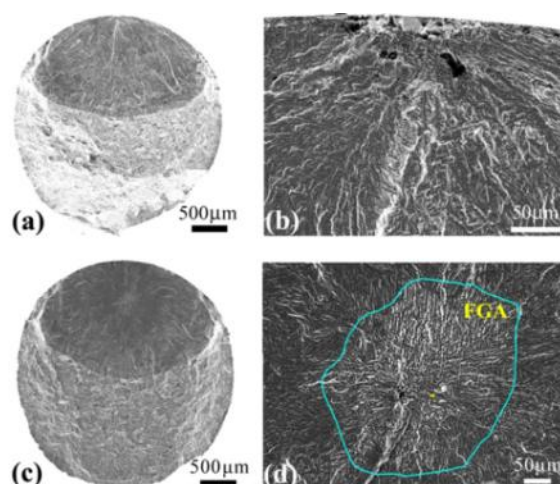


Figure 2-1 SEM observation of fatigue fracture surfaces: (a) and (b): Crack initiation from specimen surface, $\sigma_a=590$ MPa, $R=-1$ and $N_f=5.51\times10^7$; (c) and (d): Crack initiation from specimen interior, $\sigma_a=550$ MPa and $N_f=1.21\times10^8$. The short line in (d) denotes the location where the sample along the loading direction is extracted for TEM observation.

¹Institute of Mechanics, Chinese Academy of Sciences. SUN Chengqi: scq@lnm.imech.ac.cn

TEM observation of microstructure beneath fatigue fracture surface

Transmission electron microscopy (TEM) observation shows that the microstructure of the AM Ti-6Al-4V beneath the fracture surface in FGA exhibits the feature of discontinuous refined grain regions, as shown in Figure 2-2. Based on the results, it is thought that the mechanism of the crack initiation and early growth of titanium alloys in VHCF regime is attributed to the formation of grain refinement caused by the dislocation interaction over a number of cyclic loadings followed by cracks combined with the cracks formed at α -phase, interfaces, etc. during cyclic loadings.

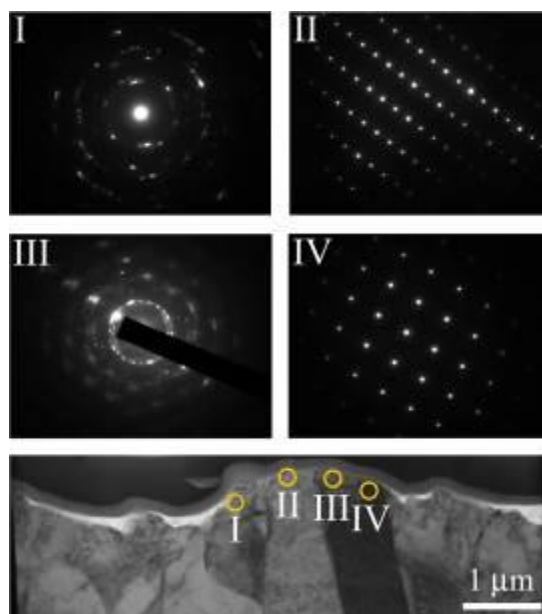


Figure 2-2 TEM observation of the extracted sample at the short line position in Figure 2-1(d), in which the circles indicate the locations where the selected area diffractions are obtained..

2.1.2 Fatigue Failure Mechanism and Life Model in Additive Manufactured Titanium Alloys²

In this project, the fatigue failure mechanism and fatigue life prediction model of laser metal deposition (LMD) titanium alloy materials were studied by means of test and theoretical analysis.

There are three key techniques in the present research: the failure mechanism of LMD titanium alloy materials under fatigue load was studied and classified based on the bimodal lognormal distribution. The P-S-N curve of LMD titanium alloy material was established to predict the fatigue life of the LMD titanium alloy materials. The mechanism of fatigue failure induced by pore defects was studied, and the crack initiation modes caused by internal pores were classified.

The main findings of this study are as follows: the mixed failure behavior of internal crack, surface crack and subsurface crack appeared in the LMD titanium alloy materials under the state of medium and high cycle fatigue. The width of the 0.13%-99.87% dispersion band of the bimodal lognormal distribution mode in the middle and long life period was larger than that of the P-S-N curve based on the traditional unimodal lognormal distribution model. The spherical internal pores with random size and position are the main factors of fatigue failure of LMD titanium alloy materials.

Mixed failure models and P-S-N life curves

² Beihang university. HE Xiaofan: xfhe@buaa.edu.cn.

The mixed failure behavior of internal crack, surface crack and subsurface crack appeared in standard smooth LMD Ti-6.5Al-2Zr-1Mo-1V titanium alloy under medium and high cycle fatigue state. The proportion of internal crack was related to the stress level. With the increase of stress level, the proportion of internal crack decreased. For the internal porosity failure model, there was no significant positive or negative correlation between fatigue life and the size and location of porosity defects as shown in Figure 2-3.

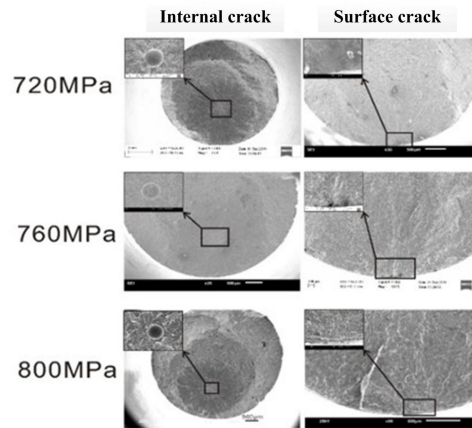


Figure 2-3 Typical fracture surfaces of specimens with internal crack initiation and specimens with crack initiating from surface under three stress levels.

Based on the bimodal lognormal distribution (BLG) of five variables, a bimodal lognormal distribution model was established to describe the fatigue life of LMD titanium alloy by using Basquin equation and linear superposition method. The fatigue life data obtained from fatigue tests were verified. The parameter estimation method based on maximum likelihood estimation (MLE) was used to estimate the parameters of the BLG distribution, and Newton-Raphson algorithm was used to solve the nonlinear equations derived from the likelihood function. Under the three stress levels, the bimodal lognormal distribution model could well describe the distribution characteristics of fatigue life, and the width of the 0.13%-99.87% dispersion band in the middle and long life was larger than that of the P-S-N curve based on the traditional single peak lognormal distribution model as shown in Figure 2-4

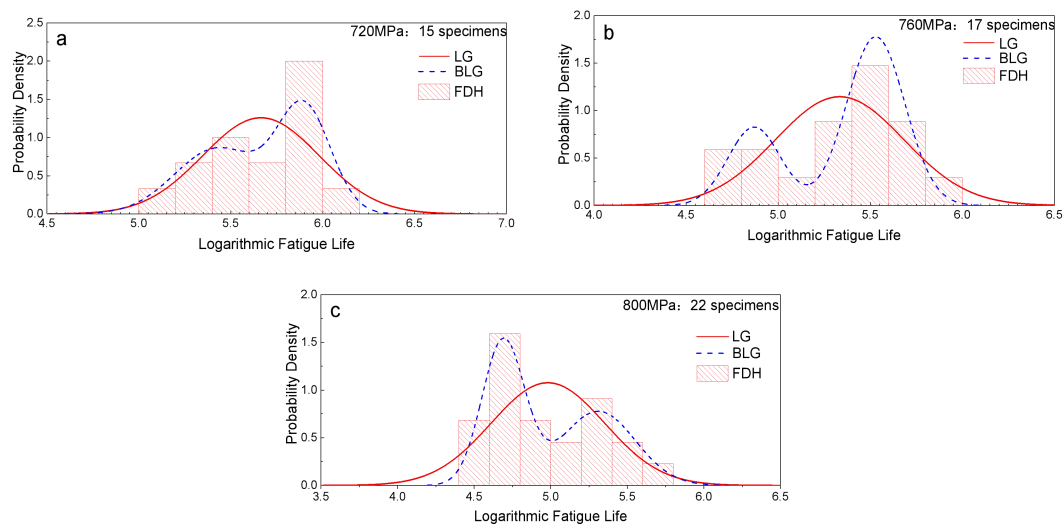


Figure 2-4 Probability density function (PDF) curves and frequency distribution histograms (FDHs) of specimens under (a) 720, (b) 760, and (c) 800 MPa

The mechanism of fatigue failure induced by pore defects

In three kinds of stress level in the alternating stress under constant amplitude fatigue test, 31 pieces of LMD Ti-6.5-Zr-Mo-2V, whose cracks were initiated from the internal porosity of sample, using scanning electron microscope (SEM) and energy spectrometer (EDS) and electron back scattering diffraction test results with electron backscattered diffraction (EBSD), were analyzed and the characteristics of the pore defects were found: (1) the ball-shape, and the size and location of random internal porosity was the main factor of LMD titanium alloy fatigue damage. (2) Aluminum segregated on the surface of the pores, which made the surface of the pores brittle, and had high crack sensitivity, and was prone to fatigue failure. (3) Cleavage of columnar grains was the mechanism of pore induced fatigue crack initiation. Due to the existence of pores, incomplete grain boundaries appeared around pores, and micro-cracks were formed under the action of cyclic stress. The micro-cracks cleavage along the specific plane of microscopic columnar grains. (4) According to the size of pores, columnar grains and small size α phases in columnar grains, the crack initiation modes caused by internal pores could be divided into four types: the crack initiation from small pores, the crack initiation from medium pores and the crack initiation from large pores (contains a main facet or does not contain a main facet) as shown in Figure 2-5 and Figure 2-6.

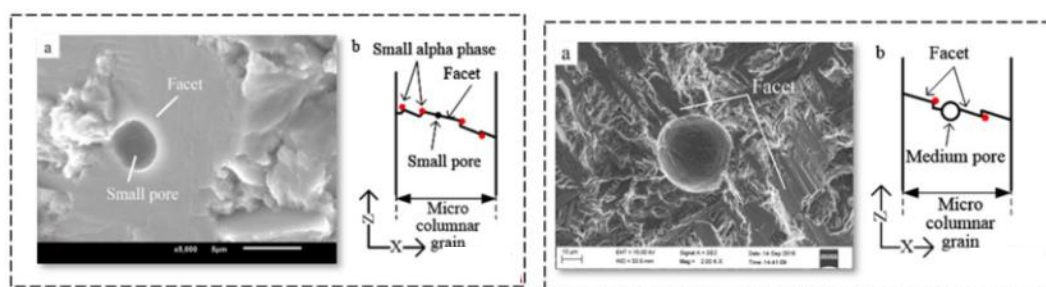


Figure 2-5 (1) (a) Typical small pore morphology and (b) schematic diagram. (2) (a) Typical medium pore morphology and (b) schematic diagram.

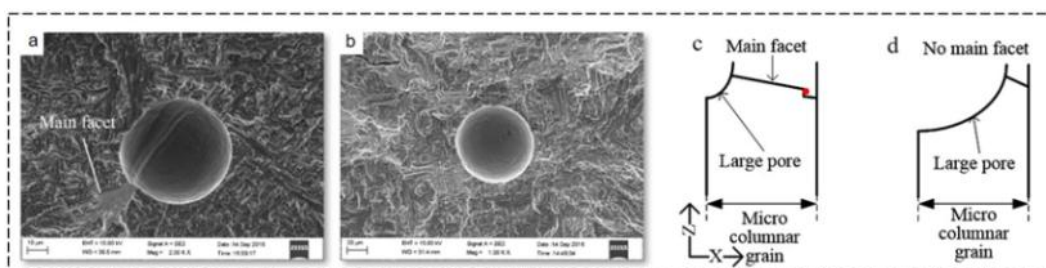


Figure 2-6 (a) Typical large pore including cleavage and (b) Typical large pore without cleavage. Schematic diagrams of large pore that (c) contains a main facet (d) does not contain a main facet.

2.1.3 Study on The Residual Stress Effects and Anisotropic Fatigue Performance of Additive Manufacturing Titanium Alloy³

There are two key techniques in the present research, which are as follow: the experiment investigation on the anisotropic fatigue strength and fatigue crack growth behavior due to build direction; The effect of heat treatment and notch cutting processing on the residual stress distribution of AM titanium were analyzed. And then the fatigue crack growth rate and crack path of AM alloy with different residual

³ Northwestern Polytechnical University. MA YuE: ma.yu.e@nwpu.edu.cn

stress were compared and analyzed.

The key finds in the present research are as follows: The anisotropy of fatigue performance was governed by the coupling effects of the microstructure and textures. When the interlayer interaction due to texture was weaker than the interaction of columnar grain due to microstructure, the horizontal sample appeared lower fatigue strength than the vertical sample. On the contrary, the vertical sample will have good fatigue performance. Build direction can affect the residual stress distribution due to different laser vector length. The compressive residual stress on the specimen surface will turn to tensile stress after SR and surface treatment processing that can improve the fatigue resistance. In addition, the fatigue crack path is also influenced by the build direction.

Effects of the build direction on fatigue life

The microstructure and texture of AM titanium are affected by the build direction. The columnar grain grows along the build direction during printing processing. The texture and lack of fusion defects will occur in the interlayers due to imperfect overlap. Different angles between the load direction and build direction will lead to entirely different mechanical and fracture response, shown as Figure 2-7.

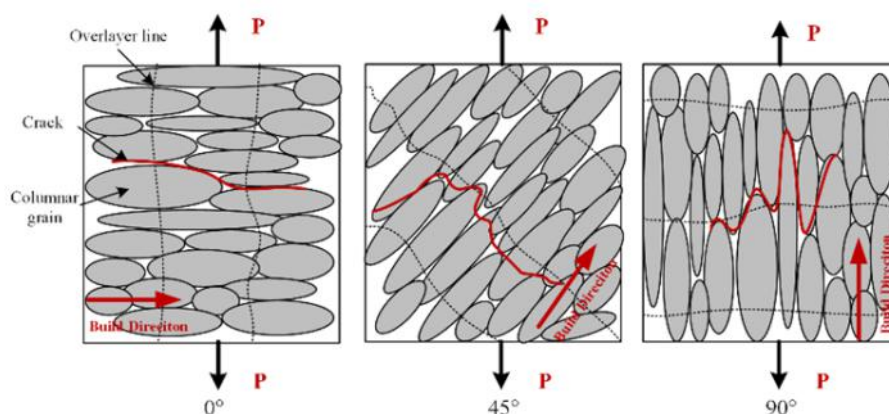


Figure 2-7 Illustration of microstructure, texture and build direction

Nowadays, the static strength of AM titanium alloy can compare favorably with the conventional one. But the fatigue performance still has a large scatter and need to be improved due to the defects and texture. In this study, the interlayer interaction due to texture performs well, and that lead to a better fatigue strength of the 90° sample than that of the 0° sample, shown as Figure 2-8. The fracture morphology analysis show that the pore defects locating in sub-surface are the main reason for the fatigue crack initiation. Several crack initiation sources can be observed on the 0° sample, shown as Figure 2-9.

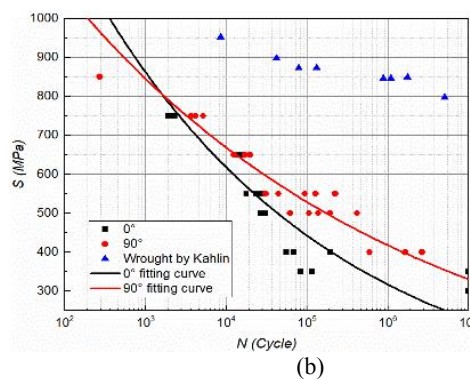
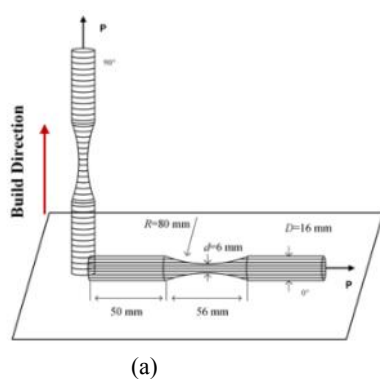


Figure 2-8 Fatigue strength of different build direction samples: (a) Definition of the build direction, (b) Comparison of the S-N curves

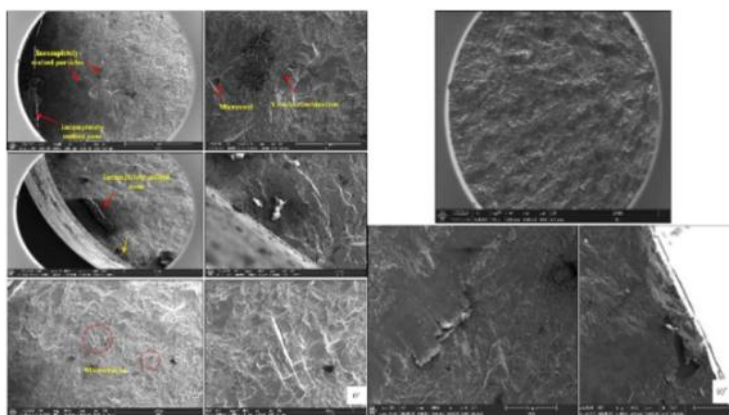
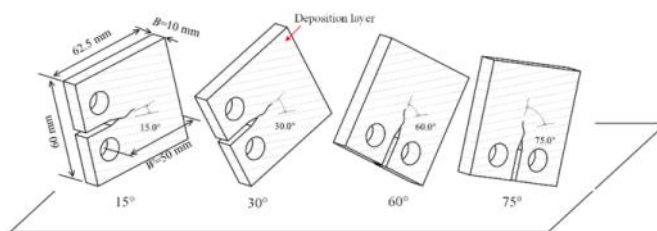


Figure 2-9 Fracture morphologies of the 0° and 90° sample

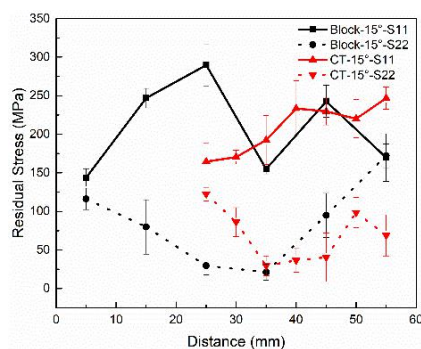
Effects of residual stress and build direction on fatigue crack growth behavior

CT samples with different build directions (0° , 15° , 30° , 45° , 60° , 75° , 90°) were designed and shown as Figure 2-10(a). The residual stress field near the crack tip will redistribute after notch cut in Figure 2-10(b). The stress along the crack path (S11) decreased while the stress vertical to the crack path increased. The increase of S22 will accelerate the fatigue crack growth rate. Build direction can affect the fatigue crack growth life. The fatigue crack growth life of the 45° sample was about 1.37 and 1.19 times longer than that of the 0° and the 90° samples respectively. Curves of fatigue crack growth rate versus stress intensity factor range of three kind samples were similar, shown in Figure 2-10(c).

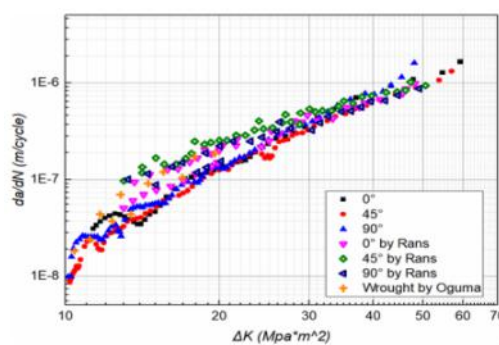
Different textures and morphologies can be observed on the CT fracture surfaces, shown in Figure 2-10. Stress relieving and surface treatment processing can turn the compressive residual stress to tensile residual stress, and improve the fatigue performance. Residual stress and build direction can change the fatigue crack path, but SR has no effect on the crack path, shown in Figure 2-11.



(a)



(a)



(c)

Figure 2-10 Residual stress and fatigue crack growth rate: (a) Build direction definition of CT samples, (b) Residual stress before/after notch cutting, (c) Comparison of fatigue crack growth rates

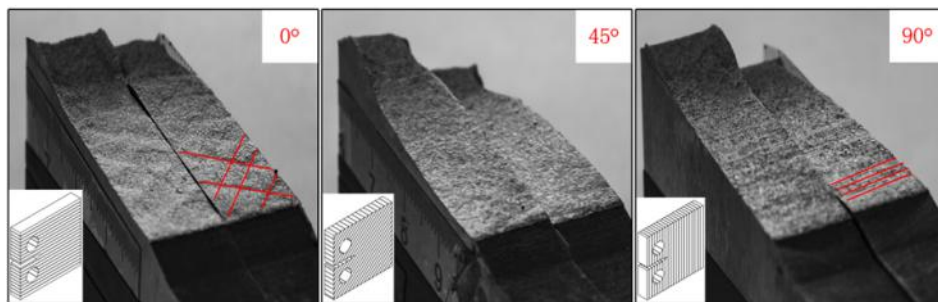


Figure 2-11 Fracture surfaces of different build direction samples

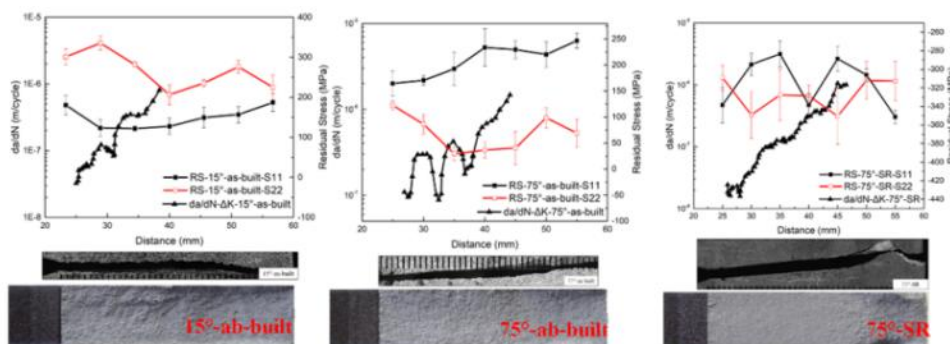


Figure 2-12 Crack paths for different build direction samples and residual stress field

2.1.4 Research on Influence of Defect and Mechanical Properties of High Strength Aluminum Alloy Based on Selective Laser Melting⁴

The research includes three key contents: preparation and experimental testing of high-strength aluminum alloy SLM material specimens; establish a finite element model of material with defects based on micromechanics based on the test data, and on this basis, the influence of the characteristic parameter changes of pore defects on the tensile properties of the material is studied.

Studies have shown that the Al-Mg-Sc-Zr alloy formed by SLM has the effect of pinning the grain boundary by the enriched Al₃ (Sc, Zr) particles at the boundary of the molten pool, which had an important contribution to grain refinement and improvement of mechanical properties. But the current SLM process cannot eliminate a small number of pore defects and inclusion defects in the Al-Mg-Sc-Zr alloy under the optimized process parameters. In order to study the influence of internal defects of additive manufacturing materials on the mechanical properties of materials, The finite element model with defects is established by the method of representative volume element. The prediction results of the model in terms of elastic modulus, tensile strength and stress-strain curve are in good agreement with the experimental results. Further simulation analysis shows that the porosity size has an effect on the elastic modulus and tensile strength of the material. With a certain porosity, within the range of pore size from 25 μm to 175 μm , the change of pore size has a small effect on the elastic modulus and tensile strength of the alloy, and is not as significant as the porosity. In addition, the overall orientation of the pores has a significant effect on the uniaxial tensile load.

Preparation and Experimental Test of High-strength Aluminum Alloy SLM Material Specimen

⁴ Civil Aviation University of China. CHEN Kun: cknuaa@gmail.com

The room temperature quasi-static tensile test piece adopts the same batch of SLM formed Al-Mg-Sc-Zr alloy as the microstructure and defect morphology analysis, and is processed in accordance with ASTM E8/E8M. In order to test the quasi-static tensile properties of the material, in a quasi-static uniform load was applied to the test piece at room temperature (25°C), and the tensile performance data obtained are shown in Table 2-1.

Table 2-1 Al-Mg-Sc-Zr alloy static tensile properties

Specimen	Modulus of Elasticity (GPa)	Tensile strength (MPa)
1	64.25629	506.3
2	66.88485	510.5
3	67.25676	507.7
average value	66.1326	508.1667
Dispersion coefficient (%)	2.0193	0.3436

In order to measure and analyze the internal defects of materials, metallographic sectioning, Archimedes and X-ray computed tomography (XCT) methods are usually used to evaluate the morphology and content of defects. Figure 2-13 is a three-dimensional reconstruction of pore defects. In order to analyze the characteristics of defects, statistical methods can be used to study the distribution characteristics of defects. For this material, the normal distribution function (Gauss) is selected to fit the outer contour of its frequency histogram. The expression of the fitting function is:

$$y = y_0 + \frac{A}{w\sqrt{\pi/2}} \exp(-2(x - x_c)^2 / w^2) \quad (2-1)$$

where y_0 , x_c and A are scale parameters; w is shape parameter of the fitted curve. The fitting results show that the size distribution of material pore defects obeys the normal distribution, as Figure 2-14.

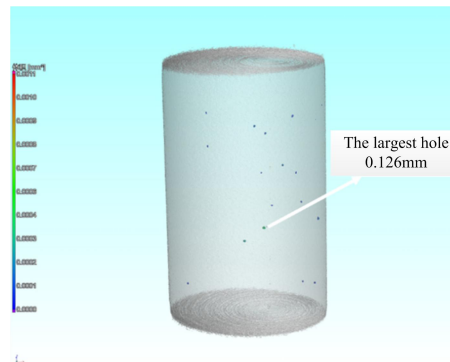


Figure 2-13 Three-dimensional reconstruction of the internal pore defects of the sample

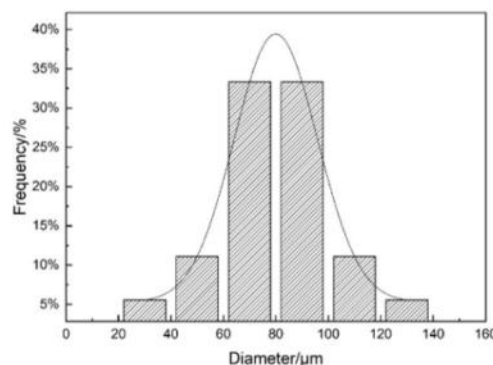


Figure 2-14 Fitting curve of normal distribution of pore defect size

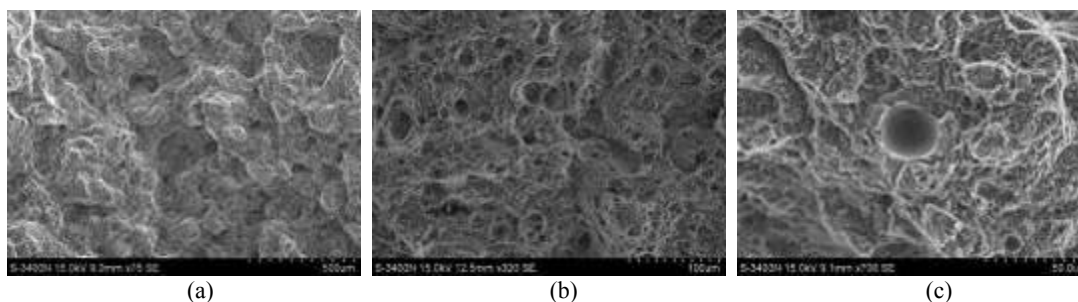


Figure 2-15 Fracture characteristics of Al-Mg-Sc-Zr alloy tensile test pieces: (a) Macro overall topography, (b) Cleavage plane and dimples, (c) Spherical pore defects

According to the fracture observation results of the tensile test pieces in Figure 2-15, the fracture mode of the Al-Mg-Sc-Zr alloy is a mixed mode of toughness and brittle fracture.

Influence of Pore Defects on Alloy Tensile Behavior

Based on our meso-level finite element model with defects, the influence of porosity, pore diameter, sphericity and pore orientation on the tensile properties of the alloy is analyzed.

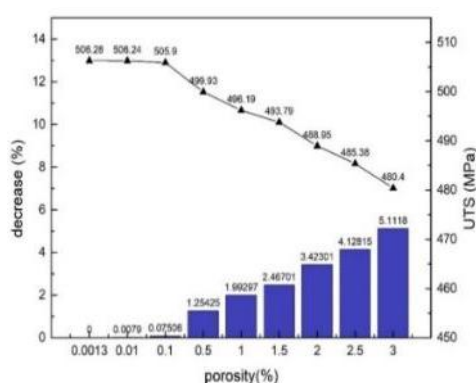


Figure 2-16 The change law of material tensile with porosity

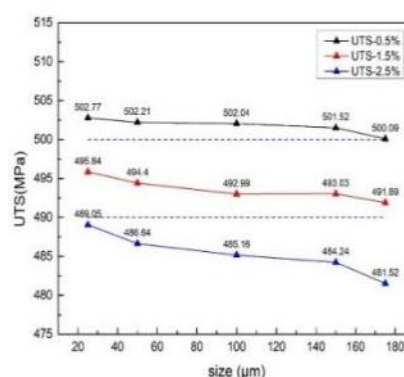


Figure 2-17 The change law of material tensile strength with pore size

So far we have only studied the static mechanical properties of the material. It can be foreseen that internal pore defects will have a more significant impact on the fatigue of high-strength aluminum alloy materials manufactured by additive manufacturing. We will carry out fatigue tests in the future and study fatigue crack growth based on multi-scale Predictive simulation method.

2.1.5 Fatigue Property Evaluation and Creep Crack Growth Simulation of AM Titanium Alloy With Manufactured Defects⁵

According to the ASTM standard, specific AM CT and fatigue samples are designed and performed to get the fatigue performance and crack growth results (samples shown in Figure 2-18). It is observed that micro structure feature plays important role on the fatigue performance besides internal defects. The internal defects and micro features are shown in Figure 2-19 and Figure 2-20. These features are observed to recognize the relationship between that and fatigue properties.

⁵ AVIC Aircraft Strength Research Institute. XI Jiangjing: asri_xijiangjing@163.com

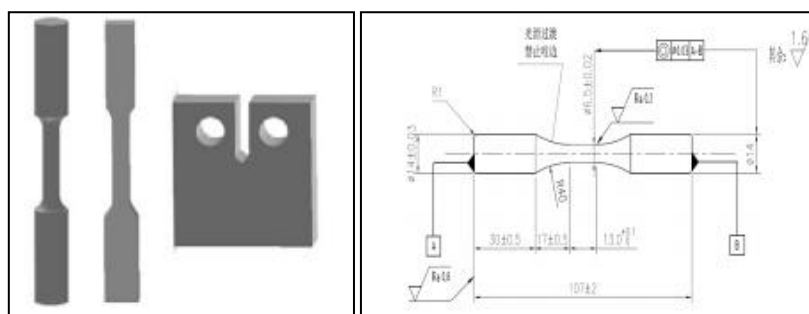


Figure 2-18 Fatigue and CT samples geometry

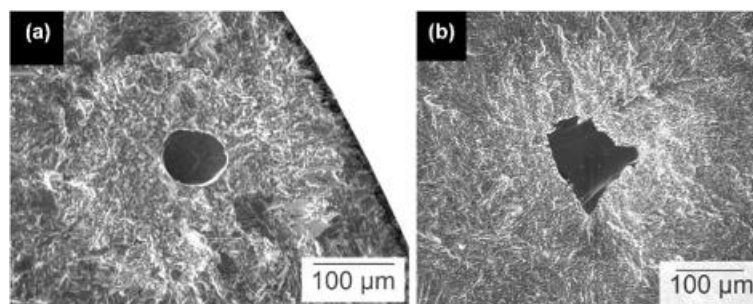


Figure 2-19 Fractography of AM fatigue samples

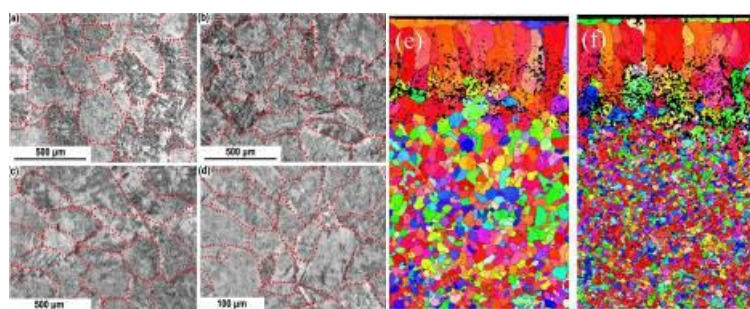


Figure 2-20 Microstructure of multi manufacturing parameters AM structure.

Creep fatigue crack growth simulation of AM titanium alloy

Based on the damage model, creep fatigue crack growth was researched and grain size, volume ration and distribution of defects are taken into consideration to verify their effect on creep fatigue. As shown in Figure 2-21, crack tip a crack growth path area are meshed specifically based on the micro structure characterization. In the crack tip, two types of crack growth methods are taken into consideration to verify the failure mechanism. As shown in Figure 2-22, intergranular and trans granular failure are both simulated and crack tip stress are shown as well.

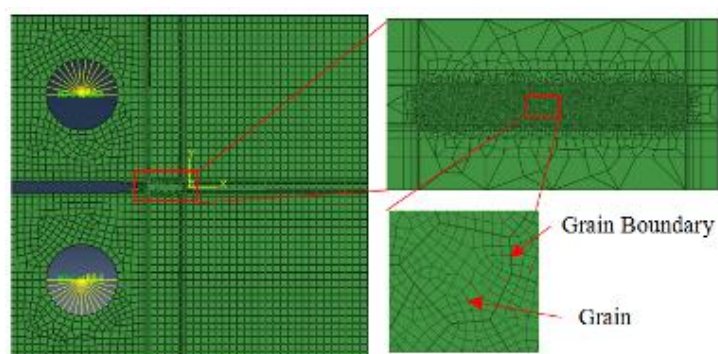


Figure 2-21 CT simulation model

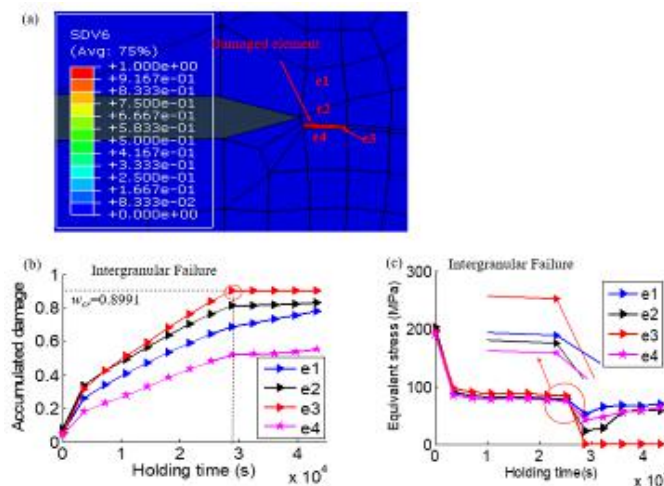


Figure 2-22 Intergranular failure and stress at crack tip grains

Based on the damage model, 8 micro structure features cases of crack growth model were performed without defects. Besides the micro structure, defects like voids are also critical to the crack growth, the simulation and defects which take the voids density and distribution are taken into consideration. The results are shown in Figure 2-23.

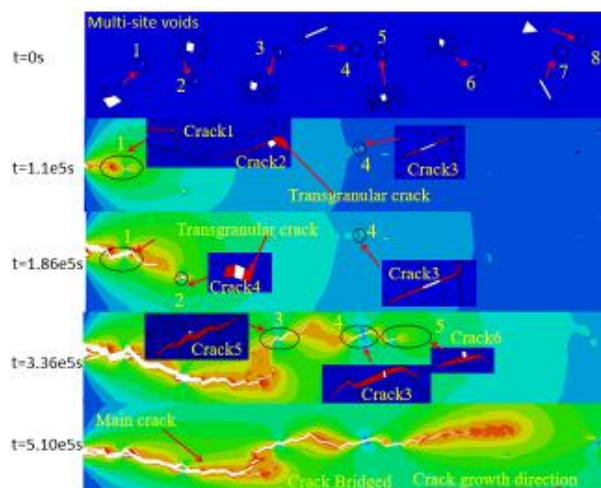


Figure 2-23 Simulation creep fatigue crack growth results considering the defects density

The future work is to verify the CT samples to compare to the simulation results and the aim of this project is to establish a acceptable AM titanium alloy fatigue property predicting model.

2.1.6 Fracture Performance of Ti-Alloy Made by DED Additive Manufacturing⁶

The present research is to investigate the fracture toughness and crack propagation rate of the Ti-alloy parts made by both LMD and micro-casting and forging process. Based on the experimental results, the two additive manufacturing processes were evaluated and compared.

In the present research, both of the LMD and the micro-casting and forging process can provide a good damage tolerance performance for the Ti-alloy structural parts which is at least as good as the traditional forging process. Compared to the LMD, the micro-casting and forging process was proved to be a success alternative to improve the fracture toughness and decrease the crack propagation rate.

⁶COMAC Beijing Aircraft Technology Research Institute. ZHANG Ye: zhangye2@comac.cc

Introduction of the micro-casting and forging process

The scope of the micro-casting and forging process is shown in Figure 2-24. It applies a suitable rolling force to continuously rolling the weld bead formed by the free fusion deposition material. The free-growing coarse columnar crystals are broken and the purpose of grain refinement and performance isotropy is achieved. At the same time, the residual stress is more possibly eliminated and the occurrence of the internal defects are reduced. Therefore, a better internal microstructure of Ti-alloy is obtained and the overall material properties can be significantly improved.

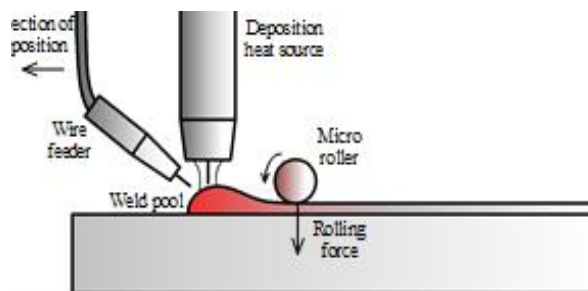


Figure 2-24 Scope of the micro-casting and forging process of additive manufacturing.

Experiments of fracture toughness and crack propagation rate

The fracture toughness tests were carried out based on ASTM E399 standard and a typical specimen's configuration is shown in Figure 2-25(a). Following the ASTM E647 standard, a constant amplitude cyclic load is applied to the compact test specimen as shown in Figure 2-25(b) and the crack propagation rate was experimentally obtained.

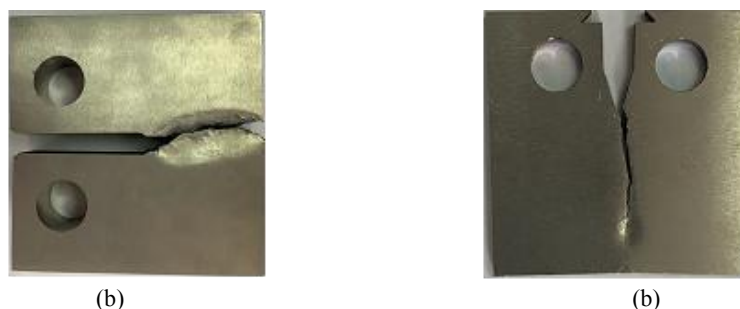


Figure 2-25 Atypical specimen (failed) for (a) fracture toughness and (b) crack propagation rate tests

In order to consider the anisotropic material properties of additive manufacturing, the direction of the specimens is defined and the schematic diagram of the specimens is shown in Figure 2-26. The material is defined as Z-direction. The specimen for fracture toughness is arranged in ZX and XZ direction as while as the specimen for crack propagation rate test was arranged in ZX, ZY and XY directions.

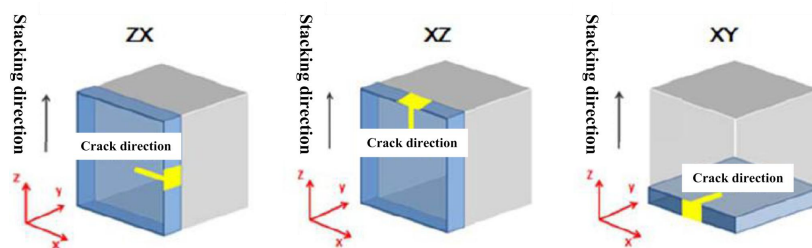


Figure 2-26 The direction of specimens.

Comparison of experimental results

The fracture toughness of Ti-alloy specimens made by LMD and micro-casting and forging process is compared in Figure 2-27, considering the specimen arrangement direction of XZ and ZX. Both additive manufacturing processes were proved to be able to provide fracture toughness performance at least as good as the traditional forging process. Moreover it indicates by employing the micro-casting and forging process, the fracture toughness was significantly improved by around 35% in both XZ and ZX directions.

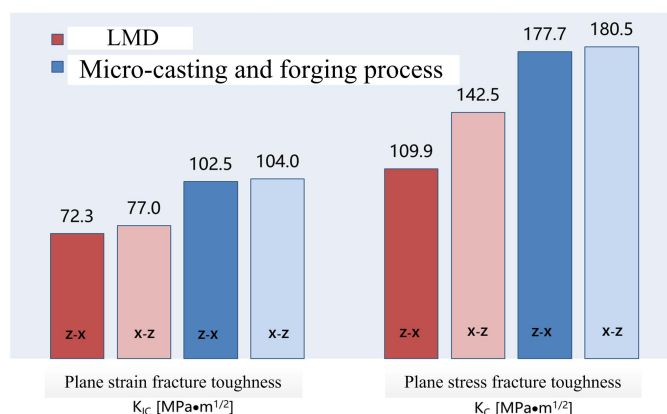


Figure 2-27 Comparison of fracture toughness experimental results.

The crack propagation rate of Ti-alloy specimens made by LMD and micro-casting and forging process is compared in Figure 2-28, considering ΔK having a value of 11 MPa with $R=0.1$. Both additive manufacturing processes have given acceptable results of crack propagation rate. The specimens made of the micro-casting and forging process exhibited a much slower crack growth compared to the LMD process.

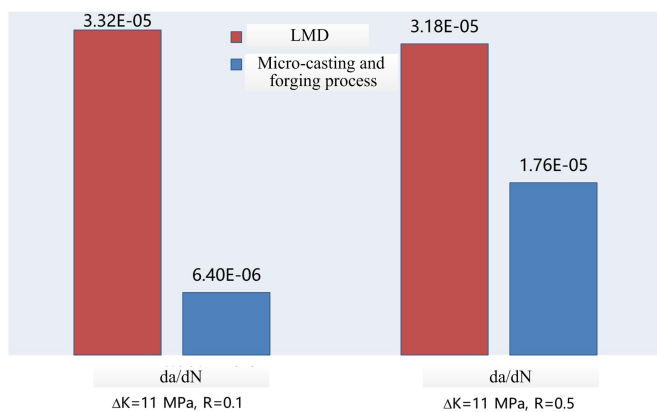


Figure 2-28 Comparison of crack propagation rate experimental results.

2.1.7 Fatigue Evaluation Method of Titanium Alloy Additive Manufacturing⁷

Aiming at the structure of titanium alloy (TC11) laser additive manufacturing, the relationship between microstructure and fatigue properties, mechanical properties test and characterization, multi-defect stress intensity calculation, probabilistic damage tolerance modeling, typical parts/ components test were carried out, and the fatigue evaluation method was established to meet the characteristics of titanium alloy structure.

⁷AVIC The First Aircraft Institute. LEI Xiaoxin: rentian1234@126.com

Study on the relationship between microstructure and fatigue properties of materials.

The microstructure morphology of TC11 titanium alloy produced by laser addition is shown in Figure 2-29. The results show that the fatigue properties of TC11 titanium alloy can be decreased by the presence of defects as shown in Figure 2-30. The main defects in TC11 titanium alloy made by laser addition are stomata. The position and size of the stomata are random, but most (more than 60) are distributed in the annular region less than 1mm from the surface of the specimen, and the diameter is less than 150 μ m. When the stomatal size is equal, the greater the distance between the stomata and the surface has the better the fatigue property of the specimen. When there are other kinds of defects near the hole, the fatigue performance of the specimen is worse than that of the sample containing only the hole defects. When there are many defects in the sample, the fatigue cracks often arise from the defects near the surface of the specimen.

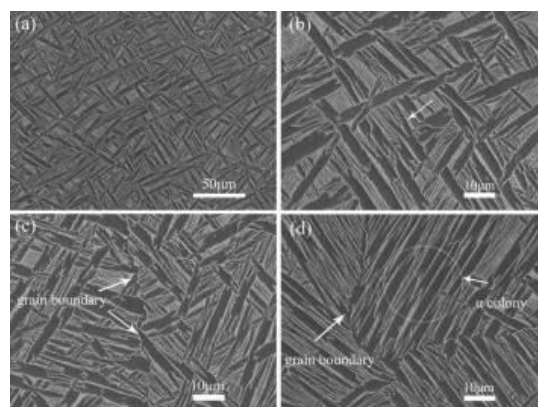


Figure 2-29 Microstructure Morphology of TC11 Titanium Alloy additive manufacturing

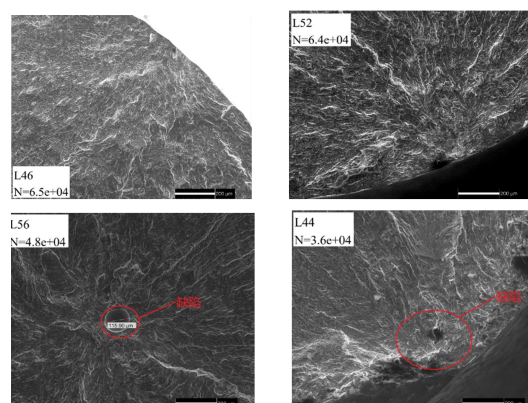


Figure 2-30 Comparison of fracture surfaces between non-obvious defect samples and defect Samples

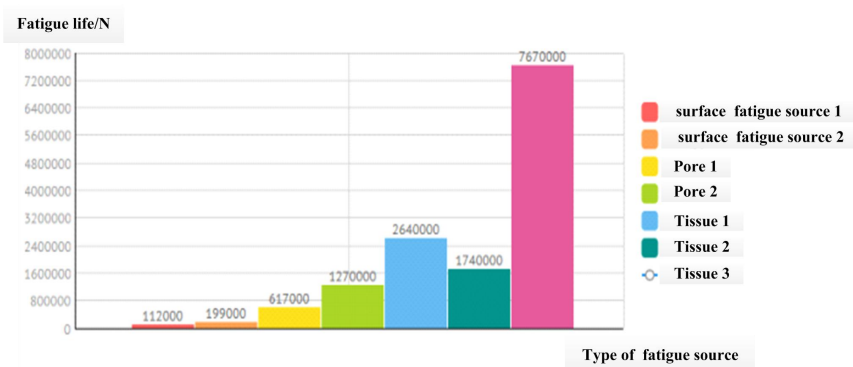


Figure 2-31 Comparison chart of test life of different types of defects

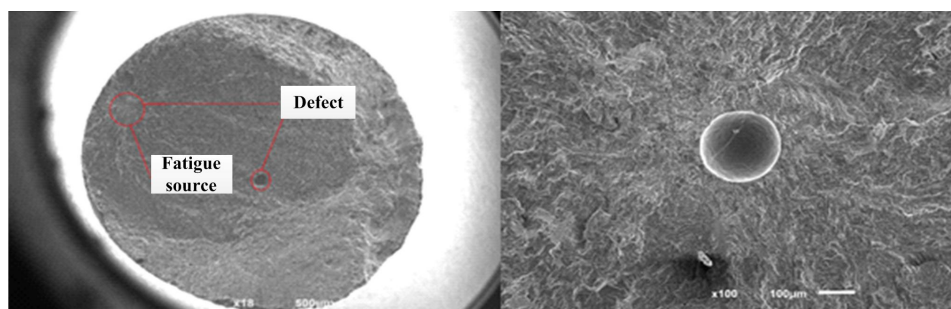


Figure 2-32 Fatigue sample stomatal defect schematic diagram

Study on Evaluation Method of Durability and Damage Tolerance.

The DFR_{cutoff} and DFR_{base} of titanium alloy were obtained by means of complementary testing and a large number of fatigue test data. The corresponding fatigue life Weibull distribution shape parameter α and shape parameter value of 2.5. The value of DFR_{cutoff} is 533 MPa for L direction and 510 MPa for ST direction, respectively. The value of DFR_{base} is 136 MPa for L direction and 141 MPa for ST direction, respectively. On the basis of considering the uncertainty of the type, size and location of internal defects in typical titanium alloy structures, a method and program for evaluating the probability damage tolerance of typical components (lug, joint plate) considering surface defect, embedded defect and penetrating defect are established, which includes random distribution, extension and connectivity of the defects.

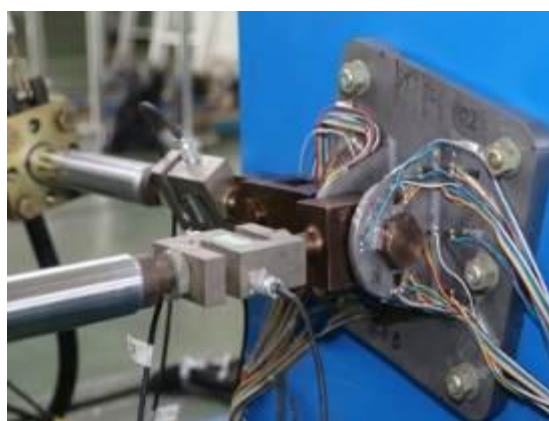


Figure 2-33 Diagram of durability and damage tolerance test for typical lug joints

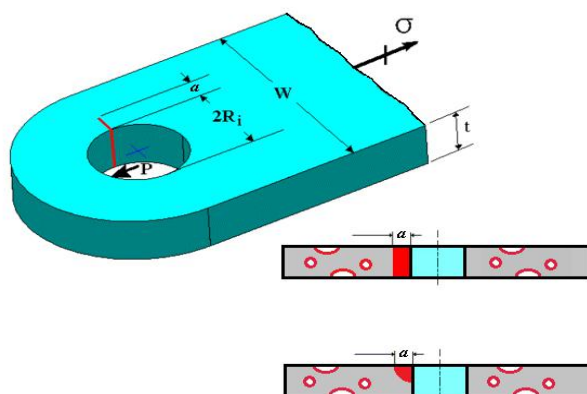


Figure 2-34 Typical lug structure and defect schematic diagram

2.1.8 The Validation Technology of Additive Manufacturing⁸

The validation technology of fatigue properties of AM titanium alloy structure by LMD should in the test and analysis pyramid, including the raw material, fabrication method, product specification, structure characteristics and the product test. The pyramid model of AM titanium alloy can see the Figure 2-35 below.

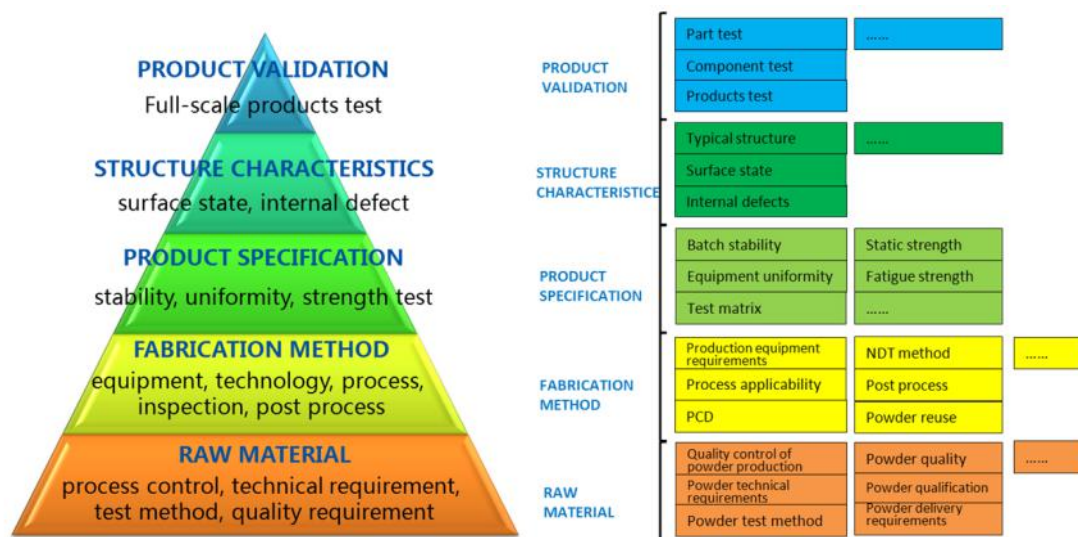


Figure 2-35 The pyramid model of AM titanium alloy by LMD

The lowest level is the raw material validation, including the physical and chemical composition requirements of titanium alloy powder, qualification requirements and delivery requirements, ensure the powder quality is stable.

The second lowest is the fabrication method validation, including the process of AM fabrication and the post process method of the AM roughcast, validate the stability of fabrication process.

The third level is the product specification. Through the fatigue crack growth and high cycle fatigue tests on the standard specimens of different heats and batches, validating the requirements in product specifications of fatigue performance of material level on the basis of stable fabrication process.

The forth level is the structure characteristics validation. Validate the fatigue crack growth, low and high cycle fatigue performance of typical structural features, surface state and internal defects.

The top level is the product validation. For the full-scale products, carry out the test of part, component and even the whole products, validating the compliance of the products under the actual fatigue loads.

⁸ COMAC Shanghai Aircraft Design & Research Institute. Xi Wei: xiwei@comac.cc

2.2 WELDING TECHNOLOGY

2.2.1 Study on Mechanical Properties and Residual Stress of Friction Stir Welding⁹

There are three parts in this work. First, the mechanical properties and microstructure of FSW joint in different regions were studied. Secondly, residual stress profiles of the 2024/7075 dissimilar FSW welded plate were measured. A three-dimensional finite element model was used to calculate and compare with the measurements. Then residual stress distribution of the multi-welded stiffened panel was analyzed.

The main conclusions of this study are as follows. Tensile properties of the heat affected zone (HAZ) were higher than that of the welded zone (WZ) and the thermo-mechanically affected zone (TMAZ). 7075 advancing TMAZ showed typical deformed grains. Fine and equiaxed grains were presented in the WZ. In TMAZ, larger local plastic deformation was larger than that of the WZ. The neutron diffraction result was shown that the longitudinal residual stress presented a "bimodal" shape near the weld, and the peak stress slanted to the 7075 side. The maximum residual stress decreased from the top scan line to the bottom scan line. The numerical simulation results agreed with the neutron diffraction measurements. The residual stress distribution of stiffened panel was affected by the welding sequence, and the maximum residual stress appeared on the stringer that was welded later.

Microstructure of FSW joint and its relationship with mechanical properties

The dynamic tensile test results of 2024 welded joint in different zone is shown in Figure 2-36. For 2024 aluminum, the yield stress of the HAZ was 28% higher than that of the WZ. The peak flow stress of the HAZ was 7% higher than that of the TMAZ. Fracture strain of the HAZ is higher than that of the TMAZ and the WZ.

The 2024/7075 EBSD measuring position is shown in Figure 2-37(a). The orientation map shows the elongated grains in the middle of the advancing TMAZ, as plotted in Figure 2-37(b). In Figure 2-37(c), very fine and equiaxed grains in the middle of the WZ were presented. Grains in the retreating TMAZ (Figure 2-37 (d)-(f)) are slender than that in the WZ. The grain size close to the bottom surface is smaller than that near the top surface.

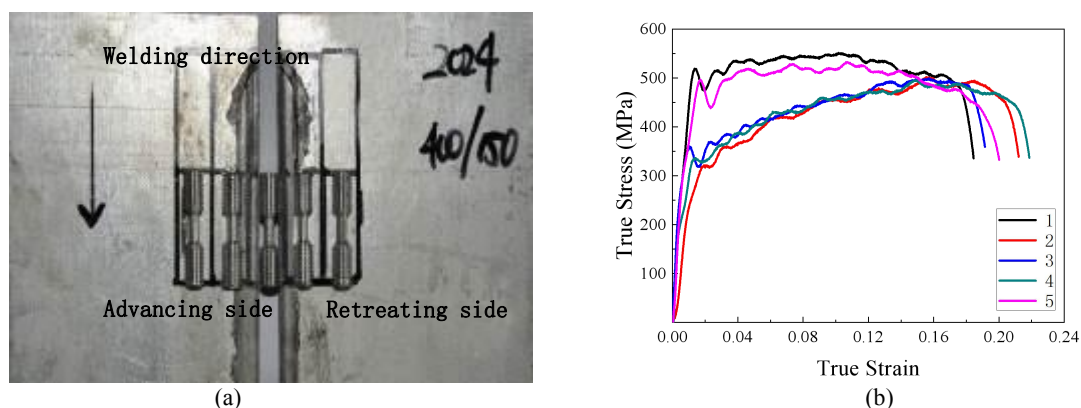


Figure 2-36 The dynamic tensile test results of 2024: (a) position of tensile test samples, (b) stress-strain curves

⁹ Northwestern Polytechnical University. MA YuE: ma.yu.e@nwpu.edu.cn

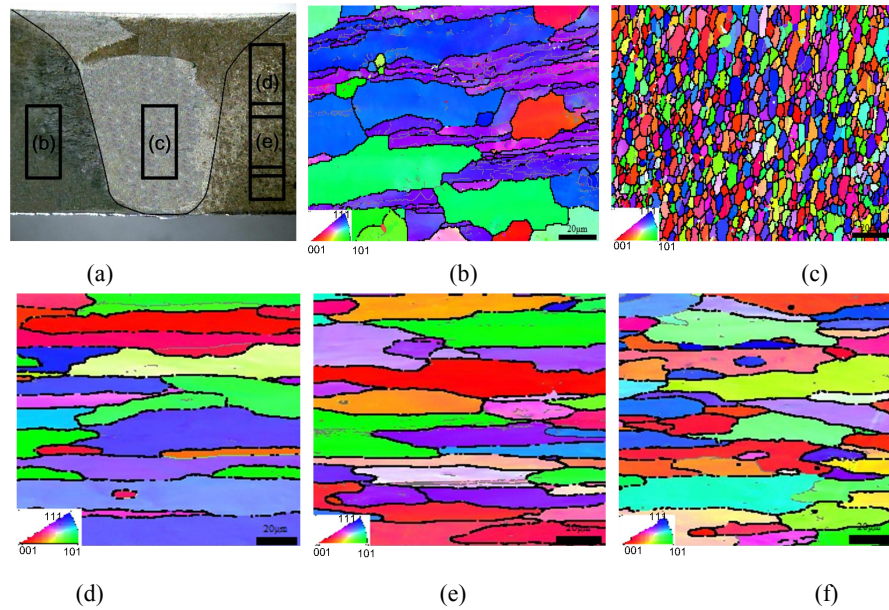


Figure 2-37 2024/7075 EBSD orientation maps and grain boundaries: (a) cross-section of joint, (b) the advancing TMAZ of middle scan line (7075 side), (c) the WZ of middle scan line, (d) the retreating TMAZ of the top scan line (2024 side), (e) the retreating TMAZ of the middle scan line (2024 side), (f) the retreating TMAZ of the bottom scan line (2024 side)

Residual stress profiles of welded structures

The distribution of residual stresses in 2024/7075 dissimilar welded plate was conducted with the Residual Stress Neutron Diffractometer (RSND). The residual stress profiles along the thickness of the sample were measured at the top surface, mid-section and bottom surface, respectively. It was shown that the longitudinal residual stress (LD) presented a "double peak" shape in the weld (Figure 2-38(a)). The transverse (TD) residual stress profile is similar to the normal (ND) residual stress profile, and the maximum residual stress decreased from the top to the bottom surface (Figure 2-38(b)). According to the welding process, the numerical welding parameters were obtained. The temperature and residual stress distribution of FSW were calculated by sequential coupling method and compared with the experimental results acquired by neutron diffraction. The numerical simulation results agree well with the experimental results.

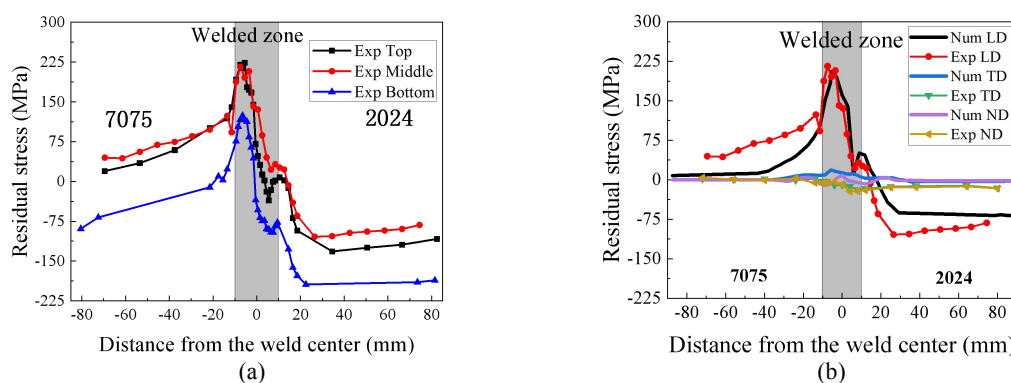


Figure 2-38 FSW residual stress distribution: (a) LD, (b) Experimental and numerical residual stress profile

Master curve method with residual stress factor is proposed to predict fatigue life of welded integral panels

The master curve method with residual stress factor is proposed to predict fatigue life of welded

integral panels, and this method is proved by the experimental results.

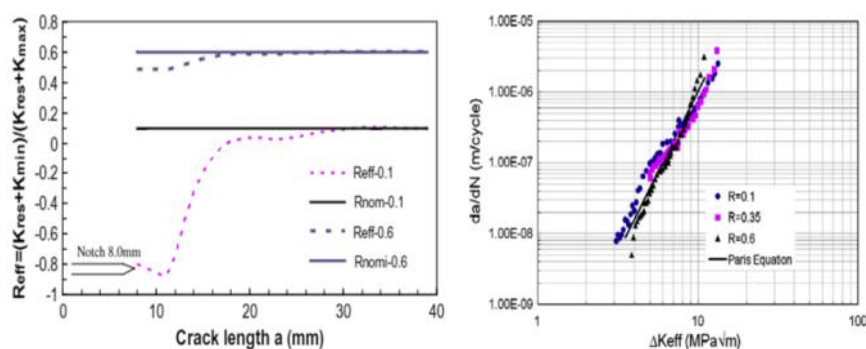


Figure 2-39 Prediction of fatigue life of welded overall structure by master control curve method

2.2.2 Analysis of Crack Propagation Behaviors in Friction Stir Welding Joint Panels with Stringers¹⁰

Friction Stir Welding (FSW) technique provides an easy way to weld the high strength aluminum alloys which used to be considered as non fusion weldable. And the good performance on weight and cost saving, ease on inspection makes it as a new trend in aircraft design. Comparing with traditional rivets joints, the FSW longitude joints have great advantages on weight saving due to elimination of the overlapping area, fasteners and sealing. In addition, it is easier to run automatically, which reduces the cost and labour in the manufacture process. It also provides an easy way for inspection.

Design of typical stiffened panel

Friction Stir Welding (FSW) technique provides an easy way to weld the high strength aluminum alloys which used to be considered as non fusion weldable. And the good performance on weight and cost saving, ease on inspection makes it as a new trend in aircraft design. Comparing with traditional rivets joints, the FSW longitude joints have great advantages on weight saving due to elimination of the overlapping area, fasteners and sealing. In addition, it is easier to run automatically, which reduces the cost and labour in the manufacture process. It also provides an easy way for inspection.

In order to compare different design concepts and damage tolerance performance of fuselage longitudinal joints, two specimens have been prepared for test. The skins are both welded using the FSW method. The stringers are connected to skins using either riveted method or bonded method. The material is Aluminium alloy 2198-T8. The nominal skin thickness is 1.6 mm. The stringer in the Concept 5 is riveted on the skin just upon the welding area. In Concept 6, the stringer is bonded on a doubler and then bonded on the skin. The stringer position is upon the welding area, too. The pad-up area (skin + doubler) is designed to be 2.8 mm thickness to reinforce the weld affected zone in order to compensate the reduce strength property in weld area. The welded centre line is perpendicular to the loading direction. A 30 mm starter notch was machined on the retreating side, 5 mm in Concept 5 and 6 mm in Concept 6 from the welding centre line, using the Electron Discharge Machining (EDM).

¹⁰AVIC Shenyang Aircraft Design & Research Institute. CHEN Liang: 5692864@qq.com

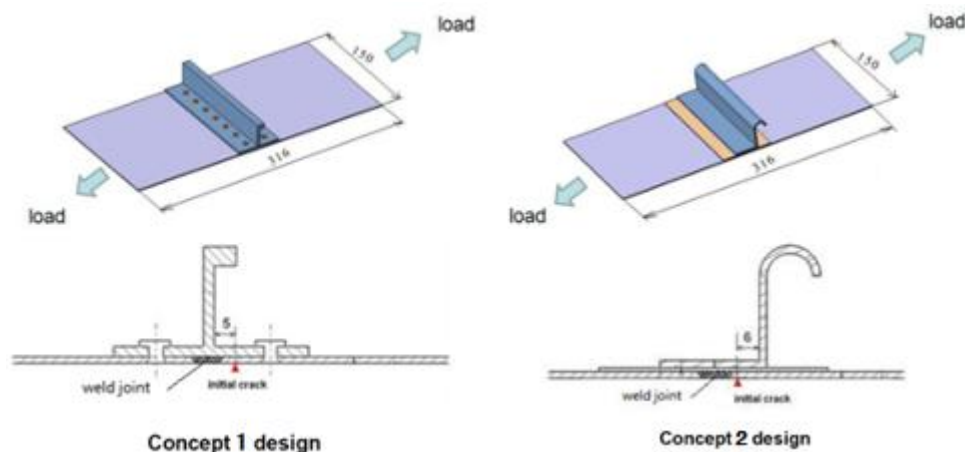


Figure 2-40 Two concepts of design for stiffened panel

Simulation analysis of crack propagation in typical stiffened panel

The displacement extrapolation method was to calculate the K value. The 3D FE models for two concepts were built in which the crack varied from 15mm to 64mm. According to Since the skin is friction stir welded, the effect of welding should be considered in the fatigue life calculation. The crack growth rates in different specimens which reflect the effect of welding are shown in Figure 2-41. According to the relationship between K and β , the β variation with the crack length can be obtained. Using the AFGROW computer program, the fatigue crack growth life and crack growth rate can be calculated and the results are shown in Figure 2-42 and Figure 2-43.

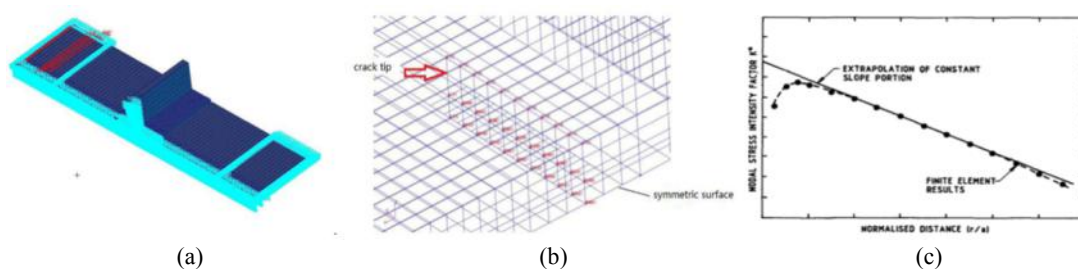


Figure 2-41 Finite Element Simulation of Crack Structure: (a) 3D FE model, (b) crack face, (c) K-r curve

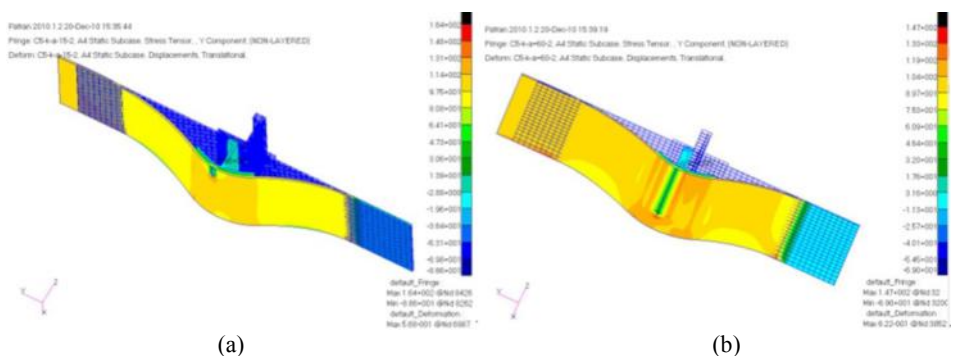


Figure 2-42 Stress distribution under different crack length in design 1: (a) $a=15\text{mm}$, (b) $a=60\text{mm}$

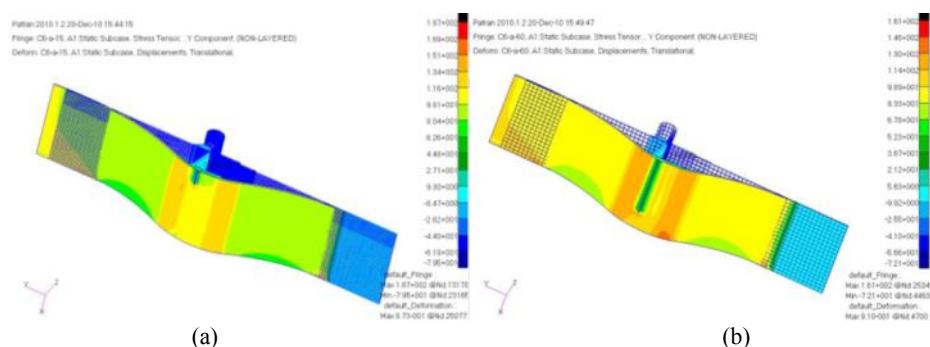


Figure 2-43 Stress Distribution under Different Crack Length in Design 2: (a) $a=15\text{mm}$, (b) $a=60\text{mm}$

Experimental verification of crack propagation in typical stiffened panels

Through the damage tolerance test of typical stiffened panel, the results of crack propagation life and crack propagation rate are obtained, and the validity of the simulation results is verified. The test photos and results are shown in Figure 2-44. The comparison between the experimental results and the simulation results is shown in Figure 2-45. According to the test results, the fatigue life of design 2 is more than 10 times that of design 1. The test results are similar to the results of the welding plate, and are larger than the calculated results of the base metal, which shows that the friction stir welding area has a certain effect on fatigue performance. The main difference between design 1 and design 2 is the connection between the long truss and the skin. In design 1, the truss is directly connected to the skin by a rivet. In design 2, the long truss, the reinforcing plate and the skin are bonded together. At this point, the entire adhesive surface provides a constraint on the crack tip to prevent the crack tip from opening. As the crack tip tends to close, the crack growth rate slows, prolongs the life and increases the damage tolerance. Design 1 has the effect of this constraint only on the connection point, so the effect of the constraint on the crack tip is greatly weakened. Therefore, the crack propagation velocity of design 1 is much faster than that of design 2. In addition, no holes in design 2 reduce the risk of fatigue. Design 2 has more advantages over design 1 in weight reduction.

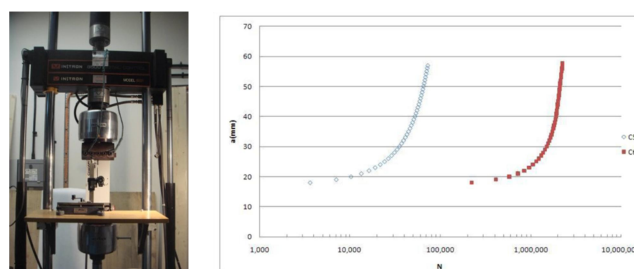


Figure 2-44 Fatigue test and the test results

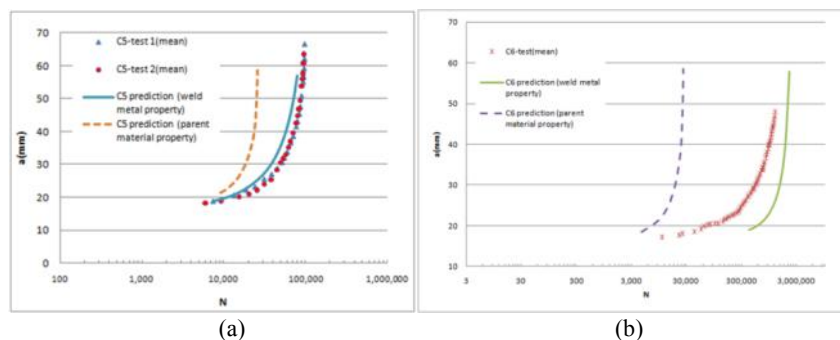


Figure 2-45 Comparison between experimental results and simulation results: (a) Comparison of design 1, (b) Comparison of design 2

2.2.3 Fatigue Crack Growth in Welded Joints of 18Ni High-Strength Steel¹¹

There are two main contents in the present research, which are as follows: experimental research on anti-cracking performance of welded joints of 18Ni high-strength steel, and the fatigue threshold values of the typical areas of welded joints were analyzed; experimental research on crack growth resistance of welded joints of 18Ni high-strength steel, and the fatigue crack growth rates of typical areas of welded joints were analyzed.

The key finds in the present research are as follows: the microstructure characteristics of welded joints of 18Ni high-strength steel have significant influences on the joints' anti-cracking and crack growth resistance. The fatigue threshold value of the welded seam zone with coarse columnar dendrites is higher than that of other zones of welded joint, which indicates that it has better anti-cracking performance. The fatigue crack growth rate of the base metal zone with equiaxed fine-grained structure is lower than that of other zones of welded joints, which indicates that it has higher resistance of crack growth.

Test and analysis of fatigue threshold for welded joints of 18Ni high-strength steel

Fusion welded joint of 18Ni high-strength steel consists of three areas: welded seam zone, heat-affected zone (HAZ) and base metal zone. Microstructure of welded seam zone is dominated by the cast structure of coarse columnar dendrites, and grains have significant directional growth. Microstructure of base metal zone is dominated by the forging structure of equiaxed fine grains. Heat-affected zone is the transition area between welded seam zone and base metal zone, including coarse grains, structure of connecting-junction growth and grain boundaries with severe segregation phases, as shown in Figure 2- 46. The mechanical properties of various types of microstructures are different.

The fatigue threshold values of three typical zones of welded joints of 18Ni high-strength steel were tested with C(T) specimens, as shown in Figure 2-47. The fatigue threshold value of welded seam zone is higher than that of other zones, which is related to the relatively-low strength value and larger grain size of the welded seam material. Additionally, the fatigue threshold value of heat-affected zone is the lowest among all the zones of the welded joints, which indicates that the presence of serious non-uniformity characteristics of microstructure in heat-affected zone has a negative effect on its anti-cracking performance.

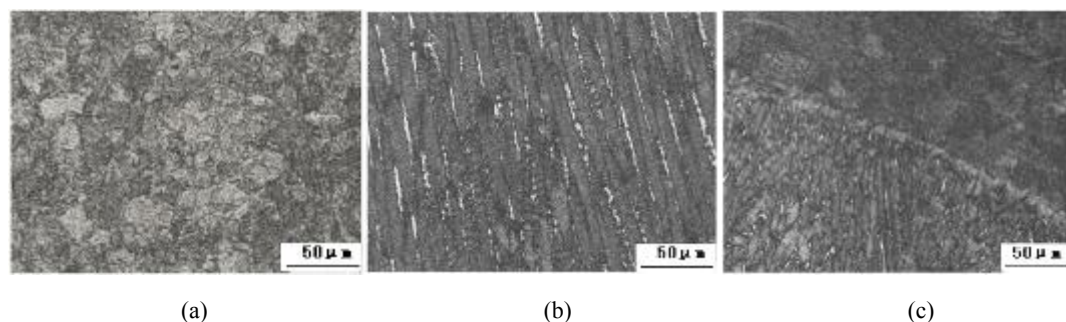


Figure 2- 46 Microstructure and morphology of welded joints of 18Ni high-strength steel: (a) base metal zone; (b) welded seam zone; (c) heat-affected zone

¹¹ AVIC Manufacturing Technology Institute. GUO Delun: zhtbuaa@163.com

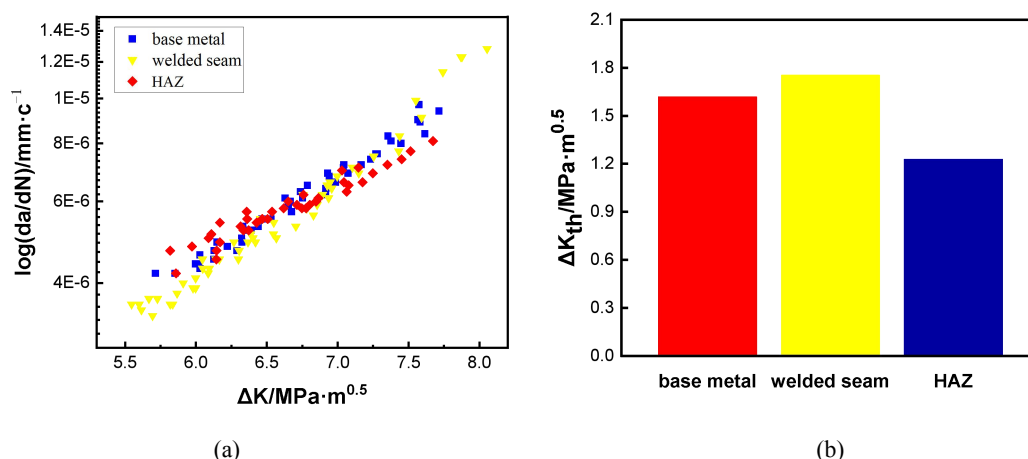


Figure 2-47 Test results of fatigue threshold of welded joints of 18Ni high-strength steel: (a) test data of fatigue crack growth rate; (b) fatigue threshold value

Test and analysis of fatigue crack growth behavior of high-strength steel welded joints

The tests of fatigue crack growth rate for welded joints of 18Ni high-strength steel were carried out with small crack specimens. Especially, the fatigue crack growth behaviors of base metal zone and welded seam zone were analyzed, as shown in Figure 2- 48. The crack growth rate of small crack in welded seam zone is higher than that of base metal zone in the stages of both the near-threshold growth and stable growth. In addition, it is worth noting that the test data of small crack growth rate in the welded seam zone are dramatically dispersive, which indicates that the directional distribution of coarse columnar dendrites in welded seam zone has an effects on the behavior of small cracks growth.

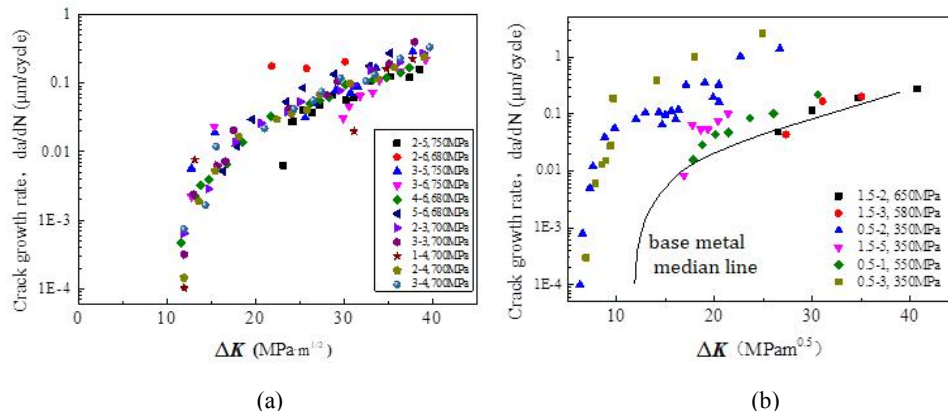


Figure 2- 48 Test results of fatigue crack growth rate of welded joints of 18Ni high-strength steel: (a) base metal zone; (b) welded seam zone

2.2.4 Fatigue Property of Friction Stir Welded Butt Joints for 6156-T6 Aluminum Alloy¹²

In this research, the fatigue property of FSW butt joints for 6156-T6 Al-alloy was investigated. The DFR value of FSW joints was obtained by statistical analysis of experimental data. The micrographs of weld structure were observed by optical microscope (OM) and the microhardness distributions of the FSW joints were also researched.

Microstructure

¹² AVIC Aircraft Strength Research Institute. CHEN An: andychen1986@16.com

The micrographs of weld structure are shown in Figure 2-49. All macrosections of the three different welding conditions (Figure 2-49 (a)) showed such characteristically asymmetric weld structure, which can be generally divided into three regions: nugget zone (NZ), thermo-mechanically affected zone (TMAZ) and heat affected zone (HAZ). It can be seen in Figure 2-49(b) that the NZ is composed of equiaxed grains caused by dynamic recrystallization. The grain size is significantly smaller than in the parent material due to the higher temperature and extensive plastic deformation. As seen in Figure 2-49(c), the grains in the TMAZ are coarsened and partly recrystallized compared to the NZ. The grain structures of the TMAZ are elongated and deformed in an upward flowing pattern around the NZ due to the mechanical action from the welding tool. The distinction between the NZ and the TMAZ can be more easily identified on the advancing side compared with the retreating side. The HAZ is mechanically unaffected by the welding tool. The grains in the HAZ are defective, which is similar to the base material (BM) as seen in Figure 2-49(d) and (e).

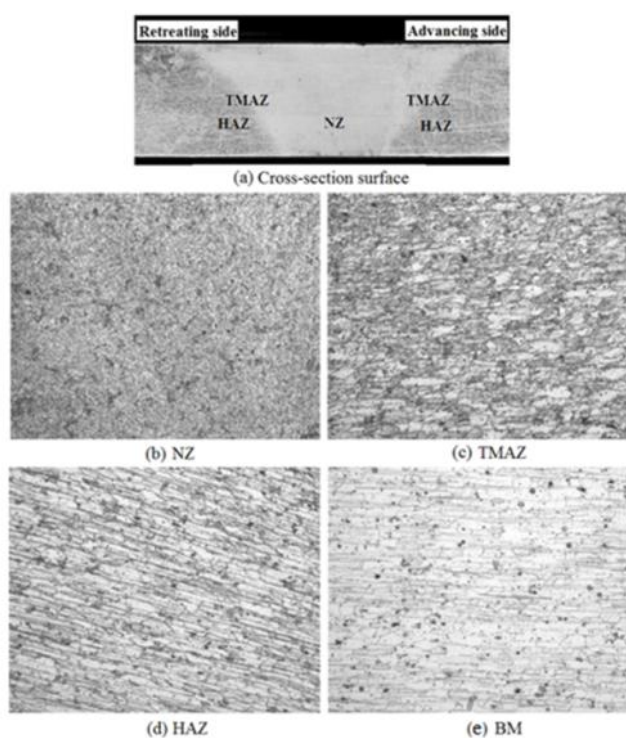


Figure 2-49 Micrographs of FSW

Microhardness distribution

Figure 2-50 shows the microhardness distributions of the FSW joints. Hardness was measured at top and bottom region along the transverse section. The hardness distributions of the FSW joints reveal W-shaped profiles. Generally, the hardness of the NZ is slightly lower than the BM and HAZ, but higher than the TMAZ. Local softening occurs in the 6156-T6 FSW joints, as commonly observed in the conventional FSW of high-strength aluminum alloys. Lower microhardness in NZ and TMAZ is the main reason for the FSW joints fracture.

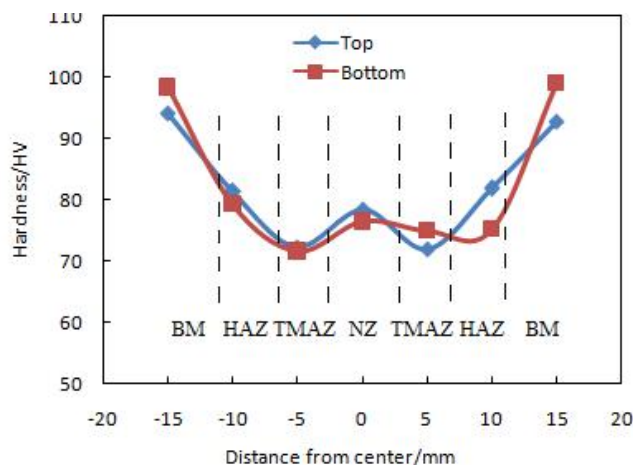


Figure 2-50 Microhardness distributions of the FSW joints

Fatigue property

Table 2-2 shows the calculated results of fatigue reliability assessment of 6156-T6 FSW joint. The DFR value of 6156-T6 aluminum alloy with FSW butt joints is 153.31MPa.

Table 2-2 Test results of fatigue life

σ_{\max} (MPa)	Fatigue life (cycle)	β	$N_{95/95}$	DFR(MPa)
150	287929	346237	110284	153.31
	255696			
	491659			
	226132			
	275061			
	301912			

2.3 COMPOSITE STRUCTURE

2.3.1 Research on Low Velocity Impact Behavior and Residual Compressive Strength of Composite Laminate¹³

In this research, through the composite material plate impact test, the influence of various test variables on the damage resistance characteristics is studied. With the help of the plate impact compression test, the influence of the test variables on the impact damage tolerance characteristics is obtained. Test variables include: layup, impact energy, punch material and punch geometry.

The main research findings include: the relationship between impact energy and pit depth, delamination area and residual compressive strength; impact energy corresponding to initial damage, damage inflection point, BVID damage and penetration damage of each ply; each ply after BVID damage The residual compressive strength of the punch; the punch material has little effect on the damage resistance and damage tolerance characteristics of the laminate, and the punch diameter has a significant effect.

The impact of impact energy

¹³ COMAC Shanghai Aircraft Design & Research Institute. LI Weiping: liweiping@comac.cc

As the impact energy increases, the depth of impact pits and the area of delamination also increase, while the residual strength of compression and failure stress decrease accordingly. Among them, the pit depth-impact energy curve has an inflection point, which satisfies the bilinear relationship, while the impact layered area-impact energy curve basically satisfies the quadratic function relationship, as shown in Figure 2-51. The residual strength of compression -impact energy relationship and the failure strain-impact energy relationship both satisfy the logarithmic function relationship. But the impact energy has almost no effect on the equivalent compressive modulus of compressibility.

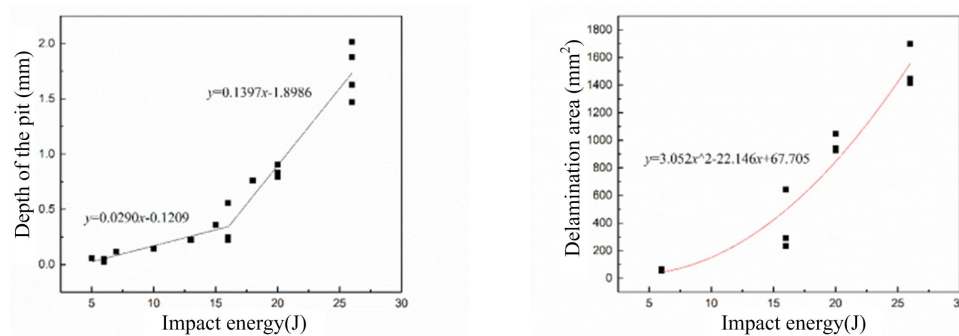


Figure 2-51 F1 layer impact damage-impact energy relationship

The influence of layer thickness

The layer thickness will not change the bilinear relationship of impact pit depth-impact energy curve and the logarithmic function relationship of residual strength of compressive-impact energy. As the thickness of the ply increases, under the same impact energy, the depth of the impact pit of the thick plate decreases, which makes the energy corresponding to the inflection point and BVID increase significantly; however, for the thick plate, when the impact energy exceeds the critical value, the delamination area is significant Increase, so that when the impact energy is much lower than the inflection point energy, there will be a large range of delamination damage. Under the impact of the same impact energy, the thickness of the ply is increased, which can significantly increase the residual strength of compressive of the thin plate.

The influence of the ply form

When the ply thickness is the same, the ply form has almost no effect on the impact pit depth-impact energy relationship, and basically does not change the corresponding impact energy such as the inflection point and BVID; For the layer with a higher proportion of 0° ply, since the 0° ply changes the impact layer morphology, the delamination area is larger, but at the same time, the residual strength of compressive is significantly improved compared with other types of layup; But for other types of layup, the change of the layup ratio has no obvious effect on the delamination area and the residual strength of compressive.

The impact of punch material

The two punch materials of steel and aluminum have little effect on the impact damage resistance characteristics and impact damage tolerance characteristics of composite laminates, as shown in Figure 2-52.

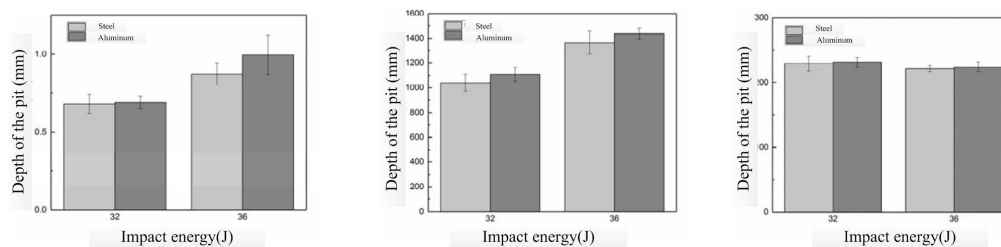


Figure 2-52 The damage effect of a ply with different material punches (diameter 16mm)

The impact of punch diameter

The punch diameter has a significant impact on the damage resistance characteristics and impact damage tolerance of the composite laminate. The smaller the punch diameter, the more severe the impact damage and the lower the residual strength of compressive of the laminate, as shown in Figure 2-53.

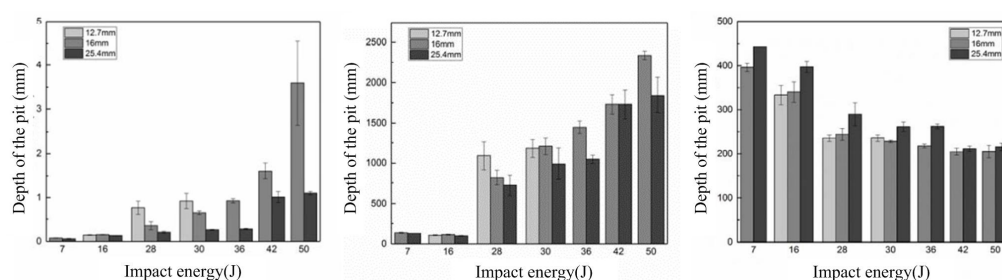


Figure 2-53 Damage effects of steel punches of different diameters used in a certain layer

The impact has a great influence on the residual strength of the laminate. After the damage occurs, the strength of the laminate decreases a lot, mostly above 30%.

2.3.2 Effects of Matrix Cracks on Delamination of Composite Laminates Subjected to Low-Velocity Impact¹⁴

The study mainly consists of two parts: the analysis of delamination distribution of quasi-isotropic laminates based on thermal-deeply images; simulation and analysis of low-velocity impact delamination from the perspective of fracture mechanics.

The main findings of this study are as follows: each fan-shaped delamination is confined between two matrix cracks; in the interface, locations of matrix cracks vary with the adjacent fiber orientations, but there is a constant crack initiation angle; in the thickness direction, the distribution of matrix cracks is determined by the distribution of the peak out-of-plane shear stress in each ply. Due to the interaction between adjacent cracks, inter-laminar cracks growing towards each other show higher stress intensity factors and are thus more likely to form delamination. This crack propagation pattern eventually leads to the formation of two centrosymmetric fan-shaped delamination in each interface.

The delamination distribution of quasi-isotropic laminates

Delamination morphology of each interface is obtained by thermal-deeply tests after impact on quasi-isotropic laminates. The typical delamination morphology in each interface is two centrosymmetric fan shapes. Each fan-shaped delamination is confined between two matrix cracks, and locations of the matrix cracks are determined by the adjacent fiber orientations. Besides, through

¹⁴ Beihang University. BAO Rui, OuYang Tian: rbao@buaa.edu.cn

experimental measurement and theoretical calculation, it is found that there is a constant 22.5° angle (half of the mismatch angle) for matrix cracks, which is defined as the matrix crack initiation angle. Not considering the change of delamination diameters along the thickness direction, the ideal delamination shapes in different interfaces is shown in Figure 2-54. On the upper and lower sides of the mid-plane, delamination connected by the matrix cracks are distributed in an anticlockwise spiral and a clockwise spiral respectively. Meanwhile, with the constant 22.5° angle, it can be seen that the ideal shape of the undamaged region below the impactor is a regular octagon

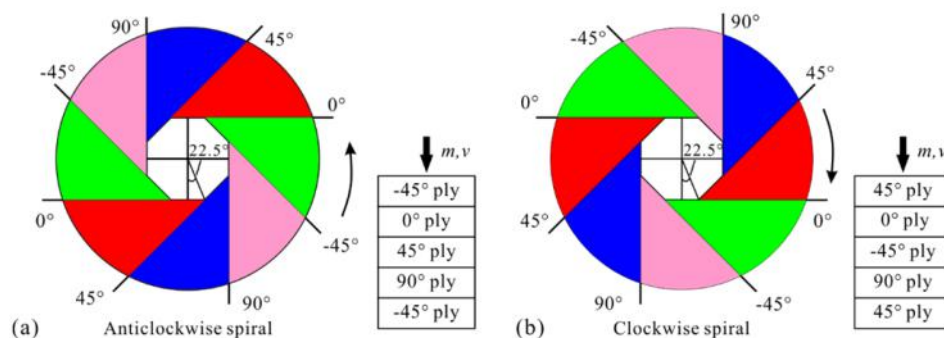


Figure 2-54 Ideal delamination (a) in an anticlockwise spiral and (b) in a clockwise spiral.

Figure 2-55 shows the matrix crack spacing (the distance s between two parallel matrix cracks) along the thickness direction. Straight lines are used to fit the matrix crack spacing of each interface, and they are then compared with the out-of-plane shear stress (τ_{rz}) distribution of the laminate under elastic response. It can be seen from Figure 2-56 that the fit lines are basically consistent with the distribution of peak out-of-plane shear stress in each ply along the thickness direction, indicating that the conical distribution of matrix cracks is determined by the distribution of peak out-of-plane shear stresses.

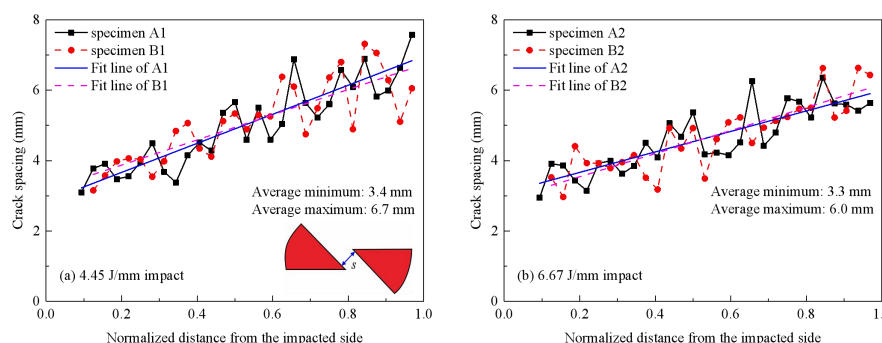


Figure 2-55 Matrix crack spacing (a) under 4.45 J/mm impact and (b) under 6.67 J/mm impact.

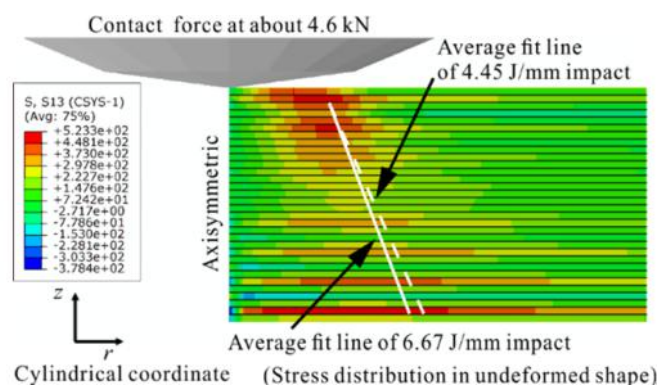


Figure 2-56 The τ_{rz} distribution along the laminate thickness under elastic response.

Delamination mechanisms of quasi-isotropic laminates

Figure 2-57 shows the fan-shaped delamination mechanisms obtained through numerical simulation. As can be seen in Figure 2-57 (a), there are four potential matrix crack paths in each interface. The cracks will propagate along certain sections of these paths. For path I and path III, there are two potential propagation regions for matrix cracks, region A and region B (see Figure 2-57 (b)). If matrix cracks appear in region A, then delamination triggered by these matrix cracks will propagate towards each other. However, if matrix cracks appear in region B, then delamination triggered by these matrix cracks will propagate away from each other. Due to the interaction between adjacent cracks, cracks growing towards each other show higher stress intensity factors, which makes delamination is more likely to occur. With this propagation pattern, matrix cracks propagate only in region A. For path II and path IV, the scenario is the same. When four matrix crack paths are determined, a pair of centrosymmetric fan-shaped delamination will eventually form in the interface.

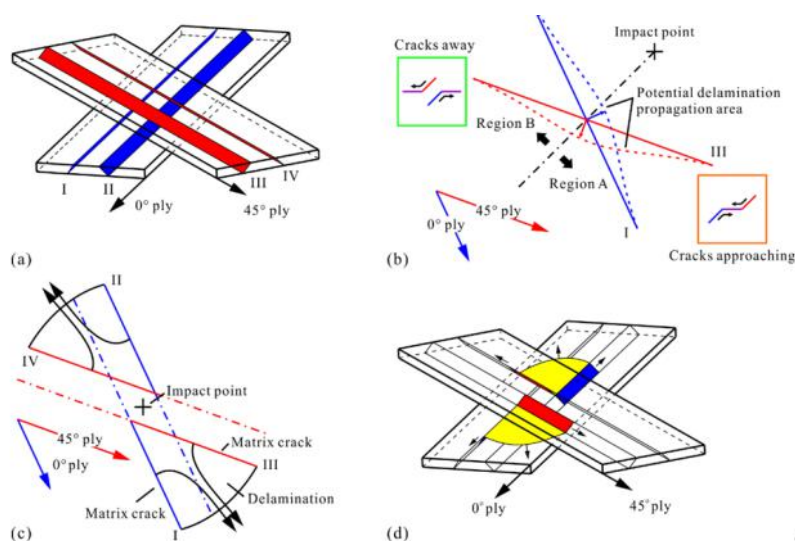


Figure 2-57 The delamination propagation process: (a) four potential matrix crack paths, (b) selection of matrix crack paths, (c) four determined matrix crack paths and (d) formation of fan-shaped delamination

2.3.3 Study on Dynamic Mechanical Behavior and Failure Mechanism of Typical Ceramic Matrix Composite Riveted Structures¹⁵

Due to their high specific strength and stiffness, high fracture toughness and excellent mechanical behaviour at high temperatures, continuous carbon fiber toughened SiC ceramic-based composites (C/SiC) are widely used as thermal structural and thermal protection system materials in aerospace vehicles. An online riveted technique for C/SiC components based on the chemical vapor infiltration process (CVI) solves the difficulties in the manufacturing of such C/SiC complex components (shown in Figure 2-58). And it has been successfully used in internal and external thermal protection structures of aerospace vehicles. However, the mechanical property of the C/SiC-CVI riveted structure is quite different from its of metal bolted or riveted structures, because of the complex mechanical property of C/SiC itself and the defects inside the CVI riveted structures, so that the designing of the CVI riveted structures is also special and different from the metal joints. The structural connection is the weakest link to resist various loads, and its damage and failure under fatigue, impact and other loads seriously threatens the service safety of the aerospace vehicles.

¹⁵ AVIC Aircraft Strength Research Institute. ZHANG Xinyue: nwpuzhangxinyue@163.com

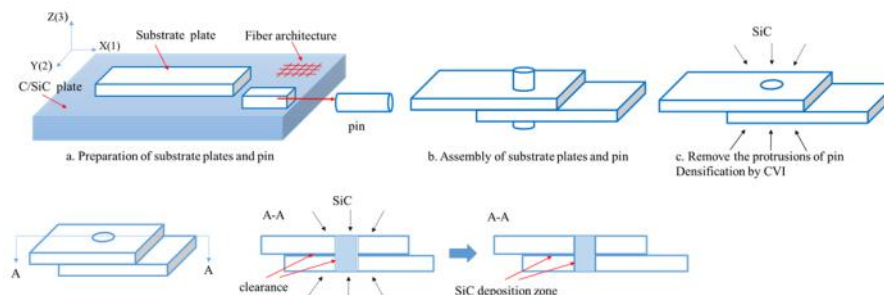


Figure 2-58 Procedures for the preparation of C/SiC-CVI structure

The research includes: carry out quasi-static mechanical performance test of C/SiC-CVI riveted structure and establishes a finite element simulation method of the structure to analyzes the influence of different design parameters on the mechanical properties of the structure; develops fatigue and residual strength test of the riveted structure to reveal the influence of fatigue cycles on the residual strength of the structure and its mechanism; on this basis, carry out dynamic loading tests and simulations to study the influence of loading rates and loading angles on the bearing capacity and failure modes of the riveted structures, and to clarify the dependence of the deformation and failure behavior of the C/SiC-CVI riveted structure on the loading rate and the loading angle.

The key finds in the present research are as follows: the material density, assembly direction of the pin, assembly gap, SiC bonding state at the hole, the dimension of SiC at the lap area and the diameter of the pin all have influences on mechanical properties of the C/SiC-CVI riveted structure; The residual strength increased first with the fatigue cycles then decreased after 10^5 cycles. The acoustic emission (AE) analysis also provides a supplementary understanding of the damage mechanism. The results show that damage fully developed at the early stage of fatigue. When the specimen was reloaded, less AE events were collected before the maximum fatigue stress.

Research on fatigue behavior and residual strength of C/SiC-CVI riveted structure

Fatigue loading was conducted to investigate the fatigue behavior of the C/SiC-CVI riveted structure. The C/SiC-CVI riveted structure was loaded in axial direction of the pin. The residual strength was determined for the surviving specimens to study the effects of the fatigue cycles on the residual strength of the structure. Meanwhile, an acoustic emission system was used during the tests to monitor in situ damage appearing inside the specimens (shown in Figure 2-59). The AE responses analysis show that AE events are dense with the curve of cumulative energy increasing rapidly during initial $10^2 \sim 10^3$ cycles. Then fewer AE events appearing and the cumulative energy curve also tends to rise slowly after 10^3 fatigue cycles (shown in Figure 2-60).

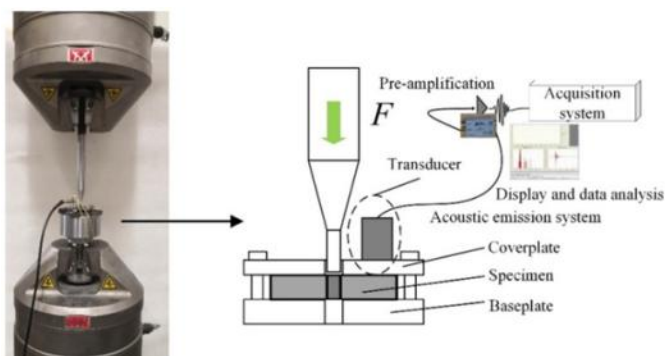


Figure 2-59 Photograph of test equipment and fixing arrangement

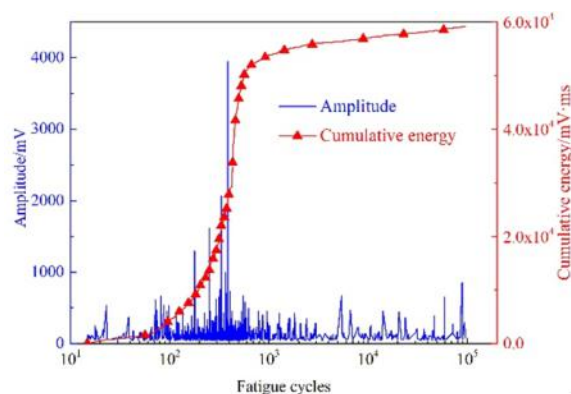


Figure 2-60 AE amplitude and energy evolution during fatigue test

Compared to the original strength, the residual strength of the specimens increased to a maximum of 17.8% after 5×10^4 fatigue cycles; then the residual strength began to decrease after 10^5 fatigue cycles (shown in Figure 2-61). That is, the short-period fatigue loading may introduce a positive effect on the strength of the structure. The formation and propagation of cracks during the fatigue loading, completely or partially eliminated thermal residual stress and redistributed the local stress. This resulted in the strength enhancement observed at the structure. When the specimen is reloaded, fewer AE events occur at the early stage of loading. Only when the stress exceeds the historic maximum fatigue stress, does the AE events begin to appear rapidly, as well as the corresponding accelerating rate of the cumulative energy curve increases (shown in Figure 2-62), indicating more new cracks being generated inside the structure.

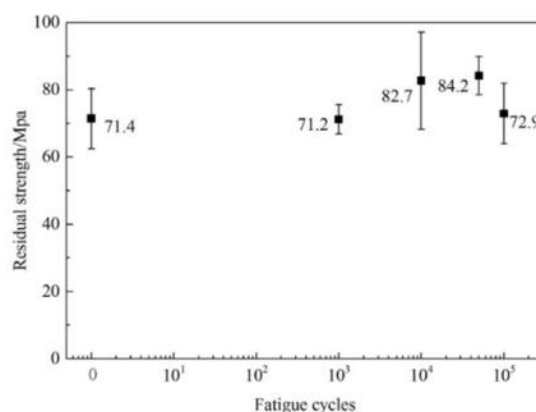


Figure 2-61 Residual strength of the joints versus number of fatigue cycles

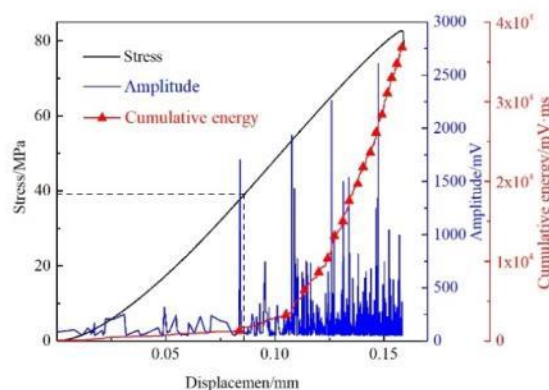


Figure 2-62 Stress-displacement curves with AE amplitude and energy evolution of reloading test after fatigue

2.3.4 Study on Thermal Response and Prediction Method of Fiber Reinforced Polymer Matrix Composites in Aviation Fire¹⁶

This research includes three parts: the thermal response model of polymer matrix composites considering thermal decomposition reaction, the thermal response law of polymer matrix composites under unilateral heat flux, and the identification of thermal decomposition reaction kinetic parameters and mechanism of carbon fiber epoxy resin.

A three-dimensional thermal response model was developed to simulate the thermal response of composites such as carbon fiber epoxy, glass fiber phenolic, glass fiber vinyl ester and glass fiber epoxy in fire. The results show that the fiber direction has a significant effect on the heat transfer of the material, and the relationship between the degree of matrix decomposition and the temperature is related to the depth, the peak decomposition rate and the time to reach the peak decomposition rate. By means of Simultaneous Thermal Analysis(STA), Fourier transform infrared spectroscopy and mass spectrometry, the thermal degradation mechanism and pyrolysis products of carbon fiber epoxy resin were identified, and the reaction kinetics model was established, which provided data, theoretical and analytical support for the application of carbon fiber epoxy resin in aviation industry.

Thermal response model of polymer matrix composites considering thermal decomposition reaction

A three-dimensional thermal response model of composites under the action of one side flame was established. Considering anisotropic heat transfer, matrix decomposition heat absorption and release and gas diffusion, as shown in formula (2-2) (2-3) (2-4), a three-dimensional thermal response model is developed, from which temperature, density, decomposition degree and decomposition rate can be extracted, and the finite element simulation analysis of material decomposition process is carried out. The comparison of numerical simulation and experimental results shows that the model can analyze the thermal response of carbon fiber epoxy, glass fiber phenolic, glass fiber vinyl ester, glass fiber epoxy and other composites in fire.

$$\frac{\partial}{\partial t}(\rho h_s) - \nabla \cdot \left(k_1 \frac{\partial T}{\partial x} \mathbf{i} + k_2 \frac{\partial T}{\partial y} \mathbf{j} + k_3 \frac{\partial T}{\partial z} \mathbf{k} \right) + \frac{\partial}{\partial z}(m'_g h_g) + Q \frac{\partial \rho}{\partial t} = 0 \quad (2-2)$$

$$\frac{\partial \rho}{\partial t} = -A(\rho_v - \rho_d) \left[\frac{\rho - \rho_d}{\rho_v - \rho_d} \right]^n \cdot e^{-E/RT} \quad (2-3)$$

$$\frac{\partial m'_g}{\partial z} = -\frac{\partial \rho}{\partial t} \quad (2-4)$$

Thermal response of polymer matrix composites under unilateral heat flow

The thermal conductivity of fibers in different directions has a significant effect on the heat transfer. In addition, with the increase of depth, the maximum temperature rise rate gradually decreases, and after reaching the peak, the temperature rise rate gradually decreases, as shown in Figure 2-63. This is because when the material reaches the matrix pyrolysis temperature, the thermal decomposition reaction takes place, absorbs a lot of heat, completes the chemical bond breaking, and the gas produced

¹⁶ Civil Aviation University of China. LI Han: cauc_lihan@126.com

by the decomposition escapes and migrates to take away part of the heat, which further leads to the decreasing of the rate of temperature rise and the slow increasing of temperature. The temperature of the material at different times continuously decreases with the increase of the depth, as shown in Figure 2-64. At the same depth, the temperature increases and gradually approaches with the increase of time, further indicating that the temperature rise rate gradually decreases. At the beginning of the decomposition reaction, the temperature distribution of the material with the depth presents a more obvious nonlinear law, which is due to the pyrolysis of the material near the heat source region at this time; with the increasing heating time, the temperature of most materials exceeds the pyrolysis temperature, and the temperature distribution of the material with the depth presents a linear trend.

The higher the depth is, the smaller the residual mass fraction is, and the higher the degree of carbonization is. The temperature reaching the same residual mass fraction decreases with the increase of depth. This is due to the different temperature rise rates of materials with different depths at the same temperature, which leads to different carbonization degree and different residual mass fraction. At the same temperature, the slower the temperature rising rate is, the smaller the residual mass fraction is. This is because the smaller the temperature rise rate, the more sufficient the oxidation reaction of resin matrix in air.

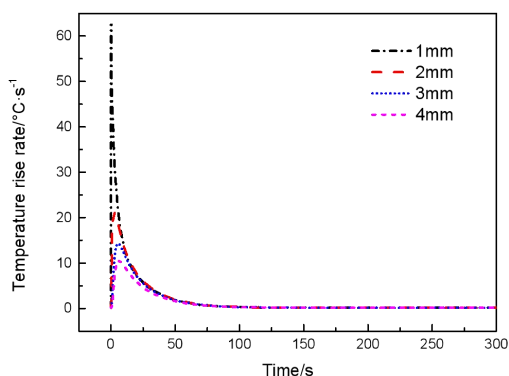


Figure 2-63 Variation of temperature rise rate
time at different positions

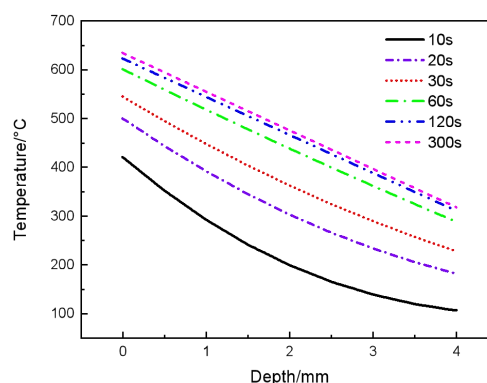


Figure 2-64 Temperature-depth distribution
in different time

Kinetic parameters and mechanism identification of thermal degradation of carbon fiber epoxy resin

The thermal degradation mechanism and pyrolysis products of carbon fiber epoxy resin were studied by means of STA, Fourier transform infrared spectroscopy and mass spectrometry. The kinetic model was established by Kissinger / Friedman / Ozawa / coats Redfern method. The results show that the thermal degradation can be divided into three steps in inert atmosphere and four steps in air atmosphere. The first two steps are almost the same in both environments, including drying, carbon dioxide escape and epoxy resin decomposition. In the third step of inert atmosphere, phenol forms, methane decreases, carbon monoxide disappears and carbon dioxide production increases. The mechanism of thermal degradation is consistent with F4 model. These results provide basic and comprehensive support for the application of carbon fiber epoxy resin in aviation industry.

In conclusion, for the thermal behavior of fiber reinforced polymer matrix composites in aviation fire, the mechanism of material degradation has been mastered, the thermal response model of polymer matrix composites considering thermal decomposition reaction has been developed, and the thermal response law of polymer matrix composites under unilateral heat flow has been revealed. In the future,

the thermal mechanical coupling behavior and damage evolution of fiber reinforced polymer matrix composites in aviation fire will be studied, so as to support the fire protection design and verification planning of aircraft composite structures, and the airworthiness compliance verification technology.

2.3.5 Fatigue Performance in Fiber Metal Laminates (FMLs)¹⁷

There are three key techniques in the present research, which are as follows: the images captured during testing were calculated by DIC; the shapes and sizes of delamination and the crack lengths were obtained; the fatigue crack growth rates of FMLs with different notch sizes were analyzed; the effect of fiber bridging mechanism on crack propagation are studied.

The key finds in the present research are as follows: the delamination area increases with increasing of notch size; the delamination area decreases with increasing of stress ratio; the crack growth rate increases and the fatigue crack growth life decreases with increasing of notch size; the crack growth rates in FMLs keep the constant with crack growing; the crack initiates easily in aluminum layers and crack growth will be suppressed by the bridging effect of the fiber; FMLs have better fatigue resistance than aluminum alloy panel.

Effects of notch size on delamination in FMLs

The fatigue tests of sample were performed with different fatigue load, DIC images are shown in Figure 2-65. Under the same notch size and the same stress amplitude, the delamination area of the specimen decreases with the increasing of stress ratio.

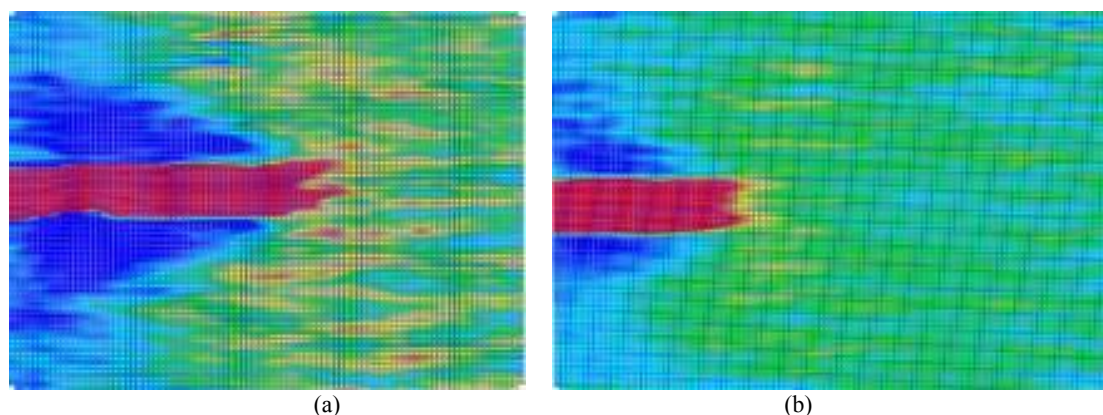


Figure 2-65 Delamination of FML20-1, FML20-2, FML10-1 and FML10-2 FML20-1: (a) FML20-2(45mm), (b) FML10-2(26mm)

Effects of notch size on fatigue crack growth rate of FMLs

The effect of fiber bridging decreases with the increasing of notch size. In Figure 2-66 the crack growth life of FMLs decreases with the increasing of notch size. The effect of fiber bridging is depending on notch size, the effect of fiber bridging decreases with the increasing of notch size.

¹⁷ Northwestern Polytechnical University. MA YuE: ma.yu.e@nwpu.edu.cn

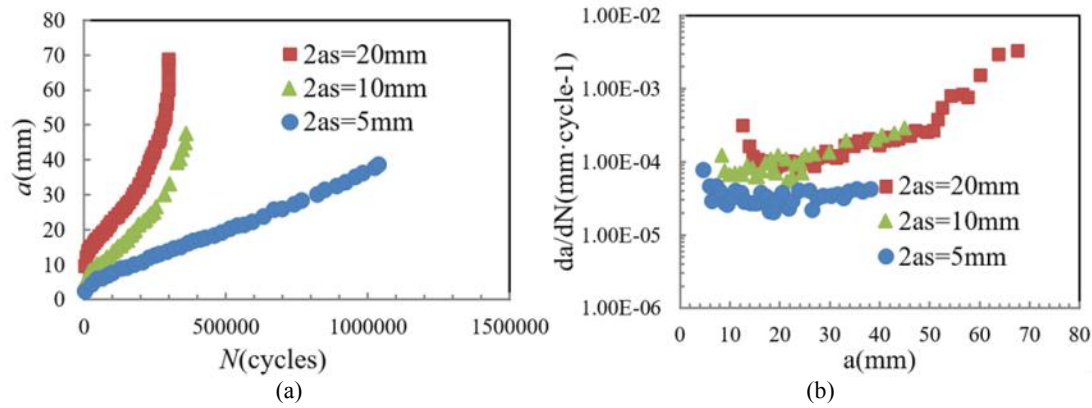


Figure 2-66 The a - N curves and da/dN - a curves of FML with different initial crack: (a) a - N curves, (b) da/dN - a curves

Effects of fiber bridging on fatigue crack growth rates of FMLs

The load on the aluminum layer was redistributed and transferred to the fiber layer with the crack propagation because of the effect of fiber bridging. In Figure 2-67, the crack growth rates of 2024-T3 aluminum alloy panel are significantly higher than that of FMLs and show an obvious upward trend. While the crack growth rates of FMLs keep the constant with crack growing. It is found that FMLs have better fatigue resistance than aluminum alloy panel.

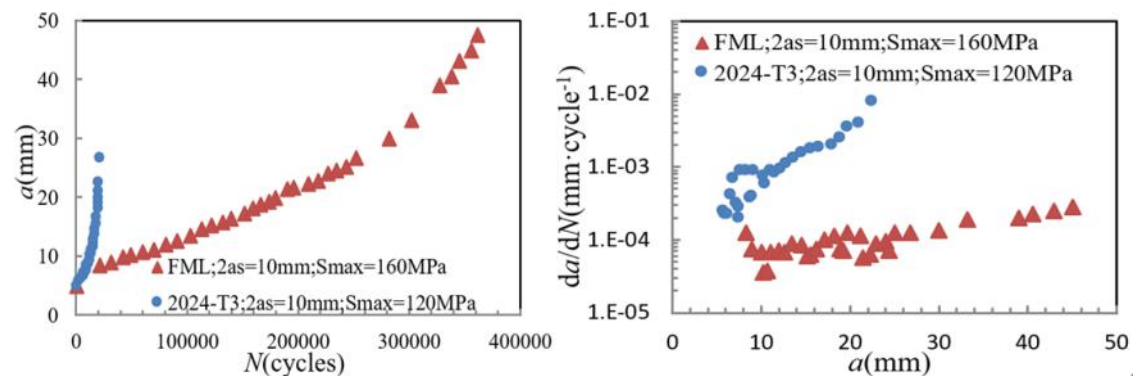


Figure 2-67 The a - N curves and da/dN - a curves of FML and 2024-T3 aluminum alloy panel

Fatigue life prediction model with delamination growing and fatigue crack growing

In this research, one numerical method is proposed to calculate fiber bridging, and the delamination growing is studied with fatigue crack growing, shown in Figure 2-68. One method is built to calculate fatigue crack grow rate with delamination growing and this simulation results is tested by experimental results, shown in Figure 2-69. The failure modes of FMLs are analyzed.

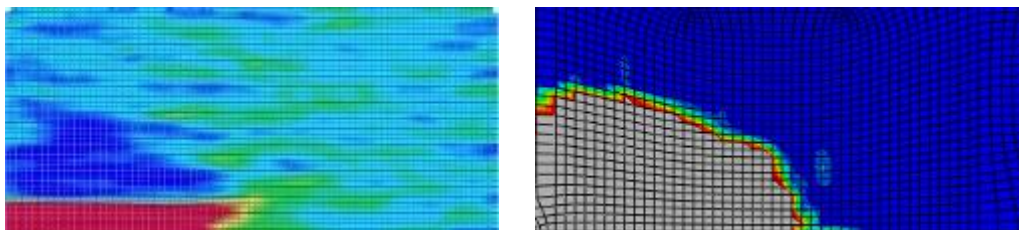


Figure 2-68 Delamination comparison of experimental and simulation results when crack length 35mm

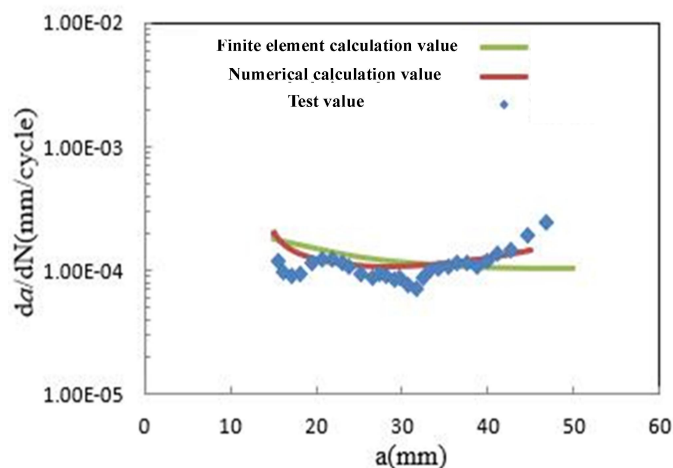


Figure 2-69 Simulation results are compared with experimental results

2.3.6 Experimental Research on Fatigue Threshold Value and Low-Load Cut-Off of Typical Laminates of Composite Fuselage¹⁸

This test is used to determine the fatigue characteristics of typical laminates of composite fuselage, including determining the fatigue threshold value of laminates and the influence of BVID damage on fatigue performance, and obtaining fatigue dispersion coefficient and load amplification factor LEF. This test is also used to determine the low-load cut-off value of typical laminates for composite fuselage, and provides a low-load cut-off basis for the compilation of load spectra for other fatigue damage tolerance tests of composite airframes.

The test piece used the material M21C, including two material specifications, automatic fiber placement (AFP) and automatic tape laying (ATL), involving 3 types of laying. The test includes three items: the open-hole tension-compression fatigue threshold test item, the compression after impact fatigue threshold test item, the double-nail single-shear connection fatigue threshold test item, involving three kinds of stress ratio $R=-1$, $R=0$, $R=-0.2$. The test environment is room temperature atmospheric environment. The test results give the static strength test data and fatigue performance data of three test items, two material specifications and three layup forms, and the comparison results of different material specifications and layup forms in the same project. The test piece form of the low load cut-off test is the same as the fatigue threshold test. The test load selects a multi-level load block spectrum, each block spectrum represents 1/10 of the load corresponding to the design service target, and the entire test loading cycle is repeated by this block spectrum. Performed 10 times, the block spectrum contains 6 levels of load, and each level of load corresponds to a different working strain.

Through the statistical analysis of the fatigue threshold test data of the composite fuselage, the conclusions are as follows:

- Fit the fatigue test data through the Sendeckyj equivalent static strength model, and obtain the Weibull distribution shape parameters of each test group;
- It is determined that the shape parameter of the material system selected for the composite fuselage is 1.328, which is greater than 1.25, so taking 1.25. Used to support the determination of the full-scale fatigue test load amplification factor and the determination of the fatigue threshold

¹⁸COMAC Shanghai Aircraft Design & Research Institute. LI Weiping: liweiping@comac.cc

value;

- c) Fit the P-S-N curve of the test item under 95% reliability and 95% confidence level, and give the fatigue threshold value corresponding to each test item to provide data support for low-load interception.

The low-load cut-off test showed that the damage did not expand under the six-level low-load cut-off limit, and the low-load cut-off limit selected for the composite fuselage flight by flight fatigue load spectrum compilation was reasonable.

Test research on fatigue threshold of typical laminates of composite fuselage

Regarding the calculation of reliability life, this article uses 95% reliability and 95% confidence life for analysis. The fatigue threshold value is determined by extrapolating the SN curve to 10^7 life, and find out the stress level corresponding to this life. The fatigue shape parameters of each test group are determined by Sendeckyj equivalent static strength model, and the shape parameters of the material system are determined by Weibull distribution mode. Estimating the Weibull shape parameter and scale parameter of the obtained experimental data, the shape parameter is 1.512, the scale parameter is 2.718, and the mode is 1.328, greater than 1.25, as shown in Figure 2-70.

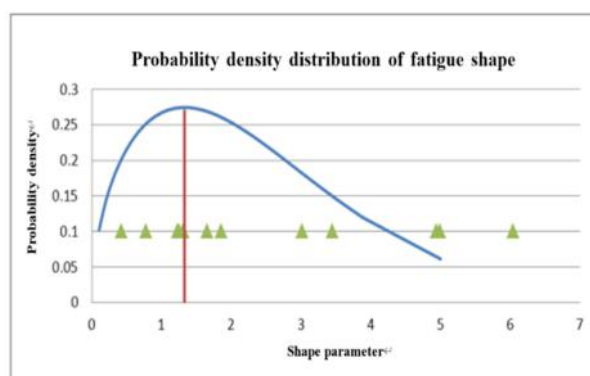


Figure 2-70 Probability density distribution of fatigue shape parameters

The fatigue SN curve under Sendeckyj's life model corresponds to the residual strength drop curve under 50% reliability and 50% confidence, and cannot be directly used to determine the fatigue threshold value. Here, the P-S-N curve is re-fitted, that is, the fatigue life has a linear relationship with the maximum cyclic stress under double logarithmic coordinates. The fitting results and threshold values are shown in Figure 2-71.

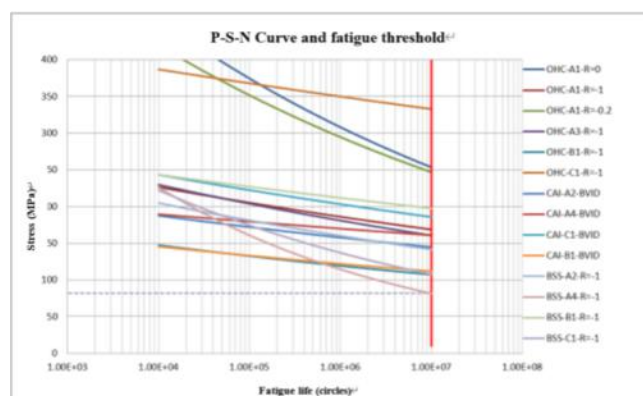


Figure 2-71 P-S-N curve and fatigue threshold value from fatigue test of composite fuselage

Low-load cut-off test research on typical laminates of composite fuselage


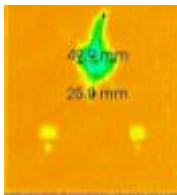

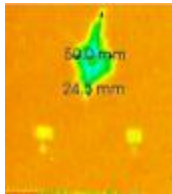
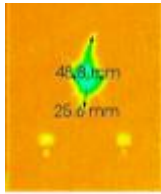
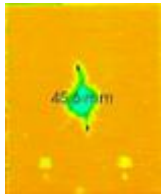
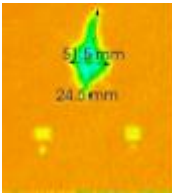
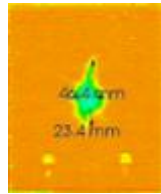
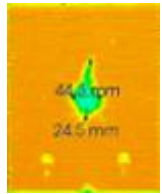
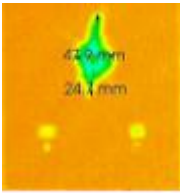

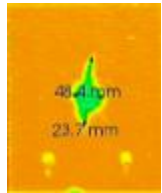
The load spectrum of this test is a multi-level load block spectrum. Each block spectrum represents the load corresponding to 1/10 of the designed service target. The entire test loading cycle is repeated 10 times by the block spectrum. The block spectrum contains 6 levels of load. Each level of load corresponds to a different working strain, and the corresponding working strain of the low-load cut-off spectrum is shown in Table 2-3.

Table 2-3 Low load cut-off spectrum working strain

Load level	Maximum strain ($\mu\epsilon$)	Minimum strain ($\mu\epsilon$)	Number of load cycles per level
First level	-4	-1996	1
Second level	-99	-1901	3
Third level	-290	-1710	35
Fourth level	-481	-1519	488
Fifth level	-672	-1328	9679
Sixth level	-742	-1258	189797

The flight by flight load is applied to the test piece, then conduct damage evolution research at a certain interval. Table 2-4 is the damage detection of the low-load cut-off test after impact.

Table 2-4 Low-load cut-off damage detection after impact

Load order	Damage detection	Load order	Damage detection	Load order	Damage detection
Initial state		Block3-6		Block7-6	
Block1- (1-5)		Block4 (1-6) +Block5 (1-5)		Block8 (1-6) +Block9 (1-5)	
Block1-6		Block5-6		Block9-6	
Block2 (1-6) +Block3 (1-5)		Block6 (1-6) +Block7 (1-5)		Block10 (1-6)	

Through the analysis of the test results, In the compressive after impact fatigue low-load cut-off test, after all 10 cycles of the loaded spectrum block are completed, the original damage did not significantly expand; in the open hole laminate test, after 10 spectrum blocks, no damage occurred on

the edge of the hole and the edge of the test piece; in the double nail single shear test, after 10 spectrum blocks, the test piece did not fail, and there was no obvious deformation on the edge of the hole. The third-level low-load cut-off limit level of this project is the low-load cut-off level used in the compilation of the load spectrum, and the test results show that the damage does not expand under the sixth-level low-load cut-off limit.

2.3.7 Correction of The Large Displacement Effect on Determination of Mode I Interlaminar Fracture Toughness of Composite¹⁹

Analytical, numerical, and experimental studies on the composite DCB under large displacement are conducted in this paper. This study aims to carefully verify the nonlinear J-integral method for measuring the interlaminar fracture toughness of the composite DCB under large displacement, and to correct the errors in ASTM D5528 and ISO 15024. More detailed information about this research is given by Xu and Ding (Xu W and Ding JC. ENG FRACT MECH 2020, 238: 107279).

J-integral for large deformed DCB

The J-integral for nonlinear elasticity with finite deformation was defined by Eshelby

$$J = \int_{\Gamma} \left(W \cdot n_1 - T_i \cdot \underline{F}_{i1} \right) ds \quad (2-5)$$

where T is the nominal traction, W is the nominal density of elastic energy, which is a function of the deformation gradient \underline{F} , and n is the unit vector normal to an element of area in the undeformed body. The path of integration Γ is in the undeformed body. The unit vector n is normal to the path of integration. The relationships between W , \underline{F} , and T are given as follows.

$$T_i = S_{ij} n_j, \quad S_{ij} = \frac{\partial W(\underline{F})}{\partial F_{ij}}, \quad \underline{F}_{ij} = \frac{\partial x_i(X)}{\partial X_j} \quad (2-6)$$

where S_{ij} is the nominal stress component, and x and X are the coordinates for the same material point in the deformed and undeformed states, respectively. For both small and large deformations under monotonic loading, the J-integral is the same as the energy release rate G . Choosing the outer surfaces of the DCB as the path of integration, the J-integral for the DCB is

$$J = \frac{2P}{B} \cdot \frac{\partial [u_2(X) + X_2]}{\partial X_1} = \frac{2P}{B} \cdot \frac{\partial u_2}{\partial X_1} = \frac{2P}{B} \cdot \sin \theta \quad (2-7)$$

where P represents the applied load, B refers to the width of the DCB and θ is the rotation angle of the single beam at the load point, which is shown in Figure 2-72. The significance of Eq. (2-7) is that the energy release rate for the DCB under large deformation can be exactly determined by this simple and closed form expression.

¹⁹ Shanghai Jiao Tong University. Wu XU: xuwu@sjtu.edu.cn

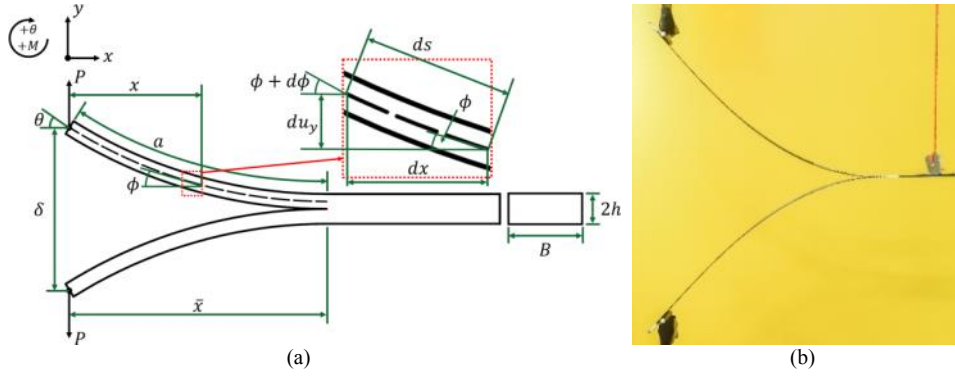


Figure 2-72 Slender composite DCB test under large deformation: (a) Nomenclature used in the analysis of the DCB, (b) DCB test

DCB tests and results

The material tested was unidirectional carbon fiber reinforced polymer matrix composite. Two piano hinges were affixed onto the pre-crack end of the DCB specimen. The ratio of the initial crack length a_0 (140mm of average) to the beam thickness h (0.58mm of average) was approximately 241, which was designed to achieve large displacement. Displacement control was used throughout the tests. The applied displacement δ and resultant load P were recorded by the testing machine and load cell with an acquisition frequency of 1 Hz. A typical image of the deformed DCB is shown in Figure 2-72 (b). The load displacement relations obtained from the tests are shown in Figure 2-73(a), where nonlinearity is clearly observed. The marked white lines at the ends of the specimen were used to measure the rotation θ by digital image analysis. The local peak load P and the corresponding rotation θ obtained from Figure 2-73(b) were substituting into Eq. (2-7) to measure the fracture toughness.

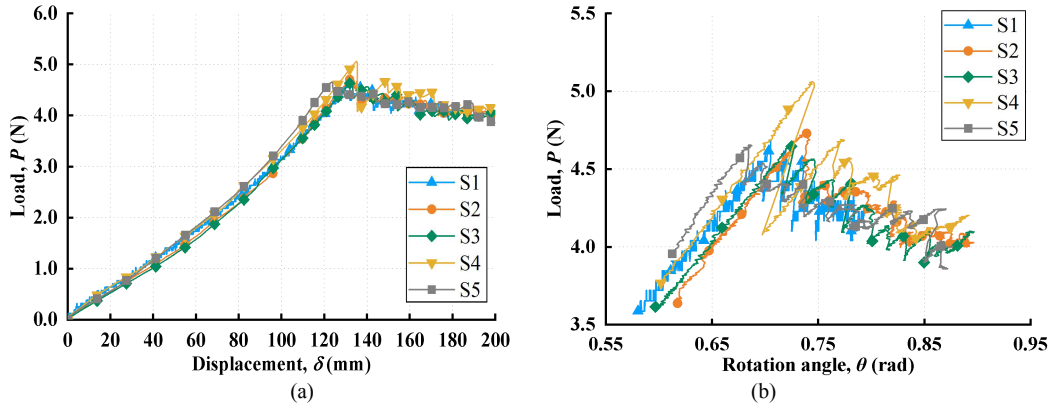


Figure 2-73 Load-displacement- rotation relations obtained from the DCB tests: (a) Load displacement relation, (b) Load P and rotation θ relation

Determination of fracture toughness G_{IC}

According to ASTM D5528 and ISO 15024, when the ratio δ/a is larger than 0.4, the influence of the large displacement on the energy release rate is corrected by

$$G_I = \frac{3P\delta}{2B(a+|\Delta|)} \cdot F; \quad F = 1 - \frac{3}{10} \left(\frac{\delta}{a} \right)^2 - \frac{3}{2} \left(\frac{\delta t}{a^2} \right) \quad (2-8)$$

Where, the correction factor Δ is determined through a least square plot of the cube root of compliance $C^{1/3}$ versus the actual crack length a , t is the distance between the center of the piano hinge and the neutral plane of the beam. Using Eqs. (2-8), the corresponding fracture toughness G_{IC} for each test was

obtained and is given in Figure 2-3. For comparison, the nonlinear J-integral was also used to obtain the fracture toughness, which is shown in Figure 2-74. It is observed that G_{IC} from the nonlinear J-integral is consistent. However, the difference between the fracture toughness values determined from the standard method and the nonlinear J-integral is obvious. The average fracture toughness from the nonlinear J-integral is 0.245 N/mm, whereas that from Eq. (2-8) is 0.140 N/mm, representing a relative difference as great as 42.8%.

Corrections of the ASTM and ISO standards

Equation (2-8) is further improved by Xu and Ding (Xu W and Ding JC. ENG FRACT MECH 2020, 238: 107279). The fracture toughness for the DCB under large deformation is

$$G_I = \frac{3P(\delta/N)}{2B(a+|\Delta|)} \cdot F, \quad N = 1 - 0.02912\left(\frac{\delta}{a}\right) - 0.1461\left(\frac{\delta}{a}\right)^2 - 0.1183\left(\frac{\delta}{a}\right)^3 + 0.02658\left(\frac{\delta}{a}\right)^4 \quad (2-9)$$

The correction factor Δ is determined through the curve fitting of the corrected compliance $(\delta/(NP))^{1/3}$ versus the crack length a . N is the ratio of the small (δ_L) and large displacements (δ_N). The above Eq. (2-9) is valid for $\delta/a \leq 1.84$. Using Eq.(2-8), the corresponding G_{IC} is shown in Figure 2-73(b), which agrees well with the result from the nonlinear J-integral method. Therefore, both Eq.(2-7) and Eq.(2-9) are accurate for the determination of the interlaminar fracture toughness of composites under large displacement. Therefore, the use of these equations to correct the effect of large displacement enables the fracture toughness to be measured for a wider range of configurations, which makes it unnecessary to design a thick DCB specimen through trial and error to meet the requirement of the ASTM/ISO standard. Both thin and thick arms can be used to measure the interlaminar fracture toughness.

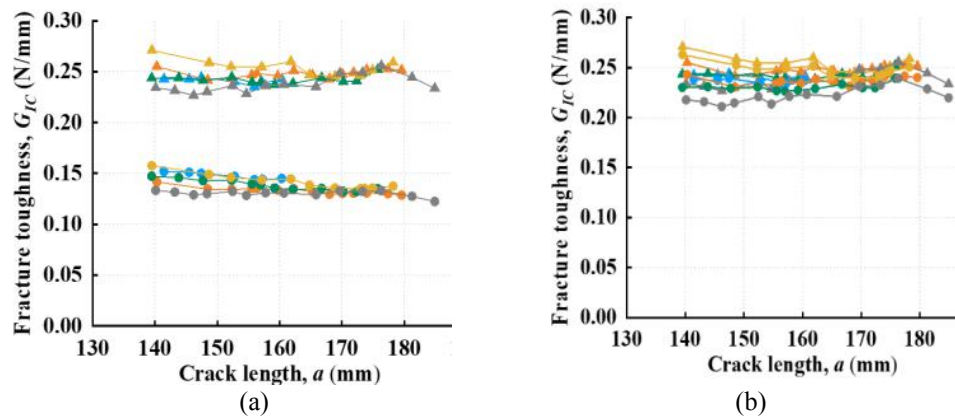


Figure 2-74 G_{IC} obtained from the ASTM method, nonlinear J-integral Eq. (2-7) and Eq.(2-9): (a) ASTM Eq.(2-8) (●) vs J-integral Eq. (2-7)(▲), (b) Eq.(2-9) (●) vs J-integral Eq. (2-7) (▲)

2.3.8 Strength Assessment and Repair for Typical Defects/Damage of Composite Structure²⁰

There are two contents in the present research, based on test data fitting and characteristic parameter setting of impact and composite laminate structure, impact damage resistance, residual strength analysis model is established and test verification are carried performed; Damage mechanism analysis on hole edge of ultra-thin metal panel honeycomb sandwich structure ,repair optimization and verification based on such structure damage mechanism.

²⁰ AVIC Harbin Aviation Industry Group CO, LTD. WANG Jinliang: wangjl008@avic.com

The main findings of this study are as follows: 1) based on test of drop-hammer impact, tension after impact (TAI), compression after impact (CAI) and shear after impact (SAI), the impact damage and residual strength evaluation model and parameters fitted by scientific test data can be used in same material system, different lay-up, boundary conditions and impact energy are considered. Stress distribution on the hole edge of Ultra-thin panel honeycomb sandwich structure is complex. And metal repair is prone to sudden changes in stiffness, resulting in stress concentration. Composite material patch can avoid stress concentration and improve the fatigue performance of repaired structure.

Evaluation of impact damage resistance and residual strength of composite laminate structures

A semi-empirical analysis model of impact damage and residual strength of composite laminated structure is established base on test data fitting. The basic idea of the residual strength analysis model is: in the impact damage assessment, the impact energy, the geometric and physical characteristics of the impact hammer, the panel material, lay-up, and boundary conditions are used as input parameters. Based on the fitting of drop-hammer impact test data and engineer experience, curves of impact energy vs damage area, impact energy vs dent depth, and damage area vs residual strength are depicted. as shown in Figure 2-76 and Figure 2-77. and impact factor of the above-mentioned relevant characteristics is obtained. Based on the damage estimation, and the residual strength of CAI, TAI, and SAI, are calculated, and verified by experiments. It is determined that analysis method is suitable for damage assessment of laminate structures when they are subjected to lateral impact.

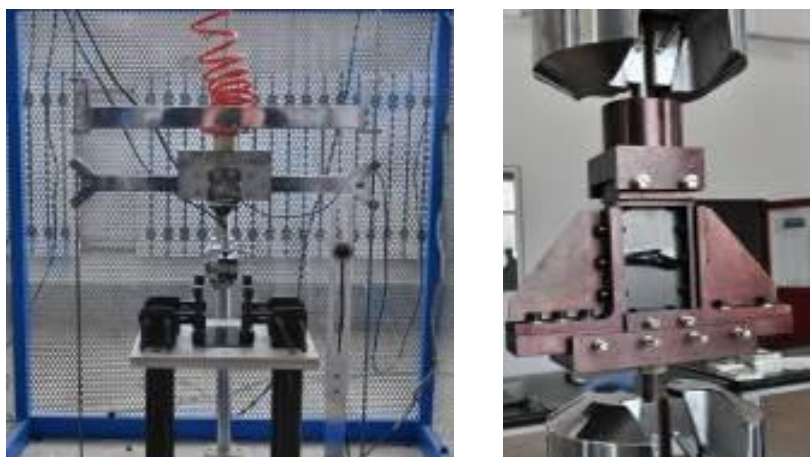


Figure 2-75 Test of drop-hammer impact and compressive after impact

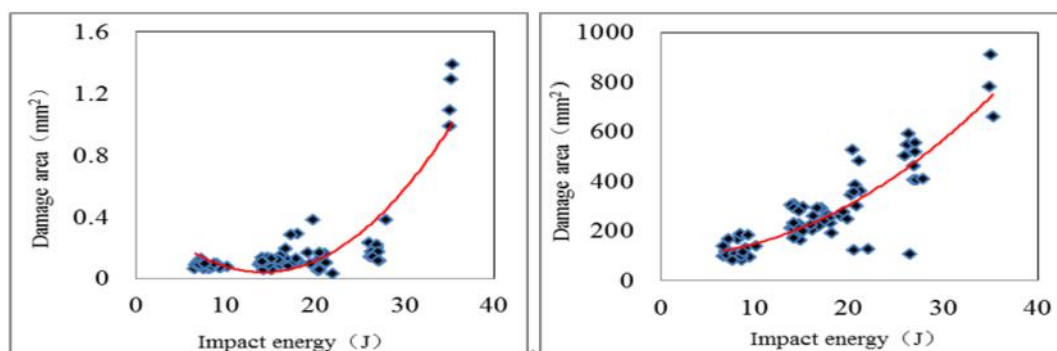


Figure 2-76 Curves of impact energy vs damage area and dent depth

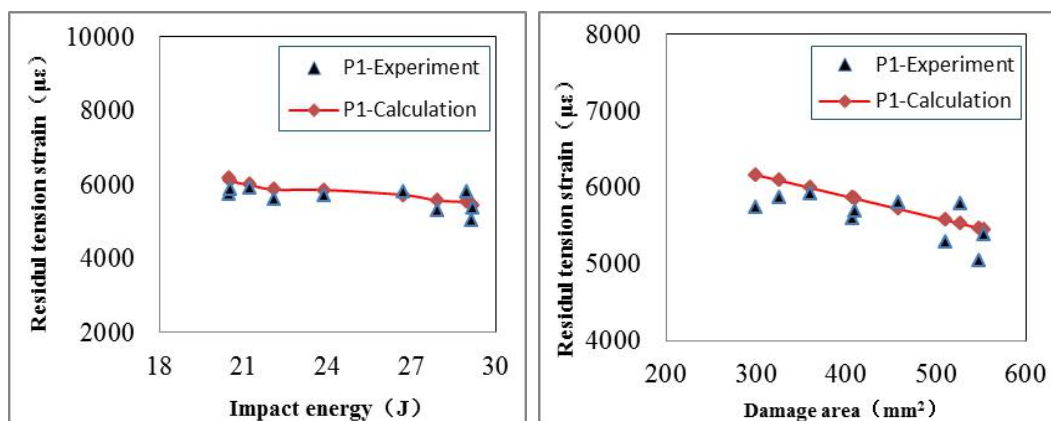


Figure 2-77 Curves of residual strength vs impact energy damage area

Damage assessment and repair of ultra-thin metal panel honeycomb sandwich structure

A research on the hole edge damage during the service and repair issues of the ultra-thin metal skin sandwich structure. Using global-local method to study responses of structure curvatures, material properties, and cross-section on the stress distribution. Stress distribution of inner skin, outer skin and the core are obtained. As shown in Figure 2-78, there is a stress concentration at the edge of the hole.

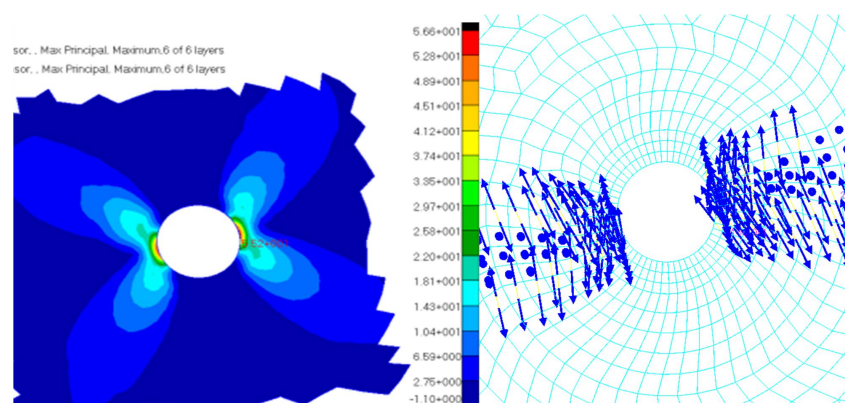


Figure 2-78 Max-principal stress distribution of the hole edge

Manufacture the thin metal skin honeycomb sandwich test article, and apply the fatigue load of tension-compression and shear-shear, the stress distribution near the hole of the skin are obtained, and the relationship of fatigue load, load cycle numbers and crack detection are constructed, when the tensile stress at the edge of the hole close to the yield strength of the skin material, a fatigue failure would be caused. The failure mode is consistent with expectation, shown in Figure 2-79.



Figure 2-79 Photos of fatigue crack on test specimen

Repair the damage structure. At first, metal patches are used to repair, but due to the sudden change in the cross-section of repair boundary, stress concentration causes regenerative cracks. Then composite wet patches are used to repair the ultra-thin skin, stress concentration of the repair boundary is avoided and the fatigue performance of repair structure is improved.

2.3.9 Helicopter Composite Material Tail Fin Structure Simulation Analysis and Damage Tolerance Experimental Verification²¹

This study report includes three important parts: The structure detail finite element modeling analysis; the defect and damage are introduced into the structure according to finite element modeling result and threat analysis; verify the structure meet the airworthiness regulation involved with damage tolerance requirement by reasonable acceleration test.

This study report main result: confirm the tail fin structure high stress area according to finite element analysis, confirm the tail fin structure is vulnerable area according to threat analysis; verify the structure meet 10,000 flight hour safe life and 2,400 flight hour inspection interval.

Helicopter composite material tail fin structure simulated analysis

Create the detail finite element mode of structure, both considering the calculate efficiency and as far as possible be consistent in real structure, induced the related structure into the finite element mode, include the tail boom structure and horizontal stabilizer, which is used to applied the load and constraint condition. The finite element mode is shown in Figure 2-80.

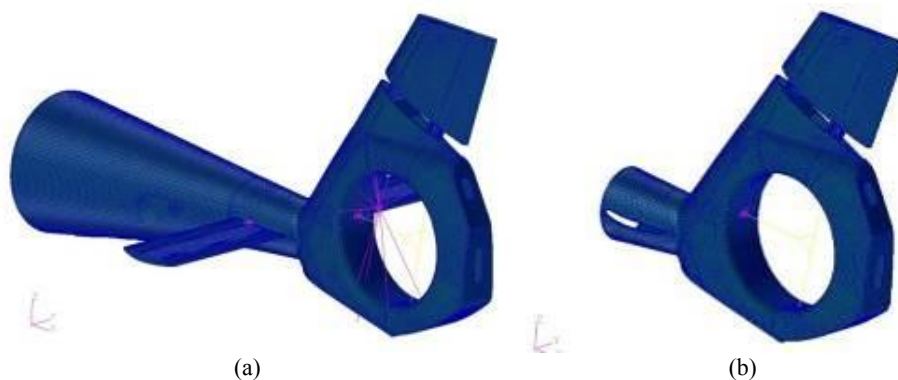


Figure 2-80 Helicopter rear structure and tail fin structure FE: (a) Civil helicopter rear structure FE, (b) Civil helicopter tail fin FE

For the composite material, considering the dispersion of the material. Be mixed up with inlay defect in the manufacture and the dimension influence. Composite material structure failure mode is complexity and random. Which mechanical property is effect by the manufacture defect, environment (wet temperature) and out-plane load sensitivity, check the structure strength by the composite material design allowable value, select the Tai-Hu Failure criterion in the strength check. The calculate result is shown in Figure 2-81. The result which is base for the defect and damage made in the structure.

²¹AVIC Harbin Aviation Industry Group CO, LTD. MEN Kunfa: menkf@avic.com

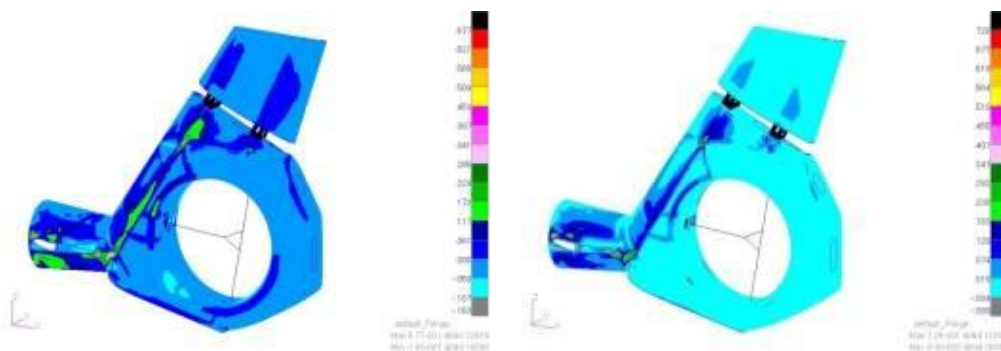


Figure 2-81 Tailfin structure Tai-Hu Failure Index plot in the critical load case: (a) Index plot in critical load case 1, (b) Index plot in critical load case 2

The damage tolerance fatigue test of structure

This test is done in the room temperature. The static test is considering 1.15 times coefficient. The fatigue test is ensured normal flight hour safe life in the B-criterion reliability test parameter, using the load amplification factor 1.148 and corresponding to lifetime dispersion coefficient 1.5, the fatigue load is applied by block fatigue spectrum. The damage tolerance test validation process in turn: the static test on the structure with BVID defect, the two thirds target flight hour in the fatigue test; the ultimate load test; make the VID defect and aggravate the original BVID defect. Continue damage tolerance fatigue test. the one thirds target flight hour in the damage tolerance fatigue test, when finish these tests, did the residual strength test in the final.

Verify the structure with BVID defect and which is no extend in the whole test process, and can withdraw the ultimate load, the structure with VID defect and which is no appear extend in the inspection periods. Did the 1.2 times ultimate load test in the residual strength test in the end. During the test, Detail visual check the critical area every day, NDI check is on the structure every 20 block fatigue spectrum. Confirm the delamination defects and impact defect which are no extent. and no new failures appear in the structure, the test flow chart and the test site as Figure 2-82, according to test result, verify the helicopter composite material tail fin structure meet with damage tolerance requirement.

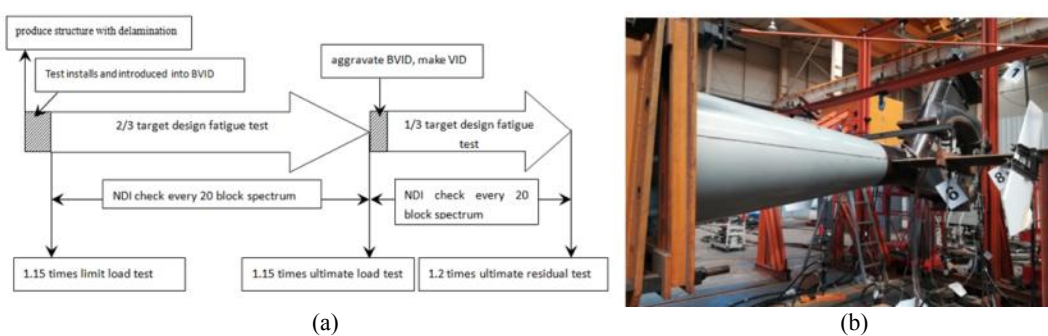


Figure 2-82 Test flow chart and test site: (a) test flow chart, (b) test site

2.4 STRENGTHEN TECNOLOGY

2.4.1 Effect of Shot Peening on Notched Fatigue Performance of Powder Metallurgy Udimet720Li Super Alloy²²

²² AECC Beijing Institute of Aeronautical Materials. DONG Chengli: dcldong@buaa.edu.cn

There are three key contents in this study: (1) Research on the structural optimization design method of the meridian plane of the turbine disc; (2) After shot-peening, the residual stress distribution and effective stress distribution of the simulation part of the meridian plane of the turbine disc were quantitatively determined; (3) To determine the influence of shot peening on the fatigue life of the simulation part of the meridian plane of the turbine disc.

The main findings of this study are as follows: (1) Shot peening increases the compressive residual stress and change the position of the maximum compressive residual stress. Meanwhile, the maximum compressive residual stress is not more located on material surface like AS notched specimen but at a depth of approximately 50~90 μ m from material surface. Meanwhile, the effective stress curve of shot peening notched specimen becomes “flat” and thus the effective stress gradient decreases compared with the applied stress. (2) The LCF lifetime of shot peening notched specimen is significantly improved compared with AS notched one and the LCF lifetime increment is between 2.05 and 7.66 times. In addition, the LCF lifetime dispersion becomes smaller after shot peening, especially for lower stresses.

According to the details of the meridian plane of the turbine disc, a simulation part of the meridian plane features was designed by adopting the principles of geometric similarity and stress state equivalence, as shown in Figure 2-83. Since the stress state of the characteristic simulator is consistent with that of the actual turbine disc at the details of the meridian plane, it is generally believed that both of them should have the same structural strength and life under the same loadings. Therefore, the design idea of characteristic simulators can be used to study the structural details of the turbine disc, which is convenient for tests, has low cost and short test cycle and can obtain large sample, and has important guiding significance for engineering applications.

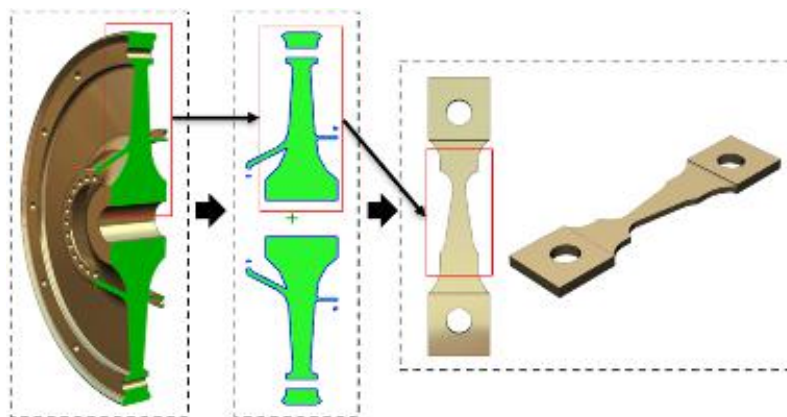


Figure 2-83 The design scheme of notched specimen

The mechanical shot peening process was used to carry out the shot peening at the gap of the simulation part of the meridian plane of the turbine disc, and the shot peening process was strictly carried out according to the actual engineering process route, so as to ensure the process consistency. Figure 2-84 shows the sketch of the shot peening process test of the simulation part of the meridian plane of the turbine disc. It can be seen that only the smallest side (notch root) of the simulation part of the meridian plane was shot peened to ensure that the shot peening position was consistent with the actual turbine disc.



Figure 2-84 Schematic drawings of shot peening treatment

Figure 2-85 shows the applied stress, residual stress and effective stress distribution along the through-thickness direction of AS and shot peening notched specimens. It should be noted that the effective stresses are obtained by adding the residual stresses to the applied stresses and the effective stress determines the final fatigue properties of the material. Interestingly, the maximum effective stress of AS notched specimen is located at the depth of 0.07~0.10mm from the surface and even somewhat higher than the applied stress. While for shot peening notched specimen, the maximum effective stress is located at the depth of 0.25~0.28mm from the surface and lower than the applied stress. On the whole, compared with the applied stress, the effective stress curve of shot peening notched specimen becomes “flat” and the effective stress gradient decreases. As described in the open literatures, the stress concentration of notched specimen is decreased due to the compressive residual stress introduced by shot peening.

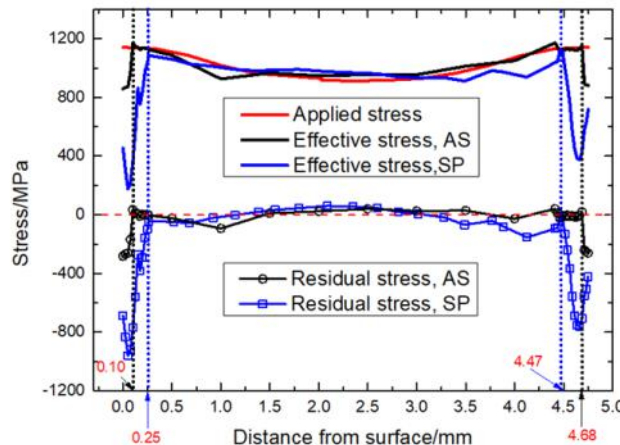


Figure 2-85 Calculation method of the effective stress

The influence of shot peening on the fatigue performance of the simulation part of the meridian plane of the turbine disc is represented by S-N curves with and without shot peening, as shown in Figure 2-86. It can be seen that the S-N curve equation can accurately predict the fatigue life of the simulation part of the meridian plane of the turbine disc with and without shot peening. After shot peening, the fatigue life of the simulation part of the meridian plane of the turbine disc increases, which indicates that shot peening has a promoting effect on the fatigue life gain. The life increase of high stress-short life area is not much, but the increase of low stress-long life area is significant, which is why the shot peening is most widely used in the field of low stress and long life high cycle fatigue.

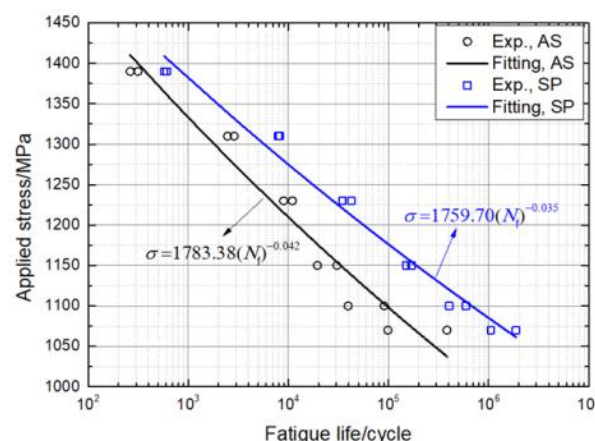


Figure 2-86 Influence of shot peening on fatigue life

2.4.2 Effect of Laser Shock Peening on Structure²³

This work mainly studies the change of microstructure and surface residual stress of typical aircraft structures after Laser Shock Peening, and compares the fatigue performance of the structure with that of the original material and shot peening. The DFR values of different materials after mechanical addition, shot peening and Laser Shock Peening are given through design-related experiments.

The test and analysis show that: Laser Shock Peening can increase the influence depth of residual compressive stress on the surface of the material, and can greatly improve the fatigue life of the structure compared with shot peening strengthening.

Influence on regional microstructure

The grain distribution of Al alloy is denser and more compact, and the distance between the grain layer and the layer decreases obviously. The grain size of Al alloy is greatly reduced because of the laser shock strengthening which induces the sub grain boundary in the material, and the coarse grain is divided into fine and uniform grain.

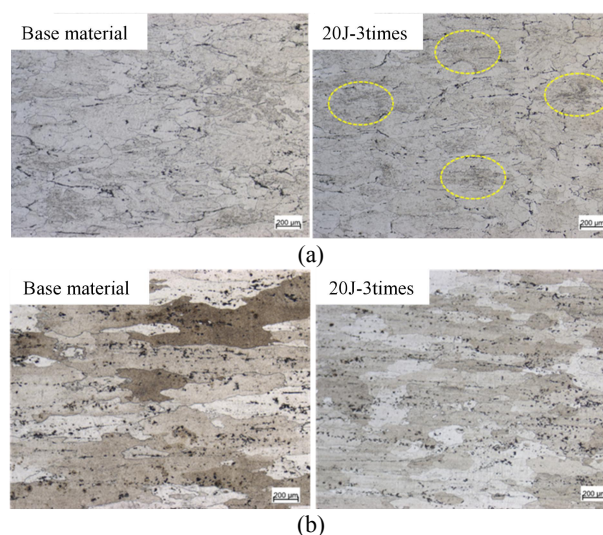


Figure 2-87 Microstructure Evolution of Laser Shock Peening Reinforced Aluminum Alloy: (a) 7050-T7451 material, (b) 2024-T351 material

²³AVIC The First Aircraft Institute. SHI Zhijun: 81707737@qq.com

Influence on residual stress

With the increase of impact times, the value of maximum residual stress increases and the depth of residual stress increases. With the increase of impact times, the net increase of residual stress decreases.

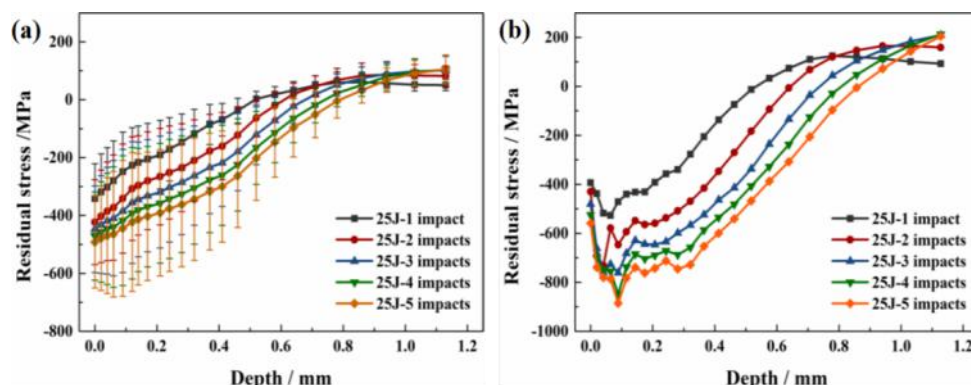


Figure 2-88 Residual stress of laser spot center depth under different impact times: (a) Body average residual, (b) stress joint residual stress

Influence on the DFR of structure

A comparative study of mechanical shot peening and laser shock peening of 2024, 7050 materials under three conditions of circular arc, notch and open-hole connection was carried out. The experimental results show that:

Arc test piece

The DFR of 2024-T351 for laser shock peening is 40% higher than that of machining and 20% higher than that of shot peening. The laser-enhanced DFR of 7050-T7451 material is 35% higher than that of machining and 25% higher than that of shot peening.

Notched test piece

The DFR of 2024-T351 for laser shock peening is 50% higher than that of machining and 10% higher than that of shot peening. The laser-enhanced DFR of 7050-T7451 material is 40% higher than that of machining and 1% higher than that of shot peening.

Test piece for open-hole connection

The DFR of 2024-T351 for laser shock peening is 15% higher than that of machining and 5% higher than that of shot peening. The laser-enhanced DFR of 7050-T7451 material is 45% higher than that of machining and 15% higher than that of shot peening.

2.5 WIDESPREAD FATIGUE DAMAGE

2.5.1 Crack Growth Simulation of Lap Joints With MSD Based on 3D Finite Element²⁴

Considering the contact and friction, three-dimensional finite element models of lap joints with MSD were established. The distribution and variation of SIFs at each crack tip with different crack lengths, rivet types, damage modes and clamping force are investigated. A predictive method for the cracks propagation of MSD is developed, in which an integral mean is adopted to quantify the SIF at

²⁴Civil Aviation University of China. ZOU Jun: sc.zoujun@gmail.com

crack tips, and the crack closure effect is considered. The Swift criterion is adopted as the crack link-up criterion, and the simplified net-section yielding is used as the failure criterion

Results show that K_I is dominant. Due to the secondary bending, rivet deformation and plate thickness, the SIF reaches minimum at outside surface, and the faying surface side is larger, while the maximum is located in the plate for almost all crack length. The SIFs values increase substantially due to the interaction of MSD cracks and the shorter the distance between cracks, the stronger the interaction. The integral average value of SIFs along the crack front for the countersunk rivet is larger than that of the flat head rivet, and the SIF value at the faying surface of countersunk rivet is larger than that of the flat head rivet, while the trend of SIF at the outside surface is opposite. The SIF reduces gradually with the increase of clamping force. A fatigue test of a lap-joint with MSD cracks is conducted to determine the cracks growth live and measure the cracks growth. The simulation result agreed well with the experimental data.

Analysis of Stress Intensity Factors of Lap Joints with Multiple Site Damage

The analysis results show that K_I is dominant for both countersunk rivet and flat rivet. Figure 2-89 gives the K_I distribution along the thickness direction when the cracks length all equal to 4mm, in which the 0mm corresponds to the fraying surface and 1.6mm corresponds to the outer surface. The value of K_I takes the maximum value of cracks. It can be seen that for both countersunk rivet and flat rivet, the minimum SIFs located at the outer surface, while the maximum SIFs located at the fraying surface, or in the interior of skin and close to the fraying surface. This is mainly due to the effect of secondary bending.

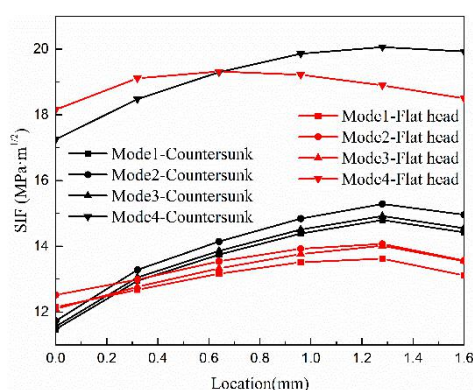


Figure 2-89 K_I along the thickness direction of lap joints with 4 mm crack length

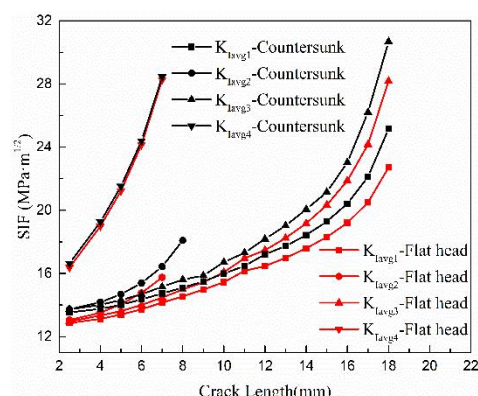


Figure 2-90 SIF of lap joints with different crack length for different crack modes

Figure 2-90 shows the variation curve of crack tip K_{Iavg} with different crack length when using countersunk rivets and flat head rivets. It can be seen that under the same crack length, the SIF of each crack modes have the following relationship: mode 4 > mode 2 > mode 3 > mode 1, and the difference in SIF value gradually increases as the crack grows. The SIF of the MSD cracks in mode 4 is significantly larger than that of the single crack in mode 1, and it increases very rapidly with the crack propagation, which indicates that the interference between MSD cracks is very significant. In the two double-crack modes, the SIF of mode 2 is greater than that of mode 3. This is because the distance between the two cracks of mode 2 is shorter and the interference effect is stronger, and the interference becomes more significant as the cracks grow.

In addition, the SIF value at the faying surface of countersunk rivet is larger than that of the flat head rivet, while the trend of SIF at the outside surface is opposite. This shows that the shape of the rivet has

a great influence on the distribution of SIF in the thickness direction, and the front edge of the crack is more concealed while using countersunk rivets. The overall change trend of the SIF curves is the same for countersunk rivets and flat rivets. When the crack length is the same in each crack mode, the SIF of the countersunk rivet is larger than that of the flat head rivet. Mode 4 has the smallest difference between the two types of rivet, indicating that the interference between cracks is the main factor affecting SIF in this case.

Multiple Crack Growth Experiment and Simulation for Lap-joints

Configuration of a three-row, six-column riveted lap-joint specimen was used in the experimental test, the configuration and dimensions are given in Figure 2-91. The specimen consisted of two 1.60-mm-thicks Al 2024-T3 alloy bare sheets, and riveted with countersunk-type, NAS1097AD6 rivets. The cracks configuration is shown in Figure 2-92, four cracks with equal 2mm length were produced at the edge of rivet holes on the row C of the lower skin.

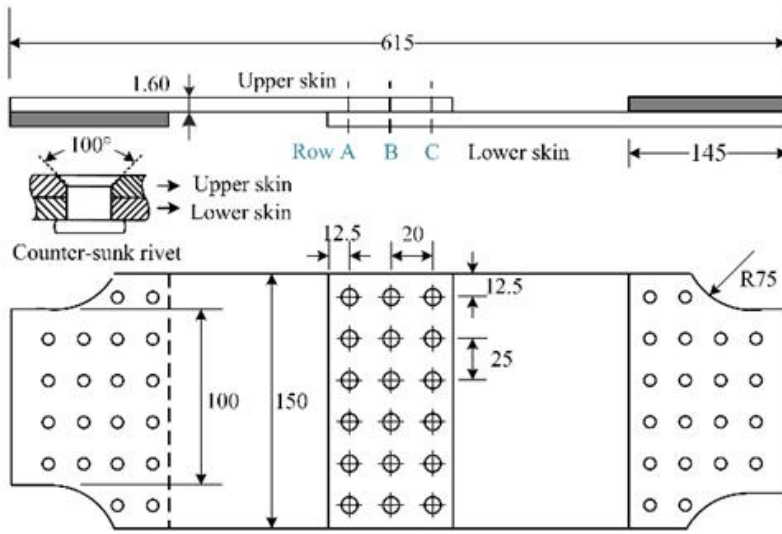


Figure 2-91 Geometry of lap-joint specimen (mm)

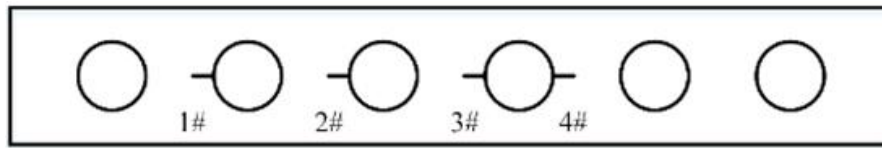


Figure 2-92 Cracks configuration of MSD

The crack-growth law proposed by Elber and the crack opening stress equation proposed by Newman are adopted to predict the propagation of each crack, which is expressed as:

$$\frac{da}{dN} = C(\Delta K_{eff})^m$$

where a is the crack length, N is the load cycle times, C and m are the material constants. The ΔK_{eff} is the effective SIF range and can be expressed as a function of ΔK_{avg} and u :

$$\Delta K_{eff} = K_{max} - K_{op} = u \Delta K_{avg}$$

where K_{avg} is the integral mean value in thickness, u is a function of stress ratio R and Newman's crack opening function f .

A comparison between the simulation results and the experimental data is presented in Figure 2-93, in which the horizontal part of the crack growth curve means the instantly link-up with the rivet hole. It can be seen that there is a good agreement between the experiment and the simulation results. The crack 3# links up with the next rivet hole at 92000 cycles in the simulation. Finally, the predicted crack growth life is 122000 cycles, which is overestimated 8.9% compared with the experiment results, which verifies the validity of the proposed method. The next step of the research is to investigate the crack growth method considering the shape of crack tips.

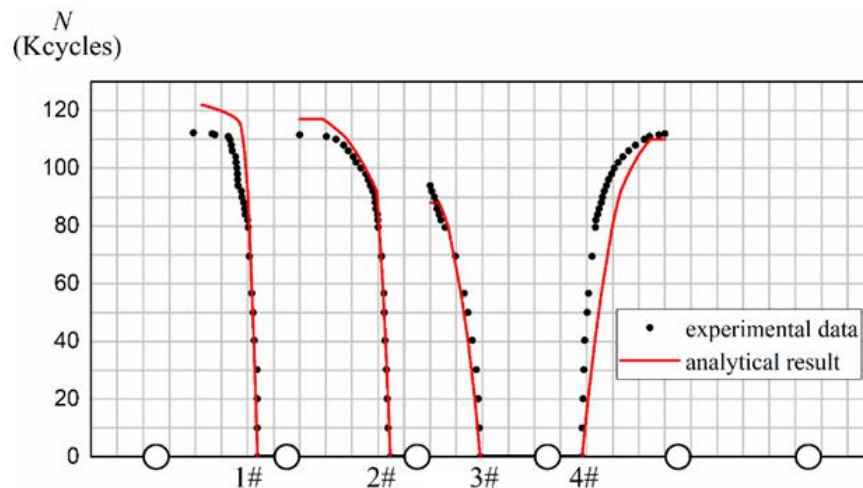


Figure 2-93 Comparison of experimental result and analytical result

2.5.2 Stiffened Panels With Multiple Collinear Cracks²⁵

Riveted stiffened panel is the elementary part and widely used in aircraft structures, for example fuselage and wing, due to its high buckling load, inherent fail-safe, and damage tolerant capability. There are numerous rivet holes in the same aircraft structure suffering from similar fatigue load. Due to stress concentration, fatigue cracks will randomly initiate from some rivet holes of the stiffened panel. In this paper, the weight function method (WFM) combined with the rivet force method is developed to calculate the SIFs and PZSs of a stiffened panel with *multiple site cracks*. Applying this method, the SIFs of a stiffened panel with two unequal length cracks and three symmetrical cracks are obtained. In addition, the critical remote stress for plastic zone coalescence of stiffened panel with two cracks are obtained. The resulted SIFs and PZSs are verified by comparing with those from FEM and existing literature. Compared to FEM, the present method is more efficient in the determination of the SIF for prediction of the fatigue crack growth behavior of stiffened panels with multiple site damage. More detailed information about this research was given by Zhang et al. (Zhang B, et al., Theor. Appl. Fract. Mech., 2020, 102816).

Stress intensity factor for a stiffened panel with multiple cracks

A stiffened panel with three collinear cracks is shown in Figure 2-94(a). The stringer is intact. The geometry and material parameters of the stiffened panel shown in Figure 2-94(a) are given in Zhang et al. The results for the center crack are normalized by $\sigma(\pi a_1)^{0.5}$, which are shown in Figure 2-94(b) for various crack length a_2 . For the same crack configuration, the rivet force method and Fredholm integral method were used by Nishimura to obtain the SIFs. Collins and Cartwright used the direct complex

²⁵Shanghai Jiao Tong University. XU Wu: xuwu@sjtu.edu.cn

stress function method. Their results are plotted in Figure 2-94(b). The SIFs from the present method and Nishimura are in good agreement, while, the results from Collins and Cartwright are slightly smaller.

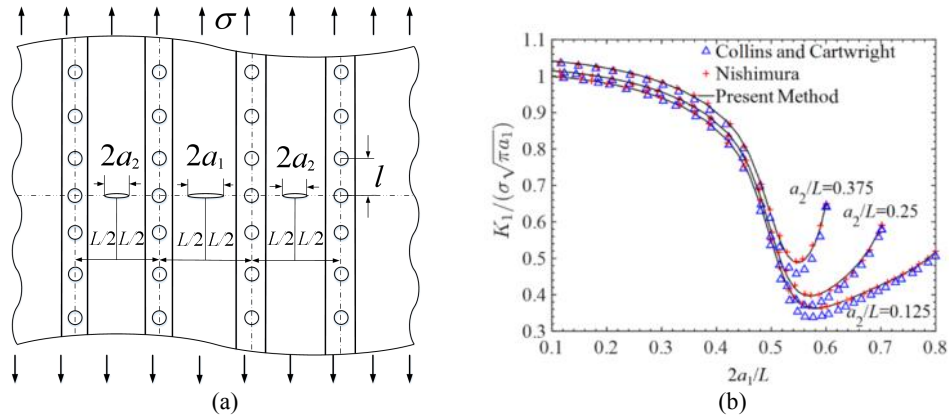


Figure 2-94 SIFs for stiffened panel with three symmetrical cracks. (a) Stiffened panel containing three symmetrical cracks; (b) SIFs obtained from different methods.

Plastic zones coalescence for stiffened panel with two collinear cracks

The strip yield model has been widely used due to its simplicity in elastoplastic analysis. The coalescence of the plastic zone is a critical state. The corresponding solution is frequently used to estimate the residual strength of panel with multiple site damage. A stiffened panel with two equal length cracks and intact stringers shown in Figure 2- 95(a) is used to apply and verify the present method. The normalized load σ/σ_s and the corresponding plastic zone R_o/a_T ($a_T=2a+R_o+R_i$) for various crack length $2a/L$ are shown in Figure 2-97(a) and Figure 2-97(b), respectively for different stringers. For the same crack configuration, the plastic zone coalescence was also studied by Nishimura (Nishimura T, Engng Fract Mech 2002; 1173-91), which are plotted in Figure 2-97 for comparison. The relative differences between the results from Nishimura and the present analysis are less than 1.6%.

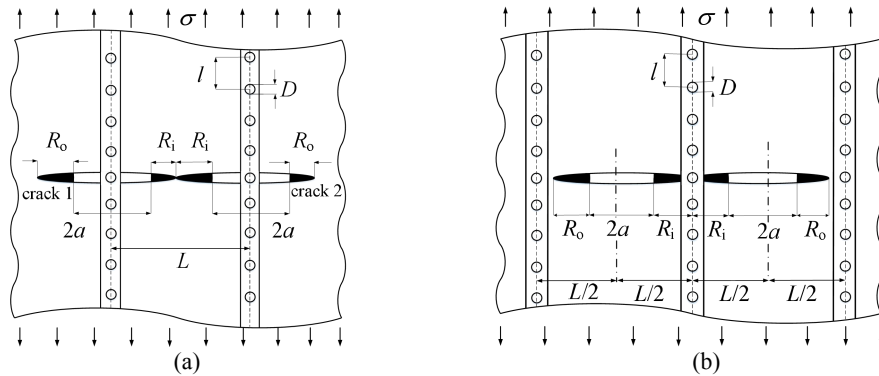


Figure 2- 95 Strip yield model of stiffened panel with two stringers: (a) Two stringers, (b) Three stringers

Another panel with two equal-length cracks and three intact stringers is shown in Figure 2- 95(b) The critical load and the corresponding plastic zones for various crack lengths are shown in Figure 2-98(a) and (b), respectively. For comparison, the results from Nishimura are also plotted in Figure 2-98. The results from these two methods are in good agreement for $2a/L < 0.6$, the differences between the present results and those from Nishimura is obvious when the cracks approach to each other ($2a/L > 0.7$). FEM is used to verify the results, the results are shown in Figure 2-98. It is observed that the present results compare well with those obtained from the FEM.

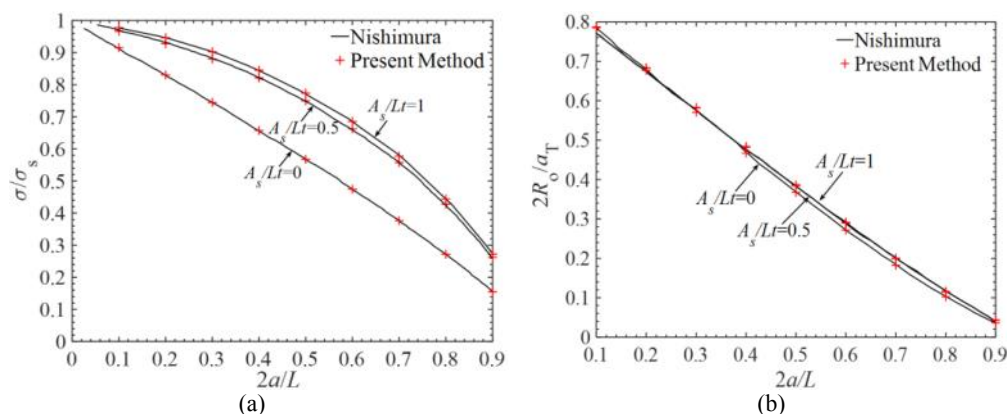


Figure 2- 96 Comparisons of the results for Figure 2-5a with those from Nishimura: (a) Normalized stress σ/σ_s for Figure 2-5a, (b) Normalized PZS R_o/a_T for Figure 2-5a

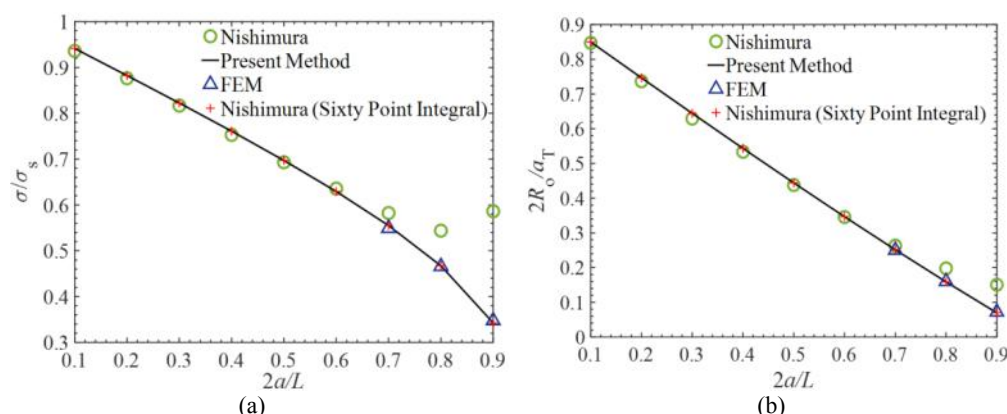


Figure 2-97 Comparisons of the results for Figure 2-5b with those from Nishimura: (a) Normalized stress σ/σ_s for Figure 2-5b, (b) Normalized PZS R_o/a_T for Figure 2-5b

2.5.3 Test Research on MSD Structure Containing Multiple Holes²⁶

In order to research the mechanism of MSD, a LY12CZ aluminum alloy panel with a thickness of 4mm was selected to prepare three parallel rows of 15 holes fatigue test specimens. After the test starting, observe the left and right sides of each hole. When a crack is found, record the number of the hole where the crack occurred and the number of load cycles at this time, until multiple damages are formed and the test piece fatigue fractures. Choose an appropriate number of cycle intervals, record the number of cycles corresponding to the condition of each crack, such as the size, morphology and distribution, and observe whether the cracks connection. When the specimen get fatigue fracture, recording the hole row number and the number of load cycle when the fracture occurred. Figure 2-98 shows the condition of the specimen after fatigue fracture.

²⁶ AVIC Aircraft Strength Research Institute. SUN Hanbin: sunhanbin623@163.com

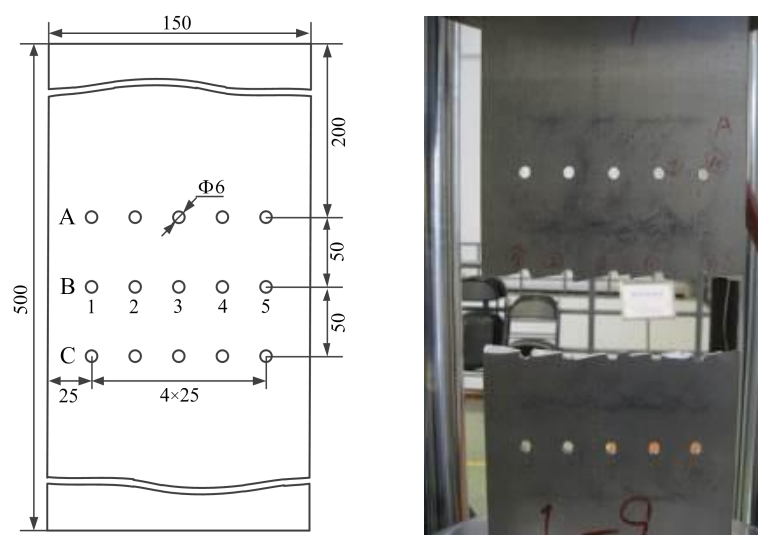
































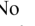



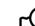

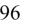



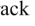



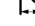











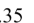


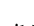














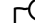

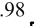
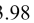
Figure 2-98 Fatigue fracture of test specimen

Three groups of the fatigue test specimens were completed, and the recorded test results are shown in Table 2-5. In Table 2-5, N_f represents the crack initiation life of the specimen, and N_l represents the fatigue life when fatigue fracture occurs. Table 2-6 shows that the crack condition of specimen 1 under the specified number of load cycles.

Table 2-5 Result of fatigue test

Specimen number	First cracked hole	N_f	Fracture row	N_l	Destruction form	Crack number	Crack connection
1	Right side of B2	330358	B	397883	MSD	11	Yes
2	Right side of C1	330708	C	417338	MSD	10	No
	Right side of C5						
3	Right side of C5	305425	C	422295	Not MSD	7	Yes

Table 2-6 Crack condition of MSD in the first specimen

Cycles	Crack growth state of row A in specimen 1					Crack growth state of row B in specimen 1				
	1	2	3	4	5	1	2	3	4	5
330 385			No crack							
			No crack							
										
										
										
										
										
										

Analyzing the test results, the following analysis results were obtained.

Since the test specimen contains many holes with similar stress levels, more than one crack is found

when the crack is first found.

It can be seen from Table 2-5 that the crack initiation life N_f of the test piece accounts for a large proportion in the entire fatigue life. It shows that when the first crack initiation until the MSD is formed in the structure, fatigue fracture will occur in a short time.

In the process of crack propagation, it will connect with its neighboring cracks and holes to form dominant cracks, and rapidly grow into a main crack. Crack connection is a common failure form of MSD.

It can be seen from Table 2-6 that while the cracks propagating, new cracks are also initiating. New cracks generally originate in the hole adjacent to the long crack. This is because the long crack increases the stress level around the adjacent hole. It is easy to initiate new cracks, and the mutual interference between the cracks affects each other's crack growth rate, accelerates the crack propagation, and causes the structure to MSD damage quickly. Therefore, it is a great significance to analyze and research the influence of MSD multi-crack interference.

2.6 FATIGUE AND CRACK GROWTH

2.6.1 High Cycle and Very High Cycle Fatigue Behavior of a TC17 Titanium Alloy Used for Compressor Blades ²⁷

The present research includes three key parts: effect of surface defect on high cycle and VHCF behavior of TC17 titanium alloy, effect of loading type on high cycle and VHCF behavior of TC17 titanium alloy, and effect of mean stress on high cycle and VHCF behavior of TC17 titanium alloy.

The main findings of this study are as follows: There exists a critical defect size less than which the defect does not affect the fatigue behavior. When the defect size is bigger than the critical size, the fatigue strength σ_w incorporating the effect of defect could be expressed as $\sigma_w(\sqrt{area})^n = C$, in which \sqrt{area} denotes the defect size and $area$ is the projection area of defect perpendicular to the principal stress direction, n and C are parameters. The fatigue strength of the TC17 alloy under rotating bending fatigue test is higher than that under axial loading fatigue test. Goodman formula could be well used to predict the influence of mean stress on the fatigue strength.

Effect of surface defect

Experimental results of the specimens with different surface drilled defects show that the effect of defect on fatigue behavior of the TC17 titanium alloy is greatly related to the defect size \sqrt{area} . There exists a critical defect size less than which the defect does not affect the fatigue behavior. When the defect size is bigger than the critical size, the crack initiates from defects, and the fatigue strength σ_w incorporating the effect of defect could be expressed as $\sigma_w(\sqrt{area})^n = C$, as shown in Figure 2-99.

²⁷Institute of Mechanics, Chinese Academy of Sciences. SUN Chengqi, scq@lnm.imech.ac.cn

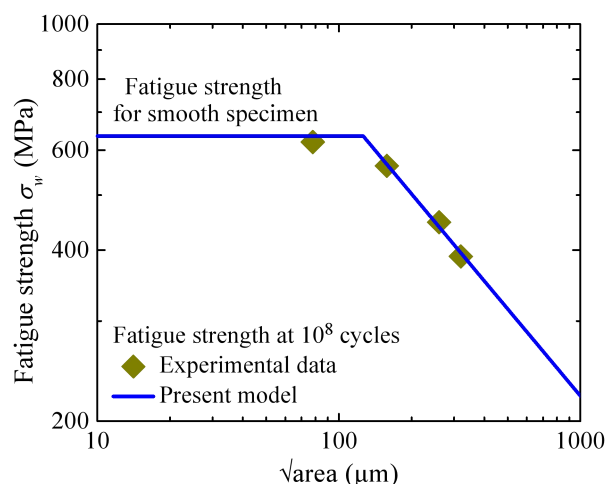


Figure 2-99 Effect of defect size on VHCF strength of TC17 alloy.

Effect of loading type

Experimental results at stress ratios $R=-1$ and $R=0.1$ indicate that the mean stress has an important influence on the fatigue performance of the TC17 titanium alloy. At the same fatigue life, the fatigue strength in terms of stress amplitude at positive stress ratio is obviously lower than that at negative stress ratio. It is found that the influence of mean stress on the fatigue strength of the TC17 alloy can be well described by Goodman formula, as shown in Figure2- 100.

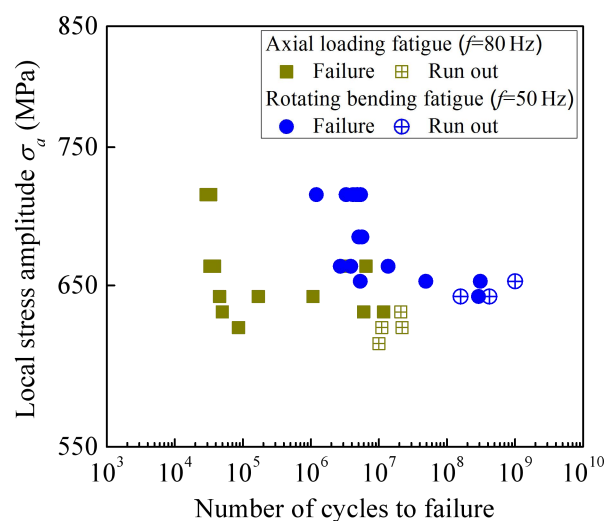


Figure2- 100 Effect of loading type on fatigue performance of TC17 alloy.

Effect of mean stress

Experimental results at stress ratios $R=-1$ and $R=0.1$ indicate that the mean stress has an important influence on the fatigue performance of TC17 titanium alloy. At the same life, the fatigue strength in terms of stress amplitude at positive stress ratio is obviously lower than that at negative stress ratio. It is found that the influence of mean stress on the fatigue strength of TC17 alloy can be well described by Goodman formula, as shown in Figure 2-101.

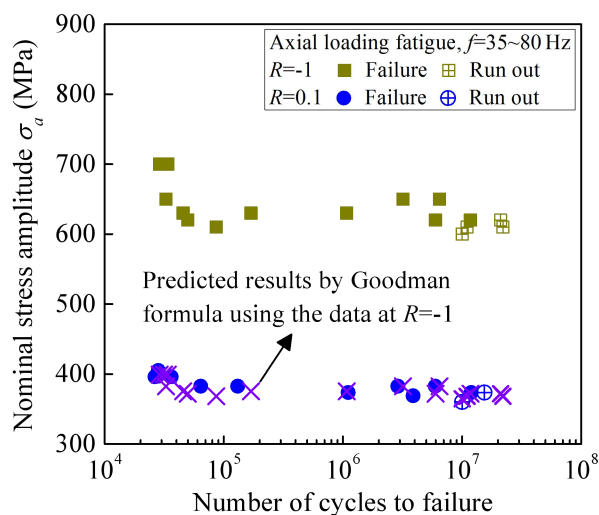


Figure 2-101 Effect of mean stress on fatigue performance of TC17 alloy.

2.6.2 Cause Analysis and Verification of Stress Corrosion Cracking²⁸

A large number of atypical cracks along the R angle or the line between the bolt holes appeared in the actual use of the aircraft, the representative cracks are shown in Figure 2-102. After scanning electron microscope analysis, it was found that the fracture surface showed obvious muddy pattern, as shown in Figure 2-103. The energy spectrum analysis showed that the content of O and CL in cracking area was high, and the metallographic analysis showed that the main crack had bifurcation phenomenon. In conclusion, it is considered that the atypical crack of the structure is a phenomenon of stress corrosion cracking (SCC) in the Cl ion environment.



Figure 2-102 The type of atypical cracks

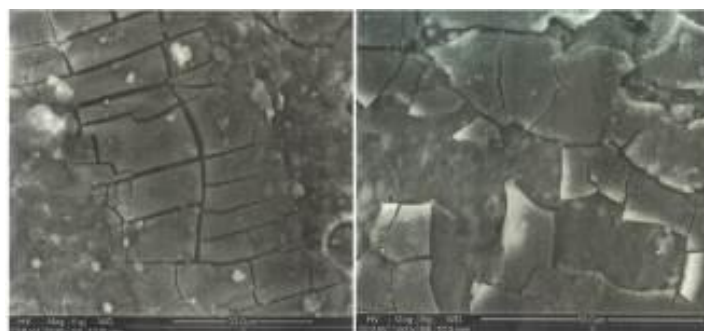


Figure 2-103 Scanning results of fracture surface by electron microscope

Cause analysis of stress corrosion cracking

²⁸AVIC Shenyang Aircraft Design & Research Institute. CHEN Liang: 5692864@qq.com

There are three basic conditions for SCC: specific environment, sensitive material and tensile stress. Because the aircraft works in the ocean atmosphere for years of service which is rich in CL ions, so the structure has a natural corrosion environment. The heat treatment state of 7B04 material is T651, and the peak aging process is sensitive to SCC. The critical stress of stress corrosion is only 120 MPa, which is much lower than other heat treatment states such as T73 and T74. The tensile stress mainly comes from the assembly stress caused by improper assembly. After the finite element analysis, as shown in Figure 2-104, the tensile stress at the root of the R angle is over 120 MPa when the assembly gap of the structure exceeds 0.4 mm, and the stress corrosion cracking will occur.

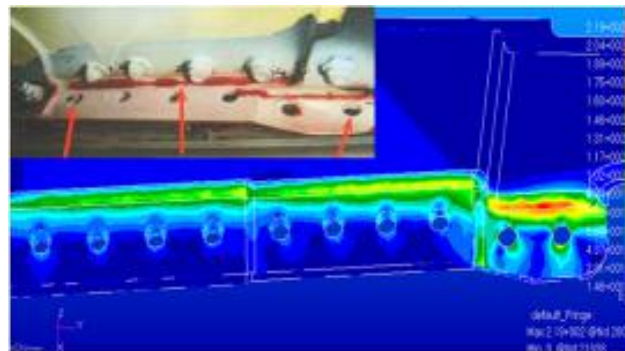


Figure 2-104 The cloud chart of assembly stress

Verification of stress corrosion cracking

Aiming at the problem of stress corrosion cracking, the SCC test of typical structures was carried out in order to find out the law of its cause and propagation. The test specimen of typical structure is shown in Figure 2-105. The main design points of the test specimen are as follows:

- The assembly of the test specimen and the fixture is connected through the web to simulate the stiffness support of the panel and beam (frame) of the aircraft;
- The test part is prefab down to simulate the assembly gap;
- The assembly stress is controlled by adjusting the tightening torque of the connecting bolt of the fixture and the test specimen.

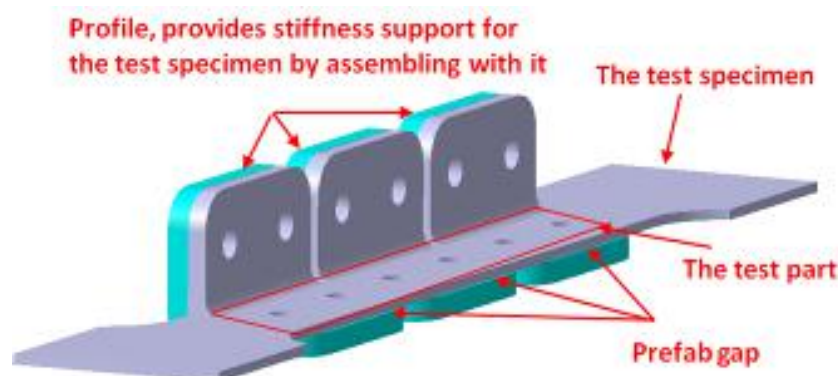


Figure 2-105 The test specimen of typical structure

The effects of assembly stress and heat treatment state of materials on the time of stress corrosion cracking were studied through the change of the material and stress. The test specimens included three heat treatment states, two gaps and two tightening torque. The test took every 30 minutes as the cycle, soaked for 7.5 minutes and stayed outside for 22.5 minutes with using far-infrared lamp to irradiate the

specimen to ensure its surface drying. The above six hours of accelerated environmental spectrum test are equivalent to one year of parking at the airport, as shown in Figure 2-106.



Figure 2-106 The schematic diagram of the SCC test

The number and the form of cracks produced by all of the specimen were statistically analyzed after the test. The result shows that the most common form of the crack in the test is the same as the position of the crack in the actual use, and the ratio is 91 % in the r angle region of the structure. Typical figures are shown in Figure 2-107.

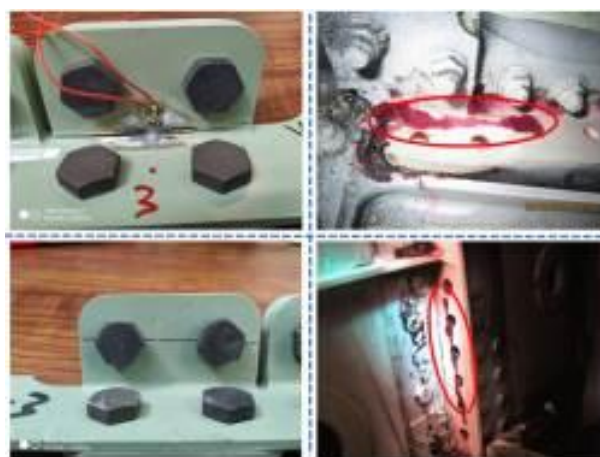


Figure 2-107 The comparison between the crack of the test and the crack in actual use

The variation of the strain of the characteristic point and gap between the holes is measured with the increase of the tightening torque. As shown in Figure 2-108, the result shows that the bigger the assembly gap and the tightening torque, the higher the assembly stress. The number of corrosion cracking at different gaps is shown in Figure 2-109. It shows that the higher the assembly stress, the easier it is to cause the stress corrosion cracking of the structure.

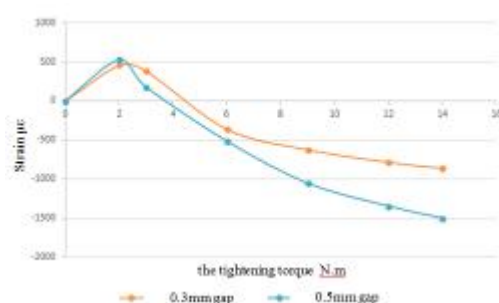


Figure 2-108 Variation of the strain between the bolt holes with tightening torque

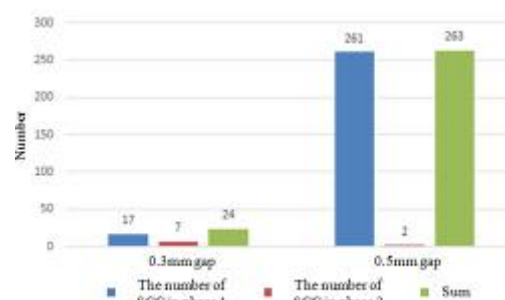


Figure 2-109 Number of corrosion cracks at different gaps

The number of corrosion cracking of test specimen of materials in different heat treatment states is shown in Figure 2-110. The result shows that the corrosion resistance of 7B04-T74 material is the best, while the resistance of 7B04-T6 material to stress corrosion cracking is better than that the B95-T1 material of the Foreign counterpart. The 7B04-T74 material should be preferred in the following design and repair.

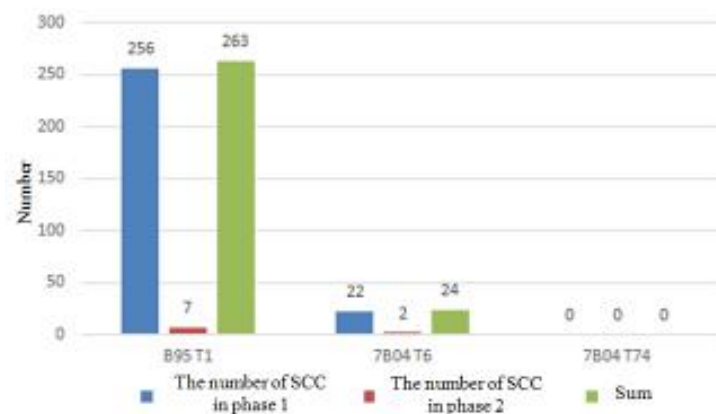


Figure 2-110 Number of corrosion cracks in different heat treatment state materials

2.6.3 Small Crack Growth Analysis²⁹

There are two key parts in this study: the determination of the size range of relatively small cracks and the corresponding crack propagation parameters. The EIFS distribution is obtained for the indentation details with the same rounded corners.

The main findings of this study are as follows: based on the approximate solution of the stress intensity factor and the FRANC3D software, the crack growth analysis was carried out, and the relative small crack size range and the method to determine the corresponding crack growth parameters were obtained. EIFS is independent of sag size and thickness.

Aiming at the need for multiple stress levels under the group fatigue tests to determine the scope and parameters of relatively small crack growth formula. At first, by expanding the stress intensity factor for polynomial correction coefficient, relatively small crack growth rate formula of durability analysis was obtained based on the material stable crack propagation of crack growth rate formula. Then, based on the approximate solution of the stress intensity factor (SIF) and the FRANC3D software, the crack propagation analysis of the centrally perforated plate subjected to far-field uniform tensile loading was carried out, and the relative small crack size range and the method to determine the corresponding crack propagation parameters were obtained as shown in Figure 2-111. Finally, durability tests of three kinds of specimens under constant amplitude alternating stress are carried out to verify the correctness of the proposed method.

²⁹ Beihang university. HE Xiaofan: xfhe@buaa.edu.cn

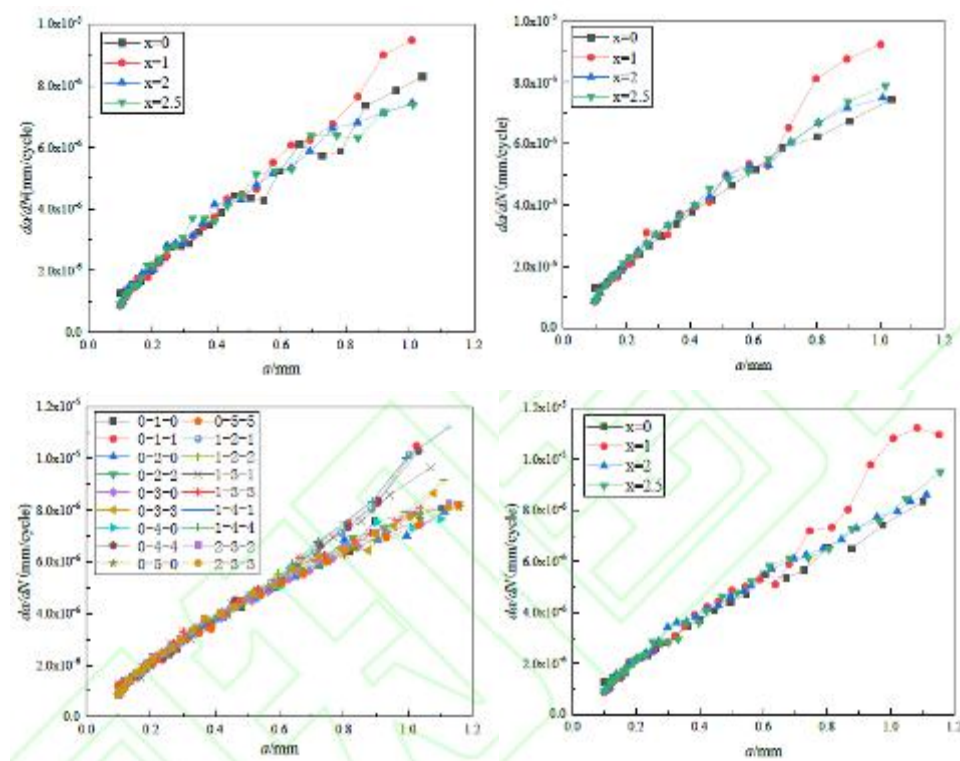


Figure 2-111 $da/dN - a^{n/2}$ curves based on FRANC3D simulation

A study of the EIFS distribution for determining the indentation details of the same fillet was carried out. The results of fracture analysis showed that the crack morphology and the crack initiation position of the specimen were all the same. Secondly, the appropriate crack growth equation is calculated based on the measured crack stress intensity factor, and the parameters of the crack growth equation were obtained by using XFEM for crack growth analysis. According to the crack growth equation and the fracture interpretation data, the EIFS of the specimen with the same fillet size was analyzed, and the hypothesis tests proved that the EIFS was independent of the size and thickness of the depression as shown in Figure 2-112.

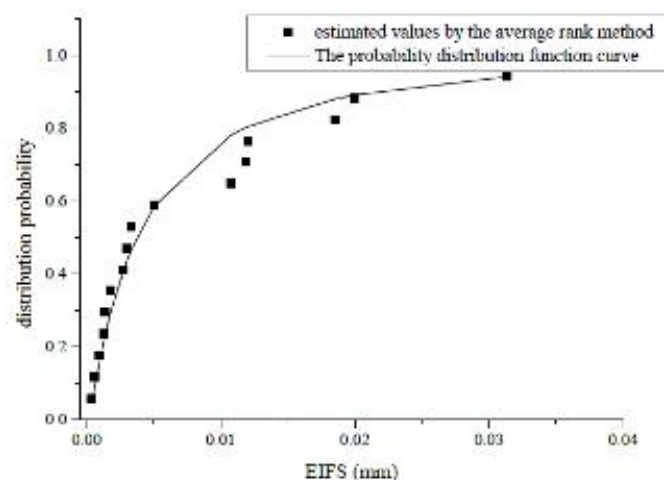


Figure 2-112 Distribution probability function curve

2.6.4 Application of 3D Slice Synthesis Weight Function Method³⁰

The SSWFM has been used to analyze a large variety of 3D crack problems involving various crack geometries and load conditions by Zhao-Wu and co-workers. The simplicity, versatility and good accuracy of the SSWFM were extensively demonstrated. The computational efficiency is several orders higher than the numerical methods.

3D Stress Intensity Factors Calculated by Slice Synthesis Weight Function Method

Let the cracked plate be divided by two series of orthogonal slices of infinitesimal thickness in y - z or x - z plane within the major/minor axis of the elliptical crack respectively. Each slice is in a generalized plane stress state. One family of the slices, say, a -slices (slices parallel to a -axis of the ellipse, with half crack length a_x), are set as the basic slices. The other, c -slices (slices parallel to c -axis of the ellipse, with half crack length c_y), as the spring slices.

WFs for the slices with elastic constraints can be constructed as follows:

$$m_i = m_{\text{collinear}} + T(R_i)(m_{\text{central}} - m_{\text{collinear}}), (i=a, c)$$

where $T(R_i)$, called transition factor, is an unknown function of restraining areas, R_i . The $T(R_i)$ should vary between zero and unity, and have the values: $T(0)=1$ and $T(\infty)=0$. Knowing the 3D WFs, the SIFs for the 2D slices can be obtained according to the WF theory as follows:

$$K_a(a_x) = \int_0^{a_x} [\sigma(x, y) - S(x, y)] \cdot m_a(R_a, a_x, y) dy$$

$$K_c(c_y) = \int_0^{c_y} S(x, y) \cdot m_c(R_c, c_y, x) dx$$

Further, the CODs for the slices can be determined by:

$$V_a(a_x, y) = \frac{1}{E} \int_y^{a_x} K_a(\xi) m_a(R_a, \xi, y) d\xi$$

$$V_c(c_y, x) = \frac{1}{E_s} \int_x^{c_y} K_c(\xi) m_c(R_c, \xi, x) d\xi$$

The CODs for the two 2D slices series should be equal, to satisfy compatibility requirement, leads to:

$$V_a = V_c$$

$$\int_y^{a_x} \int_0^{\xi} [\sigma(x, y) - S(x, y)] m_a(R_a, \xi, y) dy m_a(R_a, \xi, y) d\xi$$

$$= \frac{E}{E_s} \int_x^{c_y} \int_0^{\xi} S(x, y) m_c(R_c, \xi, x) dx m_c(R_c, \xi, x) d\xi$$

Having obtained the spring stress, 3D SIFs are able to reproduce:

$$K(\varphi) = \frac{1}{1-\eta^2} \left\{ K_a^4(a_x) + \left[\frac{E}{E_s} K_c(c_y) \right]^4 \right\}^{1/4} (-1)^n$$

Figure 2-113 shows comparisons between the SIFs from SSWFM and the analytical solutions by Shah-Kobayashi. The agreement is also very good, the maximum difference being about 5.0%.

³⁰ AECC Beijing Institute of Aeronautical Materials. ZHAO Xiaochen: melo_striving@126.com

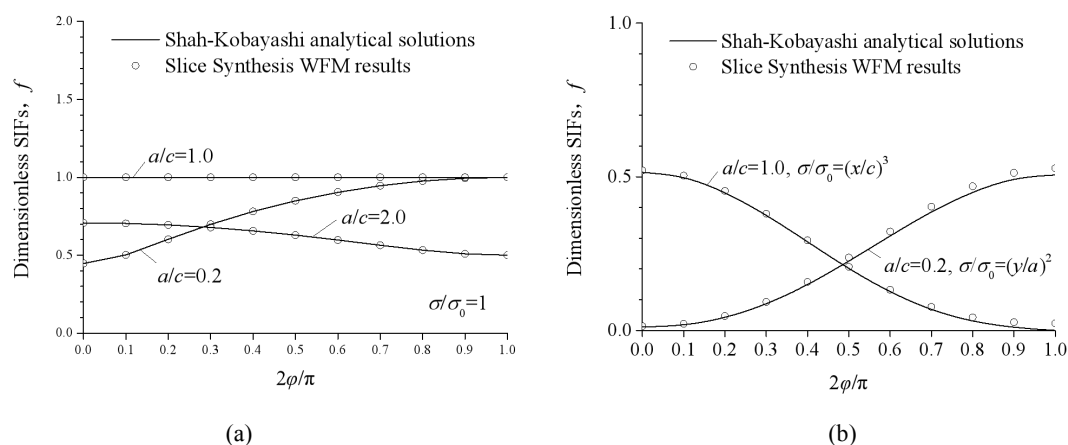


Figure 2-113 Comparisons between analytical and SSWFM SIF results for infinite embedded crack: (a) uniform stressing, (b) non-uniform stressing

Figure 2-113 shows comparisons between the SIFs for finite corner crack from SSWFM and the literature FEM results by Murakami and Newman-Raju, the maximum difference being about 5.0%.

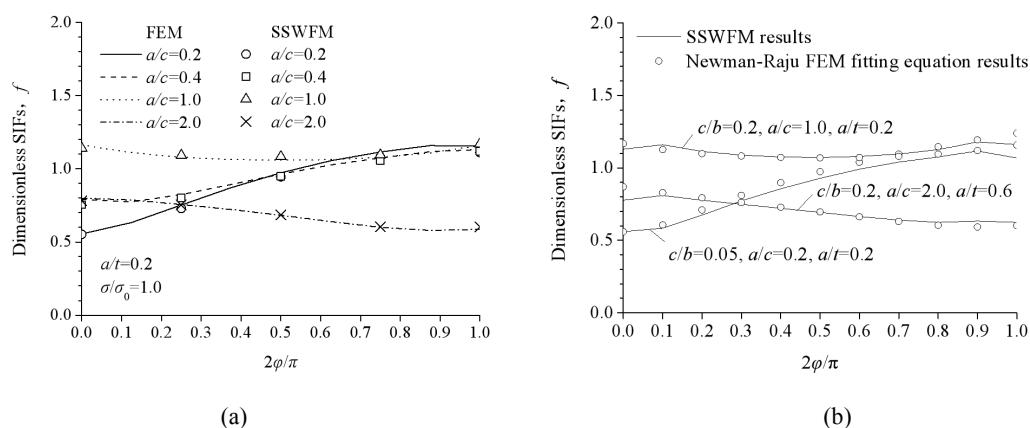


Figure 2-114 Comparisons between SIFs for finite corner crack from SSWFM and literature FEM results: (a) comparison between SSWFM and Murakami FEM, (b) comparison between SSWFM and Newman-Raju FEM fitting equations

Figure 2-115 shows comparisons between the SIFs for hole-edge corner crack from SSWFM and multiple FEM results, differences being within $\pm 3.0\%$.

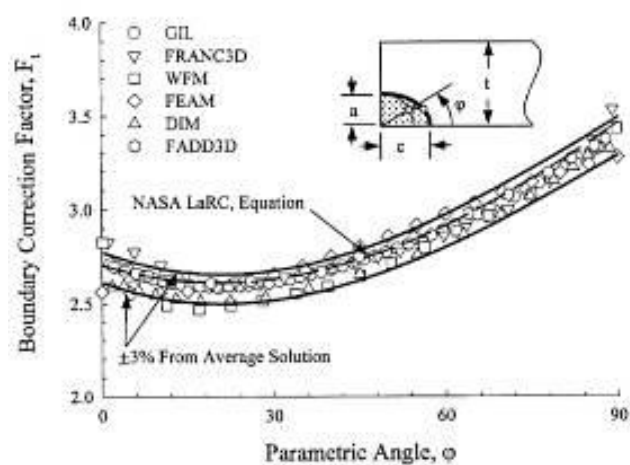


Figure 2-115 Comparisons between SIFs for hole-edge corner cracks from SSWFM and FEM results

3. APPLICATION RESEARCH IN FATIGUE AERONAUTICAL AND STRUCTURAL INTEGRITY

3.1 FATIGUE AND INTEGRITY DESIGN

3.1.1 Study on Buckling Fatigue of Thin-Walled Stiffened Structures³¹

The buckling wave of the tension field caused by the stress of the thin-walled stiffened structure produces additional tensile or flexural stress, which reduces the fatigue strength of the structure and changes the site of fatigue failure. There are few methods to control the buckling problem from the point of view of life and the evaluation method of buckling fatigue engineering.

The buckling fatigue tests of tensile field beam and shear fatigue test pieces were carried out. According to the relationship between tension field coefficient and load, S-N curve and aircraft life index, the lightweight design of fuselage panel can be carried out by controlling the severity of tension field. The method of buckling fatigue assessment is also presented.

Tension field buckling fatigue control method

The critical buckling load measured by fatigue test is in good agreement with that obtained by engineering tension field theory. According to the fatigue test results of three different load levels, the non-dimensional load-life curve and the load-tension field coefficient curve of buckling fatigue test pieces are given. The proposed tension field degree control method has been applied to the lightweight design of an aircraft fuselage stiffened panel structure.

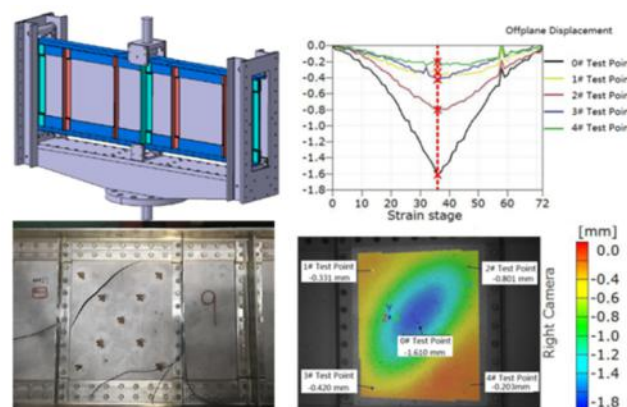


Figure 3-1 Buckling fatigue test of three-point bending beam

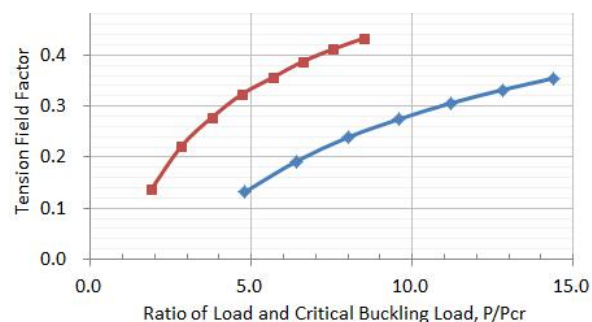


Figure 3-2 Relationship between the coefficient of tension field and the ratio of external load and critical buckling load

³¹AVIC The First Aircraft Institute. ZHANG Yanjun: sakerzyj@163.com

Buckling fatigue engineering analysis method

The buckling fatigue tests of thin-walled stiffened structures with different parameters were carried out. Based on the results of fatigue tests, a method of engineering buckling fatigue analysis based on DFR method is proposed. The influence coefficient of buckling fatigue is introduced for engineering evaluation.

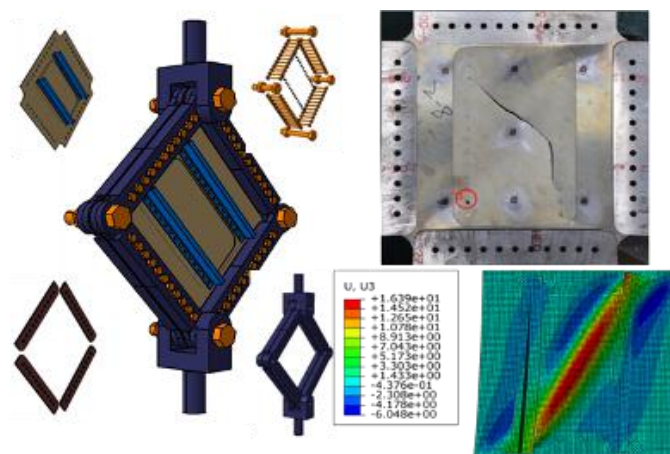


Figure 3-3 Buckling fatigue test of reinforced panel

3.1.2 The Design and Analysis of The Composite Material Concentrated Load-Bearing Joint³²

There are three key parts in this research: The design and analysis of the composite material concentrated load-bearing joint; Study on the forming technology of composite material concentrated load-bearing joint; Verification of strength performance of composite material concentrated load-bearing joint.

In this study, the design analysis, molding process and test and verification of the composite material concentrated load-bearing joint are carried out, and the typical joint is developed, and the design and analysis criteria, process rules, examination and verification methods are formed, and the weight of the composite material joint is reduced by 20% compared with that of the traditional metal joint. It lays a good foundation for the application of composite material concentrated load-bearing joint in civil aircraft.

Study on the joint of composite laminate

The traditional thin plate theory is not suitable for the analysis of large thickness laminates, so the interlayer shear effect must be taken into account. In this paper, the composite thick plate is divided into several sub-layers along the thickness direction by means of multi-scale modeling method, and the equivalent stiffness matrix of the sub-layers is calculated, and then the macro-global response of the structure is calculated. The stress/ strain of the whole is then decomposed into the stress/ strain of each layer by stress/ strain decomposition and coordinate transformation, as shown in the Figure 3-4 below. Based on the three-dimensional progressive failure theory of composite thick plates, a series of iterative operations, such as stress solution, failure discrimination and stiffness degradation, are carried out until the failure load and all single-layer failures are reached, and the damage conditions and damage modes

³² AVIC The First Aircraft Institute. CHEN Jun: 35548024@qq.com

of the structures are predicted according to the failure criteria, as shown in the diagram. The load-bearing test of full-size joints is carried out. As shown in the Figure 3-6 below, the error between the experimental failure load and the theoretical estimated load is less than 10%.

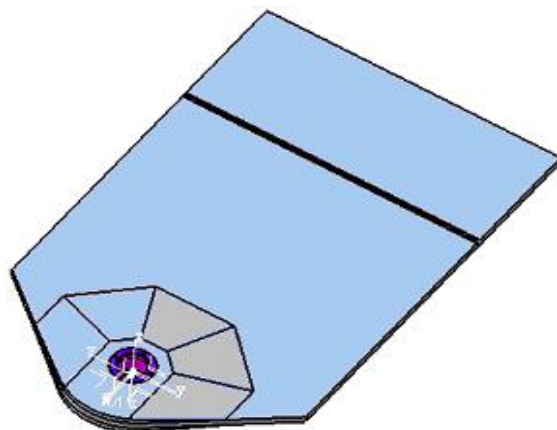


Figure 3-4 Vertical tail lug for tail and fuselage joint area

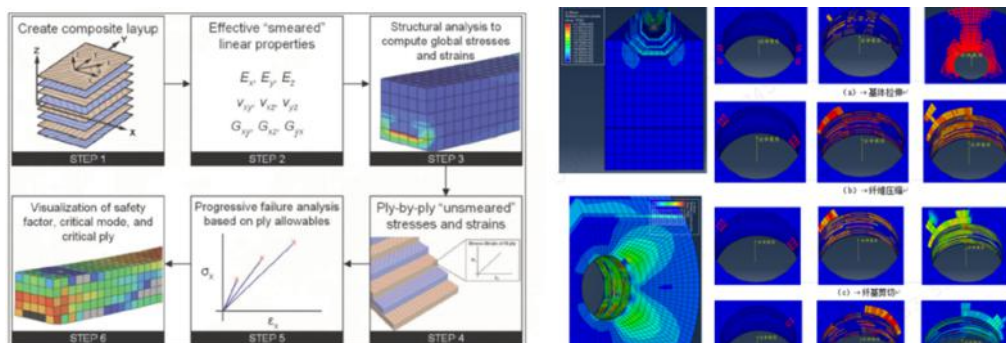


Figure 3-5 Multi-scale Modeling and Three-dimensional Progressive Failure Analysis



Figure 3-6 Full-size laminate joint damage tolerance test

Study on braided joint of composite material

This study is aimed at a civil aircraft aileron suspension control coupling joint, as shown in Figure 3-7, using 2.5D braiding technology to carry out structural design, in order to replace the original metal joint, to achieve weight reduction 20%. For the research of braided composite material analysis technology, the "building block" theory research and experiment combination scheme is adopted. The failure mechanism level analysis and experiment mainly study the calculation method of the elastic constant of 2.5D braided structure engineering and obtain the allowable value of the structure; Finite

element modeling and analysis were carried out for the ear piece, R region and key joint parts of braided joint., and the corresponding typical detail research experiment is done, verify the analysis method and get the bearing capacity; The finite element modeling and analysis of braided full-size joints are carried out, and the corresponding full-size joint verification tests are completed, which verify the effectiveness of the analysis method.

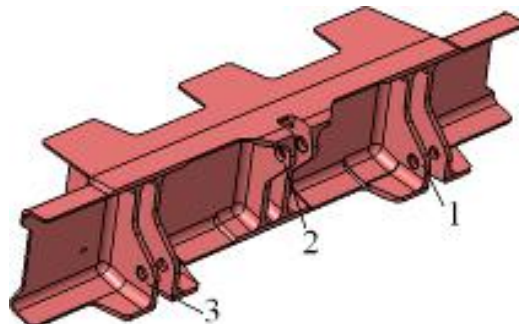


Figure 3-7 Schematic diagram of control coupling joint for aileron suspension



Figure 3-8 2.5D braided composite structure schematic diagram

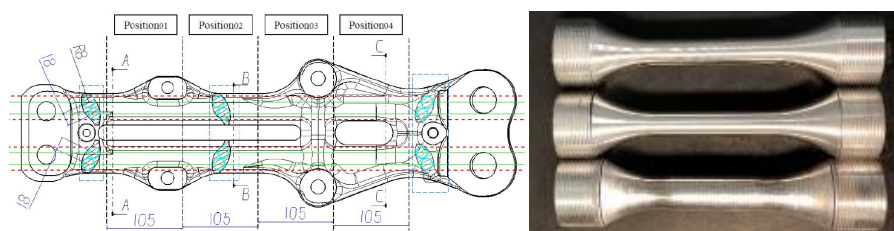
3.1.3 Effect of Surface Roughness on Fatigue Properties of Aluminum Matrix Composite Plywood³³

This research includes the research on the fatigue performance of different areas of plywood forming, the influence of aluminum matrix composites with different surface roughness on the fatigue performance, and the fatigue test of plywood with different surface roughness.

It is found that there is no difference in fatigue performance in different areas of the splint, the surface roughness has a significant effect on the fatigue performance of aluminum matrix composites, and the fatigue life of the splint is effectively improved after surface grinding in key areas.

Influence of different regions of splint on fatigue properties

By selecting different splints and dividing each splint into different areas, the test bar is made for fatigue test (Figure 3-9). It is found that there is no obvious difference in fatigue performance between different splints and different forming areas of the same splint.



³³ Harbin Aviation Industry Group CO, LTD. LI Liangcao: liliangcao@163.com

Figure 3-9 Test area and specimen of splint

Effect of surface roughness on fatigue properties of aluminum matrix composites.

Three groups of specimens with surface roughness of 1.6 μm 、3.2 μm and 6.4 μm were processed by sampling on the splint for fatigue test (Figure 3-10). The test results show that different surface roughness has a significant effect on the fatigue performance of the aluminum matrix composite, and the lower the roughness is, the greater the dispersion of the test results is.

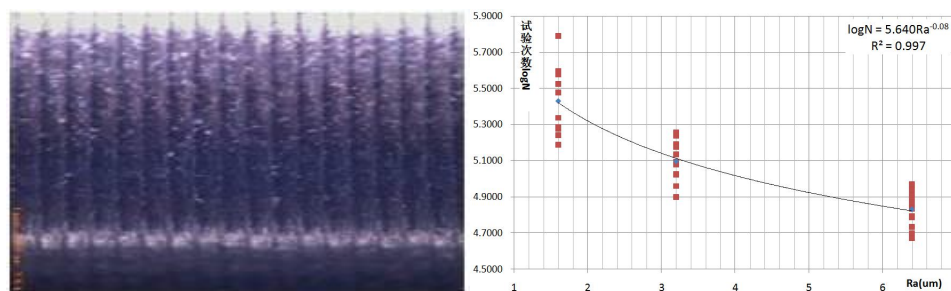


Figure 3-10 Influence curve of surface roughness on fatigue performance

Fatigue test verification of splint before and after local grinding

Through the finite element analysis of the splint under combined load, the key fatigue area is polished, and the fatigue test is carried out after reducing the surface roughness (Figure 3-11). The test results show that the fatigue test is carried out after reducing the surface roughness. The test results show that the fatigue performance of the splint after reducing the surface roughness is significantly improved, and the improvement range is basically consistent with the test results.

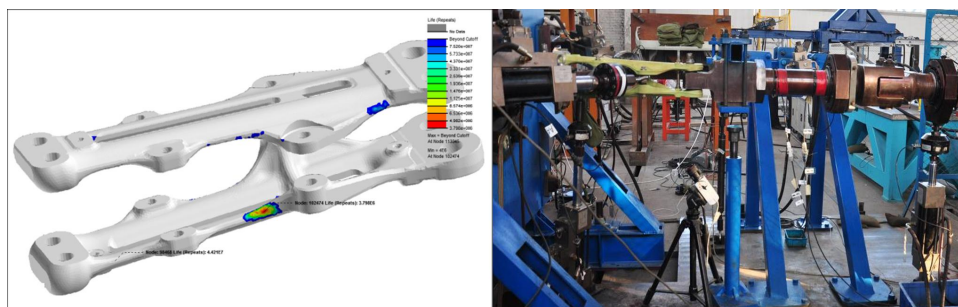


Figure 3-11 Fatigue test of splint

3.2 LOAD AND ENVIRONMENTAL SPECTRUM**3.2.1 Study on Scatter Factor of Severe Load Spectrum³⁴**

Fatigue scatter factor is used to describe the life reliability factor of fatigue analysis and test results, which is closely related to the life distribution function, standard deviation, reliability requirements and load spectrum. In order to implement the requirements of the durability load spectrum in the structural strength specification of military aircraft, this study carried out the damage distribution statistics of the fleet load spectra, the derivation of the scatter factor model and the selection of structural differential scatter factor, etc., so as to provide support for the refined structural life design and life management.

Damage distribution of the fleet load spectra

³⁴AVIC Chengdu Aircraft Design & Research Institute. DUI Hongna: duihn060379@126.com

Based on individual aircraft load tracking data in the fleet, according to maneuver identification and parametric load equation, the component load histories of various types of maneuver were obtained, and then the structural fatigue damage were calculated. By statistical test, the fatigue damage under the N_z spectrum at the center of gravity and the component load spectrum approximately follows lognormal distribution, as shown in Figure 3-12.

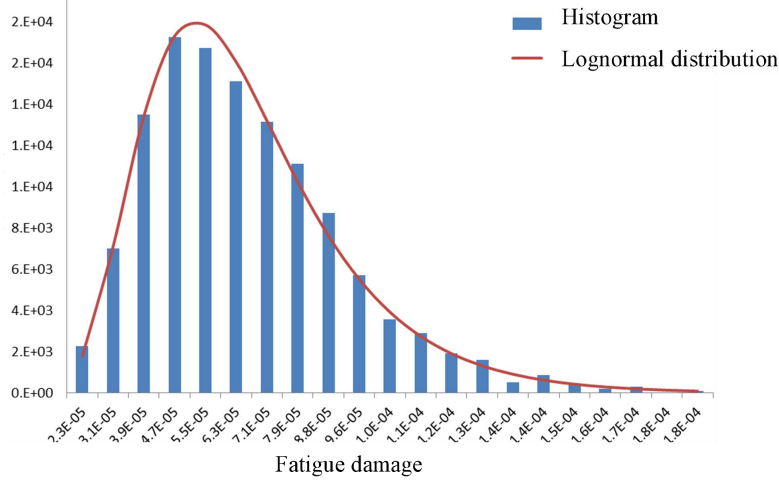


Figure 3-12 Fatigue damage distribution of wing bending spectra

Derivation of the scatter factor model

The fatigue scatter factor is mainly affected by two factors, one is the dispersion caused by structural material, assembly and process difference, the other is the dispersion caused by individual aircraft usage difference. A large number of fatigue tests at home and abroad have proved that the structural fatigue life under the specified spectrum follows the lognormal distribution. Based on the statistical analysis of individual load tracking data in the field, it has been concluded that the damage of the fleet load spectra is also subject to the lognormal distribution.

If the critical fatigue damage S of the structure obeys $LN(\mu_s, \sigma_s^2)$ and the damage L of the load spectrum of the group obeys $LN(\mu_l, \sigma_l^2)$, then the life N of the structure under any load spectrum can be expressed as S divided by L . After taking the logarithm, it can be deduced that N obeys $LN(\mu_s - \mu_l, \sigma_s^2 + \sigma_l^2)$.

When the load spectrum is specified, the life distribution only includes structural dispersion. When the severity level P of the load spectrum (also known as the reliability of the load spectrum) is introduced, the fatigue life N_p under the specified spectrum obeys $LN(\mu_s - \mu_{l,p}, \sigma_s^2)$, where $\mu_{l,p}$ can be obtained from the load damage distribution of the: $\mu_{l,p} = \mu_l + \Phi^{-1}(p)\sigma_l$

According to engineering practice, the fatigue scatter factor is the ratio of the median life ($N_{50,p}$) of the structure under the specified spectrum to the safety life ($N_{99.87}$) of the fleet (reliability is 99.87%). Therefore, the following formula can be deduced:

$$SF_p = \frac{N_{50,p}}{N_{99.87}} = 10^{(3\sqrt{\sigma_l^2 + \sigma_s^2} - \Phi^{-1}(p)\sigma_l)}$$

Based on the above derivation, the life distribution and scatter factor under 50% average spectrum and 90% severe spectrum is shown in Figure 3-13.

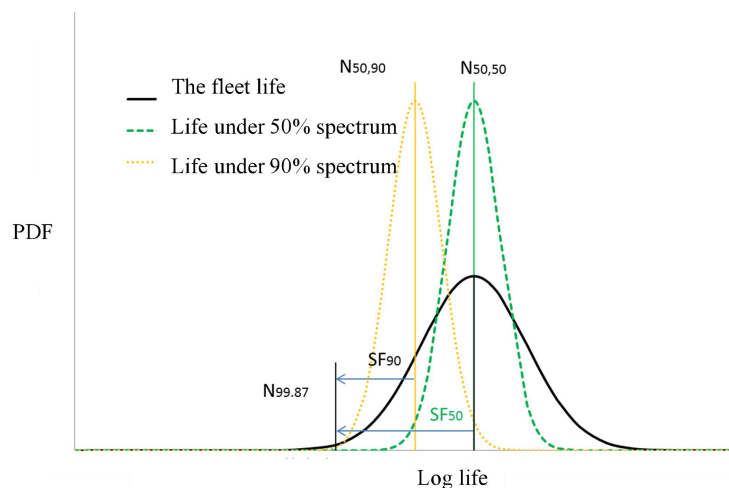


Figure 3-13 Life distributions under different spectra

Coupon fatigue test data of the last ten years were collected to calculate the standard deviation of crack initiation life, as shown in Figure 3-14.

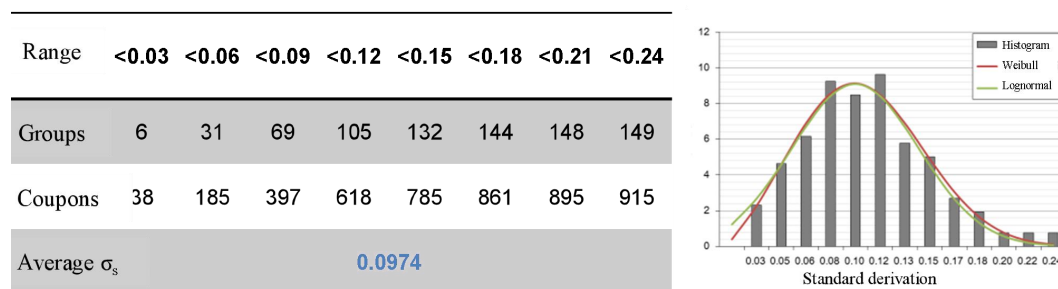


Figure 3-14 Standard deviation of crack initiation life based on coupon fatigue test data

The individual aircraft load history of more than 200 fielded aircraft in recent years was collected to calculate the equivalent damage of N_z spectra and its standard deviation. $\sigma_l \approx 0.18$

By substituting σ_s and σ_l into the above scatter factor formula, the scatter factor of load spectrum of any severity can be calculated.

The scatter factor of 90% severe spectrum can be reduced by about 40% compared with 50% average spectrum. Considering that the cycles of severe spectrum is more, the full-scale fatigue test with 90% severe spectrum can shorten the test duration by at least 30% and help to expose the structural critical areas in advance.

Structure scatter factor differentiation

In the traditional structure fatigue analysis and life management, uniform life reliability requirements (99.87%) and fatigue scatter factor are adopted for all fatigue critical structures. The advantage of doing this is simple and easy to manage, but it will cause a lot of structure design waste and a small part of the structure is still at danger.

The usage dispersion of different structures is significantly different. Table 3-1 shows the damage standard deviations of different structural details obtained based on the load spectra of different components.

In order to ensure the safety, economy and reliability of the structure, it is necessary to fully consider the differences in the use dispersion of different structures. The reliability requirements are graded

according to the importance degree, load characteristics, load transfer path, detectability degree, repair and replacement cost of the structure, and the matching fatigue scatter factor is given, so as to carry out more precise fatigue design and life management of the structure.

Table 3-1 Damage standard deviation and scatter factor of load spectrum of different components

Spectra	Detail	σ_1	scatter factor of different severity level		
			$(\sigma_s=0.1)$		
			50%	80%	90%
Structure A	Open hole	0.1679	3.86	2.79	2.35
Structure B	Open hole	0.1468	3.41	2.57	2.21
Structure C	Fillet	0.0742	2.36	2.05	1.9
Structure D	Fillet	0.0802	2.42	2.08	1.91

3.2.2 Measured Load Analysis of Helicopter³⁵

There are two key techniques in the present research, which are as follows: the extraction of load characteristic value and the compilation of measured load spectrum.

The key findings in the present research are that the high cycle fatigue damage of some body structures cannot be ignored, and even the high cycle fatigue damage is higher than the low cycle fatigue damage.

Extraction of measured load characteristic values

After state recognition and validity analysis of the measured load data of a helicopter, eigenvalues of each refined case and load were extracted, including static load, dynamic load, maximum load and minimum load, etc. Figure 3-15 is the distributions of static load, dynamic load, maximum load and minimum load of pitch rod.

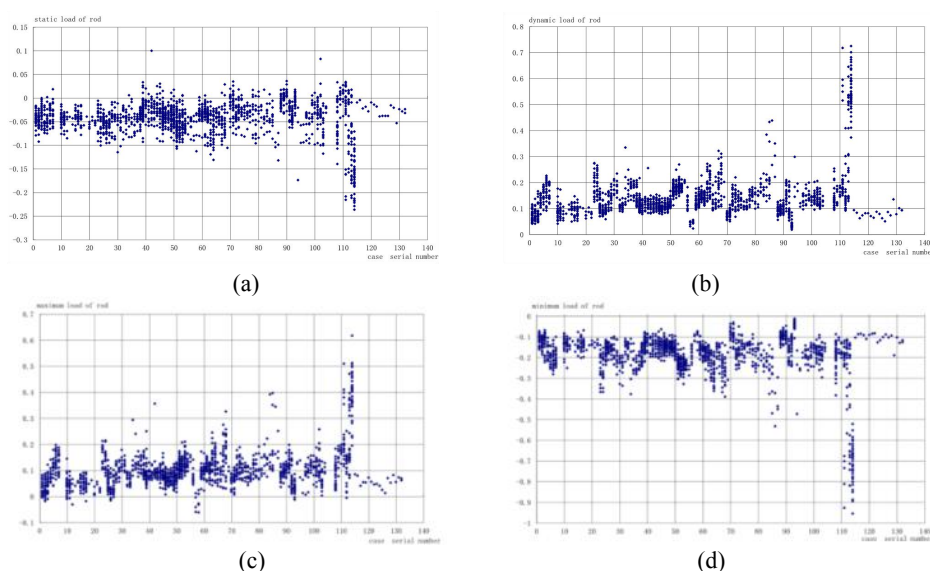


Figure 3-15 Load eigenvalues distributions of pitch rod with respected to refined cases: (a) static load, (b) dynamic load, (c) maximum load, (d) minimum load.

Compilation of low and high cycle measured load spectra and damage comparison

³⁵AVIC Helicopter Research and Development Institute. YU Jianjian: yujianjian000@sohu.com

Generally speaking, the main fatigue damage of body structure is low cycle fatigue damage. However, by observing the time domain curves and characteristic values of the measured loads of a helicopter, it is found that the dynamic loads near the main reducing gear box connection area and the flat tail are relatively large. A low cycle fatigue load spectrum compiling method for helicopter is established, and the spectrum cut-off law is determined. This method is suitable for automatically compiling spectrum with computer program based on more detailed caseloads.

By compiling the low-cycle and high-cycle fatigue load spectrum at the same time, the fatigue damages were compared and analyzed. The results show that the high cycle fatigue damage near the main reducing gear box connection area is not negligible and the high cycle fatigue damage of the flat tail is higher than the low cycle fatigue damage. Figure 3-16 shows the time domain curve of flat tail bending moment, Figure 3-17 shows the judgment diagram of low cycle fatigue load spectrum cut-off law, Figure 3-18 compares low-cycle and high-cycle fatigue damage near the main reducing gear box connection area.

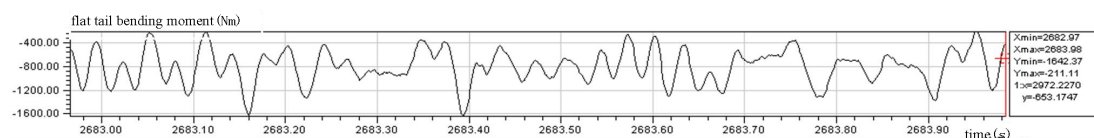


Figure 3-16 The time domain curve of flat tail bending moment

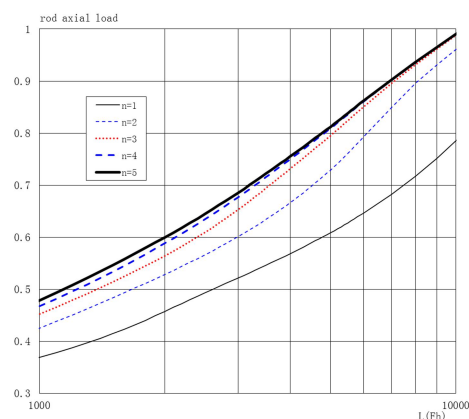


Figure 3-17 The judgment diagram of low cycle fatigue load spectrum cut-off law

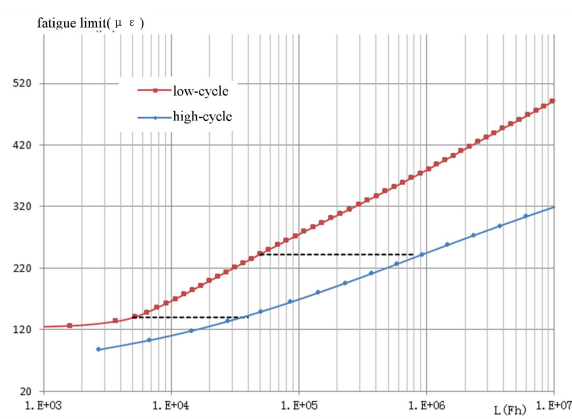


Figure 3-18 Comparison between low-cycle and high-cycle fatigue damage

3.2.3 Study on Service Environment of Aircraft Structure and Compilation Method Of Environment Spectrum of Aviation Aluminum Alloy ³⁶

There are three key parts in this study: collecting and analyzing the meteorological environment data of typical areas of atmospheric environment in China and conducting regional study on atmospheric corrosion; Research on local temperature and humidity environment of ground parking aircraft; Laboratory accelerated corrosion method for simulating coastal atmospheric corrosion of aluminum alloys.

The main conclusions of this study are as follows: the atmospheric environment in China is divided into five regions, and the regional map of atmospheric environment corrosion in China is drawn. The temperature and humidity of 14 local compartments of a certain type of aircraft were measured for one

³⁶ Air Force Engineering University. HE Yuting: heyut666@126.com

year, and the variation rules of temperature and humidity in different compartments were analyzed. The general temperature and humidity models were established respectively, and the model was verified by comparing the measured temperature and humidity data with the predicted data. A laboratory accelerated corrosion method was proposed to simulate the coastal atmospheric corrosion of aluminum alloy, and the accelerated corrosion test of aluminum alloy sheet was carried out. The feasibility of the accelerated corrosion method was verified by comparing the corrosion morphology, corrosion products and thickness degradation of the atmospheric corrosion test and the accelerated corrosion test.

Zoning of atmospheric environment in China based on corrosion of aviation metal materials

The main factors affecting the atmospheric corrosion of aircraft metal structure are: temperature, humidity, rain, fog, atmospheric pollutants, salt spray, etc. In view of the above factors, the meteorological environment data of typical regions of atmospheric environment in China are collected, and the meteorological environment data of 17 regions such as Beijing, Xiamen, Xigaze and so on are obtained. The meteorological environment of each region was equivalent converted, and the atmospheric environment was equivalent converted to standard humid air (air with temperature of 40°C and relative humidity of 90% RH). The action time of standard humid air equivalent to one year of atmospheric corrosion in a certain place was used as a unified index. The "Systematic Cluster Analysis" function of SPSS software was used to make a preliminary classification of the corrosion equivalent time of the collected 17 regions. The final zoning of atmospheric environment in China was drawn, as shown in Figure 3-19.



Figure 3-19 Zoning results of atmospheric environment in China based on corrosion of aviation metal materials

Study on local temperature and humidity environment of ground parking aircraft

The local environment (temperature environment and humidity environment of aircraft structure cabin) was studied with a certain type of aircraft. It is found that the temperature of different aircraft cabins in the same closed state can vary greatly, and the local temperature of aircraft structure is obviously affected by sunshine, temporary rainfall, and the form and position of cabin structure. The mathematical expression of the local temperature model of the aircraft cabin is as follows:

$$t_i = s_i t_0 + m_i + (1 - s_i) t_t \quad (3-1)$$

Where: t_i is the local temperature of the i th cabin; s_i and m_i are the corresponding sunshine coefficient and structure coefficient of the cabin respectively. t_0 is the ambient temperature, that is, the temperature of the louver; t_t is the ambient temperature at the beginning of the effect of sunshine. In order to assess the response degree of cabin humidity with cabin temperature, the temperature and humidity data are processed according to the following formula:

$$\begin{aligned} t_{kl} &= t_k - t_{k+l} \\ h_{kl} &= h_k - h_{k+l} \\ (l &= 1 \sim n-1; k = 1 \sim n-l) \end{aligned} \quad (3-2)$$

Where, h_i is the i -th humidity data, t_{ij} is the difference of two temperature data separated by j data, h_{ij} is the difference of two humidity data separated by j data.

Laboratory accelerated corrosion method for simulating coastal atmospheric corrosion of aluminum alloys

Taking the atmospheric environment of Wanning, Hainan as an example, the accelerated environmental spectrum of aluminum alloy was compiled. The equivalent concentrations of H_2SO_4 and HNO_3 in the dissolved equilibrium state of SO_2 and NO_2 in the local environmental elements in Wanning were calculated. The concentration of NaCl (4.23E-01 g/L) was determined by the concentration ratio of HNO_3 and NaCl in EXCO solution in GB/T 22639-08. The dipping time (7min) and drying time (53min) in the periodic infiltration test were determined by the ratio of the mean action time of fog and dew to the total amount of time in the atmospheric environment spectrum of Wanning, Hainan Province. The annual average temperature in Wanning atmospheric environmental spectrum was taken as the temperature of weekly immersion solution and drying, and the annual average relative humidity was taken as the relative humidity of drying. Finally, the ambient temperature for accelerated corrosion test was set at 23.9°C, and the relative humidity during drying was set at 87.56%.

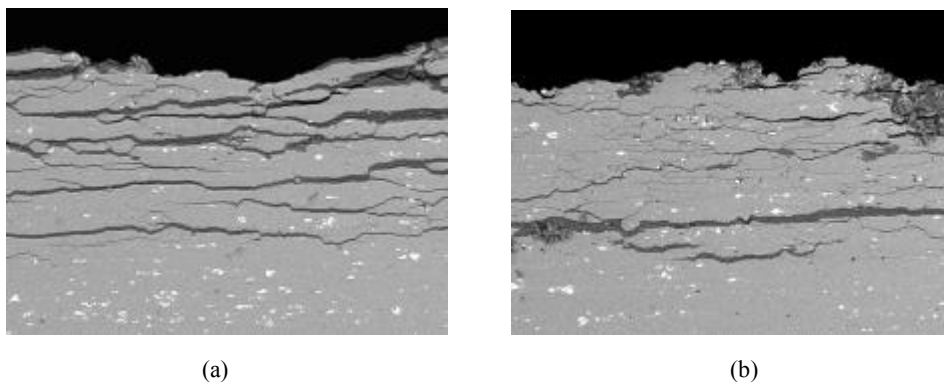


Figure 3- 20 (a) and (b) show the erosion morphology of the test piece after 20 years of atmospheric corrosion and 802 h of accelerated corrosion, respectively

As shown in Figure 3- 20, by comparing the corrosion morphology of the atmospheric exposure test piece and the accelerated corrosion test piece, it is found that both corrosion environments are denuded and the corrosion morphology is very similar. The reduction of residual thickness and life degradation of accelerated corrosion test pieces are very similar to atmospheric corrosion. The acceleration coefficient of accelerated environmental spectrum was determined to be 30.1 h/year, and the correlation

coefficient between the accelerated environment and the actual environment was 0.99.

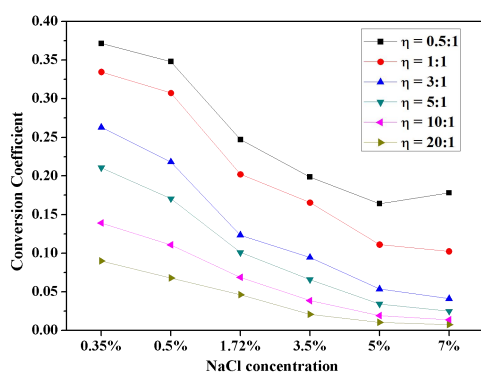
3.2.4 Equivalent Accelerated Relationship and Numerical Simulation of Corrosion of Aircraft Structures³⁷

There are two key techniques in the present research, which are as follows: corrosion equivalent accelerated relationship of typical dissimilar metals of aircraft; numerical simulation and experimental verification of corrosion of typical aircraft structures.

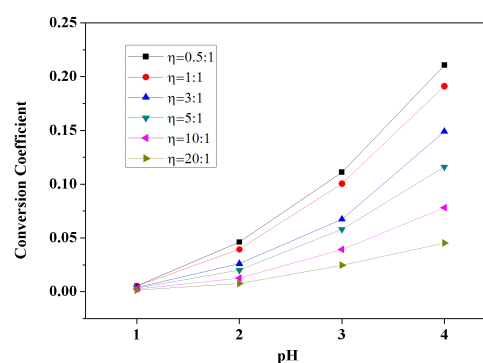
The key finds in the present research are as follows: the equivalent conversion coefficients of aluminum-titanium, aluminum-steel, aluminum-composite materials, and a variety of materials coupling in different concentrations of NaCl solution and water medium are obtained; based on the steady-state corrosion field and the parametric scanning equation, the corrosion numerical simulation models for structures composed of two materials and multiple materials are established with polarization data as boundary conditions, and the predicted results are in good agreement with the experimental results.

Equivalent accelerated relationship of galvanic corrosion of typical dissimilar metals

Corrosion equivalent conversion relationship is a bridge connecting the laboratory accelerated environment and the field service environment, which is used to determine the laboratory accelerated corrosion environment spectrum. The basic theories are the law of conservation of charge and the law of conservation of matter. The basic principles are the same corrosion mechanism and the same amount of corrosion damage. At present, the equivalent accelerated relationship of single metal is generally adopted at home and abroad, and the effect of galvanic corrosion of aircraft dissimilar metal structures is not considered.



(Figure 3-21)



(Figure 3-22)

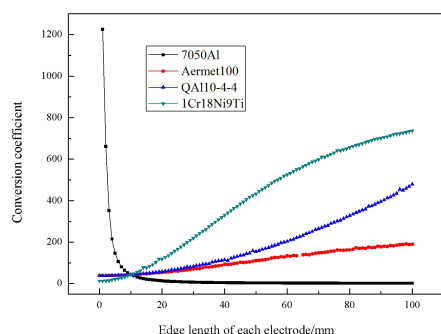
Figure 3-21 Conversion coefficients at different NaCl concentrations and area ratios

Figure 3-22 Conversion coefficients at 3.5% NaCl and different pH values and area ratios

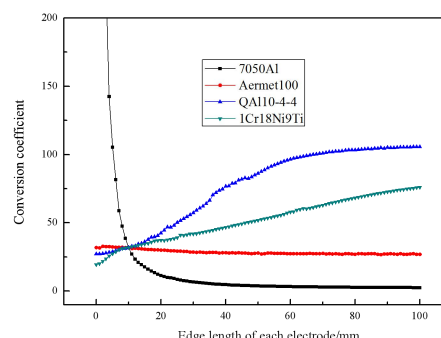
This part studies and analyzes the corrosion equivalent accelerated relationship under different material coupling and different corrosive media, namely conversion coefficient. The conversion coefficients of NaCl solution with different concentrations and water medium in the presence of galvanic corrosion of aluminum-titanium with different area ratios of anode and cathode are calculated, as shown in Figure 3-21. The conversion coefficients of different pH values and different area ratios of anode and cathode under 3.5% NaCl concentration are shown in Figure 3-22. Under the influence of the IR drop on the

³⁷ Naval Aviation University Qingdao Campus. CHEN Yueliang: cyl0532@sina.com

electrode surface, the potential distribution range in the liquid film state of the multi-electrode system is larger than that in the solution state. The conversion coefficients of 7050 aluminum alloy with different area ratios in the four-electrode system under the solution state and the liquid film with a thickness of 100 μ m are shown in Figure 3-23 and Figure 3-24, respectively.



(Figure 3-23)



(Figure 3-24)

Figure 3-23 Equivalent conversion coefficients of 7050 aluminum alloy with different area ratios in solution

Figure 3-24 Equivalent conversion coefficients of 7050 aluminum alloy with different area ratios under the liquid film with a thick

Numerical simulation and experimental verification of corrosion of typical aircraft structures

The numerical physical model is based on the multi-particle migration theory and electrode dynamics model. A set of partial differential equations are obtained by sorting and transforming the theoretical equations. The potential distribution and current density distribution of corrosion electric field can be obtained by solving the equations. The corrosion of the 7050 aluminum alloy-Aermet100 steel-QA110-4-4 copper lap joint and structural part was predicted by numerical simulation and an accelerated corrosion verification test was carried out in the laboratory.

The potential distribution and corrosion test result of the lap joint are shown in Figure 3-25 and Figure 3-26 respectively. The distribution results of current and corrosion depth are shown in Figure 3-27, and the corrosion test result is shown in Figure 3-28. The results show that the simulation results are consistent with the test results.

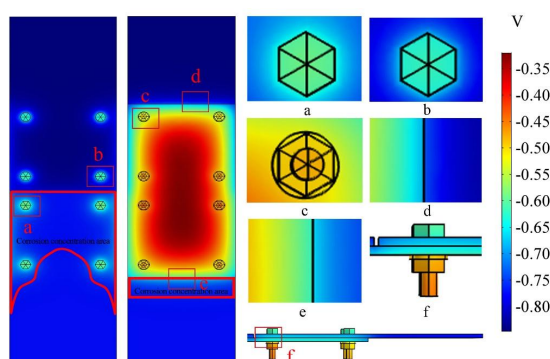


Figure 3-25 Potential distribution of the lap joint

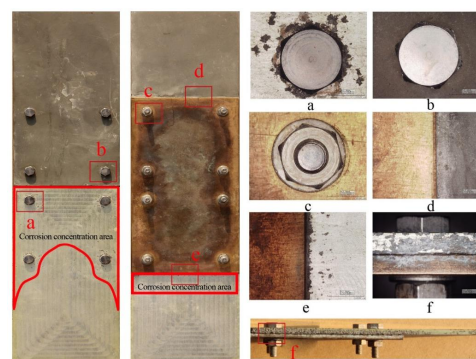


Figure 3-26 Corrosion test result of the lap joint

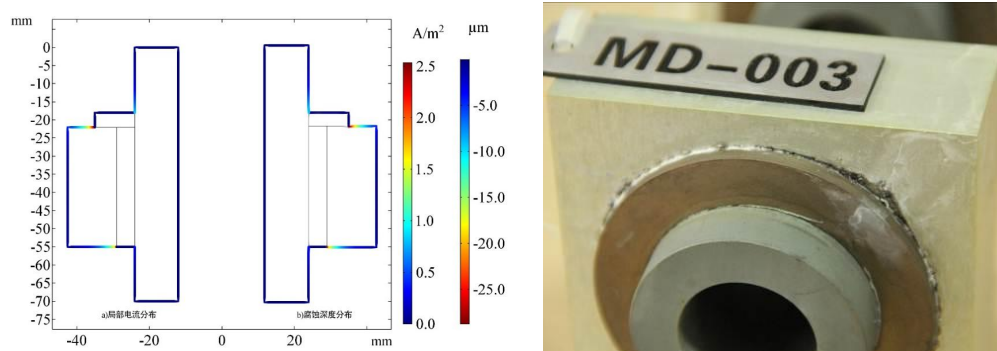
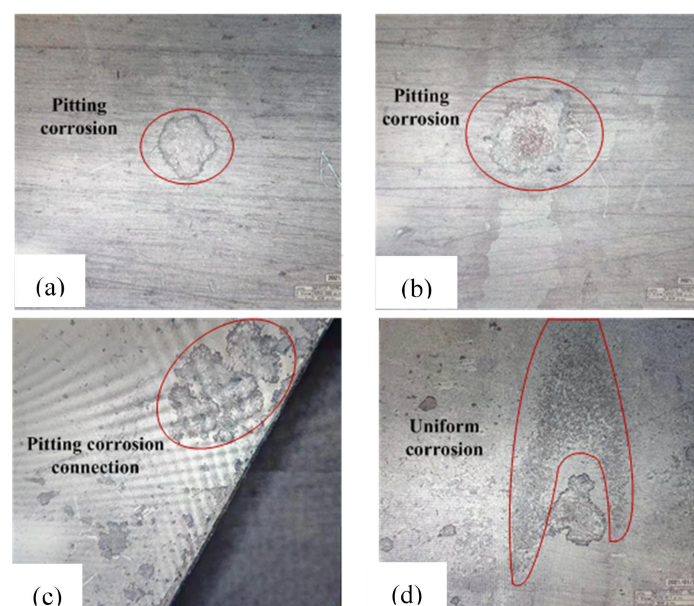


Figure 3-27 Distribution result of current and corrosion depth Figure 3-28 Corrosion test result of the structural part

3.2.5 Research on Corrosion Damage of Aviation Aluminum Alloy in Equivalent Accelerate Corrosion Environment³⁸

Aluminum alloy has the advantages of low density, good plasticity and high specific strength, and is widely used in important structural parts of aircraft structures. Aircraft are often exposed to corrosive environment such as rainwater, salt spray, sea water and humid air in the process of use, and aluminum alloy structure is easy to produce corrosion damage in the corrosive environment. Under the combined action of corrosion and fatigue load, aircraft structure is easy to initiate fatigue cracks at the corrosion damage site, which reduces the fatigue life of the structure, poses a major threat to the safety and reliability of aircraft structure, and even causes aircraft flight safety accidents.

The KH-7709 three-dimensional optical microscope and its measurement software were used to observe the specimens after different corrosion times. As shown in Figure 3-29, the morphology of the corrosion pits at different corrosion times under a 100x magnification factor. The subsequent measurement of different corrosion times The principle of the size of the etch pit of the lower test piece is to focus on the measuring object multiple times at different heights, and measure the size of the pit according to the focal length difference.



³⁸ AVIC Aircraft Strength Research Institute. SUN Hanbin: sunhanbin623@163.com

Figure 3-29 The morphology of corrosion pit with different corrosion time ($\times 100$): (a) 5a, (b) 10a, (c) 20a, (d) 30a

It can be seen from Figure 3-29 and Figure 3-30 that after the equivalent accelerated corrosion time of 5a, the corrosion degree of the specimen surface is relatively slight, resulting in a single independent corrosion pit with small depth and width. The depth of the corrosion pit after the equivalent accelerated corrosion time of 10a, as the corrosion time continues to increase, the depth and width of the corrosion pits further increase. When the equivalent accelerated corrosion is 20 years, multiple etch pits are connected to form a large pit, and the edge part of the specimen is corroded more severely; When the equivalent accelerated corrosion is 30a, the specimen has uniform corrosion and a large number of pits, which destroys the surface integrity of the structure.

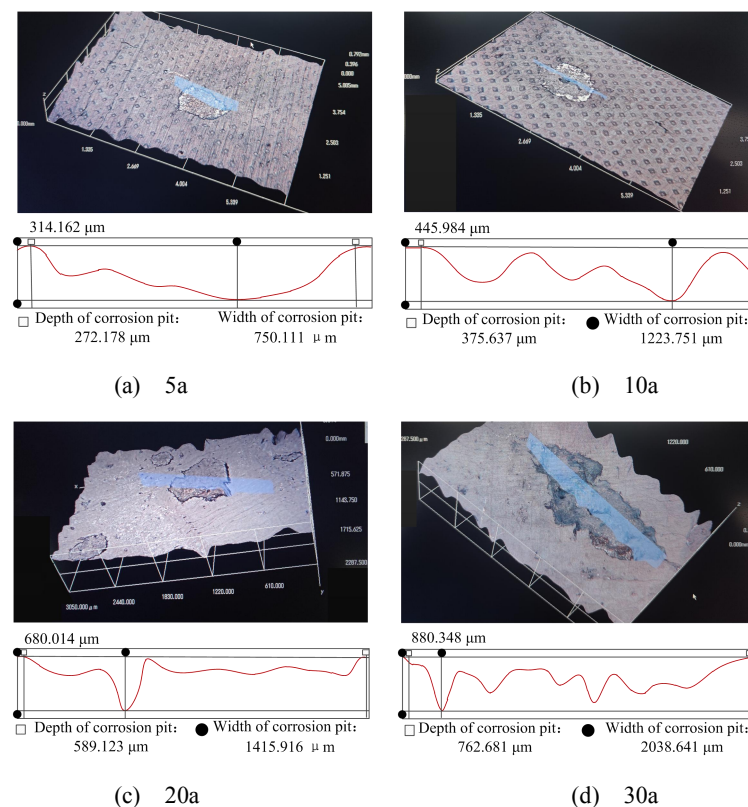


Figure 3-30 Corrosion pit depth and width with different corrosion time

The weight of each test specimen before and after corrosion in each group of tests was measured and recorded, and results are shown in Table 3-2. It can be seen from Table 3-2 that the average weight gain rate of the specimens after corrosion are all negative values, indicating that corrosion causes the weight of the specimens to decrease, and as the corrosion time increases, the weight reduction rate of the specimens becomes larger.

This is because the corrosion products produced by the test specimen are continuously dissolved and fallen off in the surrounding immersion solution. With the extension of the corrosion time, the material produces a large amount of dissolved and fallen off corrosion products, which leads to the increase of the depth and width of the corrosion pits and the weight reduction of the test specimen.

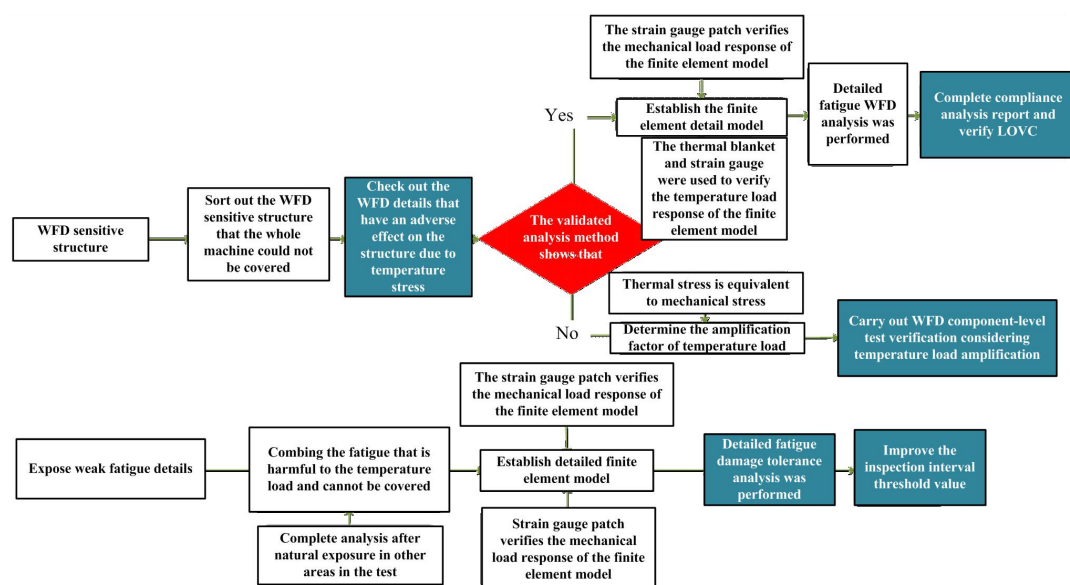
Table 3-2 Weight of specimens with different corrosion time

Corrosion time (a)	Weight with different corrosion time (g)							Average weight gain rate (%)
10	Before	105.432	105.580	105.205	105.144	105.315	105.315	-0.012
	After	105.422	105.569	105.202	105.134	105.525	105.303	
20	Before	105.568	105.279	105.605	105.381	105.497	105.453	-0.033
	After	105.547	105.257	105.522	105.36	105.459	105.426	
30	Before	105.600	105.462	105.416	105.511	105.592	105.700	-0.357
	After	105.226	105.027	105.032	105.14	105.146	105.381	
40	Before	104.983	105.617	105.67	105.507	105.316	105.560	-0.456
	After	104.556	105.206	105.229	104.967	104.887	104.980	

3.3 STRUCTURAL INTEGRITY REQUIREMENT AND AIRWORTHINESS COMPLIANCE ASSESSMENT

3.3.1 Airworthiness Compliance Verification of Hybrid Structure³⁹

In the full-scale test, the fatigue performance of the hybrid structure cannot be fully verified by applying temperature cycles, so it is necessary to establish a component level test verification technology based on analysis and / or considering load amplification factor to verify the LOVc of the hybrid structure. It should be noted that the additional load caused by temperature is usually the internal force of the structure, and the load amplification factor is not feasible most of the time, some of time it makes other structures over examined. Therefore, it is necessary to analyze and verify the airworthiness compliance of WFD sensitive structures with the help of thermal stress equivalent mechanical stress or thermal stress equivalent fatigue life. The idea of verification is shown in Figure 3-31.



39 COMAC Shanghai Aircraft Design & Research Institute. ZHANG Yibo: zhangyibo@comac.cc

Figure 3-31 Full scale test verification idea of hybrid structure

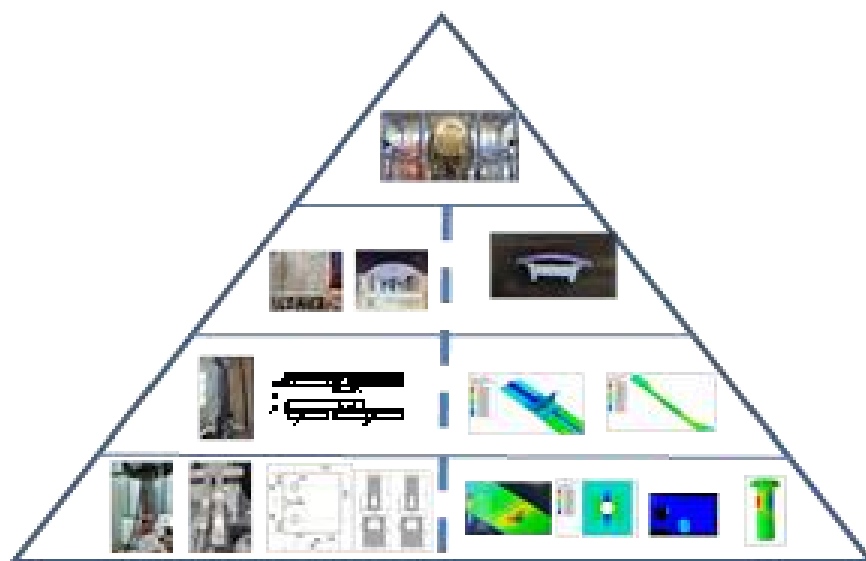


Figure 3-32 Test matrix of hybrid structure

For the verification of full-scale test, building block test is needed to support the integrity and airworthiness compliance of hybrid structure connection analysis, as shown in Figure 3-32. The thermal stress equivalent mechanical stress method and the F&DT analysis method of hybrid structure established by theoretical analysis and low-level test must be verified by higher-level test and complex fatigue load spectrum, so as to support the verification of the whole structure. It should be noted that not all WFD sensitive structures are harmful under temperature loading, but some structures are beneficial, which can be directly verified in full-scale tests. For harmful structures, additional analysis must be carried out (for example, the reliability of the analysis method is verified by component test, and the rationality of mechanical stress and thermal stress is verified by full-scale test). For the parts with complex force transmission and structure, the method of load amplification or life amplification can be used to verify the airworthiness compliance through some component level tests.

3.3.2 Research on Aircraft Seat Dynamic Simulation and Occupant Head Injury Simulation Device ⁴⁰

Aircraft seat is one of the most complex airborne equipment in commercial airplanes with complicated certification process and airworthiness compliance method. To assess whether the aircraft seat/occupant constraint system meets the airworthiness requirements, it is necessary to launch a series of sled impact tests in accordance with CCAR25.562. However, the huge cost and the long duration of sled impact tests are not friendly for airworthiness certification of aircraft seat. The advisory circular AC 20-146A updated by FAA in 2018 citing SAE ARP 5765A, states that simulation analysis can be used to support or partially substitute for full-scale sled tests. On the other hand, development of simplified test device to partially substitute for full-scale sled test will also benefit the development and airworthiness certification of aircraft seats. The aircraft industry has a long history in Europe and US, with tremendous experience in airworthiness certification. The product from Europe and US took over more than 80% of global aircraft seat market. On the other hand, as the aircraft seat industry in China was comparatively young than that in Europe and US, the mainly method for product design, analysis and

⁴⁰ Civil Aviation University of China. SHI Xiaopeng: xpshi@cauc.edu.cn

airworthiness certification in China was traditional full sled impact test, which suffered from huge economic cost.

To solve the above issues in China's aircraft seat industry, the research team conducted investigations of compliance method based on dynamic simulation of aircraft seats and developed an occupant head injury simulation device. The outcomes greatly supported the design, production and airworthiness certification of aircraft seats in China.

Through present research, a "building block" approach based on "V & V" certification of aircraft seat modeling was implemented. The effect of row distance, location of seat belt anchor and occupant position on dynamic response of the seat, occupant and restraint system was investigated using above numerical models. The injury of occupants' head and neck (HIC and N_{ij}) were also investigated under different loading conditions. An occupant head injury simulation device was designed. The key parameters of cabin partition that affect passenger safety were identified, and the correlation mechanism between them and occupant injury was established.

Compliance method based on dynamic simulation of aircraft seats

According to "V & V" certification process of dynamic simulation in SAE ARP5765A, the research team conducted a joined study cooperating with JiaTai Aircraft Equipment Co., Ltd on "building block" approach of aircraft seat model (Figure 3-33) based on China's new generation of aircraft seat. In the material level, material tests and model validation under static and dynamic loads were carried out. In the component level, the modeling and test verification of the seat tube and seat cushion were carried out. The impact test and numerical model verification of the rigid seat, ATD, safety belt and seat cushion system were carried out in the sub-system level. Finally, a full-scale numerical model of the sled, ATD and restraint system was established, and the full-scale sled impact test was carried out.

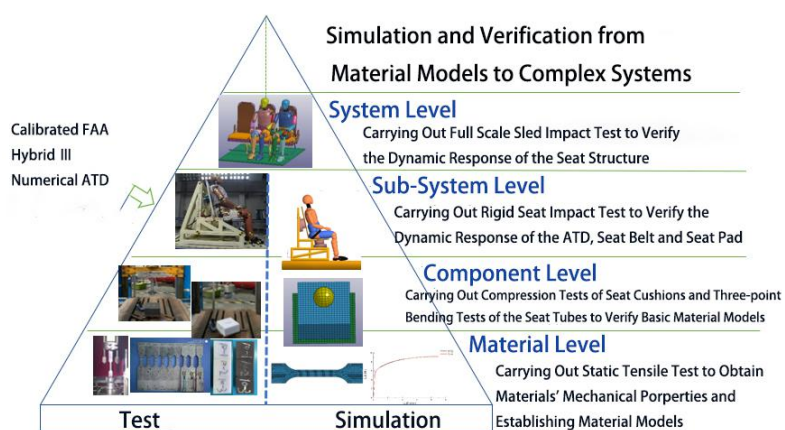


Figure 3-33 Building Block Approach of Modeling Aircraft Seat

The impact response and injury level of ATD with different sitting positions are evaluated using multi-body dynamic (MBD) model, and suggestions of protective posture for the first-row occupants in emergency landing were given. Finite element (FE) model which includes sled, triple seats, two points safe belt and FAA Hybrid III 50 ATD was used to identify the effect of different parameters of aircraft seats, occupants and restraint systems, and the head and neck injuries of occupants under different working conditions (HIC, N_{ij}) were studied. This research greatly supported the design of China's new aircraft seat. Finally, MBD-FE coupling simulation research of aircraft seat was carried out. The MBD-FE coupled model was established and verified.



Figure 3-34 Simulation and dynamic sled tests of single row and double row aircraft seats

Study on The Occupant Head Injury Simulation Device

Firstly, the MBD simplified model of “pendulum mechanism-actuator” was established. Then the virtual prototype was established based on the occupant motion characteristics, and the dynamic analysis was carried out to determine the parameter requirement of the power device. Finally, the structural strength of the device was analyzed, and the physical prototype was made. The effect of the bulkhead on the dynamic response of the first row seat occupant was investigated by using the head injury simulation device. The key parameters of cabin partition that affect passenger safety were identified, and the correlation mechanism between them and occupant injury was established.

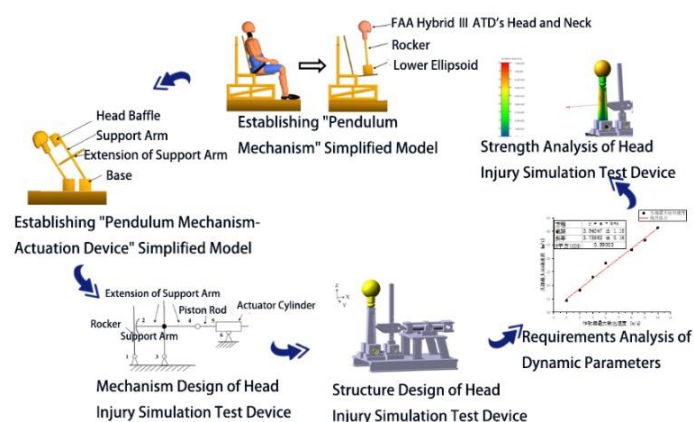


Figure 3-35 Occupant head injury simulation device

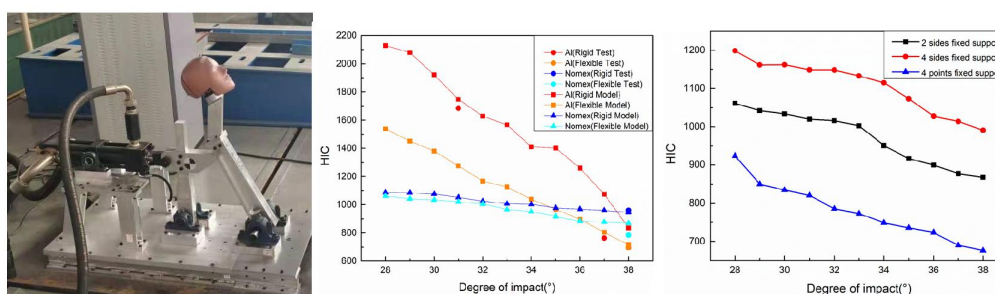


Figure 3-36 Relationship between occupant HIC and impact angle, materials of bulkhead and restrain condition of the bulkhead

The research team has been continually and systematically investigating the protection of aircraft

occupants for years. The outcomes have supported the formulation and revision of technique standards for China's aircraft seat including CTSO-C127b and CTSO-C100c which were drafted by the research team and released by CAAC. Meanwhile, the research team collaborated with aircraft seat producer such as JiaTai Aircraft Equipment Co., Ltd and scientific research institutes in China such as ASRI-AVIC and CATARC Tianjin in developing compliance method of aircraft seat which can substitute for full-scale sled test including CBA (Certification by analysis) and head injury simulation device which is the first prototype in China. The outcomes of present research have been used in new generation of China's aircraft seats which saved "R & D" cost. The research team aims to extend the investigation in future such as aircraft seat high-energy absorption technique, light-weight technique of aircraft seat, occupants head and neck injury protection technique, aviation children safety device, biomechanics in occupants' injury and high-precision numerical ATD.

3.3.3 Crashworthiness and Numerical Simulation of Civil Aircraft Structure⁴¹

Crashworthiness is the ability to protect the occupants to the maximum extent during the airplane crash or emergency landing event. Analyzing the deformation, failure mode and impact response process of fuselage structures, and mastering the structural energy-absorbing capacity is the key to deeply understand the crashworthiness of civil aircraft structure, and is also the basis to reveal the crash failure behavior of civil aircraft structure, which can effectively support the crashworthiness design of civil aircraft structure and improve the crashworthiness characteristics of fuselage structures. At present, the crash deformation mode, acceleration response and energy-absorbing characteristics of fuselage structure have been carried out, however, there some shortcomings in the effective verification of simulation model and modeling technology.

There are four key techniques in the present research, which are as follows: Material mechanical performance test and constitutive model research; Dynamic impact failure test and numerical simulation of columns; Failure test and numerical simulation of joints; Crash test and numerical simulation of sub-component and sub-component level.

Based on the "building block approach", the crash analysis method and numerical analysis model of fuselage structure can be effectively verified by conducting the various tests of material level, element level, joint level, sub-component level and component level, which could deepen the crashworthiness research of aircraft fuselage, and provide support for crashworthiness design and certification.

Material mechanical performance test and constitutive model research

For the Al 2024-O-T42, the tensile tests of 'dog bone' specimens under different strain rates and the quasi-static tensile tests of notched specimens are carried out. Within 100s^{-1} strain rate, the strain rate effect on flow stress is not obvious. Based on the established maximum plastic failure strain criterion, Johnson-Cook failure model and GISSMO damage model, the tensile simulation is performed for six notched specimens. For the GISSMO damage model, the failure displacement is closer to the test result, and the simulation accuracy is higher.

⁴¹ Civil Aviation University of China. XIE Jiang: xiejiang5@126.com

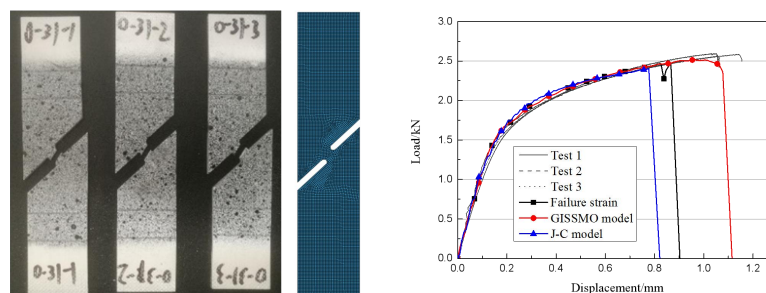


Figure 3-37 Comparison of test and simulation results of notched specimens

Dynamic impact failure test and numerical simulation of columns

For the C-channels, the dynamic axial impact test and dynamic three-point bending impact test at three different velocities are carried out, and the simulation analysis are also carried out. Compared with the maximum plastic failure strain criterion and J-C model, the stress state and nonlinear damage accumulation are considered for the GISSMO damage model, which is more consistent with the experimental results in terms of plastic deformation and failure.

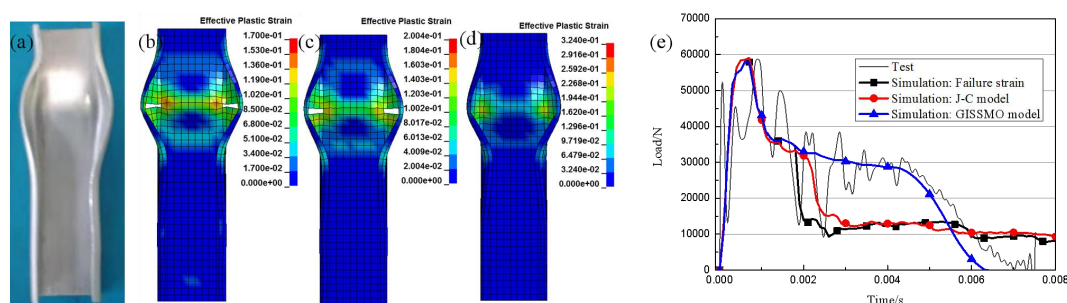


Figure 3-38 Comparison of axial impact test and simulation results (4m/s): (a) Test result, (b) Maximum failure strain, (c) J-C model, (d) GISSMO model, (e) Load-time curve

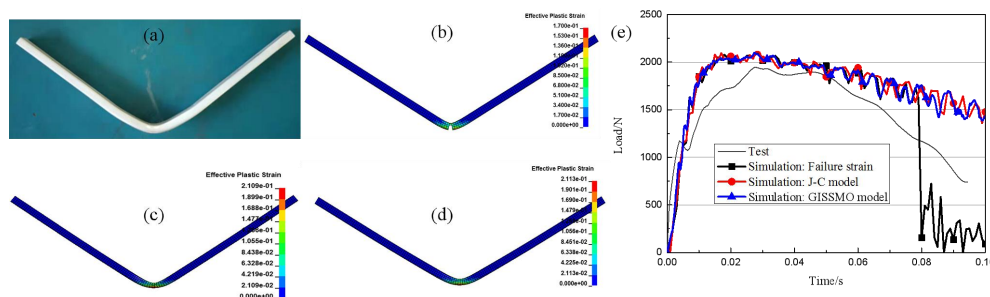


Figure 3-39 Comparison of three-point bending impact test and simulation results (2m/s): (a) Test result, (b) Maximum failure strain criterion, (c) J-C model, (d) GISSMO model, (e) Load-time curve

Failure test and numerical simulation of joints

For bolt lap joints, the dynamic tensile tests (1, 3, 5 m/s) and simulation analysis (maximum plastic failure strain criterion, J-C model and GISSMO damage model) are carried out. At different loading speeds, the peak load values are relatively close, the maximum difference is 1%, and the failure displacement increases with the increasing of loading speed. The results show that the strain rate effect of the flow stress of Al 2024-O-T42 is not obvious, and its failure strain has a certain strain rate effect; the simulated load-displacement curves of three material model are higher than the test results, but the

simulation results are more accurate for the GISSMO damage model.

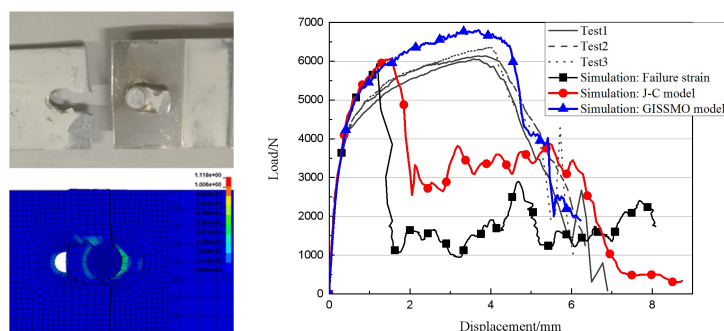


Figure 3-40 Comparison of dynamic tensile test and simulation results (1m/s)

Crash test and numerical simulation of sub-component and sub-component level

The inverted impact tests are conducted for sub-cargo fuselage section. At 3.95m/s, the structure remains relatively complete, and the frames and middle stanchions are bent and deformed; At 5.53m/s, the rivets at the connections between the middle stanchions and frames are failed, and the sub-cargo fuselage section is seriously compressed. The 6.02m/s crash test is conducted for the sub-cabin fuselage section, three plastic hinges are formed, and the connections between cargo floor beams and fuselage frames are failed. The finite element models of fuselage section are established. The simulation results are in good agreement with the experimental deformation mode, the value and time of acceleration peak can be simulated well.

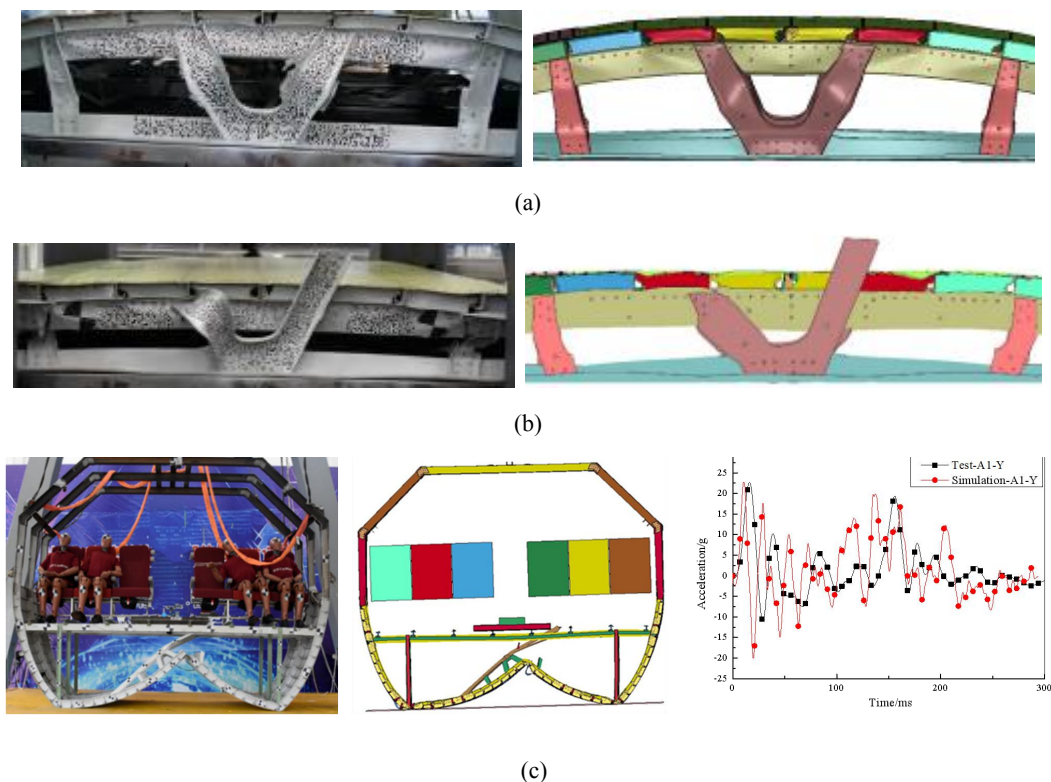


Figure 3-41 Crash test and simulation results of sub-component level and component level: (a) 3.95m/s, (b) 5.53m/s, (c) 6.02m/s

3.4 INSPECTION AND MAINTENANCE

3.4.1 Research on Probability of Detection of Damage and Its Calculation Method⁴²

Probability of Detection (POD) is a critical evaluation technical index for reliability of damage inspection and an important element in the damage tolerance design of aircraft structures. It is related to the determination of damage inspection methods and the calculation of inspection interval.

When making evaluation on the damage tolerance of aircraft structures, The minimum detectable crack size which should satisfy a certain detection probability is the design parameter to calculate the crack propagation and the interval of repeated inspection during the process of damage tolerance design.

Thus, based on the theory of statistical modeling analysis, through the development for typical aircraft aluminum alloy structure damage of near surface eddy current testing, reliability demonstration and evaluation methods for near surface characterization of eddy current testing are established based on POD. It makes a technical foundation for the establishment of the data of "minimum detectable crack size" in aircraft damage tolerance design, and meanwhile provides a reliability evaluation method for damage inspection method to meet new detection requirements of the aircraft model.

Research Procedure

The research procedure mainly includes the design and production of testing samples, conducting test and data collection and the processing of data analysis. Finally, the POD curve is established to obtain the defect size with the detection probability reaching 90% at the confidence level of 95%. The research procedure is shown in Figure 3-42.

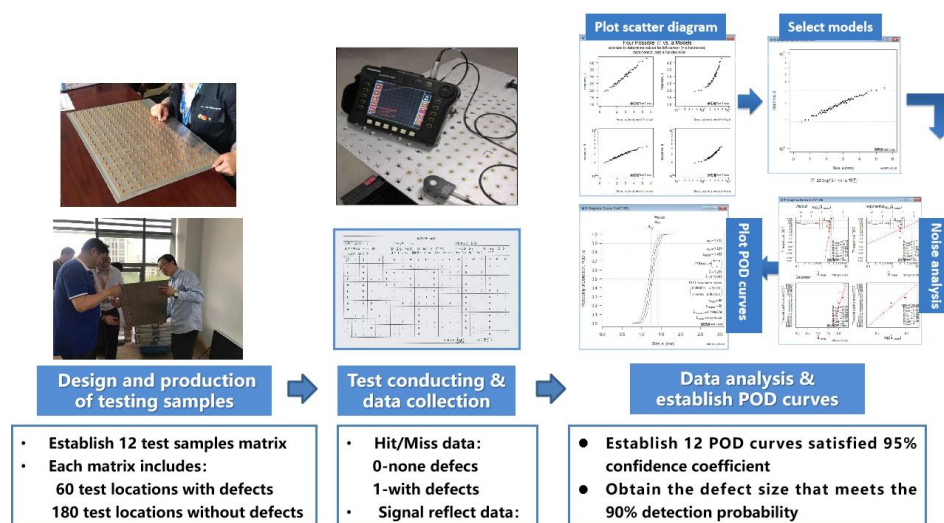


Figure 3-42 Research Procedure

The mathematical modeling methods such as binomial distribution method, linear regression method and generalized linear model method are studied based on the positive relationship between defect detection probability and the crack length. Different statistical analysis models were established by analyzing HISS/MISS data and signal response data, the typical analysis models are shown in Figure 3-43. Meanwhile, the research of signal noise analysis technology was carried out to lay the foundation for the subsequent results analysis and the establishment of POD curves.

⁴² COMAC Shanghai Aircraft Design & Research Institute. LI Weiping: liweiping@comac.cc

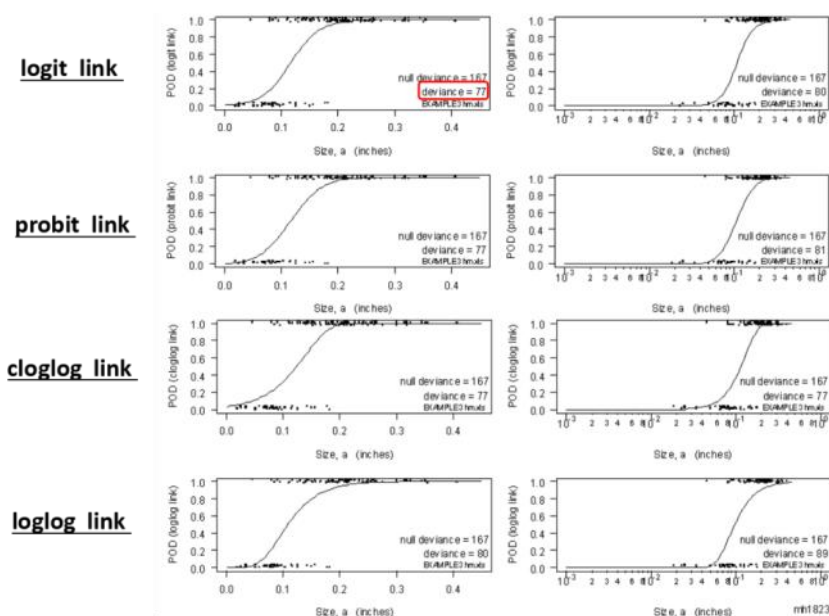


Figure 3-43 Typical analysis models

Through the research experiment, the POD curve and its 95% confidence interval were obtained by statistical modeling analysis method, and the crack size satisfying the 90% detection probability under the 95% confidence was obtained accordingly. Thus, a POD-based reliability evaluation method for damage inspection was established. This research lays a technical foundation for the subsequent establishment of the "minimum detectable crack size" data, and also provides an evaluation method for the detection reliability to solve new damage inspection requirements constantly appearing on civil aircraft in the future.

3.4.2 Application of Cold Spray Reinforcing Material Repairing Technology⁴³

A key bearing structure is located in a small space within the fuel tank area of aircraft, once destroyed, the flight safety will be directly endangered. The long truss hole on the structure is the weak link that affects the fatigue life of the whole part, which restricts the life of the whole aircraft. Whether it is traditional repair methods such as local reinforcement(bolt connection, adhesive joint), or new repair techniques such as 3d printing, friction stir welding, laser cladding, are difficult to implement because of the harsh construction conditions. Based on the above characteristics, the cracked aircraft can only be decommissioned in the past.

The Cold Spray opens a new idea for crack repair of the structure. The Cold Spray(CS) is also referred to Cold Gas Dynamic Spring or Supersonic Particle Deposition(SPD). The CS is a kind of coating preparation method based on high-speed particle solid state deposition. The principle of the coating is high pressure accelerating medium, and the powder is fed into the spray gun by powder gas. The advantage of CS in the field of structural repair is that there is no mechanical connection and no additional damage to the matrix. The surface temperature of the substrate can be controlled below 150°C without damage to the substrate ; there is no interface oxide ; and there is pressure stress on the surface. The work consists of three highlights: A new equipment for repairing CS coating material is developed, and the mechanical properties of CS coating is studied, and the technical standards and technology of CS are studied.

⁴³AVIC Shenyang Aircraft Design & Research Institute. CHEN Liang: 5692864@qq.com

In this study, no collateral damage repair of key bearing structures by CS in narrow space is realized, crack propagation is effectively suppressed, and fatigue quality of repair structure proved.

Establishment of mechanical property test evaluation system for CS

As a new technology, the mechanical characteristics and failure behavior of CS are different from that of traditional materials and processes. In this study, combined with the strength test, the strength of the CS material and the matrix was evaluated, and the mechanical properties of the CS were tested by static and fatigue tests.

On the basis of mastering the basic mechanical characteristics of the CS, the repair design method of the CS coating was optimized and formed by the simulation part test with structural details. The repairing effect of CS coating is better than that of composite adhesive bonding.

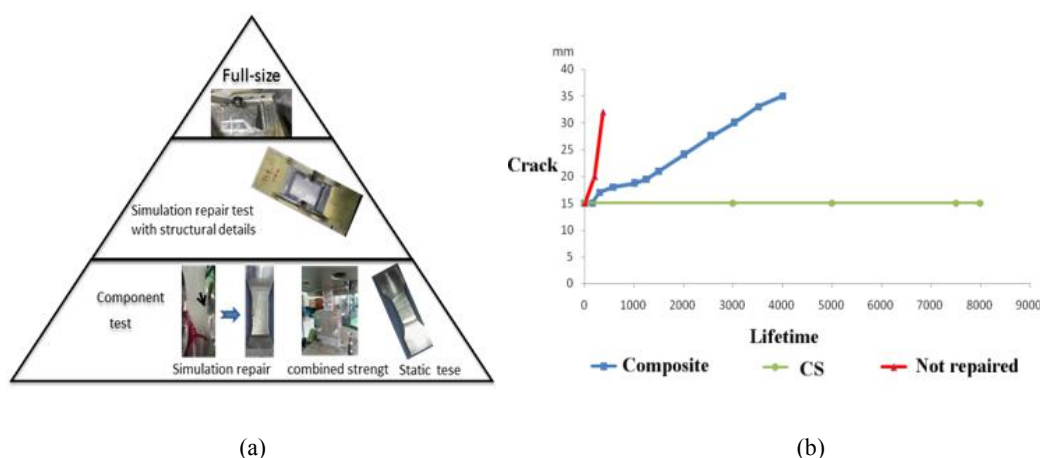


Figure 3-44 The CS test system and repairing effect: (a) mechanical properties test system, (b) Repair Effect of 15mm Crack

Establishment of technical standards and processes for CS

The CS and 3D printing belong to the field of increasing material manufacturing, production quality is heavily dependent on process. Through the iterative process cycle, the selection criteria of main and auxiliary raw materials, combined with strength control method, key parameters of process, construction environment control standard, dust protection and collection technology on board, quality inspection standard, formed a complete process control chain and process parameters system, established a complete technical standard and preparation quality evaluation standard.

3.4.3 Study on Repair And Fatigue of Super-Strength 300M Steel Structure⁴⁴

The 3D printing technology can process and repair all kinds of complicated parts with different materials. Compared with the additive manufacturing, it has a wider application range and is more flexible in the additive repair of parts. It can achieve more accurate, more time-saving and faster in the repair of parts. It can greatly reduce the repair cost and shorten the repair cycle. Therefore, 3D printing repair technology has been developing rapidly at home and abroad.

This research includes several key parts: 1. Determination of repair materials and repair methods; 2. Determination of repair process parameters; 3. Analysis of the difference between repair materials and matrix materials; 4. Quality assurance of repair parts; 5. Verification of parts properties after repair;

⁴⁴AVIC The First Aircraft Institute. ZHOU Xiaodan: zxd_67@qq.com

The main findings in this study are as follows: the repair materials, powder transport, laser power, spot diameter and printing speed are the key factors affecting the repair; the shape of the repair area, the quality control of the repair process and the residual stress treatment of the repair area have some effects on the repair quality.

Performance test of 300M steel additive repair

The mechanical property test results of the repaired area are shown in the figure below. The test results show that the repair can meet the strength requirements of the parts.



Figure 3-45 Hardness test of reinforced material repair area

Additive repair process and test of 300M steel

The test piece of 300M steel landing gear outer barrel is additive repaired. The repair process is completely based on the index selected in the performance test of 300M steel. After completion of the repair, the test pieces were stained and fluorescent magnetic powder and other non-destructive inspection. Finally, the repaired test piece completed the fatigue loading test of 100,000 cycles. The repair process and test are shown in figures below. The results show that the repairing method of super-strength 300M steel is feasible and should be further studied and popularized.



Figure 3-46 Repair shape and area



Figure 3-47 hardness test of additive repair area

3.4.4 In-situ Nondestructive Testing Approaches for Impact Damage of Honeycomb Sandwich Structures⁴⁵

There are two key techniques in the present research, which are as follows: a manufacturing method of honeycomb core impact damage reference block close to the real damage form was established; Based on it, the applicability of in-situ nondestructive testing methods for honeycomb impact damage was

⁴⁵ AVIC Aircraft Strength Research Institute. WANG Dan: 326337758@qq.com

studied.

The key finds in the present research are as follows: the impact damage simulation method proposed in this study can truly reflect the damage morphology, and is conducive to evaluating the detection ability of each method for impact damage type; when both sides of the honeycomb structure can be approached, the dry coupled ultrasonic penetration method and low-frequency ultrasonic reflection method can be used for impact damage detection; When the honeycomb structure can only be approached by one side, the low frequency ultrasonic reflection method can be used to detect the impact damage of that side.

Artificial simulation method of impact damage

Through the fracture analysis of the real impact damage area of honeycomb sandwich structure, the impact damage characteristics of honeycomb sandwich structure are obtained, which may include skin delamination, skin and honeycomb core disbond and honeycomb core damage, as shown in Figure 3-48.

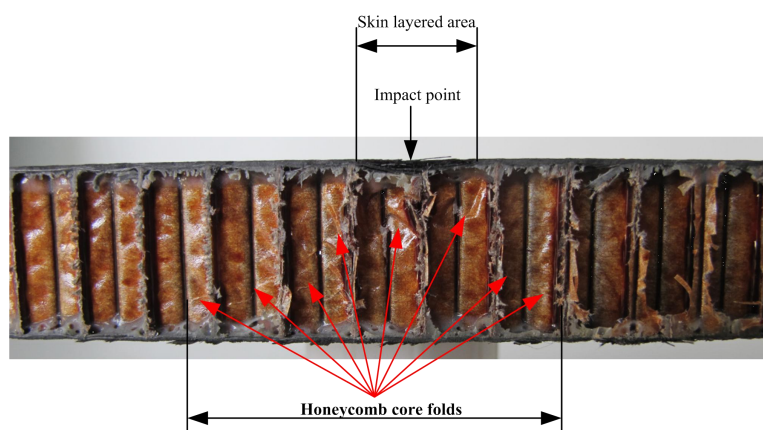


Figure 3-48 Low velocity impact damage morphology of the honeycomb sandwich structure

The impact test was carried out on the honeycomb core, as shown in Figure 3-49(a). The impact energy value was estimated according to the size of the impact head and damage expected, and the core crushing was estimated by visual measurement, as shown in Figure 3-49 (b). In order to ensure that the crushing area can be bonded with the skin after the curing, it is necessary to modify the impact area of the honeycomb core, as shown in Figure 3-49 (c).

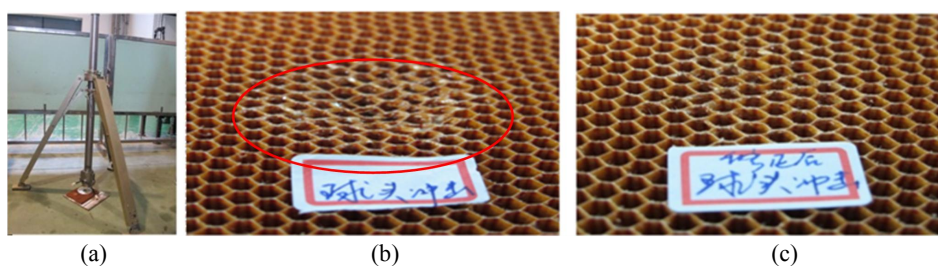


Figure 3-49 Honeycomb core impact damage: (a) impact test, (b) core crushing area, (c) modified impact area

The face with artificial defects of delamination and disbonds (including one between the skin and film adhesive, and the other between the film adhesive and core) were cured with the modified honeycomb core, and finally the impact reference block including the delamination, disbond up/down to film adhesive and impact core crushing was formed, as shown in Figure 3-50(a) and (b), the location,

quantity, shape and size of various artificial defects were evaluated by water jet ultrasonic penetration C-scan method, as shown in Figure 3-50 (c).

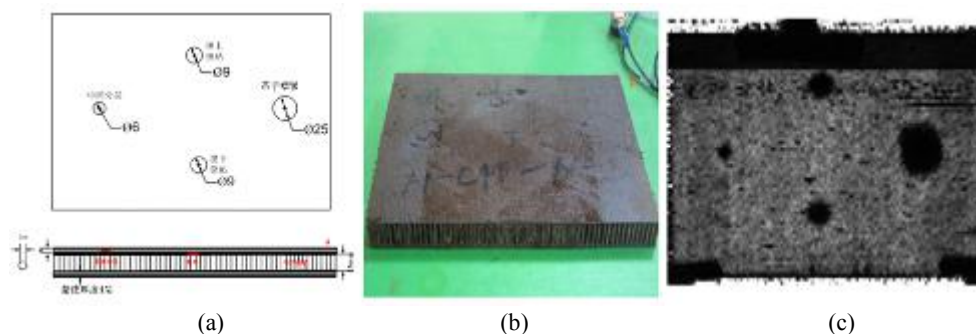


Figure 3-50 Reference block and ultrasonic C-scan results: (a) design, (b) physical photo, (c) ultrasonic C-scan results

Applicability of in-situ nondestructive testing methods

According to the Figure 3-50 reference block, the ultrasonic pulse reflection (high frequency pulse reflection method, low frequency pulse reflection method), dry coupling ultrasonic penetration and infrared thermal imaging method were carried out respectively, and the applicability of each non-destructive testing method was shown in Table 3-3 for different impact damage forms. All damage forms of honeycomb structure can be detected completely by dry coupled ultrasonic penetration method and low frequency pulse reflection method, but the core damage cannot be detected by high frequency pulse reflection and infrared thermal imaging method.

Table 3-3 Applicability of nondestructive testing methods for different impact damage forms

Test method		High frequency	Low frequency	Dry coupling	Infrared thermography
Damage type					
Nearside	Delamination	√	√	√	√
Farside	Delamination	×	×	√	×
Disbond up	nearside	√	√	√	√
	farside	×	√	√	×
Disbond down	nearside	×	√	√	√
	farside	×	√	√	√
Core Crushing		×	√	√	×

NOTES: √=suitable, ×=not suitable

3.4.5 Research on The Failure Behavior of Stiffened Composite Repair Structure⁴⁶

With the increase application of composite materials in aircraft structures, more attention has been paid to its repair problems. Mechanically fastened repair is more suitable for field use. Mechanically fastened repair has the characteristics of simple operation and low requirements for surface treatment and reliable performance. Mechanically fastened repair has the advantages of good peeling performance, small environmental impact, and easy being detachable. It is widely used in aircraft composite material bearing structures. When an aircraft has damage during service, it often needs quick repair, and mechanically fastened repairs is the best choice. Mechanically fastened repair introduces

⁴⁶ AVIC Aircraft Strength Research Institute. YANG Pengfei: ypei029@163.com

new stress concentration due to the addition of connecting holes, and its failure mode has also changed. Research on the failure mode of composite mechanically fastened repair is of great significance to the application of composite in large aircraft structures.

In this paper, the simulation analysis model of typical repair structure was established for stiffened composite vertical tail panels, and the displacement load changes and failure modes of intact structures, damaged structures and repaired structures under tensile and compressive loads were analyzed.

The results show that under tensile load, the failure mode of the repaired structure was that the fracture and expansion of the outermost bolt hole section of the repair area leads to the failure of the structure along the outer row of bolts; Under compressive load, the stiffened panel was greatly enhanced due to the axial compression stiffness of the patch. The middle of the stiffened panel will not buckle, and the bolt fasteners strengthen the out-of-plane strength of the rib/skin interface in the repair area. Compared with the unrepaired parts, the interface near the repair area was not prone to peeling, so the final damage of the repaired structure was manifested as the pressure-bearing fracture of the ribs at the buckling position.

In view of the discrete source damage of the composite vertical tail structure, a typical stiffened panel structure was selected for the repair design, as shown in Figure 3-51.

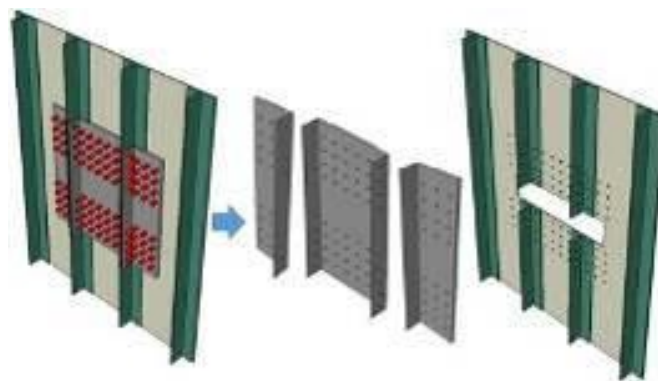


Figure 3-51 Details of repair parts for vertical tail stiffened panels with discrete source damage

Failure behavior of stiffened panel repair structure under tensile load

The damage process of the mechanically fastened repairs vertical tail stiffened panel is (Figure 3-52): when the load reaches 90% of the peak load, the fiber tensile damage appeared at the position of the screw hole in the lower right corner of the skin perpendicular to the direction of the loading axis. As shown in Figure 3-52 (a); when the load reached about 93% of the peak load, because fibers around some of the bolt hole edge have been completely broken, the external load cannot be transmitted to the patch through these bolts, which increases the load of damage hole edge. And eventually lead to the failure of damage hole edge due to stress concentration, as shown in Figure 3-52 (b); when the structure fails completely, the damage at the outermost row of bolt holes in the skin has been connected into pieces, and the damage area around the damage hole did not extend to the nearby bolt holes, so the failure mode of the vertical tail repair stiffened panel is the fracture and expansion of the bolt hole section on the outermost side of the repair area which lead to the structure break and fail along the outer row of bolts. In addition, unlike the damaged part, the ribs on both sides are deboned in the middle area, as shown in Figure 3-52 (c).

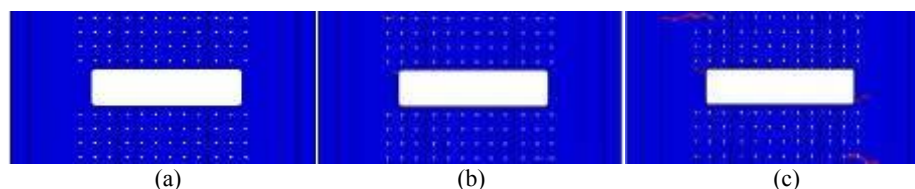


Figure 3-52 The damage process of mechanically fastened repairs vertical tail stiffened panel: (a) 90% peak load (b) 93% peak load, (c) Peak load

Failure behavior of stiffened panels under compressive load

Under the axial compression load, the first-order positive buckling mode of the vertical tail stiffened panel is shown in Figure 3-53. The first-order buckling mode of the intact wall panel presents three buckling half-waves along the loading direction and perpendicular to the loading direction; the first-order buckling mode of the damaged panel is the half-wave at the edge of the discrete source damage hole, which is mainly due to the rectangular opening edge lack of support which makes the compression rigidity low. Because the presence of the patch will greatly increase the compression rigidity of the structure, the first-order buckling mode of the tail repair stiffened panel appears a half wave near the loading end along the loading direction, the repair area will not buckle at this time. The eigenvalue buckling analysis results show that the first-order buckling loads of the damaged and repaired panels are 90.3kN and 336.8kN, respectively. Compared with the buckling load of 287.9kN of the intact vertical tail stiffened panel, the residual buckling strength of the damaged part is 0.314, and the buckling load of the vertical tail repair stiffened panel is significantly higher than that of the intact structure. The buckling strength recovery rate is 1.170.

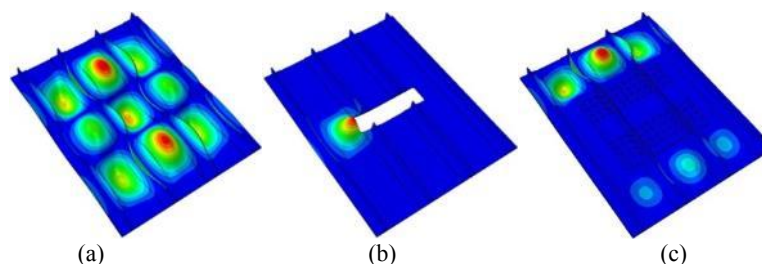


Figure 3-53 First order buckling mode of vertical tail panel under axial compression load: (a) Intact part, (b), Damaged parts, (c) Repair parts

The first-order buckling mode was introduced as the initial geometric disturbance, and the post-buckling damage behavior of the vertical tail stiffened panel was analyzed. The displacement-load curve was shown in Figure 3-54. The load-displacement curve was linear in the initial stage, the curve slope of the damaged part was obviously lower than that of the intact part, and the repair part has higher compression stiffness than the intact wall plate due to the reinforcement of the patch, so the curve slope was higher than that of the intact part. Under the axial compression load, the post-buckling loads of the damaged and repaired panels were 254.3kN and 575.5kN, respectively. Compared with the post-buckling load 488.9kN of the intact vertical stiffened panel, the remaining post-buckling strength rate of the damaged part was 0.520, and the post-buckling load of the vertical tail repair stiffened panel was higher than that of the intact structure. The post-buckling strength recovery rate was 1.177.

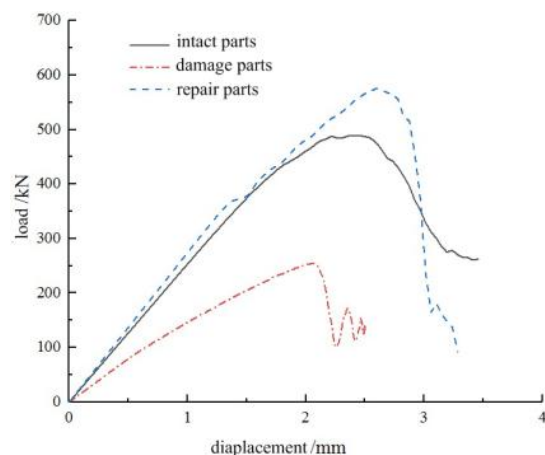


Figure 3-54 Compression load-displacement curve of vertical tail stiffened panel

In terms of damage morphology, the intact vertical tail stiffened panel under the axial compression load was mainly manifested by the peeling of the rib edge strip and the skin interface at the buckling node line or the anti-nodal line, and no fiber damage occurred when the maximum load was reached Figure 3-55; similarly, the dominant failure mode of the damaged stiffened panel at the peak of the axial load was the debonding of the rib/skin interface near the rectangular opening, as shown in Figure 3-56; however, for the repaired stiffened panel, due to the patch was greatly enhanced so that the middle of the stiffened panel would not buckle, and the bolt fasteners strengthened the out-of-plane strength of the rib/skin interface in the repair area. Compared with the unrepaired parts, it makes the interface near the repair area was not prone to peeling, so the final failure of the repaired stiffened panel was manifested by the pressure-bearing fracture of the ribs at the buckling position, as shown in Figure 3-57. Because of the enhancement effect of the repair area on the skin/rib interface, the dominant failure mode of the repair part was no longer the main failure mode of interface debonding which reasonably explained the phenomenon that the peak compressive load of repair part was the highest.

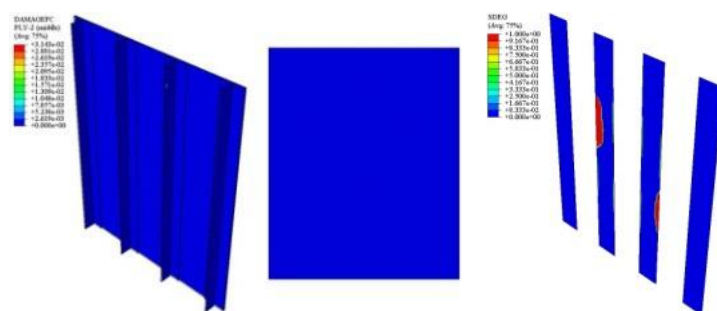


Figure 3-55 Failure of intact panel under maximum load

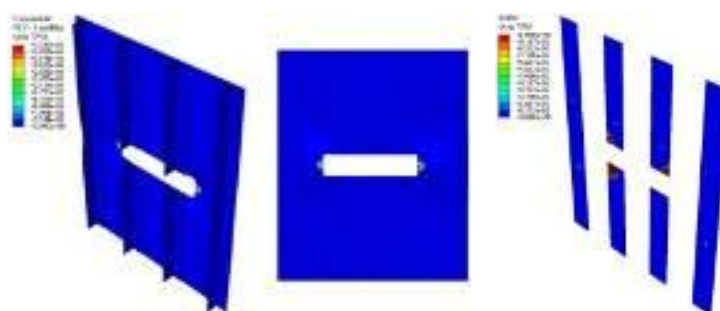


Figure 3-56 Failure of damaged panel under maximum load

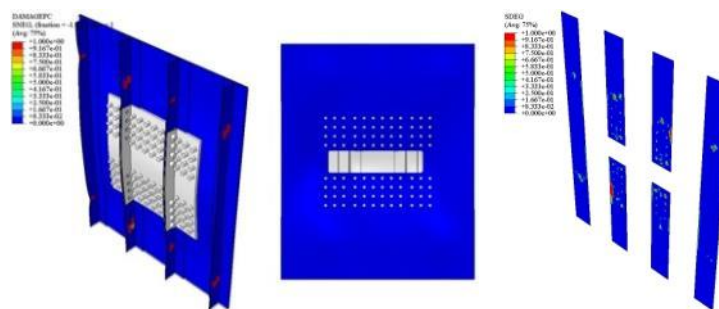


Figure 3-57 Failure of repair panel under maximum load

4. AERONAUTICAL FATIGUE WITH DIGITAL TECHNOLOGY

4.1 NUMERICAL FATIGUE ANALYSIS

4.1.1 Determination and Analysis of Material Dispersion Coefficient of Aging Aircraft ⁴⁷

Whether the dispersion coefficient of the old aircraft material and the new material is different is a prominent problem in the aging aircraft's life extension. In order to support a certain aircraft's life extension work, the experimental and comparative analysis research work was carried out to determine the dispersion coefficient of the old and the new aircraft structure, to determine whether there are differences and differences between them, and to provide technical support for the aircraft's life extension and overhaul.

After comprehensive analysis and combining with the actual damage condition of the service aircraft, the typical structural test specimen was processed by choosing its intact structure(six kinds of aluminum alloy), and the corresponding domestic material specimen was made to carry out and compare the structural life test of the new and old materials. Using PFMA(Probability Fracture Mechanics Analysis), a general EIFS distribution describing the original fatigue quality(IFQ)of detail group is established based on the fatigue test(a,t) data set, and p(i,t) is determined by the crack growth control curve of each stress zone(SCGMC), which is used by PFMA. The main tasks were as follows:

- Calculation of the crack overpass probability p(i,t) and the number of the crack overpass for each stress zone at given time t of use;
- The number of the crack overpass and the damage degree under given reliability r [L_R] of structural details groups at given time t of use;
- The damage degree curve of the structure([L_R]-t curve).

The following conclusions were obtained by comparing and synthesizing the data of 250 typical test specimens in 7 groups:

- The initiation life, fatigue dispersion coefficient and equivalent initial defect size distribution were obtained, and the damage degree of different parts was evaluated by using PFMA;
- Compared with the dispersion coefficient of the old and the new aircraft, the average dispersion coefficient of the former is 2.48 at the medium stress level and the latter is 2.19 at the mean

⁴⁷AVIC Shenyang Aircraft Design & Research Institute. CHEN Liang: 5692864@qq.com

dispersion coefficient, which is similar to the results of the aluminum alloy material tests already carried out in our country, and the results are credible;

- c) The experimental data of different parts were analyzed using PFMA, and the crack growth control curves(SCGMC) in service and the damage curves of different stress areas of the structure were obtained.

Test contents and process

According to the typical subject order of the load spectrum of the center of gravity, the overload of the center of gravity-the time history, high load position, the loading-time history of a single spectral block are compiled.

Conversion of overload spectrum into load spectrum based on the lower formula:

$$P = n_y * \sigma(lg) * F$$

In the formula , n_y is the overload spectrum; $\sigma(lg)$ is the nominal stress of the section corresponding to lg overload under each load condition, and F is the net cross section area of the specimen.

After each spectral block test, the test specimen was inspected and the crack was observed. After the detectable crack appeared, the crack location, length and circulation number were recorded in detail, which provides the necessary reference for fracture interpretation.



Figure 4-1 Test loading and crack interpretation site



Figure 4-2 Sketch map of hole edge crack detail of typical test specimen

Test data processing and analysis

Data processing and post-processing analysis are shown in Figure 4-3.

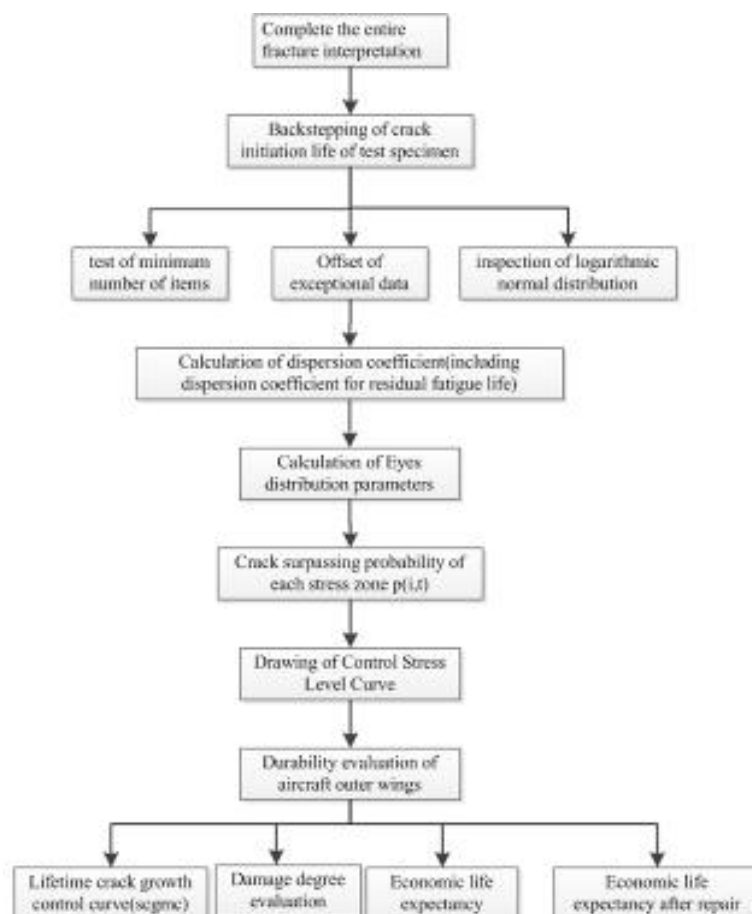


Figure 4-3 Data analysis content and process

For military aircraft, the fatigue life of the same aircraft under the same load spectrum is usually subject to the logarithmic normal distribution, and the structural dispersion coefficient is:

$$L_f = 10^{\left[\frac{u_\gamma}{\sqrt{n}} - u_p\right]ks}$$

L_f is the fatigue dispersion coefficient, u_γ is the normal distribution of γ site determined by the significant level γ , n is the sample volume, u_p is the upper P point of the standard normal distribution determined by reliability P. The reliability, the sample size and the confidence level are taken into account in the formula, and the structural dispersion coefficient generally corresponds to the reliability of 99.9 % and the confidence of 90 %. k is the corrected coefficient for standard deviation as shown in Table 4-1.

Table 4-1 corrected coefficient for standard deviation

n	2	3	4	5	6
k	1.2533	1.1284	1.0854	1.063	1.051
n	7	8	9	10	11
k	1.042	1.036	1.031	1.028	1.025

The logarithmic life fit test and the logarithmic life distribution curve of typical test specimens' data are as follows.

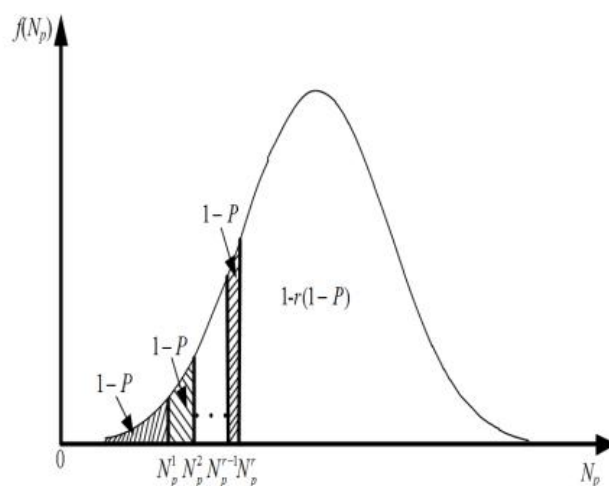


Figure 4-4 structural logarithmic fatigue life normal distribution function diagram

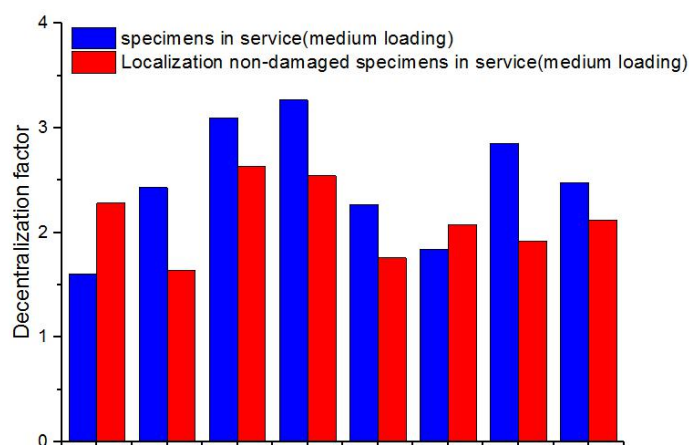


Figure 4-5 Comparison of dispersal coefficient of residual life of the aging and the new specimens

4.1.2 Rapid Stress Analysis With High Accuracy of Complex Structure⁴⁸

Critical areas are the focus of structural fatigue life evaluation. To improve the accuracy of fatigue life evaluation, it is the primary means to improve the accuracy of stress analysis. It is unnecessary to consider all contact and fastener connection with refined mesh in global FEM, because the aircraft structure is complicated with complex connections and loading transmission.

Compared to direct refinement method and the stiffness reduction method, the Global-Local method based on force boundary condition is more effective when dealing with stress analysis of complex structures. There is no constraint of the mesh size and the element type in Global-Local analysis.

The fundamental of Global-Local method based on force boundary condition is that the force boundary condition obtained from the global FEM analysis is applied on local FE mode, and the boundary of local FEM and global FEM are compatible in geometry space.

The procedure of Global-Local method based on force boundary condition is shown in Figure 4-6.

⁴⁸AVIC Chengdu Aircraft Design & Research Institute. WANG Fan: wangfan_611@163.com

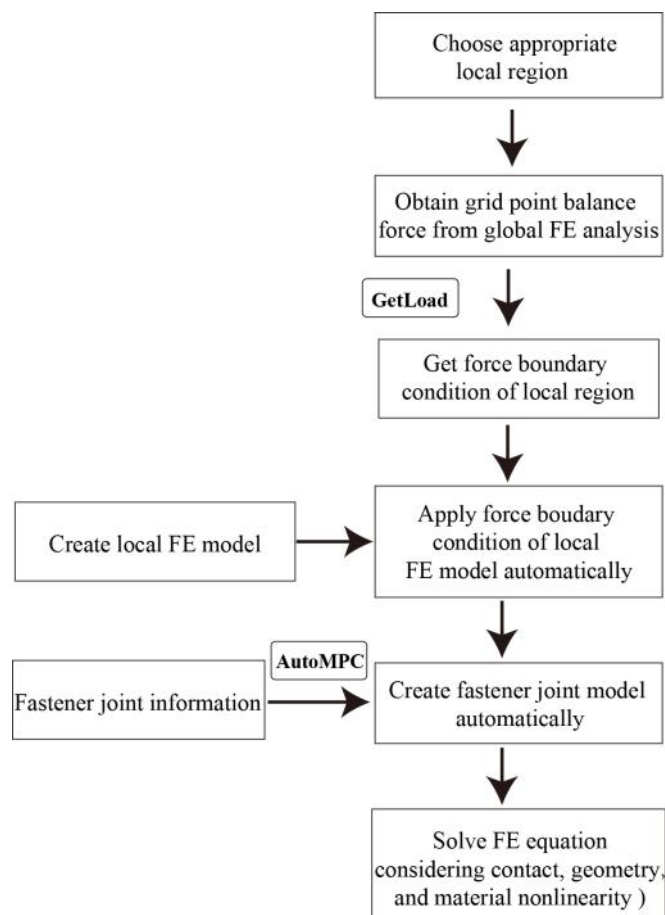


Figure 4-6 The Global-Local analysis procedure based on the force boundary condition

The Stiffness of FEM

The global FEM mainly consists of 1D element and 2D element. Especially when the structure is slender and the section shape of parts changes greatly, the stiffness difference between global FEM with coarse mesh and the true aircraft structure is much greater than FEM with refined mesh. For example, the upper and lower flange of the wing beam is modeled by shell elements at the root near wing-fuselage attachment and by beam elements at the outside without considering the eccentricity. The bending stiffness is reasonable, but the torsional stiffness cannot be captured accurately. So the force boundary condition of the local FEM is not accurate, and the accuracy of FE stress analysis decreases.

In this work, the 1D and 2D are replaced by 3D FEM with large mesh size which can capture the stiffness of structure by connecting global FEM to local FEM automatically. In fact, it is actually a direct refinement method. In order to get the accurate force boundary condition, mesh size of global FEM need not to be fine and the general FEM solver can solve quickly. As shown in Figure 4-7, the rod/beam and shell elements are replaced by 3D element with coarse mesh size.

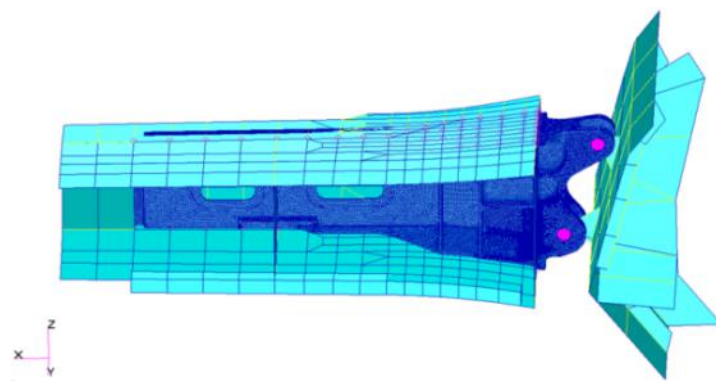


Figure 4-7 Local FEM with coarse mesh size

Automatic connection technology

There are thousands of fasteners in the aircraft structure, which are usually represented by beam element. Besides, the contact is usually taken into consideration to improve the accuracy of stress analysis.

Bearing, shear and bending stiffness of the fastener, and bearing stiffness of the plate should be taken into account in FEM, as shown in Figure 4-8. The number of the connected parts is represented symbolically by n . Nodes $N_{p1} \sim N_{pn}$ are created at mid-planes representing connected parts. $E_{p1} \sim E_{pn}$ and $t_{p1} \sim t_{pn}$ are elastic modulus and the thickness of the connected parts, respectively. Fasteners are modeled by $n+1$ beam elements, and beam nodes are represented by $N_{f1} \sim N_{fn}$ and $N_{h1} \sim N_{h2}$.

Because numerous fasteners exist in the whole FEM, the automatic connection technology is applied to greatly improve the efficiency of stress analysis.

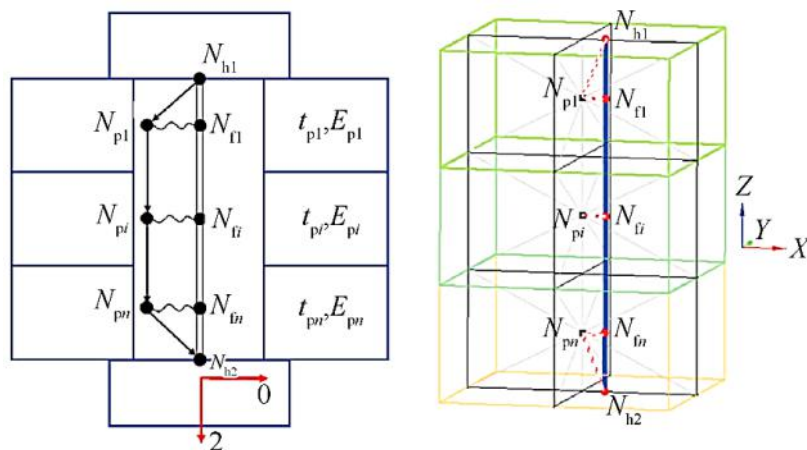


Figure 4-8 FEM of a fastener connection

Example

To improve the efficiency of stress analysis, two software programs: GetLoad and AutoMPC are developed. GetLoad is designed to get the force boundary condition of local FEM. AutoMPC is used to apply load and to automatically connect the fasteners between different parts.

Taking wing rib and front beam of some aircraft as an example, its assembly relation and boundary condition are very complex. The critical parts include beams, rib and panel. To obtain the stress distribution and stress level of critical parts accurately, stress analysis of FEM with about 40 million degree of freedom is conducted by the Global-Local approach based on force boundary condition.

Engineers completed the detail FEM modeling in short time with help of the two developed software (GetLoad and AutoMPC), as shown in Figure 4-9.

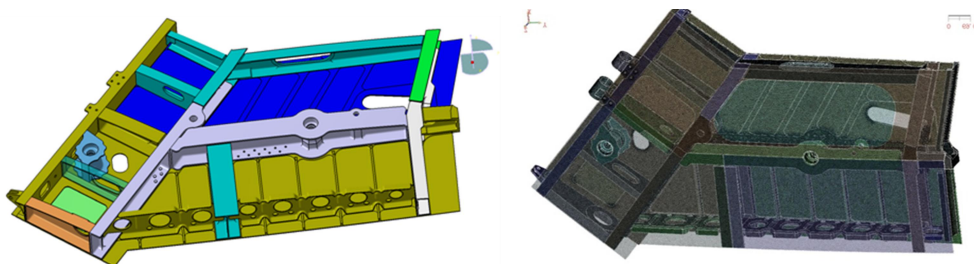


Figure 4-9 Refined local mesh

4.1.3 Peridynamics Methods for Fatigue Problems⁴⁹

Traditionally, fatigue is experimentally studied, where mechanical parameters are the focus and influences of material factors are only considered as fitting parameters or by dispersion factors; based on this methodology, a fatigue and damage tolerance (F&DT) evaluation system, which is mainly for conventionally manufactured metals, is established. On one hand, however, analysis and evaluation are required to be more and more elaborate, but it is difficult for the present theories and methods to meet the accuracy requirements; on the other hand, influences of material factors become increasingly prominent due to applications of novel materials and processes such as additive manufacturing (AM), and it is also difficult for the present theories and methods to capture the interactions of mechanics and materials. Therefore, considering and capturing interactions of mechanics, materials and processing in developing digitalized fatigue analysis methods, accords with not only discipline advances but also engineering requirements.

This study, which mainly adopts peridynamics (PD), consists of three parts: establishment of fatigue damage evolution model; material characterization for simulating interactions of mechanics and materials; considerations of initial fatigue quality dispersity.

This study obtains: that fatigue damage evolution model can deal with both fatigue crack initiation (FCI) and fatigue crack growth (FCG); that the model can well capture interactions of mechanics and materials in FCG observed in experiments if material features are properly characterized; (c) that the model can well capture the stochasticity of crack patterns in widespread fatigue damage (WFD) problems if material initial fatigue quality is properly characterized.

Fatigue damage evolution model in peridynamics

The fatigue damage evolution model is established by considering PD bonds as fatigue elements, i.e. regarding PD bonds as possessing the same fatigue performance as smooth specimens and regarding FCG as progressive bond breakage of crack-tip PD bonds, as shown in Figure 4-10. The model consists of elastoplastic stable cyclic constitutive, load-lifetime curve, mean-stress model and damage accumulation law.

⁴⁹ Beihang University. BAO Rui & LIU Binchao: rbao@buaa.edu.cn

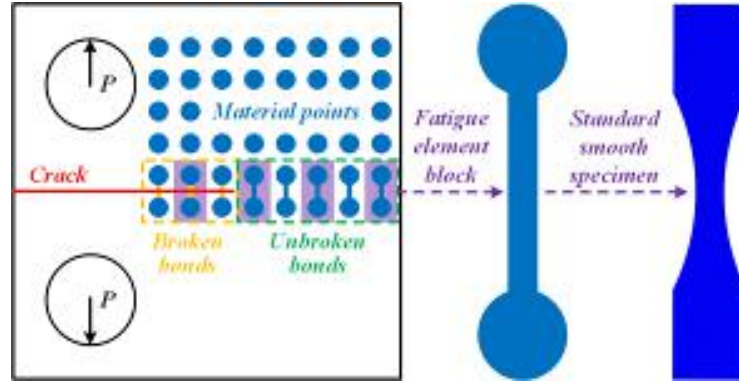


Figure 4-10 Fatigue damage evolution model in peridynamics

The obtained model can well predict fatigue lifetime under constant-amplitude loads, and can also predict fatigue crack growth rates (FCGRs), as shown in Figure 4-11. It should be noted that there are no inputs involved with Paris relationships or any fitted parameters in other FCGRs relationships, i.e. the proposed model predicts FCGRs with parameters only involved with FCI performance.

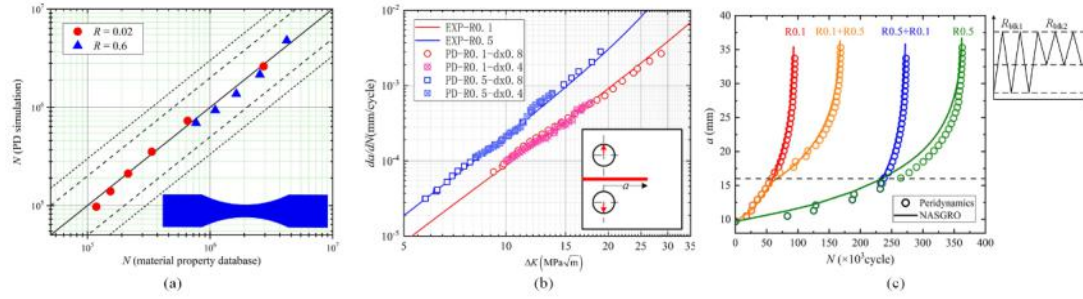


Figure 4-11 Verifications of the proposed model: (a) predictions of fatigue lifetime and comparisons with experiment results; (b) predictions of FCGRs and comparisons with experiment results; (c) predictions of FCGRs under simple variable-amplitude loading and comparisons with NASGRO results.

Simulations on FCG behaviors in AM titanium alloy

The previous studies revealed that fatigue crack path will be deflected by α lath orientations, which show quasi-isotropy in equiaxial grain (EG) areas but obvious anisotropy in columnar grain (CG) areas. Therefore, PD bonds are set to be anisotropic in CG areas, and influences of α lath orientations as well as anisotropy intensity factors are then studied. Simulation results successfully capture the three crack deflection modes observed in experiments, as shown in Figure 4-12; moreover, the simulation results accord also with experiment observations in a statistically quantitative sense, as shown in Figure 4-13.

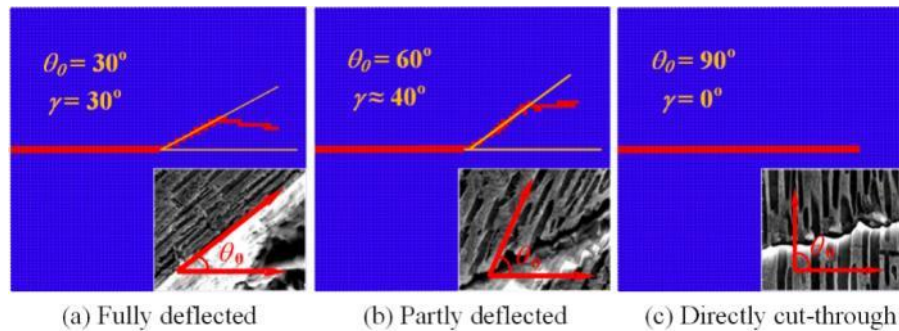


Figure 4-12 Three deflection modes of fatigue crack path

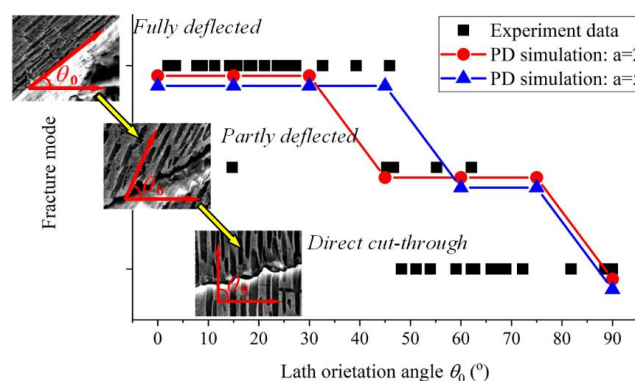


Figure 4-13 The statistic relationships between the fracture mode and the lath orientation angles in PD simulations, and comparisons with experiment observations.

Considerations of initial fatigue quality dispersity

There exists dispersity of initial fatigue quality in material locals, which can be described in the PD model by enriching deterministic load-lifetime mid-value curves with dispersity considerations, i.e. PD bonds are stochastically endowed with fatigue performance matching a certain distribution. The obtained model can well capture stochastic crack patterns observed in WFD problems, and can also predict residual strength of specimens, as shown in Figure 4-14.

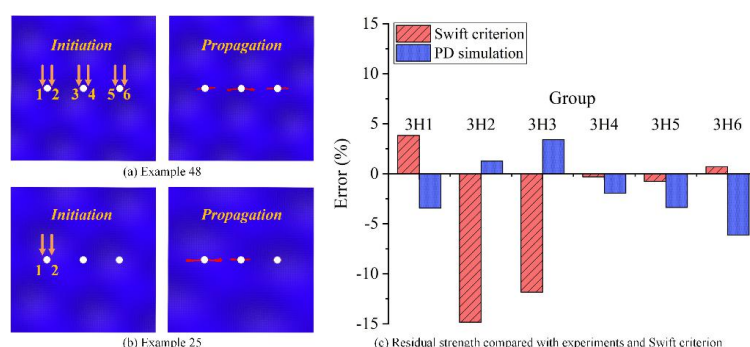


Figure 4-14 Simulations of WFD problems by the stochastic extensions of the proposed model: (a)&(b) stochastic crack patterns; (c) predictions of residual strength and comparisons with Swift criterion.

4.1.4 Numerical Study on Vibration Fatigue Load of Seaplane Wing During The Taxing on Wavy Surface⁵⁰

The main findings of this study are as follows: the effects of increasing velocity and shortening wavelength on wing vibration and aircraft overload are similar.

Specifically, an increase in glide speed or a decrease in wave length makes the wing vibration response and overload response more intense, but both tend to converge.

By comparing the effect of glide speed and wave length, it can be found that the influence of glide speed on wing vibration and aircraft overload is more severe than that of wave length.

The effect of taxiing speed

There are three general forms of overload during taxiing. As is shown in Figure 4-15, when the speed is small, the plane keeps a stable taxiing on the water surface, so the vertical overload of the plane is very gentle. As the speed gradually increases, the aircraft overload experiences two peaks. The reason can be

⁵⁰ Nanjing University of Aeronautics and Astronautics. TONG Mingbo: tongw@nuaa.edu.cn

seen from the contour in Figure 4-16. After passing the wave crest position, the front part of the aircraft leaves the water. Then, as the center of gravity of the aircraft drops and lowers its head, the frontpart of the aircraft experiences a slamming overload with the descending position of the wave, which leads to the first peak on the overload curve. The airplane then glides toward the trough and encounters the next wave upward position, generating a second peak; when the speed is close to the limitation of takeoff velocity, the peak of vertical overload reach 5-8g.

With the increment of velocity, the vibration range of the wing experiences three stages: gentle, rapid andgentle. This phenomenon is closely related to the vertical overload of the aircraft. The first two load changes correspond to the steady increase of the first stage of wingtip vibration. The transformation from the second load to thirdresults in the rapid increase of the wing tip vibration. Then, the characteristics of the load remains the same, but the peak value increases.

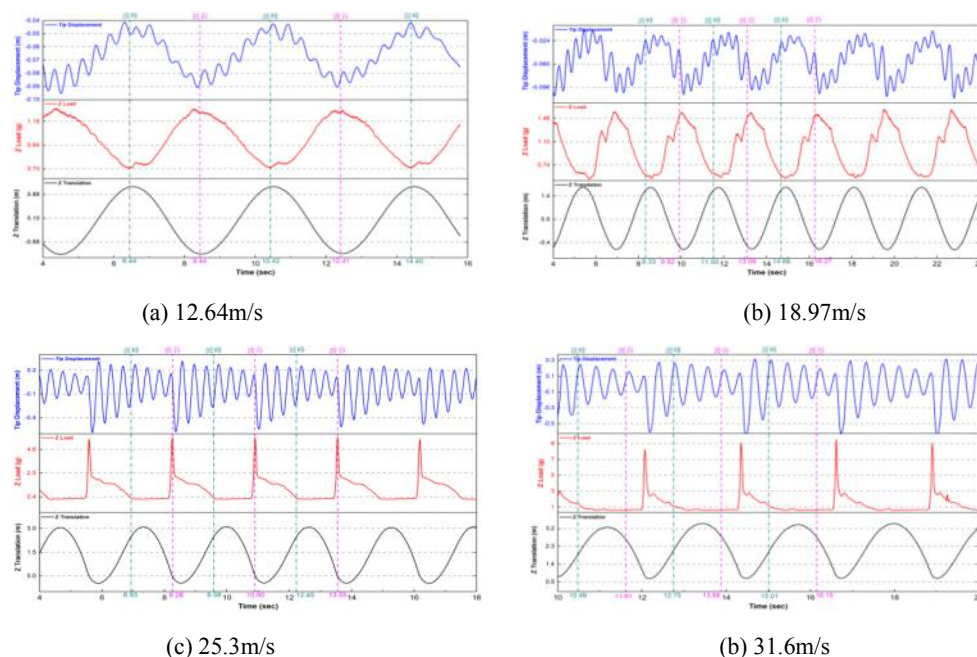


Figure 4-15 Wings vibration and vertical overload history curves at different taxiing speeds

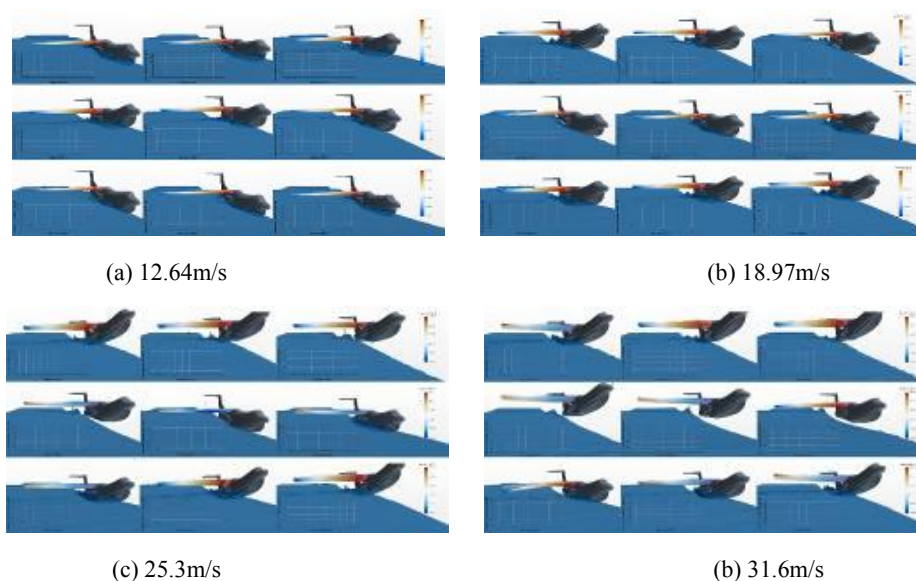
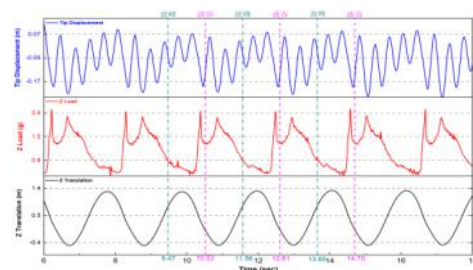


Figure 4-16 Cloud image of aircraft state at different taxiing speeds

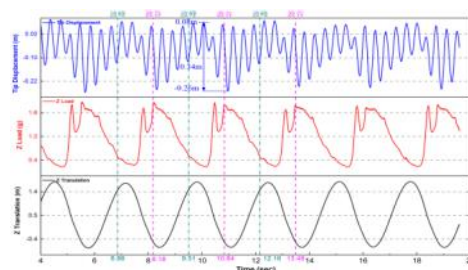
The effect of wavelength

With the increase of wavelength, the peak value of vertical overload decreases gradually and the shape changes. When the wavelength is short, the time-history of vertical overload of the aircraft has double peak phenomenon, and the first peak is greater than the second peak. When the wavelength increases, the vertical overload gradually decreases, and the first peak with wavelength to further increase to 120 m, at this time no longer exists in the overload curve of double peak, instead of a relatively flat overload "plateau".

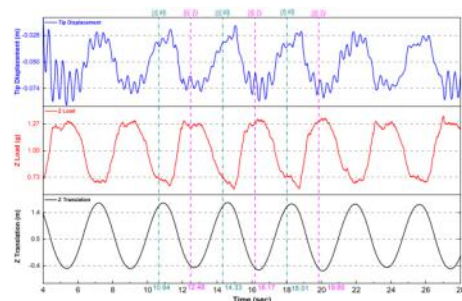
With the increase of wavelength, the vibration range of the wing experiences three stages: gentle, fast and gentle until the convergence decreases. The occurrence of this phenomenon is closely related to the vertical overload of aircraft. When the wavelength is small, the vertical overload changes more dramatically, accompanied by sharper overload peak, and these sharp overload peaks cause a larger amplitude of wingtip vibration. On the contrary, when the wavelength is large, the vertical overload changes gently, so that no large wingtip vibration occurs.



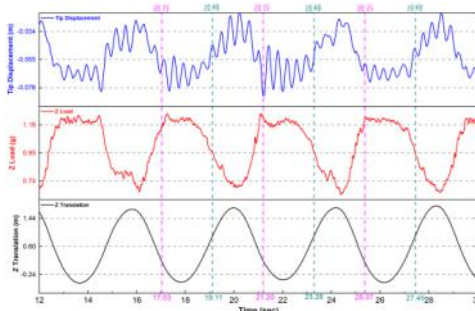
(a) 60m wavelength



(b) 80m wavelength

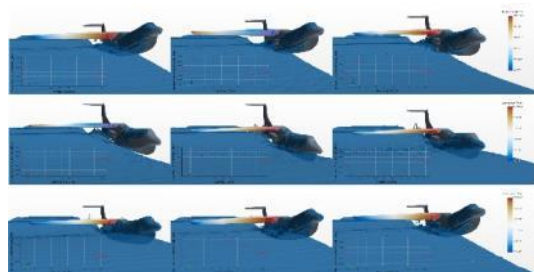


(c) 120m wavelength

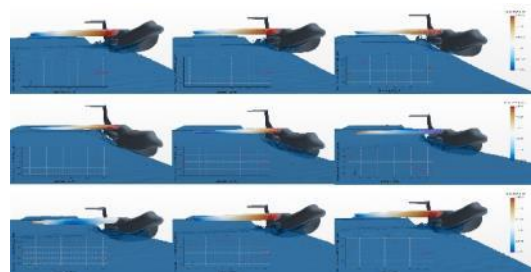


(d) 140m wavelength

Figure 4-17 Wings vibration and vertical overload history curves at different wavelength



(a) 60m wavelength



(b) 80m wavelength

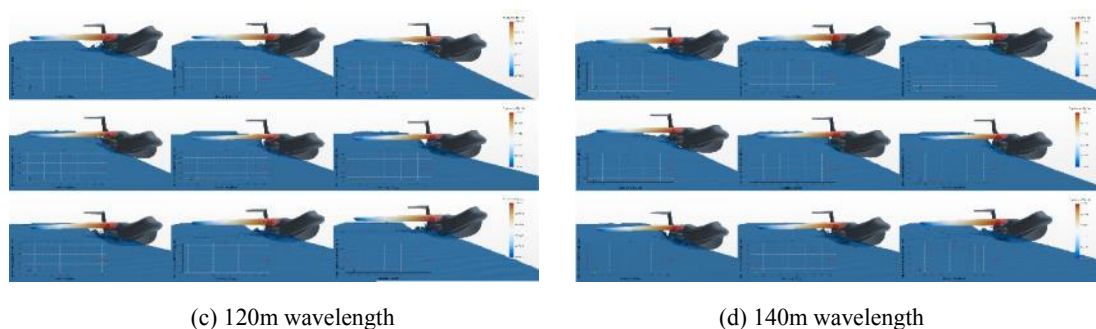


Figure.4 Contour of aircraft state with different wavelength

4.1.5 Damage Tolerance Analysis of Mixed-Mode Cracked Structures⁵¹

With the development of advanced manufacturing technology on aircraft, integral structure becomes more and more popular in the engineering design owing to its characters of lightweight and high safety. The new type of aircraft structure may be supposed on mixed-mode loads, which is supposed on the combination of tensile, bending or shear stress state. Consequently, the damage tolerance studies of structures under mixed-mode loading play an imperative role in its structural integrity assessment.

Refunding by Aeronautical Science Foundation of China, there are three key techniques in the present research, which are as follows: mixed-mode I-II fracture criterions, mixed-mode crack propagation model and damage tolerance analyses and visualization tool for complicated structures.

This project continues two years, the key finds are as follows: the fracture assessment method and mixed-mode crack growth mode of CTS structures under I-II type loading are proposed based on Tanaka formula via experiments, numerical simulation and python-code realization. We compiled a Abaqus plug-in named as Damage tolerance analysis of complicated structures, which can be used for analyzing crack propagation behavior of plates with any direction form of cracks. this research will provide technical support for aircraft damage tolerance design.

Mixed-mode I-II fracture criterions

The residual strength (Figure 4-18) and initial crack opening direction of Compact Tension Shear(CTS) specimens were studied based on theoretical analysis and experiments. In view of the proposed failure load for CTS structure, the apparent fracture toughness of mixed mode I-II crack structure can be obtained by Finite Element Model, which has a good agreement with experimental results. Compared the existing fracture criterion with experimental results in crack opening angle, limit load and mixed-mode fracture toughness, mixed model fracture toughness based on Von Mises yield stress is most fit to engineering analysis(Figure 4-19), which provides a strong support for the carrying load capability analysis of mixed mode crack structure.

⁵¹ AVIC Aircraft Strength Research Institute. SU Shaopu: shaopu_su@sina.com

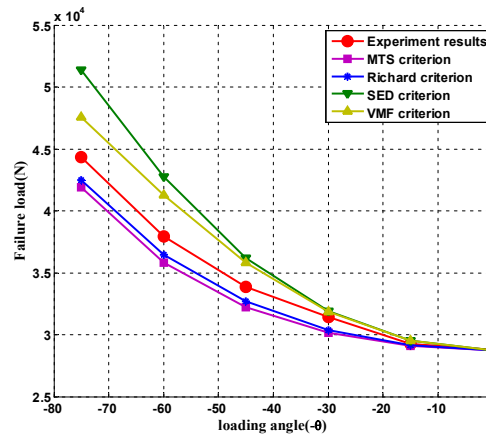


Figure 4-18 Relations between loading angle and failure load

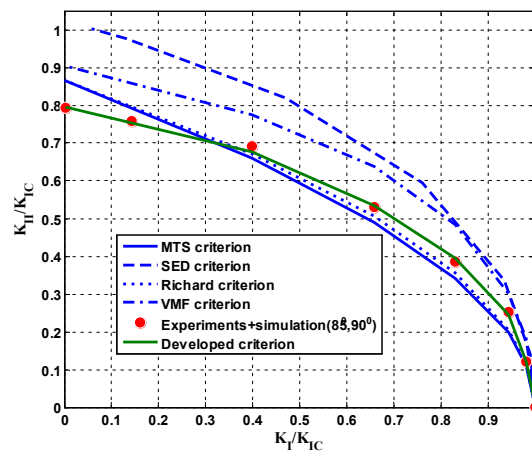


Figure 4-19 Fracture toughness curves of CTS structure based on different fracture criteria

Mixed-mode crack propagation model for CTS structure

The relation between mode-I/II stress intensity factors and crack growth step is the key point to predict the fatigue life of mixed-mode crack structures. The crack growth behavior of Compact Tension Shear (CTS) specimens was studied under different loading modes. A new model for mixed-mode crack growth evaluation was proposed based on experimental results, and the equivalent stress intensity factor was analyzed.

in view of fatigue test results of CTS specimens on 2024-T3 aluminum, the following crack growth model is discussed and verified by test results:

$$\frac{da}{dN} = ce^{\beta \left(\frac{2}{\pi} \arctan \left| \frac{K_I}{K_{II}} \right| - 1 \right)} (\Delta K_{eq})^n \quad (4-1)$$

Where c , n , β is material parameters, ΔK_{eq} is the effective stress intensity factor.

It is found that the crack of CTS structure extends vertically along the loading direction (Figure 4-20), and Tanaka formula is adequate to calculate the equivalent stress intensity factor for CTS structures. When the loading angle is in the range of $0^\circ \sim 45^\circ$, the error is less than 5.46%, which validates the correctness and feasibility of the new crack growth rate model.



Figure 4-20 Failure modes and fracture appearance of specimens under different loading angles α ($0^\circ, 15^\circ, 30^\circ, 45^\circ$ and 60°)

Damage tolerance analysis and visualization of complicated structures

Based on the secondary development platform of ABAQUS the project developed a plug-in of crack propagation life analysis for complicated structures. The plug-in interface is shown in Figure 4-21. The plug-in can analyze two types of structures: rectangular planar structures with multiple cracks, and CTS structures under complicated loads. The stress intensity factor, crack propagation life, crack length-crack propagation life curve, crack propagation path, crack deflection angle can be obtained through this plug-in.

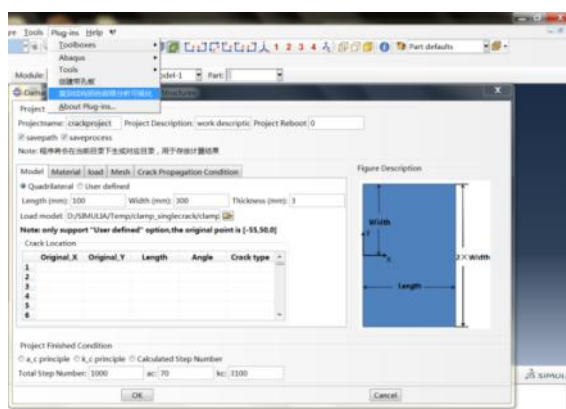


Figure 4-21 Plug-in interface of damage tolerance analysis for complicated structures

4.2 DAMAGE IDENTIFICATION AND STRUCTURAL HEALTH MONITORING

4.2.1 Flexible Eddy Current Array Sensor for Monitoring Structural Crack Damage under Varying Temperature Environment⁵²

This research includes two key parts. The first part is that establishing a quantitative characterization method of environmental impact based on sensor multi-parameter feature grid by exploring the influence mechanism of temperature variation on sensor signals. The second part is that establishing a self-suppression method of environmental interference by exploring the reverse solution model and algorithm of output signals.

⁵² Air Force Engineering University. CHEN Tao & HE Yuting & FAN Xianghong: tchen_afeu@hotmail.com

The main conclusions of this study are as follows. Firstly, the change of temperature will lead to the change of the conductivity of the measured material and lift-off distance between the structure and the sensor, resulting in the variations of output signals of the sensor. The temperature interference suppression method based on the reverse model can effectively suppress the influence of the environmental temperature variation on monitoring signals.

Influence mechanism of temperature variation on signals of flexible eddy current array sensor

The flexible eddy current array sensor is designed based on the principle of electromagnetic induction. It has a number of independent induction coils to form a series of monitoring channel, and can quantitatively monitor the crack damage at hot regions of the structural holes, which are prone to crack. As shown in Figure 4-22(a) and Figure 4-22 (b), when the temperature of the specimen increases from -55°C to 70°C, the change of the sensor output signal exceeds the crack characteristic signal, which will lead to "false alarm". Through the establishment of multi-parameter feature grid and sensor's output correction model, the test results can be transformed into feature grid for quantitative characterization, as shown in Figure 4-22(c). As shown in the grid, with the increase of temperature, the change of environmental temperature will lead to significant changes of the conductivity of the material. At the same time, due to the effect of thermal expansion, the lift-off (the distance between the sensor and the structure to be measured) will also change, resulting in changes in the output of the sensor.

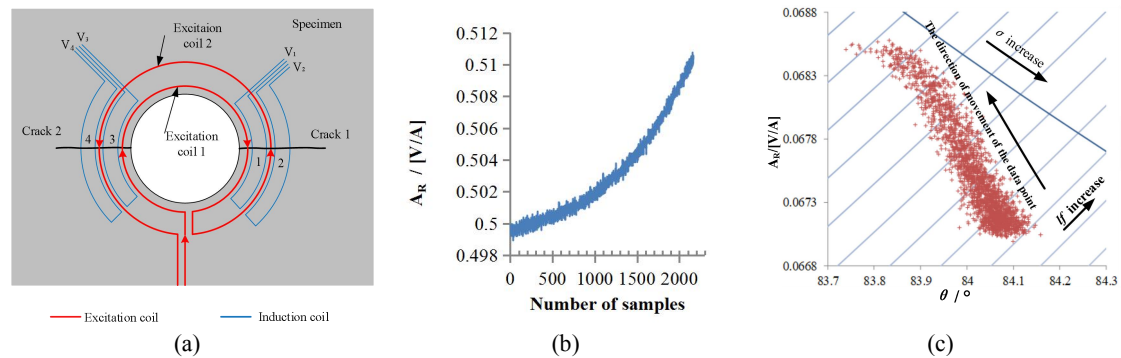


Figure 4-22 Effect of temperature change on output of flexible eddy current array sensor: (a) flexible eddy current array sensor, (b) environmental temperature test, (c) signal variations in feature grid

Through the establishment of the physical parameters reverse algorithm based on the multi-parameter feature grid of the sensor, the reverse solution of the conductivity and lift-off of the measured material is performed.

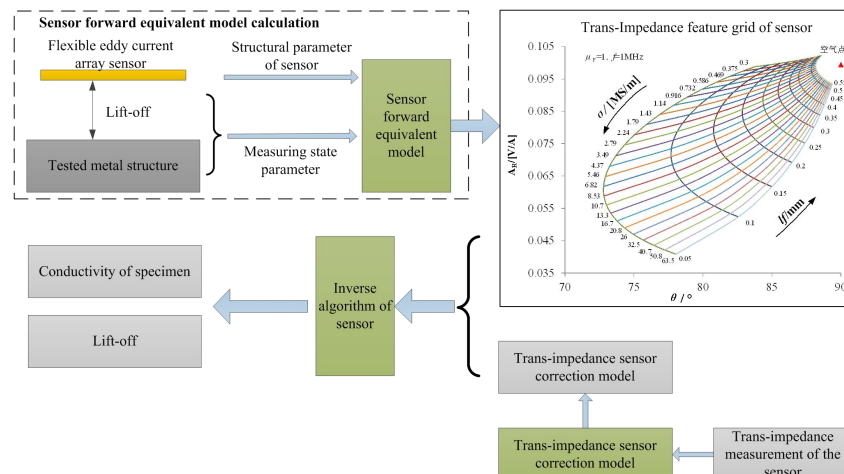


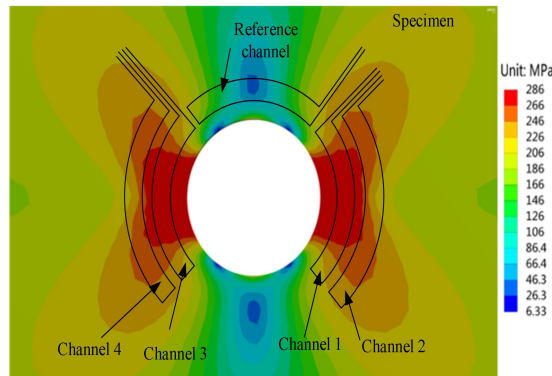
Figure 4-23 Reverse solution of conductivity and lift-off

The interference caused by the change of lift-off can be eliminated by using the conductivity signal as the monitoring signal of the sensor. When the sensor is installed, four monitoring channels are installed in the area of structural stress concentration. The characteristic signal of the sensor is defined as

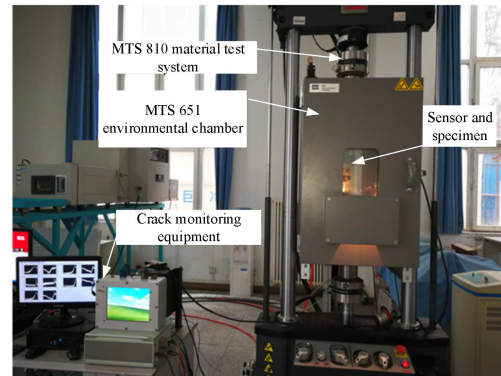
$$\Delta C = \frac{C_r - C_m}{C_r} \times 100\%$$

Where, ΔC is the characteristic signal, C_r is the conductivity value measured by the reference channel, and C_m is the conductivity value measured by the monitoring channel. The area of stress concentration is the area of structural crack initiation and propagation. When cracks are generated, the propagation of cracks can be judged by measuring the change of monitoring signal of the channel. As the stress in the area below the reference channel is small, there will be no crack, and the monitoring signal will not change. Through the environmental temperature influence test, the method can effectively restrain the influence of environmental temperature change in the temperature range of - 55°C to 70°C.

In order to verify the effectiveness of self-suppression method proposed in this paper during structural crack monitoring, the quantitative monitoring test of structural fatigue crack under varying temperature is carried out. The results show that when there is no crack in the structure, the change of ambient temperature makes the conductivity signal of each monitoring channel of the sensor consistent with that of the reference channel, which does not make the characteristic signal of the sensor change significantly. In the process of crack initiation and propagation, the change of environmental temperature does not make the characteristic signal of the sensor change significantly. The maximum variation of the characteristic signal of each measurement channel is about 30% due to the structural crack. This fully shows that the self-suppression method based on reverse model can effectively restrain the influence of environmental temperature variation on the monitoring signal, and the sensor can be used for quantitative monitoring of structural cracks under varying temperature.



(Figure 4-24)



(Figure 4-25)

Figure 4-24 Flexible eddy current array sensor with temperature self-suppression

Figure 4-25 Fatigue crack monitoring experiment under environmental temperature variation.

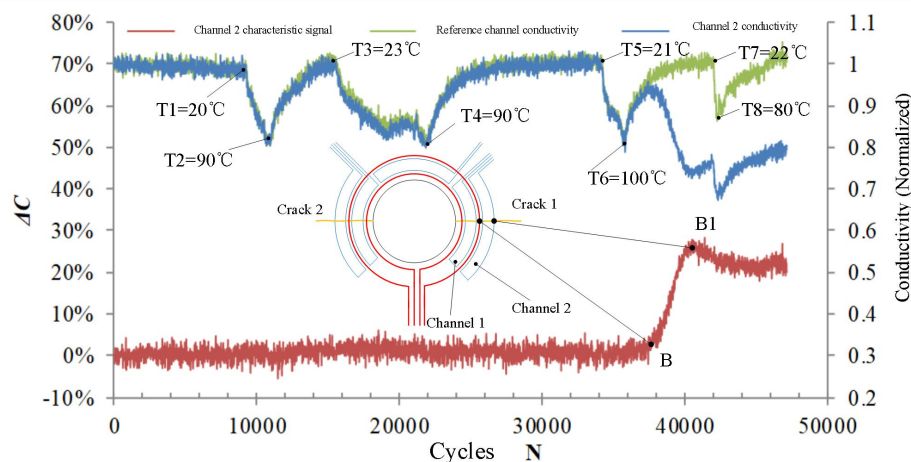


Figure 4-26 Fatigue crack monitoring test results of 2024 aluminum alloy structure under environmental temperature variation.

4.2.2 Individual Aircraft Life Monitoring Based on Artificial Intelligence and Advanced Sensing Technology⁵³

The study consists of three key components: The load prediction of critical parts based on artificial neural network (ANN), individual aircraft structural crack damage monitoring based on advanced sensors, and maintenance decision system based on health status of individual aircraft structure.

The main findings of this study are as follows: By selecting flight parameters, it can improve the calculation efficiency and accuracy of the load forecasting model of critical parts; the crack damage can be accurately identified by intelligent coating sensor and FBG sensor; based on health status of individual aircraft, we develop an expert system of aircraft maintenance based on multi-objective optimization.

Load prediction of critical parts based on artificial neural network

Depend on a wide range of preprocessing techniques, the flying parameters selection, overload peak and valley value extraction, 15 points smoothing noise reduction and load partitioning are determined, and the calculation efficiency and forecasting accuracy of the load forecasting model are improved, as shown in Figure 4-27.

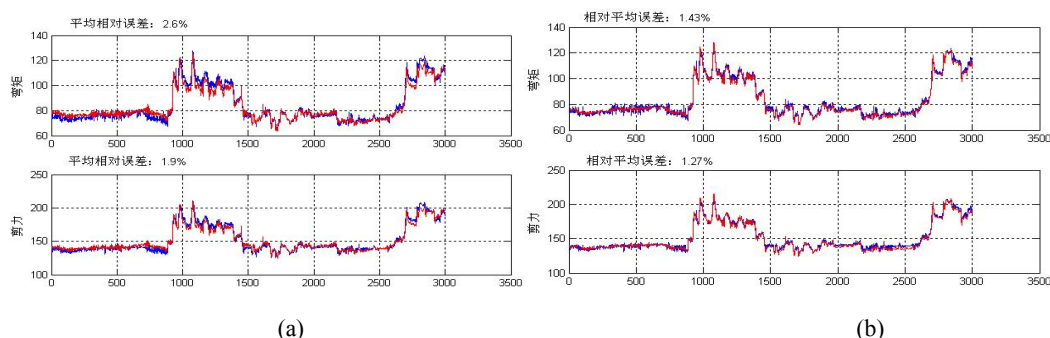


Figure 4-27 Effect of input parameter selection for load prediction model: (a) Result before selection, (b) Result after selection

Based on the artificial neural network technology, the selection method of flight parameters and the

⁵³AVIC Shenyang Aircraft Design & Research Institute. CHEN Liang: 5692864@qq.com

load identification model are established, and the application software of load identification based on flying parameters is developed. The precision prediction of structural load based on flight parameters is realized. The following figure shows the structural load history based on neural network. The red curve is the predicted result.

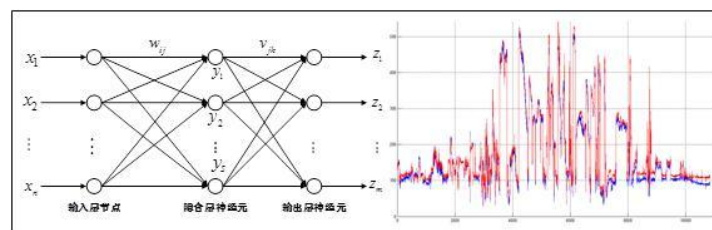


Figure 4-28 Load prediction based on artificial neural network

Crack damage monitoring of individual aircraft structure based on advanced sensor

The intelligent coating structure damage identification system (ICMS) is a new kind of structure crack monitoring technology, which can make real-time and on-line diagnosis of the whole structure and critical parts of the aircraft, detect and locate the cracks on the structure (especially the inner closed structure) in time, and provide an important basis for the safety, economic use and timely maintenance of the structure. The following figure shows the application of the intelligent coating sensor in the fatigue test.

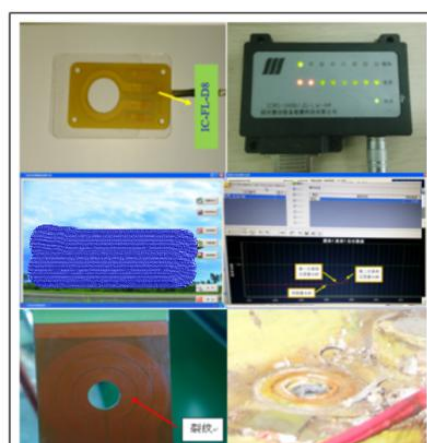


Figure 4-29 Structural crack detection based on intelligent coating sensor

In order to solve the problem that a certain aircraft life is depleting, which affect the flying training of the army, the crack propagation in the critical parts is monitored by adding an uncharged FBG sensor system. By predicting crack propagation through sensors, the burden of nondestructive testing in the field is reduced.

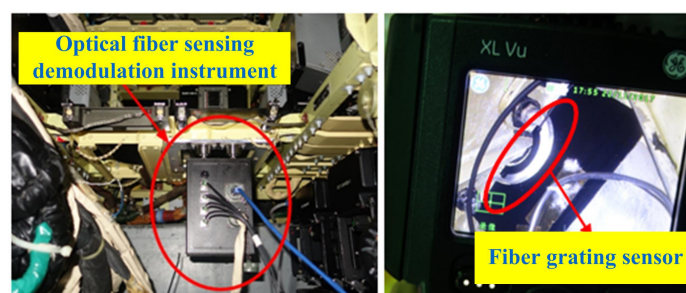


Figure 4-30 Application of FBG sensor technology in crack detection of a certain aircraft

Maintenance decision system based on health status of individual aircraft structure

In a certain aircraft research project, the research on strain monitoring and crack propagation technology based on intelligent coating was carried out. The method of equivalent life consumption and health assessment of aircraft structure was established. The decision technology of aircraft structure maintenance expert based on multi-objective optimization was broken up, and structural life database and structural maintenance expert decision system were formed.

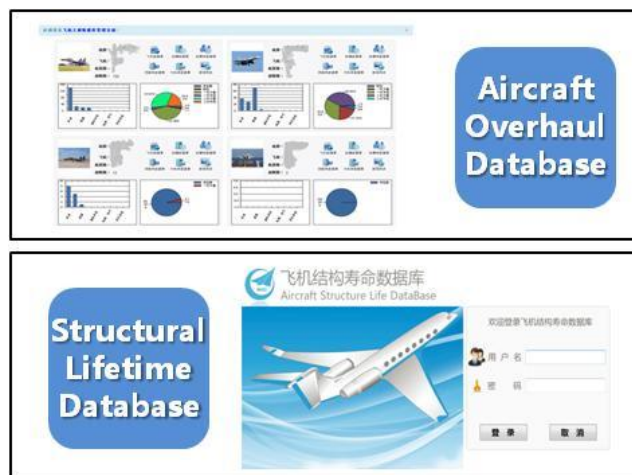


Figure 4-31 Structure Health Status Database

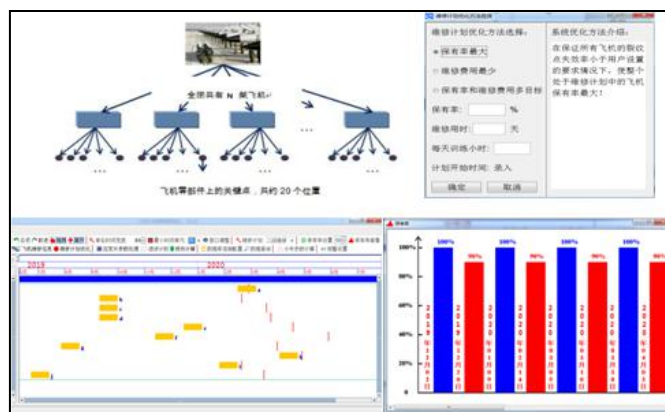


Figure 4-32 Maintenance Decision System Based on Structural Health Status

4.2.3 Fatigue Damage Assessment of Structural Critical Locations Based on Flight Parameters⁵⁴

The individual aircraft life tracking based on the damage evaluation of critical locations, compared to the overall macro tracking based on the normal acceleration N_z at the center of gravity, can more comprehensively reflect the life consumption of critical components and provide a more accurate and reliable basis for refined life management of fielded aircrafts.

This research focuses on solving key techniques such as the identification of structural flight loads and ground loads based on flight parameters, and the assessment of fatigue damage of structural critical locations, which establish the foundation for the health management and condition-based maintenance

⁵⁴AVIC Chengdu Aircraft Design & Research Institute. DUI Hongna: duihn060379@126.com

of the aircraft structure in service.

Flight Load Identification

Among the two load tracking methods, the "direct" method based on strain measurements has high refit/instrumentation cost, and the sensor are prone to failure or drift. The "indirect" method based on airborne flight parameters is universal. Once the IAT parametric equation is successfully built, it can be applied to the whole fleet of the same type.

In order to construct a high-precision "strain-load" equation, the team used virtual load calibration testing as an aid to optimize the location of strain bridges. According to the European space basis vector method, an effective approach for screening ground calibration load cases from the design load case library is proposed, which not only simplifies the ground test to the greatest extent, but also ensures the completeness and sufficiency of the load cases.

In order to simplify the scale and difficulty of load calibration tests for the batch-produced aircrafts as much as possible on the basis of meeting the requirements of load accuracy, the team proposed an in-flight load calibration method. By constructing the relationship between the strain measurements and flight parameters of each aircraft, the load equation of the reference aircraft is linearly corrected to obtain the load equations of other aircraft, so as to realize "only one aircraft is required for calibration".

In order to construct a high-precision parametric flight load equation, the team carried out researches from data cleaning, data fusion, data compression, state classification and machine learning, etc., based on a large number of flight data and load measurements in service, and established a set of structural flight load acquisition methods based on flight parameters, breaking through maneuver recognition, input parameter optimization technology, and neural Network optimization based on genetic algorithm and many other key techniques.

Select the flight parameters and wing root bending moment load samples of a load measurement aircraft under subsonic flight, and compare the fitting accuracy of different machine learning methods. It can be seen that in terms of fitting accuracy and generalization capability, BP neural network method optimized by genetic algorithm is the best. Comparison of fitting accuracy of training samples is as shown in Figure 4-33.

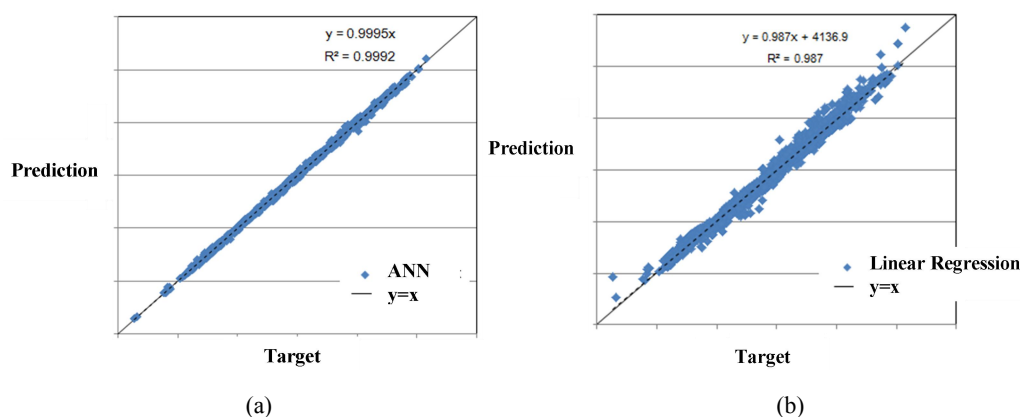


Figure 4-33 Comparison of load fitting accuracy: (a) BP neural network method, (b) Linear regression method

Ground Load Identification

In order to construct a high-precision ground load equation based on flight parameter, a set of ground load acquisition methods are established through in-depth excavation of measured load data of the

landing gears, without the need for additional sensor installation on the landing gears. First, fuzzy recognition is used to identify typical mission segments on the ground, and then data mining is used to construct a "flying parameter-ground load" model for each mission segment.

The main-landing-gear load predictions at the wheel center in a typical flight are shown in Figure 4-34. Although the errors of specific load points are large, the fatigue damage error caused by the whole load spectrum to the structure connected with the landing gear is small.

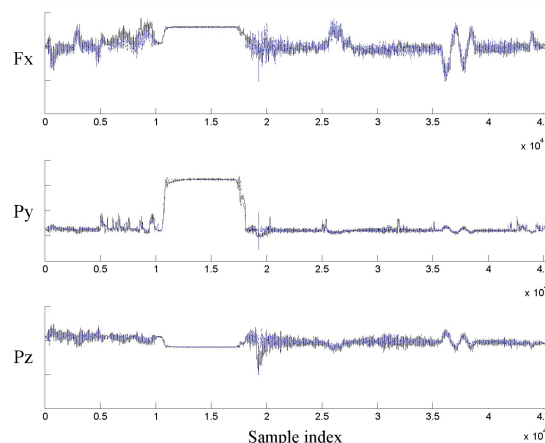


Figure 4-34 Main-landing-gear load predictions in a typical flight

Damage assessment of critical locations of metal structure

Indirect method is used to monitor and predict the damage of critical locations of metal structure. The indirect tracking is based on the monitoring results of load, obtained by "flight parameter-load" equation or "strain-load" equation. The stress history of structural critical locations is obtained by "load-stress" equation, and the fatigue damage calculation and residual life prediction are carried out according to fatigue or fracture mechanics theory.

Various fatigue analysis and crack propagation methods based on fracture mechanics should be used for different types of aircraft structures and possible fatigue/fracture failure modes. The parameterized model of fatigue damage assessment should be carried out for each critical location, and these parameters should be preliminarily determined by theoretical analysis and representation coupon test results, and verified and corrected using component/full-scale fatigue test results.

Based on data fusion of structural representation coupon /components/full-scale fatigue test, a set of fatigue damage assessment method using generalized correction method (including life correction and crack growth rate correction) was proposed. The durability and damage tolerance damage model parameters were customized according to the characteristics of different critical locations. The process is shown in Figure 4-35.

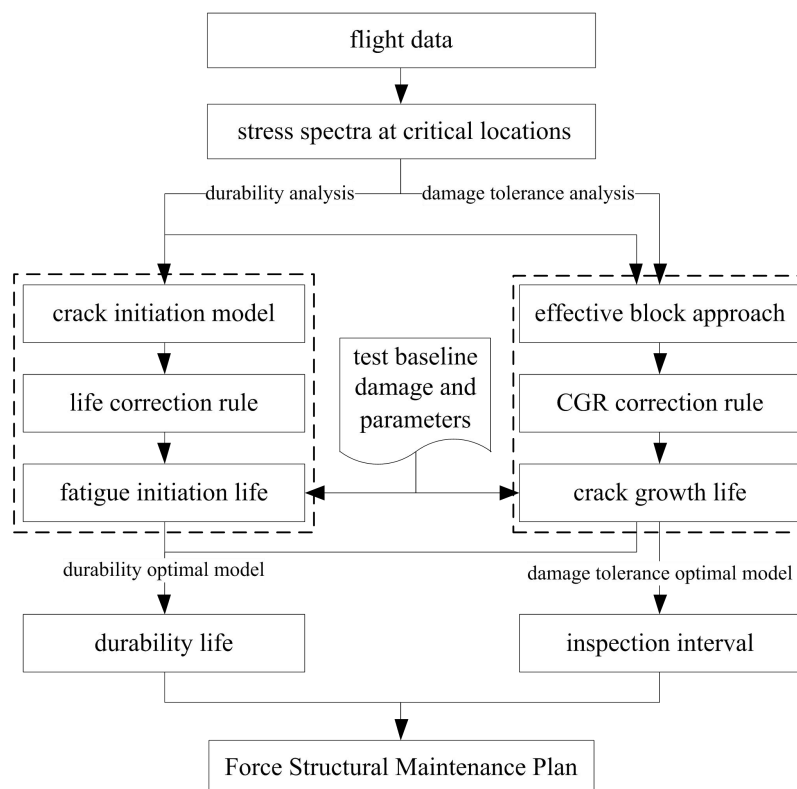


Figure 4-35 Fatigue damage assessment using generalized correction method

As for the selection of fatigue scatter factor of individual aircraft, the team carried out researches on different scatter factors and reliability factors of different structural parts and characteristics. The structural reliability factor in individual aircraft tracking is not only the traditional scatter factor, but also the error caused by load prediction model and fatigue damage algorithm.

4.2.4 Strain Monitoring Based Damage Identification in Aircraft Full Scale Fatigue Test⁵⁵

In order to solve the above problems, bases on strain measurements during the test, researches on damage identification of the test article based on strain monitoring is carried out in this paper. Through active damage identification, crack location is determined and targeted nondestructive inspection is triggered. Some researchers have proposed several methods for structural damage identification, such as threshold method, relative error method, probability distribution method and slope method. However, in the application of multiple full-scale durability and damage tolerance tests, it is found that the above methods can identify some long cracks, but the sensitivity to cracks is low, and the universality for strain data is weak, and there are still problems of time lag and missed report, which is not good for timely detection of cracks.

Based on high-precision simulation analysis, a precise strain monitoring scheme is designed for fatigue critical parts. The automatic cleaning method of measured strain data is studied. Based on the variation law of local strain field around the crack and statistical theory, a structural damage identification method driven by measured strain data is established, and a dynamic and self-adaptive damage

⁵⁵AVIC Chengdu Aircraft Design & Research Institute. PAN Shaozhen: pan_shz@163.com

identification criterion is proposed, which improved the universality, accuracy and sensitivity of damage identification.

Automatic data cleaning method

Influenced by loading error, data acquisition error, environment and other factors, noise exists in the measured strain data, which should be cleaned and eliminated before damage identification. The basic requirement of data cleaning is to be able to identify the local noise of data accurately and not to cause the loss of data features. Through the study of the measured data of thousands of strain sensors, it is found that the traditional 3σ criterion, Grubbs criterion, Romanovs criterion and other methods do not solve the above problem. Therefore, a multi-method fusion algorithm for data automatic cleaning is proposed, which is carried out in three steps:

Step 1: Preliminary cleaning. Determine whether there is obvious noise in the range of sensor and remove it.

Step 2: Data clustering. Clustering method is used to divide the data into several clusters automatically, and each segment reflects the local characteristics of the data, thus preserving overall characteristics of the data.

Step 3: In-depth cleaning. In each cluster obtained by clustering, the data is cleaned again using 3σ criterion to eliminate the local noise that does not meet the criterion.

Using the above steps, data cleaning examples are shown as Figure 4-36

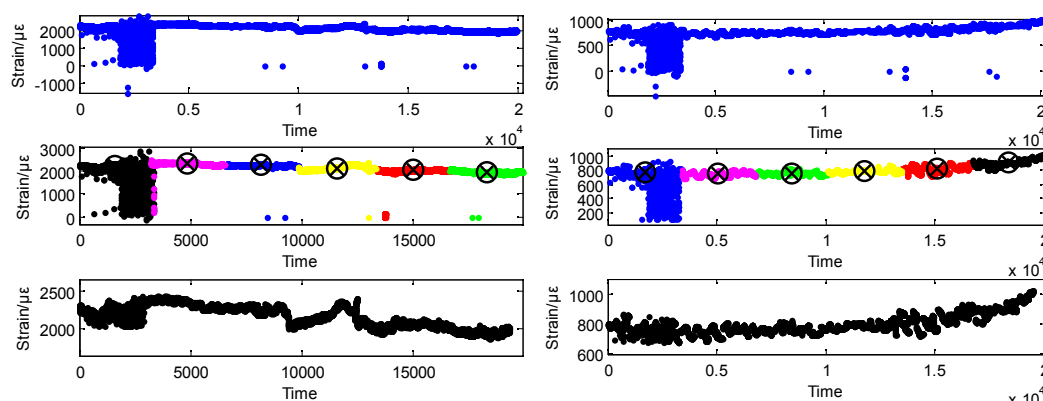


Figure 4-36 Data Cleaning Examples

Damage Identification

First of all, strain data is divided into two parts: baseline data and forecast data. The statistical characteristics such as mean value, standard deviation, coefficient of variation, and likelihood of the baseline data and forecast data are calculated respectively.

Then, a dynamic threshold function related to likelihood and coefficient of variation is constructed to statistically predict the probability that the likelihood in the forecast data is greater than the dynamic threshold function.

Finally, according to flight hours of one test spectrum block and forecast data, a scale factor is calculated to establish damage criterion. When the likelihood is greater than the probability that the dynamic threshold value is greater than the scale factor, it's judged that structural damage occurs near the strain sensor. Then damage warning is issued and nondestructive inspection is triggered for

confirmation or positioning.

The characteristic of this method is that it can amplify the damage signal in the strain data, and the threshold function of different strain sensors is different, so it is dynamic and self-adaptive. Besides, the scale factor used in the damage criterion is suitable for the prediction data of different lengths, so the sensitivity and universality of the method are enhanced.

Application

In the application of several full-scale durability and damage tolerance tests, the structural damage identification method effectively enhances the targeted guidance for NDI, and the length of minimum surface crack is only 3 mm, much lower than the vast majority of cracks found by regular NDI. Cracks are found more timely and accurate, so as to greatly reduce the difficulty of repair and the cost of repair/modification.

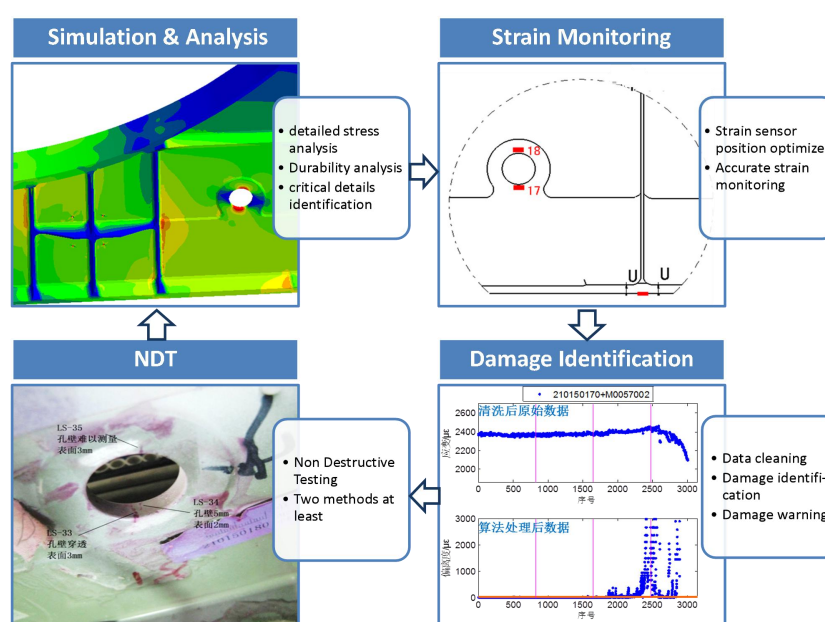


Figure 4-37 Fatigue crack identified in a full scale fatigue test

4.2.5 Research on Nondestructive Testing Method for Cold Spraying to Repair Structural Defects⁵⁶

This research contains two important parts: the detection of pores and cracks in cold spray molding; the detection of defects in the process of cold spray.

The main findings of this research are as follows: the size of defects in the cold spray forming process is small and it is difficult to detect with non-destructive methods; it is easier to find cold spray repair cracks using eddy current testing; the layering of the cold spray repair layer and the substrate is cold spray Early manifestation of cracks in the layer.

Cold spray forming defect detection

As a spraying manufacturing process that uses high-speed airflow to deposit particles on the substrate test piece, the sprayed particles are not melted during the entire spraying process and always maintain a solid form. Therefore, the existence of pores in the cold sprayed test piece is inevitable. The collision

⁵⁶ AVIC Aircraft Strength Research Institute. PENG Zhiwei: peng235@163.com

will bring about the cracking of some particles, as shown in Figure 4-38.

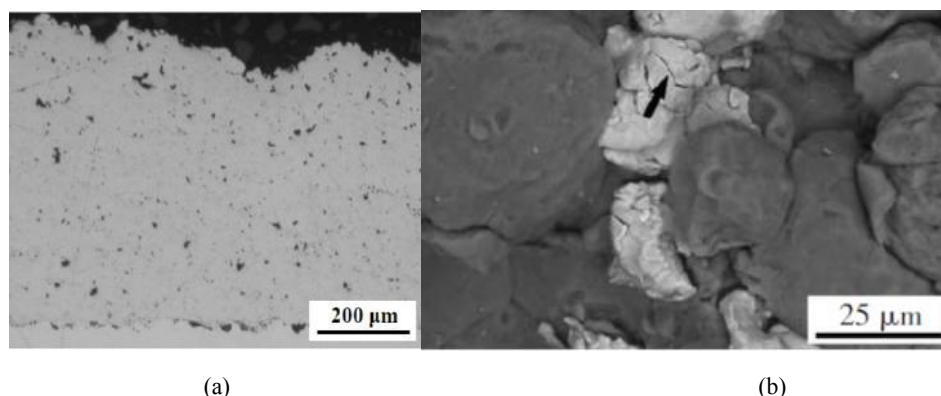


Figure 4-38 Forming defects of cold spray coating (a) Coating porosity diagram (black dots in the figure) (b) Collision cracks (pointed by the arrow in the figure)

The diameter of the spray particles used in cold spraying is only tens of microns, and the pores and cracks formed are also on the order of microns. At this stage, the measurement of them is mostly using two destructive methods, metallography and scanning electron microscopy. For the pores, infrared cameras have been used to obtain their porosity, but this method is seriously affected by the surface roughness of the particles. Therefore, at this stage, the non-destructive testing of cold spray repairs is more concerned about its use detection.

Defect detection during use of cold spray

Figure 4-39 shows the penetration display results of cold spray repairing pre-crack fatigue test pieces under three conditions. (a) It is the penetration display of the prefabricated fatigue test piece before the fatigue test. Except for the penetration display of the prefabricated crack, there is no penetration display in the rest of the parts; (b) The penetration display of the cold spray crack under load in the fatigue test, The crack length is 15mm; (c) The penetration test after disassembly of the test piece shows that the crack length is 5mm. The same crack appears in the two cases of b and c and shows different lengths. The possible reason may be that the penetration test is aimed at surface opening cracks. Under tensile load, the crack opening is larger and easy to be penetrated. Normally, the fatigue cracks are relatively small and tight. The internal compressive stress in the cold sprayed coating and the compressive stress in the coating after the external load is removed make the cracks of the coating more closely affect the detection of the penetration length of the crack.

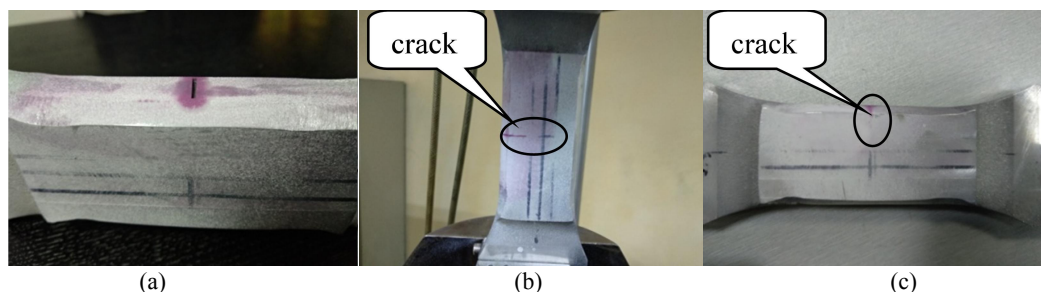


Figure 4-39 The penetration display of the cold spray repair test piece under three conditions: (a) penetration display before fatigue test; (b) crack penetration display under load; (c) crack penetration display

Using ultrasonic phased array to perform line scan and fan scan inspection on the cold sprayed test piece, the inspection chart in Figure 4-40(a), (b) and its corresponding A-ultrasound display are obtained respectively. Through the analysis of the corresponding relationship between the ultrasonic

phased array inspection chart and the thickness of the cold sprayed repair test piece, the ultrasonic phased array method cannot be used to distinguish the cracks when the substrate and the cold sprayed layer have cracks at the same time. The cracks belong to which layer. Ultrasonic phased array is also the same as ordinary ultrasonic testing, which can only obtain the layer of the matrix layer, that is, only the layer can be found in the ultrasonic phased array inspection of the cold sprayed fatigue crack test piece, but the crack display cannot be distinguished. . Therefore, how to track the growth of the cracks in the base layer when the base layer and the cold sprayed layer have cracks at the same time need to be further studied.

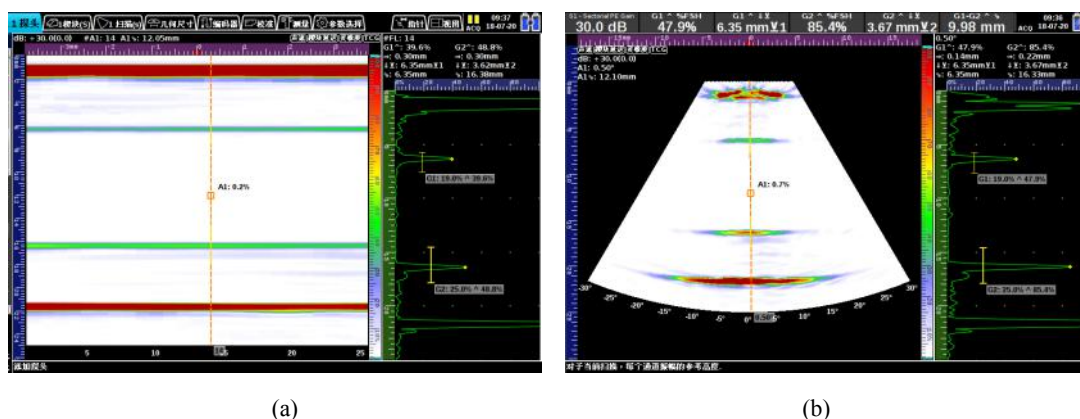


Figure 4-40 Ultrasonic phased array detection diagram: (a) Line scan result; (b) Fan scan result

4.2.6 Guided Wave Damage Diagnosis Based on Deep Learning⁵⁷

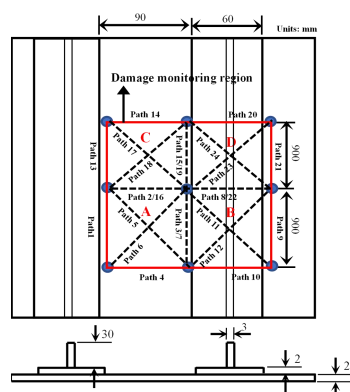
There are three key parts in this study: sample design based on energy map; model design based on Siamese convolutional neural network; experimental design and deep learning model training.

The main conclusions of this study are as follows: for deep learning damage identification technology, compared with the single path, the sample design method based on energy map has obvious advantages, which can make the sample labeling method get rid of the dependence on expert experience; the deep learning model can extract the high-level features of guided wave signals, which are less affected by structural uncertainties. The biggest limitation of the engineering application of this technology is the insufficient number of samples. Further research on the limited data-driven deep learning damage identification method is needed. With the help of feature visualization technology, damage features extracted from deep learning networks can be analyzed intuitively, but the interpretability of features extracted from deep learning networks is low at present.

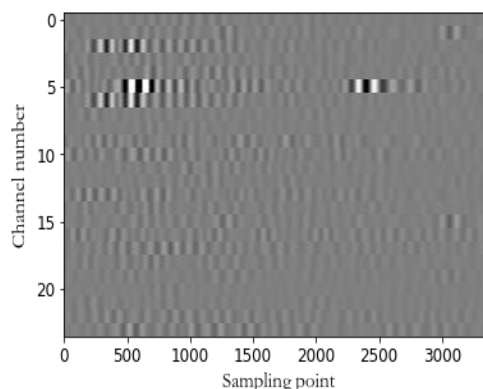
Sample design based on energy map

For the monitoring network composed of 9 piezoelectric sensors in Figure 4-41, 24 monitoring paths are used to construct the energy map (Figure 4-42) and take it as the data sample of the deep learning model. Its advantages are as follows: 1) transform the damage diagnosis problem into the image recognition problem that deep learning is best at handling; 2) Compared with single-path signals, the energy spectrum based on multi-path scattered signals contains more structural state information, which makes it easier to distinguish whether the signal changes are caused by environmental factors or damage factors; 3) It can get rid of the limitation of relying on expert experience to judge the type of sample labels (for example, with or without damage).

⁵⁷ AVIC Aircraft Strength Research Institute. LV Shuaishuai: 647817545@qq.com



(Figure 4-41)



(Figure 4-42)

Figure 4-41 Structure diagram of Lamb wave monitoring net-work

Figure 4-42 Schematic diagram of energy spectrum of 24 monitoring paths

Siamese convolutional neural networks

The Siamese strategy was adopted to design the damage diagnosis model, and its principle was shown in Figure 4-43. Compared with the traditional image recognition model, the advantage of this model lies in that the number of parameters of feature extraction network is greatly reduced by making 24 semantic extraction networks share the weight, and its essence is to realize the convolutional neural network to scan the image pixel line by line and comprehensive diagnosis.

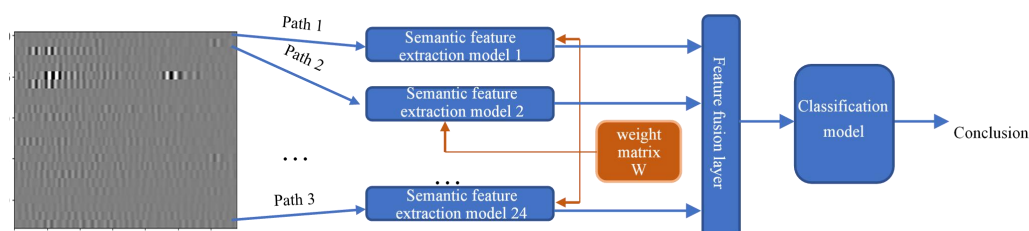


Figure 4-43 Working principle of siamese model

Convolutional neural network based on Siamese strategy is composed of semantic feature extraction model and classification model, and its basic architecture is shown in Figure 4-44 and Figure 4-45 respectively.

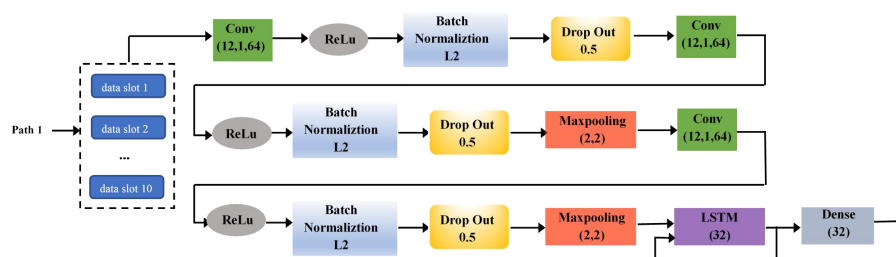


Figure 4-44 Basic architecture of semantic feature extraction model

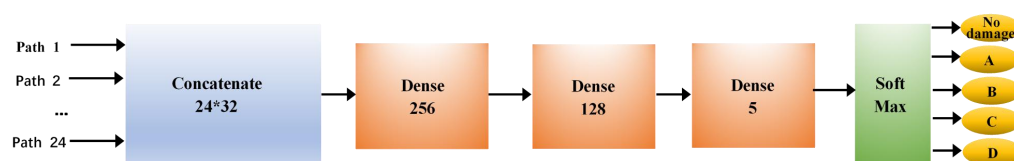


Figure 4-45 The basic architecture of the classification model

Experimental design and model training

6 CFRP stiffened panels (S1~S6) with identical structural configuration and materials were used for the experiment, and their dimensions and piezoelectric sensor network layout were shown in Fig. 1. S1-S4 and S5-S6 were used for model training and testing, respectively. The training set, verification set and test set contain 5000, 592 and 319 data samples respectively. The model converges after 60 training cycles, and the accuracy rates of damage identification and damage location are 94% and 93% respectively, which has certain advantages over traditional methods. The diagnostic results of the test set are shown in Table 1.

Table 4-2 Diagnostic results of the test dataset

Label	Damage position	Precision	Recall	F1	Sample
0	No damage	0.96	0.71	0.82	70
1	A	0.98	0.98	0.98	57
2	B	0.95	0.97	0.96	56
3	C	0.88	0.72	0.79	98
4	D	0.53	1	0.69	38
Accuracy	/	0.86	0.87	0.85	319

4.2.7 Modeling and Simulation of Structural Surface Crack Modeling Characteristics Based on Laser 3D Scanning⁵⁸

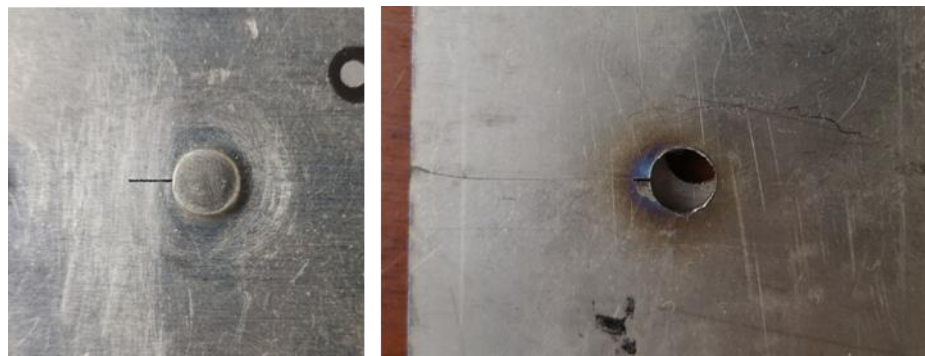
In this research, laser 3D scanning technology is applied to crack detection, and the ability of laser 3D scanning to identify surface crack characteristics is studied by performing laser 3D scanning on four typical surface crack characteristic samples representing different visually detectable degrees of difficulty.

Structural surface crack characteristics

According to the visual inspection degree from simple to difficult, produce four typical surface crack characteristics samples of hole edge cracks. 1# sample has an artificial crack, 2# sample has a crack propagating to edge of the sample, 3# sample has a visible long crack, and 4# sample has a barely visible short crack, and pictures of the typical crack characteristics in four samples are shown in Figure 4- 46.

The crack characteristics are characterized from the three aspects of crack length, crack width, and height difference between the two sides of the crack. The crack length of the samples from 1# sample to 4# sample is in Table 4-3. The crack width of the samples from 1# sample to 4# sample is in Table 4-4. The cracks in the samples from 1# sample to 4# sample are different in height on both sides as seen in Table 4-5.

⁵⁸ AVIC Aircraft Strength Research Institute. JIAO Ting: 296513713@qq.com



(a) artificial crack (1# sample) (b) crack propagating to edge of the sample (2# sample)



(c) visible long crack (3# sample) (d) barely visible short crack (4# sample)

Figure 4- 46 The pictures of the typical crack characteristics in four samples

Table 4-3 The crack length of four samples (unit: mm)

1# sample	2# sample	3# sample	4# sample
5.00	20.50	10.12	3.56

Table 4-4 The crack width of four samples (unit: μm)

1# sample	2# sample		3# sample		4# sample
	near hole	near edge	near hole	near crack tip	
299	29	43	13	12	11

Table 4-5 Height difference between the two sides of the crack of four samples (unit: mm)

1# sample	2# sample		3# sample		4# sample
	near hole	near edge	near hole	near crack tip	
0.002	0.027	0.244	0.018	0.019	0.005

The impact of crack characteristics on the ability to model and identify laser 3D scans

Laser 3D scanning modeling of four crack characteristics is carried out using the blue parallel laser fine scanning mode, and the results are shown in Figure 4-47. Laser 3D scanning modeling can identify artificial crack and the crack propagating to edge, also can identify visible long crack, but is not easy to distinguish from scratches, cannot identify barely visible short cracks.

The height difference between the two sides of the crack near the hole edge and near the edge is measured in the 3D scanning model, which was compared with the optical microscope measurements, and the results are shown in Table 4-6. The laser 3D scanning model measurements are in the same

magnitude as optical measurements. Laser 3D scanning is sensitive to the parameter of height difference on both sides of the crack.

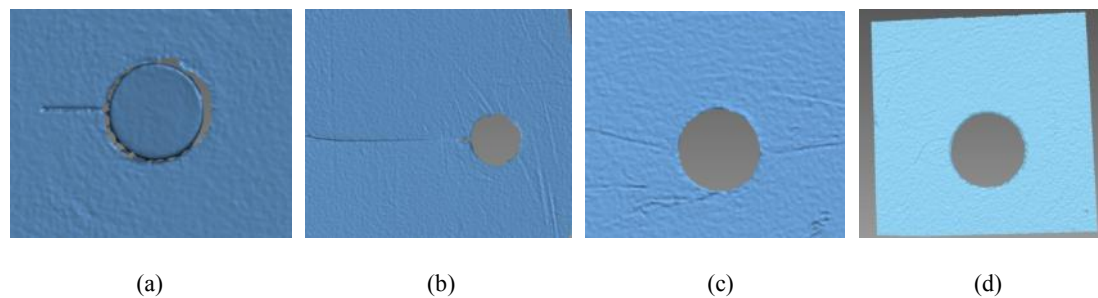


Figure 4-47 The results of laser 3D scanning modeling of four crack characteristics: (a) artificial crack model, (b) the model of crack propagating to edge of the sample, (c) the model of visible long crack, (d) the model of barely visible short crack

Table 4-6 The measurements of height difference between the two sides of the crack near the hole edge and near the edge using two methods (unit: mm)

method of measurement	near hole	near edge
optical microscope	0.069	0.244
laser 3D scanning model	0.086	0.212

4.2.8 Research on Crack Measurement Method Based on Displacement Field⁵⁹

In recent years, the crack detection method based on digital image has made great progress. One method is to establish the objective function based on displacement field near the crack tip. The measurement information of crack is gotten by optimizing the objective function during iterative process. This paper studied the robustness of crack-tip recognition algorithm. And crack growth test was designed to verify this algorithm.

Principle of crack measurement method

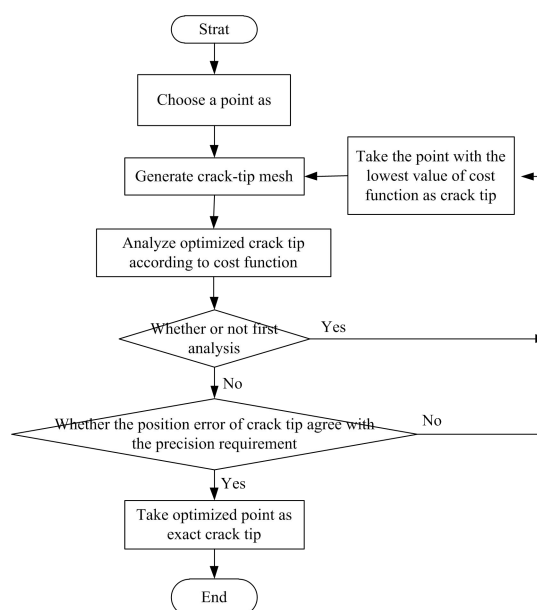


Figure 4-48 The flow chart of locating crack tip

⁵⁹ AVIC Aircraft Strength Research Institute. ZHANG Wendong: dongzi.666@163.com

The variable of the cost function is the crack tip coordinate. Different crack tip can get different cost function values, and the cost function can be optimized iteratively to obtain the exact crack tip position. The detailed analysis flow chart of the iterative process is shown in Figure 4-48.

Crack propagation test

In order to verify the application of crack measurement method in actual experiment, a schematic illustration of the 2-mm-thick center cracked tension (CCT) specimen used is provided in Figure 4-49. The specimen was manufactured from an aerospace grade 2024 aluminium alloy in plate form. The required speckles for DIC are produced on the surface of specimen using a fine spray of matt black paint. A 100 kN Instron hydraulic test machine was used to load the specimen in tension. A 2048×2560 CCD camera and a Kowa LM25XC lens with a low distortion and high resolution are used to record the images. Fatigue cracking was then carried out at a constant maximum load of 12kN and load ratio of 0.1. Figure 4-40 illustrates the experimental set-up which includes a separate camera system and image acquisition system.

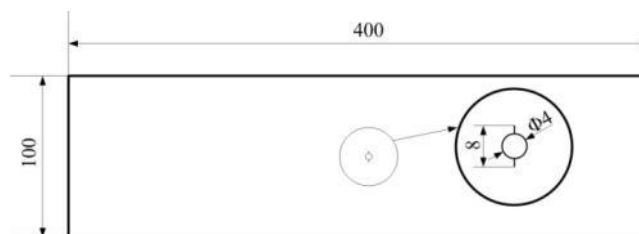


Figure 4-50 Schematic drawing of CCT specimen design(dimensions in mm)



Figure 4-40 Experimental set-up used in the work

The crack growth was paused when fatigue loading cycles are 172062. The reference image is recorded when tiny tension is applied, and the deformed image is recorded when 12kN is applied. Figure 4-41 shows a typical correlated displacement field obtained around a crack.

For the displacement field obtained in Figure 4-41, the flow chart in Figure 4-38 is used to optimize iteratively and finally an exact crack-tip position are obtained at the same time. As shown in Figure 4-42, the found crack-tip position is shown in speckle image. The crack-tip position is transformed into crack length for the convenience of comparison. Then the crack length obtained from crack measurement method is 11.84mm while the crack length obtained from optical measurement is 11.8mm. It can be seen that the crack measurement method has high accuracy in the actual test.

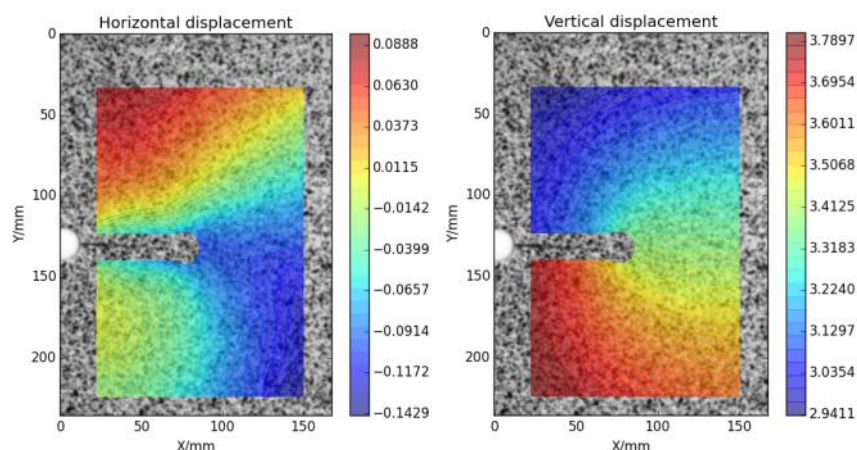


Figure 4-41 Horizontal and vertical displacements in 172062 cycles

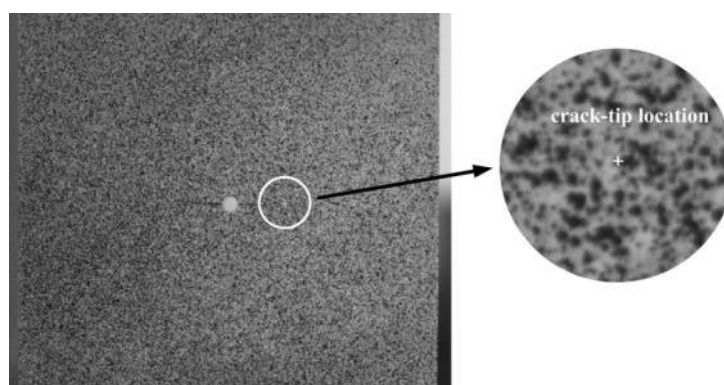


Figure 4-42 the found crack-tip position in speckle image

4.3 VIRTUAL TEST

4.3.1 Virtual test case of static strength of aircraft structure⁶⁰

Virtual assembly and interference inspection technology

Aiming at the problem of interference and collision among high-density loading equipment, test pieces, and supporting frames after the large deflection and deformation of the wing in the high-load static test of the aircraft. On the basis of the design of the lever system, based on the force transmission characteristics and geometric movement relationship of the lever, a movement analysis model of the lever system is established. Based on the simulation deformation of the aircraft structure, the space position coordinates of the loading equipment of each loading step are calculated, and the loading equipment is driven. Motion simulation during the loading process, and collision detection between the test piece, loading system and support system during the loading motion process can effectively find collision interference problems and provide technical support for the design and implementation of the experiment.

⁶⁰AVIC Aircraft Strength Research Institute. Chang Liang: changliang4201@aliyun.com

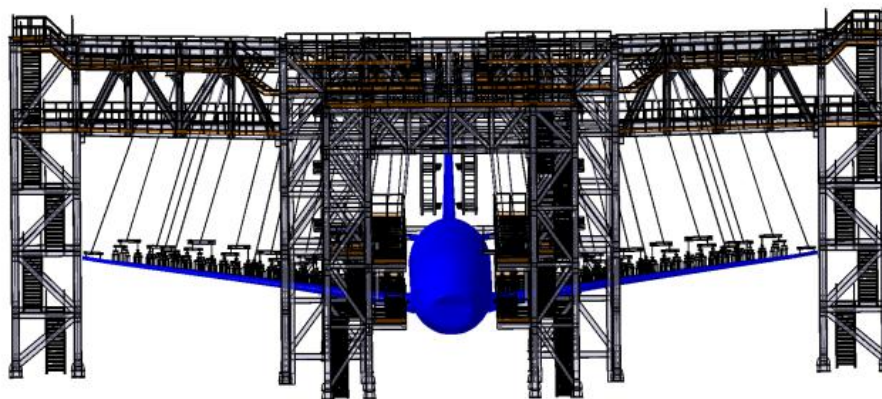


Figure 4-51 Initial state virtual assembly model

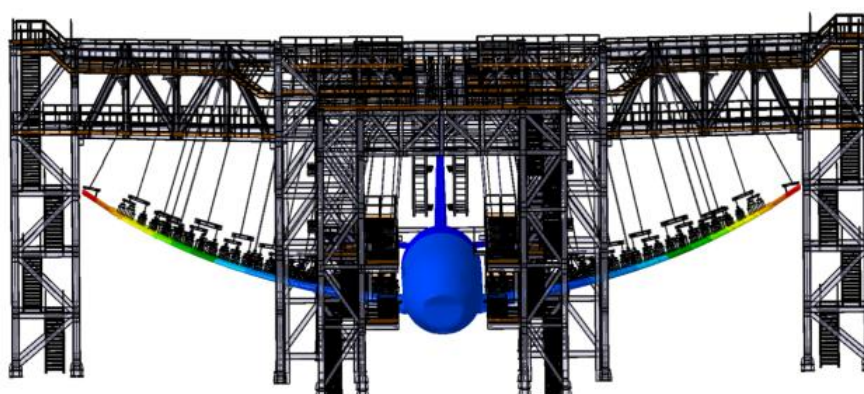


Figure 4-52 Final state virtual assembly model

Analysis technology of post-buckling bearing capacity of stiffened wall structure

In view of the problem that it is difficult to accurately simulate the failure process of complex engineering structures, the high-stress compression zone between the 13-20 intercostals of the wing is selected as the assessment section in the entire aircraft model, and two intercostals on both sides are taken as the transition section, and the establishment of refinement is limited. Meta model. The grid size of the assessment area is about 10mm. Each structure of the upper wall slab adopts BUSH elements to simulate nail elements. Considering the contact relationship, other structures are still connected by common nodes. The mesh transition is coordinated in the transition zone, the overall boundary conditions and wing loads are applied, the elastoplasticity of the metal material and the geometric nonlinearity of the structure are considered, and the arc length method is used for post-buckling analysis, which can accurately predict the failure process of the structure in the test.

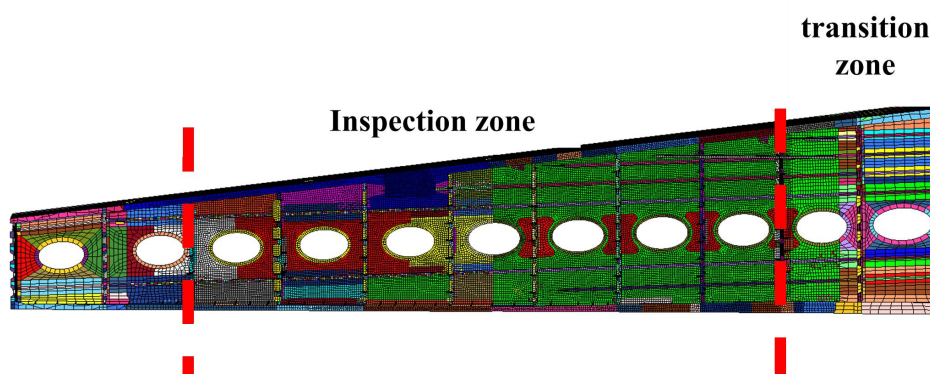


Figure 4-53 Wing detailed finite element model

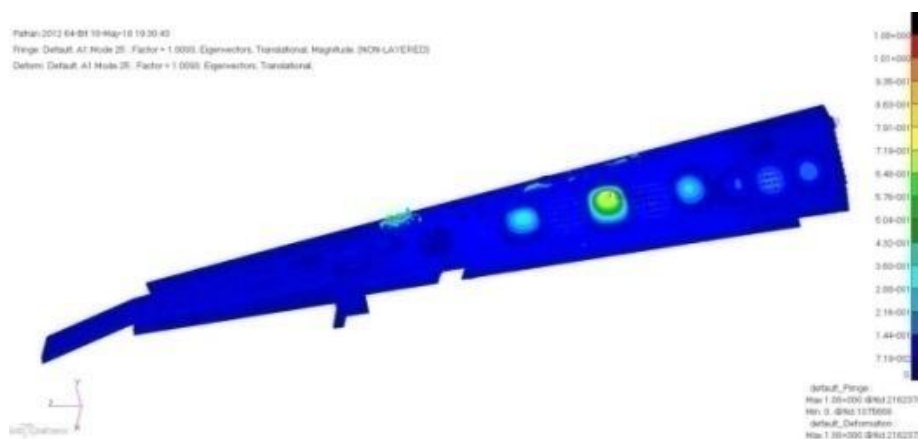


Figure 4-54 Wing instability calculation results

Virtual monitoring and real-time warning technology

Aiming at the problem of unanticipated damage risks in the high-load test of the aircraft, using the accumulated massive strength test data, carry out the research on the cluster classification method of the test data based on machine learning and the comprehensive evaluation technology of the consistency of the test and analysis results, and establish the test data anomaly Judgment algorithm library. Comprehensive utilization of real-time screening test data and comparative evaluation results with virtual tests can effectively screen out dangerous parts, monitor and warn tests, and reduce test risks.

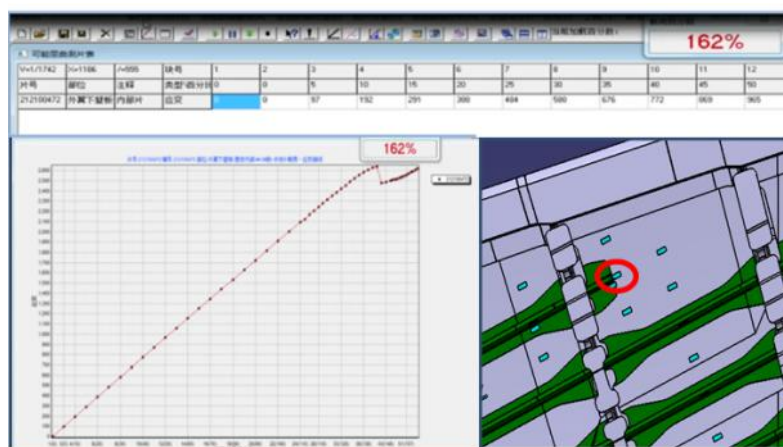


Figure 4-55 Test real-time monitoring and early warning

4.3.2 Evaluation of Residual Stress and Fatigue Life of Large-Diameter Lug with Cold Expanded Bushing⁶¹

Three important issues are the focus in this study. (a) Residual stress distribution: Stress-strain curve in installation process is obtained by 3D FE analysis which is confirmed by test. (b) Fatigue life evaluation method: By considering the effect of residual stress, the stress distribution of the expanded hole is studied to choose appropriate fatigue analysis model. The predicted fatigue life is confirmed by fatigue test. (c) The optimization technique: The cold expanded bushing parameter of the main

⁶¹AVIC Chengdu Aircraft Design & Research Institute. ZHANG Zhixian: zzx30348@qq.com

bulkhead lug of some aircraft is optimized by the above approaches.

The main results in this work are as follows:

- The stress-strain curve in the installation process can be accurately obtained by FE simulation, and the residual stress of cold expanded hole is lower and the residual stress affected zone is also smaller at entrance face than those at exit face.
- The entrance face of cold expanded hole is fatigue critical location, because the stress in the entrance face is higher than that at other thickness positions after loading.
- When the interference increases, the stress around the lug hole decreases obviously and the fatigue life increases greatly.
- The simulation results are in good agreement with test results. It is indicated that the FE simulation method and fatigue life assessment is reliable.

Residual stress distribution

Hoop residual stress distribution in the installation process obtained by FE simulation is shown in Figure 4-56.

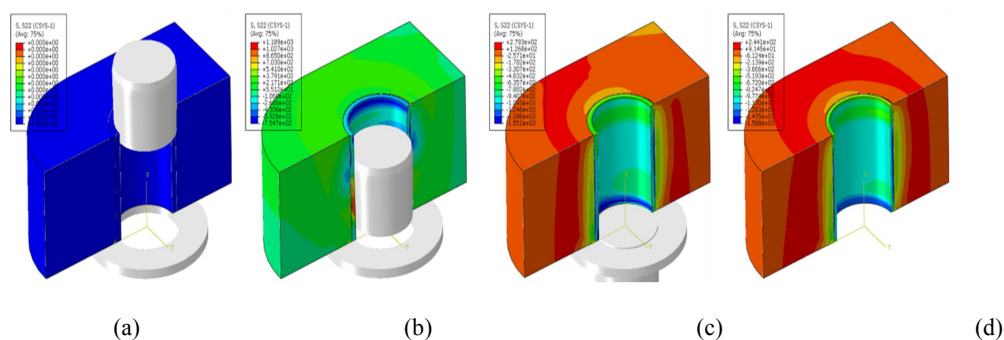


Figure 4-56 Hoop residual stress distribution (a) in the initial state, (b) in the cold expansion process, (c) after cold expansion and (e) after reaming (sectional view)

Hoop residual stress distribution of cold expanded hole after reaming is shown in Figure 4-57. It can be inferred that the bushing shrinks after reaming because its stiffness decreases, and the residual stress affected zone expands.

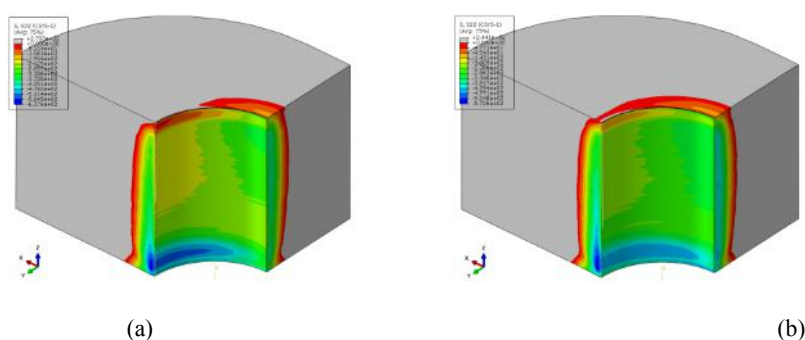


Figure 4-57 Hoop stress distribution of cold expanded bushing hole (a) before reaming and (b) after reaming (sectional view)

Hoop residual stress distribution at different thickness positions in the radial direction is shown in Figure 4-58. It can be concluded that the hoop residual stress in the entrance face is smaller than that at other thickness position. The residual stress affected zone is about 7 mm thick in the radial direction at

entrance face. It is about 10 mm thick in the other thickness position.

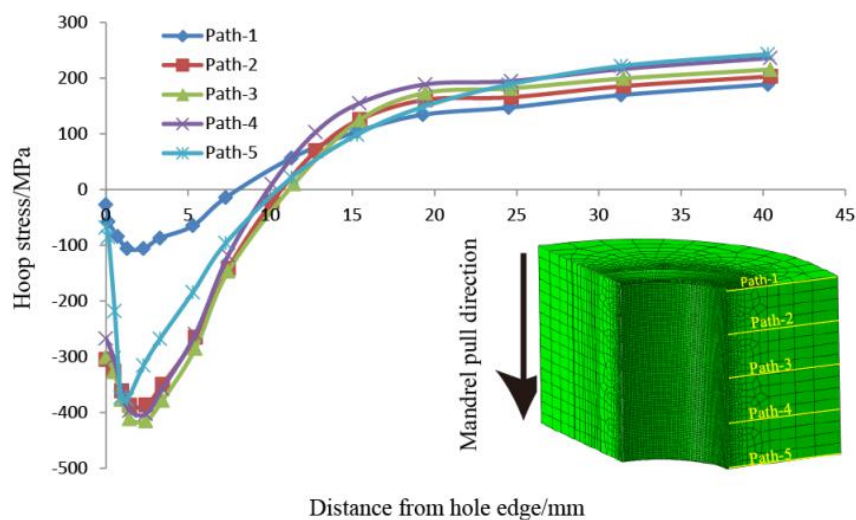


Figure 4-58 Hoop residual stress distribution of lug hole in the radial direction

The values of strain gauges obtained by FE simulation and test in the mandrel pulling process are shown in Figure 4-59. The FE simulation results agree well with the test results.

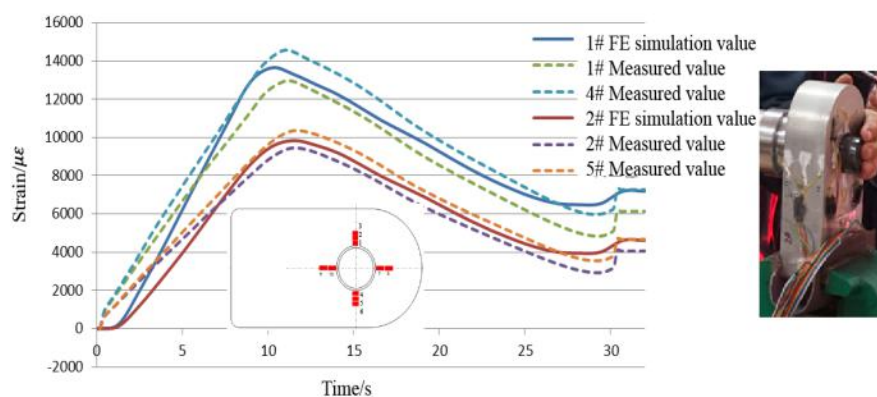


Figure 4-59 Comparison of strain from FE simulation with the measured strain in cold expansion process

Fatigue life evaluation

Local stress-strain method is used to evaluate the fatigue life. Firstly, the load-stress relation is obtained by FE simulation. The load spectrum is converted into stress spectrum as shown in Figure 4-60.

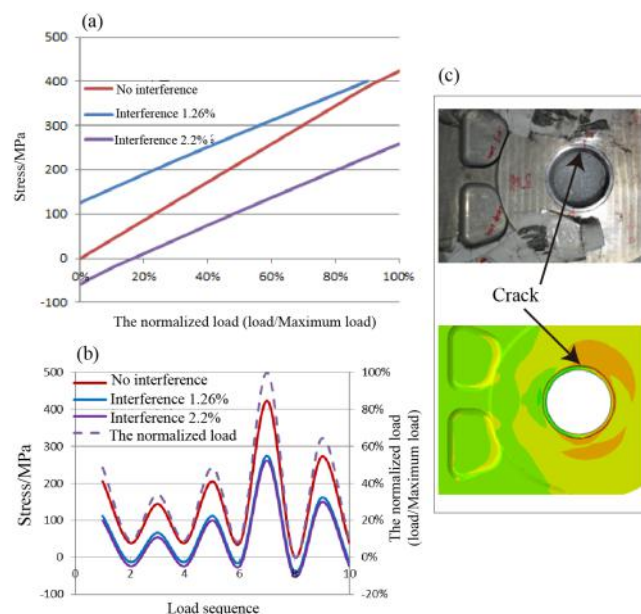


Figure 4-60 (a) Stress spectrums versus load spectrum, (b) stress versus load sequence, the normalized load versus load sequence, (c) Crack initiation site at bushing hole

According to the fatigue test data, the parameter is optimized. Fatigue life of lug with different interference is shown in Figure 4-61. The simulation results are in good agreement with test results. It is indicated that the FE simulation method and fatigue life assessment is reliable.

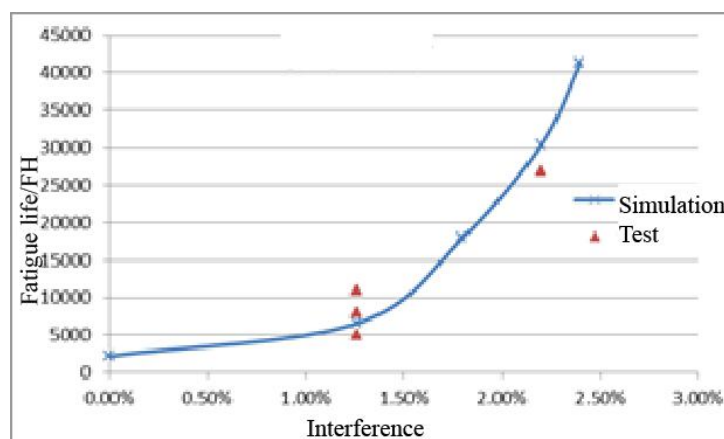


Figure 4-61 Fatigue life of lug with different interference

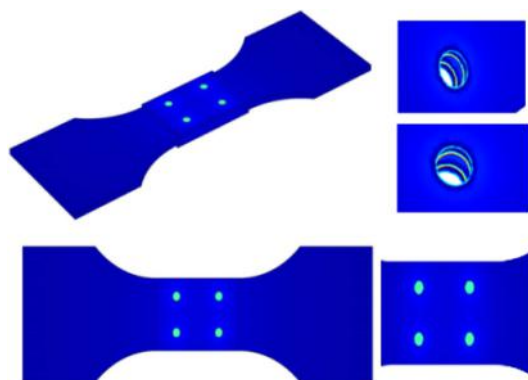
4.3.3 Research on Typical Structure Corrosion Simulation Technology of Carrier Aircraft ⁶²

For aluminum alloy lap joint, because the bolt is titanium alloy, the potential difference between them is large, so the corrosion part mainly appears at the nailing hole where the bolt is in contact with the aluminum alloy substrate. Corrosion occurs to a large extent and is the most easily used as a source of fatigue during fatigue testing. Although the potential difference between the composite and the aluminum alloy is smaller than that between the aluminum alloy and the titanium alloy bolt, the area of the composite is larger and the galvanic corrosion acceleration effect is more obvious.

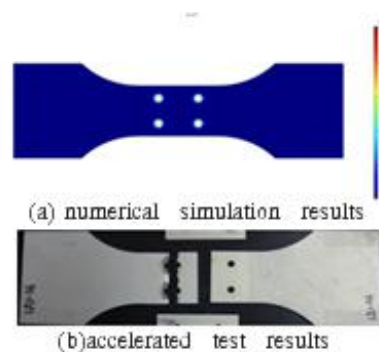
Corrosion Simulation Analysis of Aluminum Connector

⁶²AVIC Shenyang Aircraft Design & Research Institute. CHEN Liang: 5692864@qq.com

Visualization of corrosion potential distribution is shown in Figure 4-62. The electric current density of galvanic corrosion in different parts is predicted. The results are shown in Figure 4-63.



(Figure 4-62)



(Figure 4-63)

Figure 4-62 Visualization of corrosion potential distribution prediction

Figure 4-63 Numerical simulation results and Comparison of Accelerated Test Results

The distribution of current density and acceleration test results are obtained by numerical simulation respectively as shown in Figure 4-64 shows that for aluminum alloy lap joint, because the bolt is titanium alloy, the potential difference between the two is large, so the corrosion site mainly appears at the nailing hole where the bolt is in contact with the aluminum alloy substrate. Corrosion occurs to a large extent and is the most easily used as a source of fatigue during fatigue testing.

Figure 4-64 shows the result of current density distribution, that the current density of the contact position between the aluminum alloy plate lap face and the titanium alloy bolt is high. The corrosion deformation of titanium alloy bolts and aluminum alloy plates was predicted by using deformation geometry after the 2-D section, and the results are shown in Figure 4-65(a). At the same time, the corrosion deformation was predicted by using deformation geometry after 1 year of pre-corrosion, and the maximum deformation was $12\mu\text{m}$ in contact position between aluminum alloy and titanium bolt, as shown in Figure 4-65(b).

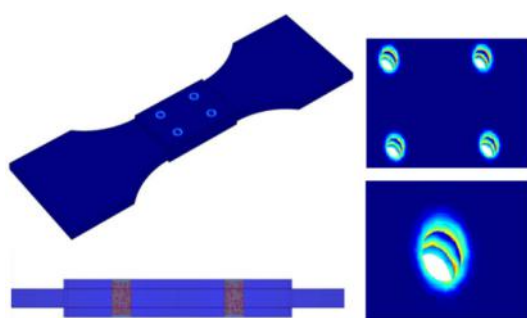


Figure 4-64 Distribution of corrosion current density

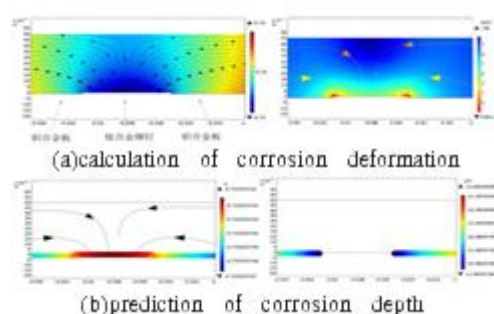


Figure 4-65 Corrosion deformation and depth prediction

Corrosion simulation analysis of aluminum complex connections

Visualization of corrosion potential distribution is shown in Figure 4-66. The electric current density of galvanic corrosion at different parts is predicted. The results are shown in Figure 4-67. The corrosion deformation is predicted by using deformation geometry after the 2-D section of the aluminum complex joint, and the results are shown in Figure 4-68.

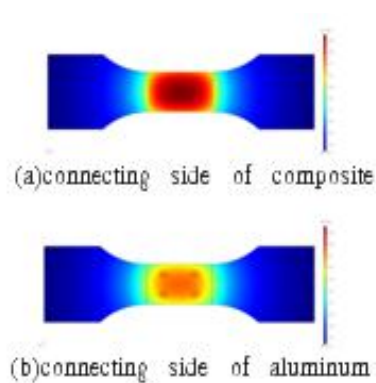


Figure 4-66 Prediction of corrosion potential

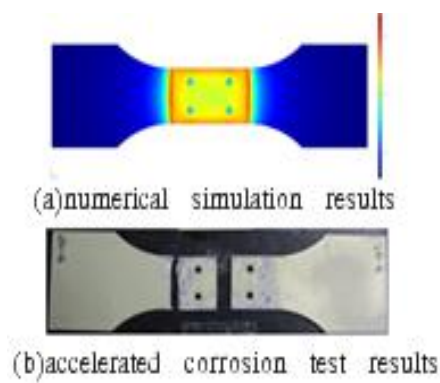


Figure 4-67 Prediction of corrosion potential

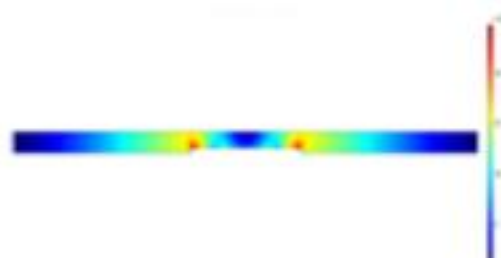


Figure 4- 68 Prediction of Cross Section Corrosion Deformation of Specimen

The comparison between simulation results and test results in Figure 4-66 shows that the potential difference between composite and aluminum alloy is smaller than that between aluminum alloy and titanium alloy bolt, but the area of composite material is larger and the acceleration effect of galvanic corrosion aluminum alloy is more obvious. Especially for the side of the composite material, the galvanic effect between the composite and the aluminum alloy is more obvious. The predicted results in Figure 4-67(a)show that the current density is the highest at the junction of aluminum alloy and composite material. At the same time, the results of accelerated corrosion tests in the laboratory are shown in Figure 4-67 (b).

Figure 4- 68 shows that the maximum deformation position of the composite specimen is consistent with the maximum current density, and is located at the joint between the composite and the aluminum alloy. It also shows the accuracy and consistency of numerical simulation.

5. STRENGTH TESTING AND VERIFICATION ON AERONAUTICAL FATIGUE AND STRUCTURAL INTEGRITY

5.1 TESTING TECHNOLOGY

5.1.1 Simulation Analysis Method of Water Load and Key Technology of Special Structure Strength Test for Large Amphibious Aircraft⁶³

This research solves the key technology of water load simulation analysis of large amphibious aircraft and the difficult problem of applying strength test load of special structure of large water and land Amphibious aircraft, and forms the simulation analysis method of wave state water load, the simulation

⁶³ AVIC Aircraft Strength Research Institute. ZHUO Yi: zhuoyid@163.com

method of unsteady load distribution under the second condition of landing water, and the simulation analysis method of water load of water tank structure. The strength test technology of high pillar statically determined landing gear, the water load application technology of ship bottom fuselage and the load simulation application technology of fuselage water tank are put forward.

Simulation and analysis technology of water load of large amphibious aircraft

The situation of landing sea of large amphibious aircraft is changeable, the structure of landing area is complex, and the landing area is large, which poses a great challenge to the simulation analysis. In this paper, LS-DYNA finite element software is used to simulate and calculate the water load and the response characteristics of water tank of large amphibious aircraft.

The simulation analysis method of water load in wave state is formed. In view of the changeable landing and sea conditions, the complex structure of the landing area and the large landing area, the reference domain is introduced into the material domain and the spatial domain to solve the possible serious distortion of the material under the description of Lagrange and the complexity caused by moving the boundary under the description of Euler. The pressure distribution of the bottom of the ship under different sea conditions is obtained by simulation analysis.

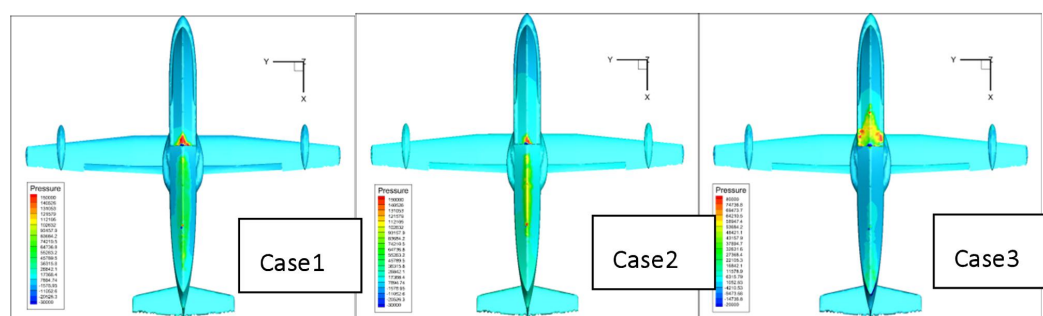
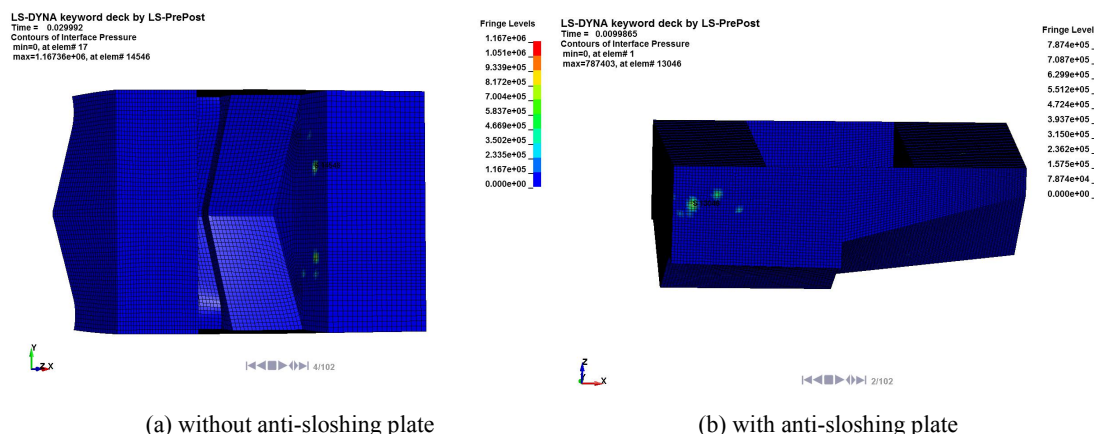


Figure 5-1 The pressure distribution at the bottom of the ship under different water conditions

The simulation analysis method of water load of water tank structure is formed. ALE and FVM methods are used to simulate and analyze the load distribution of water tank in flight state. The influence of installation of anti-sloshing plate on water load under different normal overload is studied. The results show that the anti-sloshing plate slows down the movement of fluid to a great extent, thus reducing the maximum contact pressure on the wall plate of water tank and optimizing the structural design.



(a) without anti-sloshing plate

(b) with anti-sloshing plate

Figure 5-2 Cloud image of water tank pressure distribution with/without anti-sloshing plate

Special structure test technology of large amphibious aircraft

In order to ensure its functional characteristics, the large amphibious aircraft has special-shaped structures such as V-shaped hull, broken fuselage, high pillar statically determined landing gear, large thin-wall water tank and so on. At the same time, the large-scale amphibious aircraft has been used in high humidity, heat, salt fog marine environment and other harsh environments for a long time, so it should not only bear the inherent aerodynamic load and ground load of ordinary land-based aircraft. It also has to bear the water load caused by the take-off, landing and navigation of the aircraft on the surface of the water. The load situation is diverse and the load distribution is complex. The special-shaped structure and complex load pose a serious challenge to the strength test load simulation of large amphibious aircraft structure. The conventional test loading technology and boundary constraint technology cannot meet the test requirements. The main technical achievements are as follows:

The water load simulation and application technology of large amphibious aircraft. According to the characteristics of ship bottom structure and water load of large amphibious aircraft, the feasibility and accuracy of applying compression load to V shape structure of ship bottom by loading technology such as tape belt, pull pressure pad, airbag and wooden mold are studied, the technical requirements of compression load application of complex shape structure are determined, the large area continuous compression load application technology is broken, and a superplastic sandwich loading technology is put forward. The results of load application are close to the real load part, which meets the simulation requirements of hydrodynamic load test of amphibious aircraft.



Figure 5-3 Simulation water load on fuselage hull surface

The load simulation and application technology of water tank for large amphibious aircraft. According to the structural characteristics of the fuselage water tank of large amphibious aircraft, the load distribution law of the fuselage water tank of large amphibious aircraft during the process of drawing water, flying and pouring water is analyzed in this paper. The serious load condition of water tank structure is determined: the load simulation method of water tank structure with water overload flight condition is studied. According to the distribution of fuselage water tank and the characteristics of water tank wall structure, a pressure compensation load application technology is proposed to solve the problem of water load application under overload flight condition of fuselage water tank of water and land amphibious aircraft.

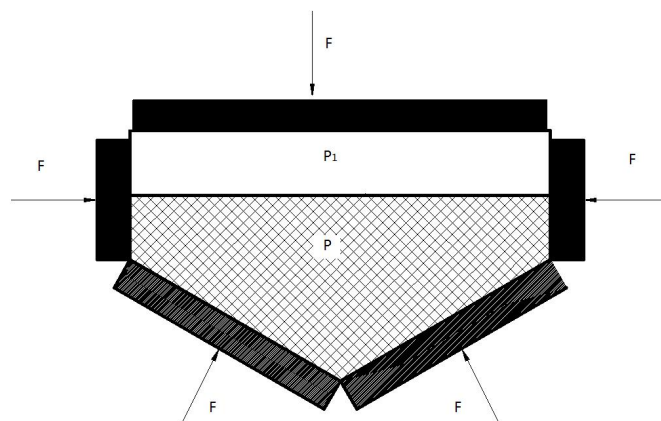


Figure 5-4 Water filling and charging test of hull bottom

The static strength test technology of high pillar statically inconstant landing gear. The boundary support stiffness simulation and mechanical boundary simulation experiments based on numerical simulation are put forward, which realizes the real distribution of the load under the statically determined connection between the landing gear and the fuselage and the accurate application of the structural load of the high pillar landing gear, and solves the difficult problem of the static strength experiment of the high pillar statically inconstant landing gear. On this basis, a self-balancing experimental device which integrates modularization, multi-function and universality is developed, and the static strength experiments of eight kinds of main landing gear of the large amphibious aircraft are completed, which effectively supports the smooth completion of the first flight on land of the large amphibious aircraft.

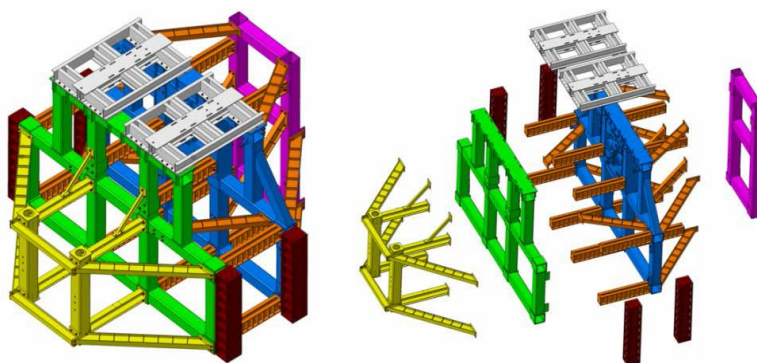


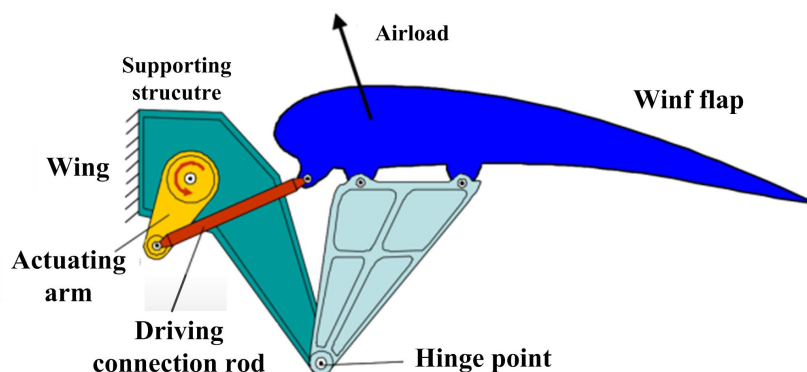
Figure 5-5 Modular, self-balancing experimental bench

5.1.2 A Function Reliability Test Technology of The Dropped Hinge Wing Motion Mechanism⁶⁴

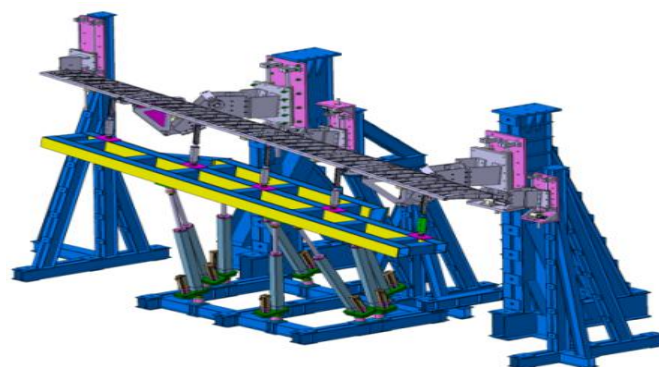
As shown in Figure 5-6 (a) is an advanced transport aircraft flap named dropped hinge flap which has simple structures with light mass and high reliability. In order to study its motion function reliability, the authors need to design a test set-up which can simulate air loads including lift and drag loads thought the whole flight course. However, the dropped flap has a much larger motion range when it moves from retract state to deploy-out state. This motion process is a kind of three-dimensional motion. It makes it is difficult to simulate air load. Traditional uniaxial actuator loading and biaxial actuator synthetic loading technology is hard to meet the test requirements.

⁶⁴ AVIC Aircraft Strength Research Institute. LI Sanyuan: 673457488@qq.com

To solve this problem, the eight-axis six-degree-of-freedom platform is used in this set-up as shown in Figure 5-6 (b). It is installed below the flap. This platform consists of a moveable steel frame, eight cylinders and a steel base. That attached between the flap and moveable steel frame are multiple parallel actors, the angle between which and the flap varies with the deflection of the flap. These actors are used to generate load distributions.



(a) Dropped hinge Wing Motion Mechanism



(b) Test set-up for Dropped hinge Wing Motion Mechanism

Figure 5-6 Function reliability test for the dropped hinge wing motion mechanism

5.1.3 Deformation Measurement Technology in Complex Environment⁶⁵

Compared with the contact high temperature strain measurement method, the digital image correlation method has become an ideal strain measurement method in the thermal environment simulation test because it can easily combine various heating equipment, and has the advantages of simple measurement process, high accuracy and full field thermal deformation measurement.

The ultraviolet three-dimensional digital image correlation method is an optical measurement method which can be used to measure the three-dimensional shape, displacement and deformation of object surface in extremely high temperature environment, its specific principle is as follow. Any object whose temperature is higher than absolute zero will emit thermal radiation, but when the temperature is low, the radiation intensity is small and the thermal radiation wavelength is mostly infrared light, which cannot be detected by human eyes and cameras. However, with the increase of temperature, the intensity of thermal radiation will be higher and higher. Wien's displacement law shows that with the

⁶⁵ AVIC Aircraft Strength Research Institute. Zheng Yao: zyroobben@sina.com

increase of temperature, the peak wavelength of thermal radiation will gradually move to the direction of short wavelength. Thus, the object radiates visible light that can be monitored by human eyes and cameras, resulting in a significant change in image brightness. The quantitative relationship between thermal radiation intensity and temperature can be described by Planck's blackbody radiation formula:

$$I(\lambda, T) = \frac{2hc^2}{\lambda^5} \frac{1}{e^{hc/\lambda kT} - 1}$$

Where $I(\lambda, T)$ is the radiation intensity expressed by wavelength λ and temperature T , h is Planck constant, c is the speed of light in vacuum, and k is Boltzmann constant. It can be seen from the above formula that the thermal radiation intensity of an object is a function of temperature and wavelength. Here, we select several specific temperatures to obtain the relationship between the radiation intensity and wavelength at different temperatures. Figure 5-7(a) shows the relationship curve between the thermal radiation energy and wavelength at 800°C, 1000°C, 1200°C, and 1400°C. The figure shows that with the increase of temperature, the intensity of the thermal radiation will gradually increase, and the range of visible light band changes greatly, which is the reason of the over exposure of ordinary optical imaging system. Therefore, we need to use the band-pass filter imaging technology to suppress this high temperature thermal radiation. In order to realize the measurement in extremely high temperature environment, we can use a narrow-band pass UV filter of 365nm±10nm. From Figure 5-7(a), we can see that the ultraviolet band-pass filter in this band effectively suppresses the influence of thermal radiation in infrared and visible bands. But the thermal radiation intensity does not change in the ultraviolet acquisition band, which ensures the stability of the collected image brightness. As shown in Figure 5-7(b), compared with the 450nm blue light band and 365nm ultraviolet band used in traditional DIC measurement, it can be found that with the increase of temperature, especially above 1400°C, the inhibition effect of ultraviolet band on thermal radiation is significantly higher than that of blue light band. Therefore, using ultraviolet light for image acquisition can better avoid the "decorrelation effect" caused by the change of image brightness, so as to achieve accurate measurement at higher temperature.

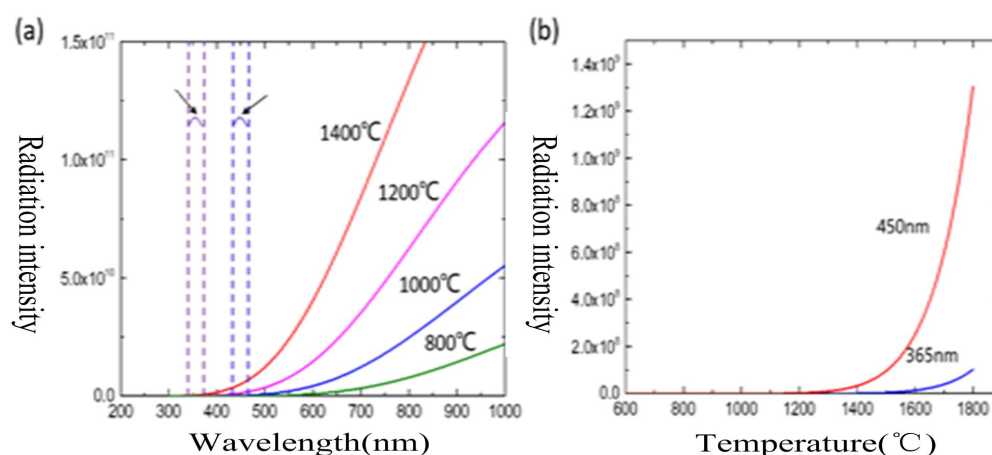
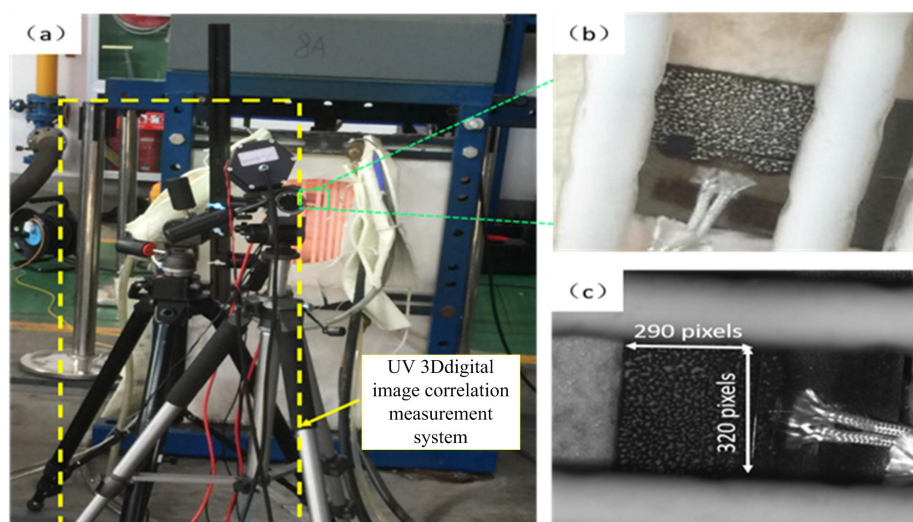


Figure 5-7 Relationship between spectral radiation and temperature: (a) Relationship between thermal radiation intensity and wavelength at different temperatures, (b) Curve of thermal radiation intensity with temperature in ultraviolet and blue light



(a) High temperature deformation measurement test site; (b) Enlarged drawing of measuring area;
(c) Surface of specimen collected by UV camera

Figure 5-8 Ultraviolet 3D digital image change measurement system

For the thermal deformation measurement of the specimen heated by the quartz lamp radiation, the self-designed UV three-dimensional digital image correlation system can effectively suppress the influence of the strong thermal radiation of the quartz lamp, so as to collect the stable and reliable surface image of the specimen. The data of displacement field and strain field obtained by DIC calculation are similar to the standard values recorded in the material manual. Compared with the traditional strain gauge and FGB sensor measurement methods, the UV three-dimensional digital image correlation method has great advantages in measurement accuracy and reliability, and this method can realize the whole field displacement and strain measurement, which is of great significance for the visibility of measurement results and the whole field displacement and strain monitoring.

5.1.4 Bidirectional Rigid Loading Technology and Its Application in Full-Scale Aircraft Fatigue Test⁶⁶

The main research contents of the bidirectional rigid loading technology include: how to make the tension-compression pads have good adaptability to the various contours of the aircraft, and are easy to paste and install; what kind of structure and connection form can be adopted in the lever system to reduce the stress concentration of each part, and the structure can be light, easy to manufacture, convenient to install at the same time; what kind of connection form between the levers can reduce the overall height of the lever system, but also can ensure the degrees of freedom so that it doesn't limit the deformation of the test sample, at the same time the lever system doesn't release too many degrees of freedom so that its loading stability and accuracy can be ensured.

Design of tension-compression pad on curved surface and vulcanization technology of rubber

Tension-compression pads on curved surface are mainly composed of single ears, bolts, aluminum blocks, bushings, rubber or polyurethane blocks, etc. A bushing structure is added to the connection between tension-compression pad and single lug for the first time, as shown in Figure 5-9. The new design form avoids the material and strength discordance between threads, and eliminates the risk of

⁶⁶ AVIC Aircraft Strength Research Institute. ZHANG lei: stone3506506@163.com

pull-out of thread of aluminum block on tension-compression pad in long-term fatigue test. The rubber of tension-compression pad of curved surface is processed by numerical control, which perfectly fits the curved surface of nodes; with the use of the vulcanization mold, the curvature of the surface of the rubber can be completely consistent with the surface of the aluminum block; and with the development of universal rubber vulcanization mold for curved surface tension-compression pad, the rubber can be vulcanized at once, which greatly reduces the test cost.

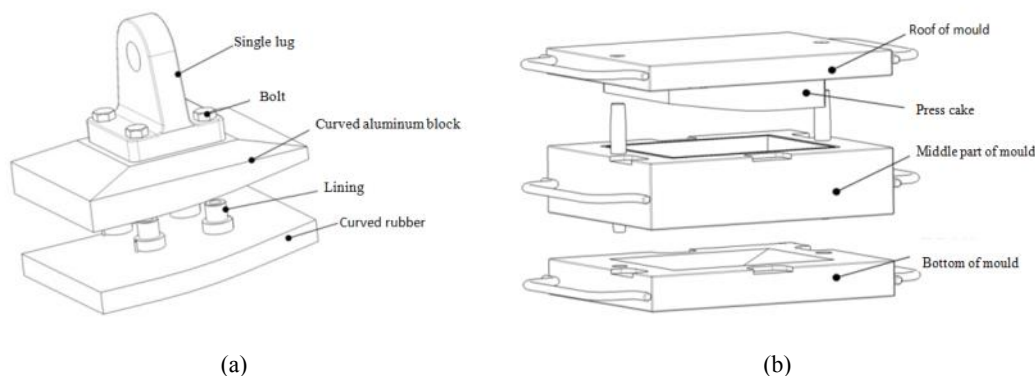


Figure 5-9 Design of surface tension-compression pad and rubber vulcanization mold (a) structure drawing of curved surface tension-compression pad (b) structure drawing of Curved surface tension-compression pad mold

The fatigue test time usually can be very long and environment of the test is complex. To ensure the stability and reliability of the tension-compression pad in the fatigue test for several years, the selection of rubber, aluminum block, adhesive and bonding process are decisive factors. The sail cloth transition mode is used to improve the bonding performance between the tension pad and the test piece, and the vacuum adsorption is studied and adopted the external pressure of the tension pad solves the problem of the pressing during the process of the pressing and pulling, and improves the bonding performance. The canvas is pasted between tension-compression pad and the test piece to improve the bonding performance. The study and adopt of vacuum adsorption technology solves the problem that the demand of pressure when pasting the tension-compression pad, with this technology, the paste performance also improved.

Technology of tension-compression pad-lever system design

The lever system includes three parts: transfer joint, lever and connecting part. The transfer joint connects the lever and tension-compression pad, it can transfers the load on the lever to the tension-compression pad, and feeds back the deformation of the tension-compression pad back to the lever. Therefore, a reasonable design of the lever system would improve the accuracy of test loading and would not affect the deformation of the test piece. The connection between the primary lever and the tension-compression pad adopts a new structure, in which the bearing is installed at one end and a long hole is used at the other end. The single lug of the tension-compression pad is divided into type A and type B. The type A is equipped with a bearing, and the type B has a long hole, as shown in Figure 5-10. The primary lever is connected with the tension-pressure pad lug A through the joint bearing to ensure the degree of freedom of the tension-pressure pad can be rotate with the deformation of the test piece.

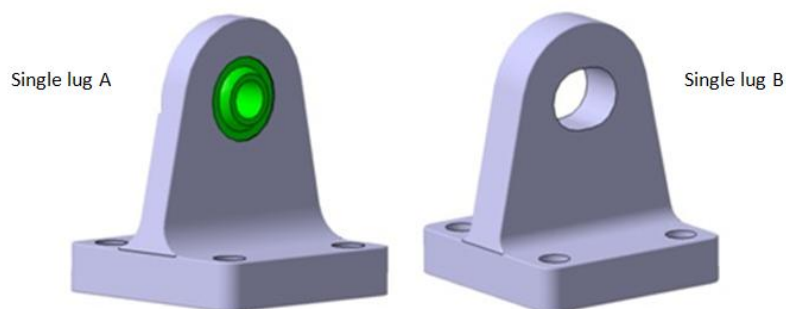


Figure 5-10 Schematic diagram of single lug of tension-pressure pad

The new type of secondary lever is designed with a claw-shaped structure, which is connected with the primary lever through The intermediate pin of the structure, so that the pin and the lever themselves can transmit loads together, which makes the load transmission between the lever systems more reasonable, and increases the safety of the structure. The claw-shaped lever is mainly applied to the connection of the secondary and the primary lever, or the secondary and last lever. The schematic diagram and stress analysis diagram as shown in Figure 5-11. The connection design of the new primary lever system and the tension-compression pad adopts the connection of single lug and double lug, which abandons the connection mode of the traditional lever in which load is transferred on a single pin and makes the load transmission more reasonable.

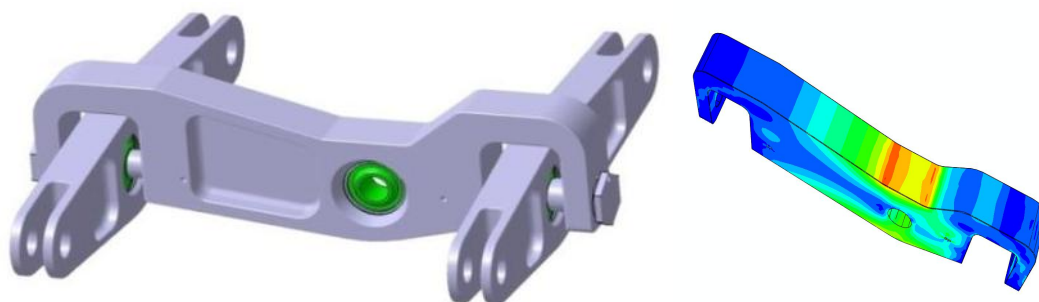


Figure 5-11 Connection and force analysis of new secondary lever system

After the design of the lever system, a typical lever system was selected, and the finite element analysis software was used to model the lever system, simulate the boundary conditions, and analyze the overall deformation, stress and stability. The degree of freedom of joints of the lever system are released according to the real force transmission route. The joints that cannot transfer bending moment were simulated as hinge joints (releasing the bending stiffness of beam element), and the hinge constraints (restraining the translational degrees of freedom of beam element in three directions) were established at the connection between the tension-compression pad at the bottom of the lever system and the aircraft.

5.2 FULL SCALE STRUCTURE STRENGTH TEST

5.2.1 J-10 Fighter Full Scale Durability/Damage Tolerance Tests and Sustainment ASIP⁶⁷

J-10 is China's high-performance fighter, which made its first flight in March 1998. Its designed service

⁶⁷AVIC Chengdu Aircraft Design & Research Institute. WANG Yongjun: renwoxingr2013@aliyun.com

life is 5000Fh (flight hours) with a maximum/minimum normal overload of 9g/-3g.

Structural Design Criteria

J-10 is the first Chinese fighter to carry out durability and damage tolerance structural design criteria. According to the structural strength specification and structural integrity requirements of military aircraft, the structural durability and damage tolerance control plan, the structural integrity master plan were formulated, the fracture critical parts were defined and selected, and the detailed stress/durability/damage tolerance analysis and structural detail optimization design of the fracture critical parts were carried out.

The structural design criteria and analytical methods are detailed in Table 5-1.

Table 5-1 Design Structural Design Criteria

Structure type	analytical methods	Load spectra	Initial flaw size (mm)	Critical size (mm)	Lifetimes
High-strength Steel	Fatigue	Design spectrum	/	/	4~6
Durability critical parts	Durability	Design spectrum	0.127	0.8	1
Fracture critical parts	Damage Tolerance	Design spectrum	1.27	failure	2
	Full-scale durability test	Design spectrum	/	/	3
	Full-scale damage tolerance test	Operational spectrum	Natural/ artificial flaw	/	1

Design load spectrum

Design mission profiles and mission mixes were defined based on the expected usage and design service life of J-10 fighter. Maneuver types of all mission segments and points in the sky (a combination of height, Mach, weight) were defined.

Then, multiple simulations of all maneuvers were completed on the flight quality simulator (FQS), the complete flight parameter history was obtained, and the N_z exceedance curve was acquired through statistical analysis of N_z at the center of gravity.

Further, probability pairing method was used to form the basic maneuver spectrum. Based on the wind tunnel test data, the load distribution of the whole aircraft was calculated. Finally, the flight-by-flight random spectrum for design analysis and test was developed.

The flow of load spectrum development is shown in Figure 5-12.

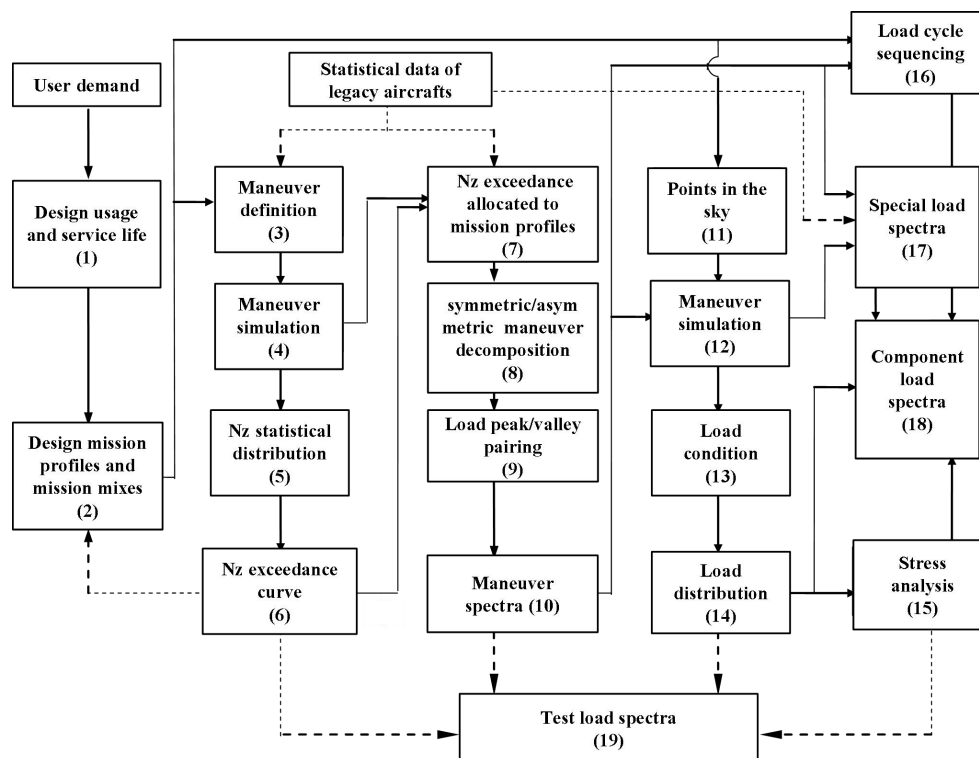


Figure 5-12 The flow of design load spectrum development

Full-Scale Durability and Damage Tolerance Tests

The objective of J-10 full-scale fatigue test was to complete 3 lifetimes of durability test, 1 lifetime of damage tolerance test, residual strength test of components and the whole aircraft, and finally the teardown inspection. The full-scale fatigue test arrangement is shown in Figure 5-13.

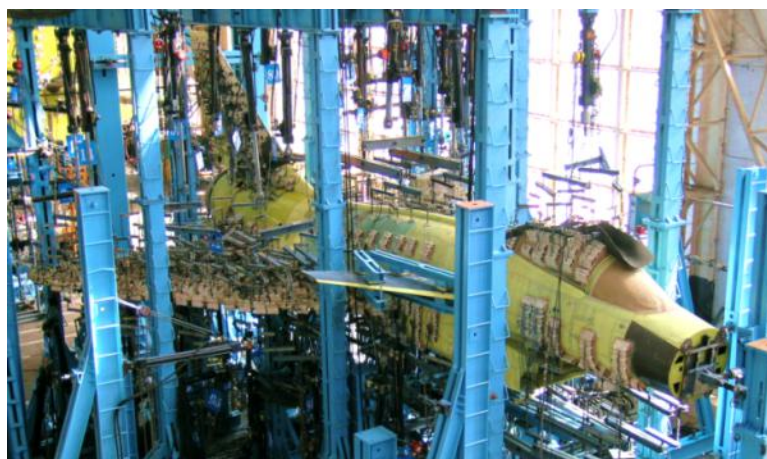


Figure 5-13 The full-scale fatigue test arrangement

Test Constraints

The fatigue test article was supported in the way of floating and statically determinate constraints. The crowbars were used to support the aircraft in the vertical direction of the front and left/right main landing gear. A total of 6 constraint points were set in the landing gear and the fuselage. The support and constraints of the test article are schematically shown in Figure 5-14.

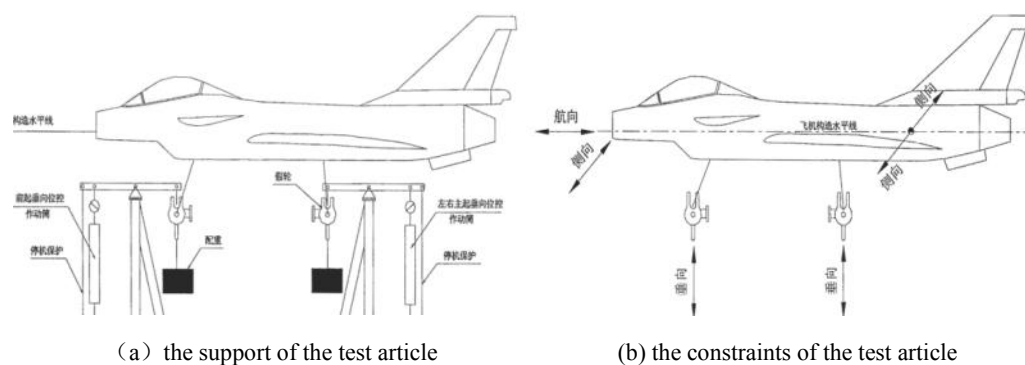


Figure 5-14 The support and constraints of the test article

Test Measurements

There were 106 load channels in the fatigue test, each loading point was equipped with force sensor and was recorded during the whole test. In order to monitor and track status and structural behavior of the testing article, 53 displacement sensors (as shown in Figure 5-15) and 1846 strain gages were arranged. The strain data was measured during the whole test, and the displacement data was measured only under specified load conditions.

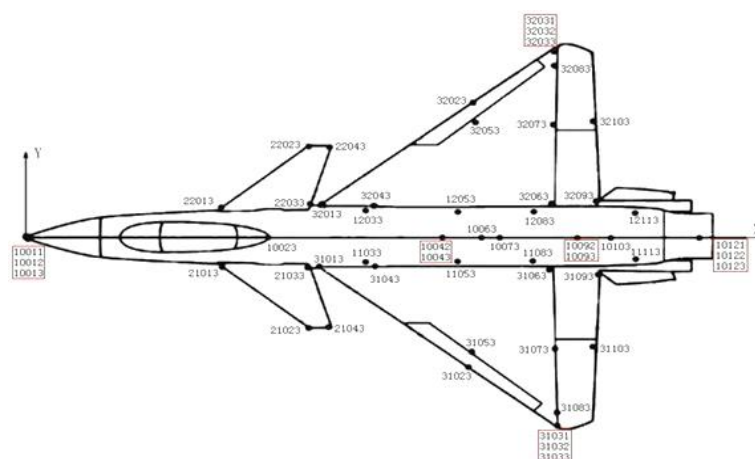


Figure 5-15 Displacement measurements

Test Load Spectra

The fatigue test load spectrum was based on the design load spectrum, which consist of the following eight categories of repeated load sources:

- Maneuvering load;
- Lateral gust and sideslip load;
- Fuel tank pressure;
- Cabin pressure;
- Inlet pressure;
- Landing gear load;
- Engine thrust;
- Resistance parachute load.

The above loads were balanced and coordinated in the fatigue test load spectrum, and were applied in the form of flight-by-flight simulating the expected usage of the aircraft. Every 500 flight hours is one loading block. The test load history of a typical flight is shown in Fig. 3.1-6.

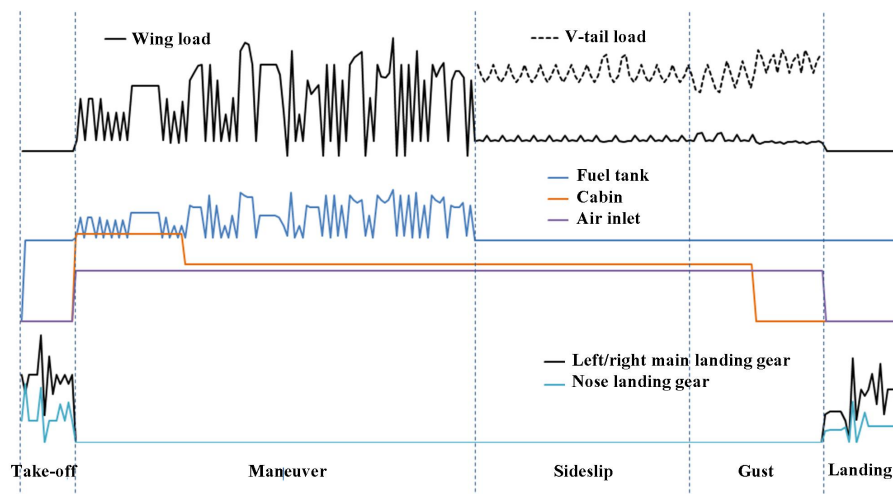


Figure 5-16 Test load history of a typical flight

Durability test

A total of 229 cracks were found on 84 parts in the durability test with 3 lifetimes completed. The accumulation of the number of cracks with test duration is shown in Figure 5-17, in which, there are 6 critical parts with 19 cracks, and 9 important parts with 26 cracks.

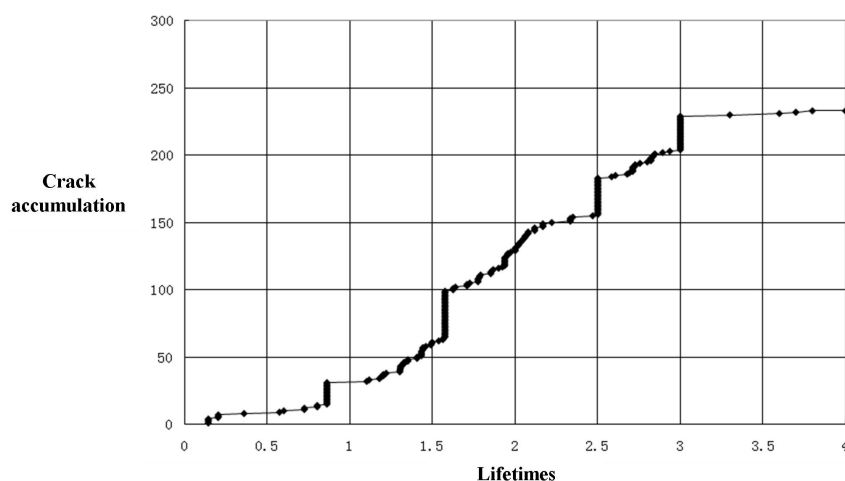


Figure 5-17 Crack accumulation

For the fatigue critical locations exposed in fatigue test, structural repairs (for testing article, fielded aircraft, and aircraft in manufacture) and modifications (for subsequent aircraft) were established, and comparative verification through fatigue life evaluation and necessary supplementary tests were carried out. Typical structural cracks are illustrated in Figure 5-18 and Figure 5-19.

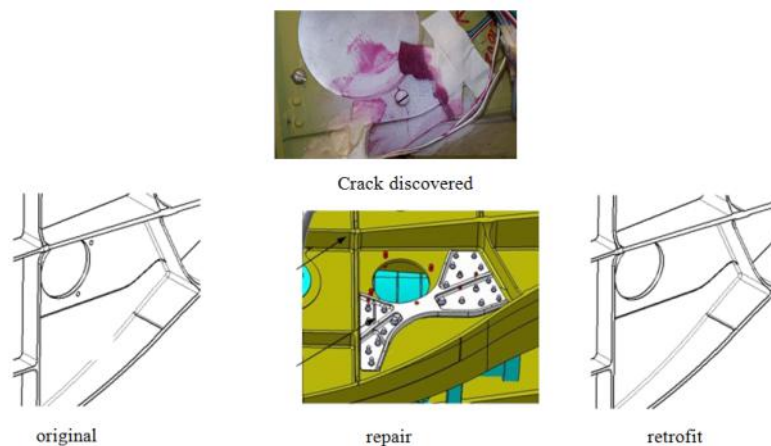


Figure 5-18 Crack of bulkhead system attach hole and repair/modification

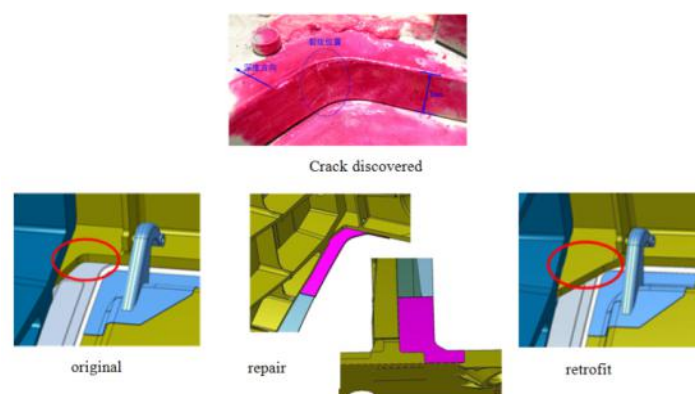


Figure 5-19 Crack of main landing gear side beam and repair/modification

Damage tolerance test

Prior to the damage tolerance test, the high stress area was identified according to the detailed stress analysis of the main bulkhead, main beam and critical joints, and artificial flaws with certain shapes and sizes were preset. Figure 5-20 shows the artificial cut of the canard rotating shaft beam. A total of 24 cracks were prefabricated on the whole structure and monitored in the damage tolerance test together with the natural cracks formed during the durability test.

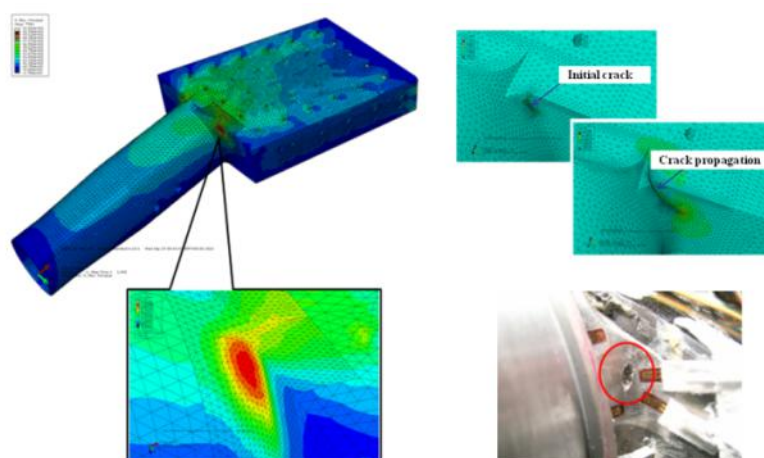


Figure 5-20 Analyses and artificial flaw of canard rotating beam

During the damage tolerance test, 4 natural cracks and 2 artificial flaws on 4 critical parts propagated. The details are listed in Table 5-2.

Table 5-2 Crack propagation in damage tolerance test

No.	structure		Crack shape	Initial size	Final size
1	Fuselage	Bulkhead A	Natural crack	19mm	25mm
2				8mm	23mm
3		Bulkhead B	Natural crack	10mm	18mm
4		Beam C	Natural crack	7mm	9mm
5	wing	3#lower panel	left	1.5mm	3mm
6			right	1.5mm	3mm
			1/4circle corner crack		

Residual strength test

After the crack growth test was completed, residual strength tests (limited loads) for canard, front fuselage, wing/middle fuselage, vertical tail/rear fuselage, and front/main landing gear supporting structures were completed respectively, all of which satisfied the residual strength capability requirements. Structural damage after the failure load test is shown in Figure 5-21.



Figure 5-21 Structural damage after failure load

Teardown inspections

After the residual strength test, a deliberate teardown inspection of the test article was carried out, as shown in Figure 5-22. NDI and fractographic examinations of critical areas were conducted. 23 new cracks were discovered in the metal structure, including 6 critical parts cracks, 6 important parts cracks, 11 general parts cracks, and 6 new damages were found in the composite structure.



Figure 5-22 Disassembly of the test article

Test data management and analysis

For ease and efficiency of use of test data and timely guidance on nondestructive inspection during the test, a test data management and analysis system was developed, as shown in Figure 5-23. All damage findings discovered in the test were classified and managed, and real-time analysis of strain measurement data, anomaly warning and damage prediction were conducted.

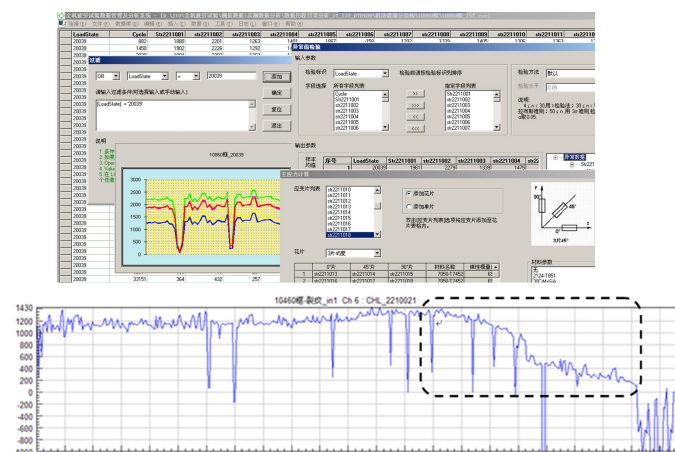


Figure 5-23 Test data management and analysis

Operational load spectrum

The operational usage of fielded aircraft is continuously tracked. Data processing and fatigue load analysis of nearly 100'000 flights were completed, and the operational load spectra reflecting the severe usage and average usage of the fleet were developed. The comparison between the operational spectrum and the design spectrum is shown in Figure 5-24.

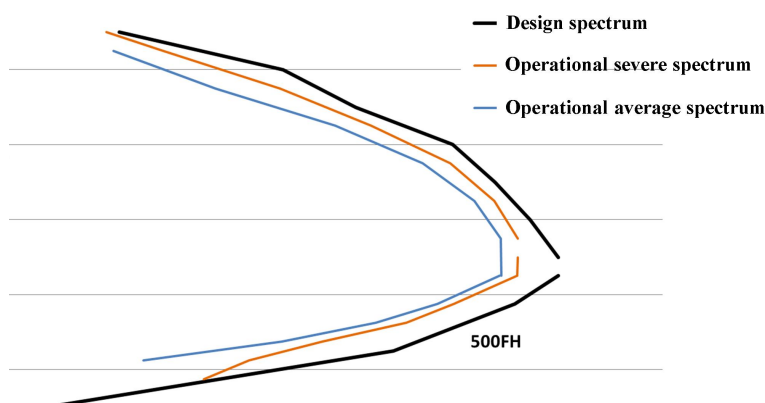


Figure 5-24 N_z exceedance curves of the operational spectrum and the design spectrum

Force structural maintenance plan update

According to the results of finite element analysis, full-scale durability and damage tolerance test and the usage/maintenance of aircrafts in service, the critical areas were selected and identified. Based on the full-scale durability test, combined with the durability analysis of critical parts and the test results of representation coupons, the generalized correction method was used to evaluate the service life under the operational severe spectrum. Then the structural maintenance plan of J-10 series aircraft was adjusted and updated: overhaul time of each critical part is determined and structural repair/modification/replacement is established.

Individual aircraft tracking

Taking into account the differences in structure, operational usage and maintenance of individual aircraft in service, system development of IAT characterized by fatigue damage monitoring of critical parts were carried out. In-depth research has been carried out on techniques such as parametric load models, load-stress equations, individual load spectrum development, damage assessment and residual life prediction. The more accurate monitoring of structural damage status has been realized, which makes the force life management more scientific and refined. The technical process is shown in Figure 5-25.

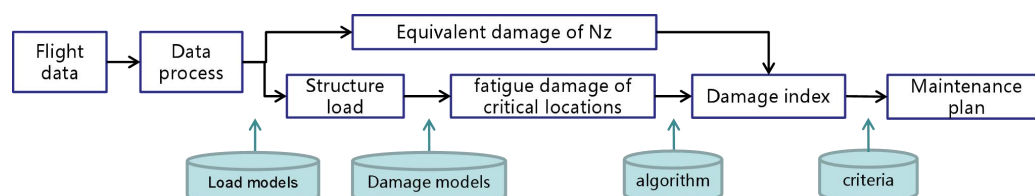


Figure 5-25 The flow of individual aircraft tracking

Structural health monitoring

Structural health monitoring (SPHM) system design adopts the method of "on-board measurement, ground analysis ", that is, the airborne system realizes the collection and record of loads/environment data, and the data is downloaded to the ground system for comprehensive data processing, structural damage assessment and residual life prediction, so as to guide the establishment of structural maintenance plan, the flow is shown in Figure 5-26.

SPHM key techniques include:

- Analysis and storage of fatigue loads/environment parameters;
- Ground load and flight load identification based on flight parameters;
- Conditional event analysis;
- Fatigue damage Calculation of critical areas;
- Residual life prediction and health assessment;
- Inspection/maintenance advice.

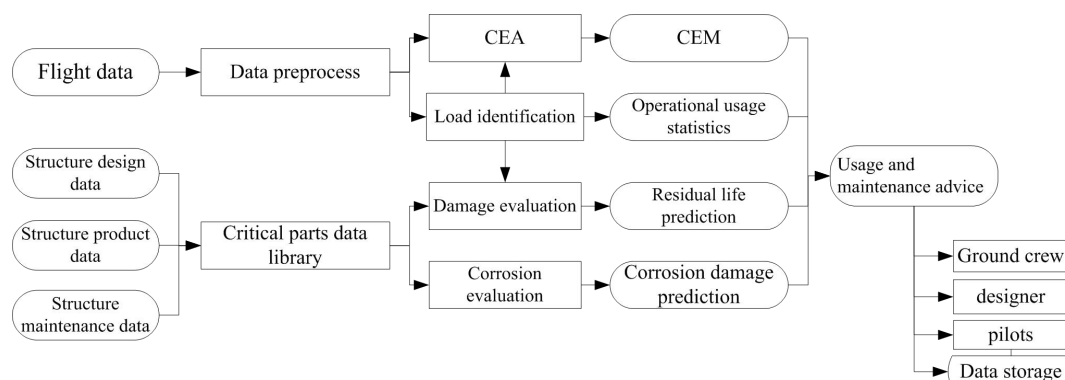


Figure 5-26 The flow of SPHM ground system

5.2.2 Research and Application of C919 Aircraft Static Test Technology⁶⁸

In order to solve the technical difficulties and risks, the C919 aircraft static test technology is proposed. This technology fills the gaps in similar domestic test technology, improves the capability and level of large aircraft testing in China, and ensure the successful completion of the static test of the C919 aircraft. It also laid a solid foundation for the determination of the structural design form and the improvement of subsequent research and further development.

Design technology of multifunctional integrated test bearing frame

Aiming at the problems of tight experiment preparation period and high system installation risk, the design idea of "system pre-built-aircraft fast entry-experimental efficient preparation" is proposed, which breaks through the frame segmented folding scheme design technology based on mobile fulcrum, as shown in Figure 5-27, to realize the fast and safe entry of the aircraft, shorten the experiment preparation period, and reduce the risk during the installation. Aiming at the problem of large load and large span of the load-bearing system, it has broken through the technology of high-load-bearing ratio and multi-redundancy frame optimization design, and considering the compatibility of multiple folding states to optimize the structural rigidity design, which improves the strength and stiffness of the load-bearing system. To solve the problems of large-scale static experimental system of large passenger aircraft, multiple subsystems, and the difficulty in integrated design, methods such as optimization design of multi-experiment system based on weight distribution and optimization design of operation adaptability under complex experimental environment were proposed, which broke through the weight integrated design technology of experimental multidisciplinary system based on the bearing frame, and improved the integration and reliability of the experimental system; developed an integrated multifunctional experimental platform integrating bearing, loading, control and other eight subsystems. It realized the rapid and accurate arrangement of large-scale and complex experimental systems in a limited space.

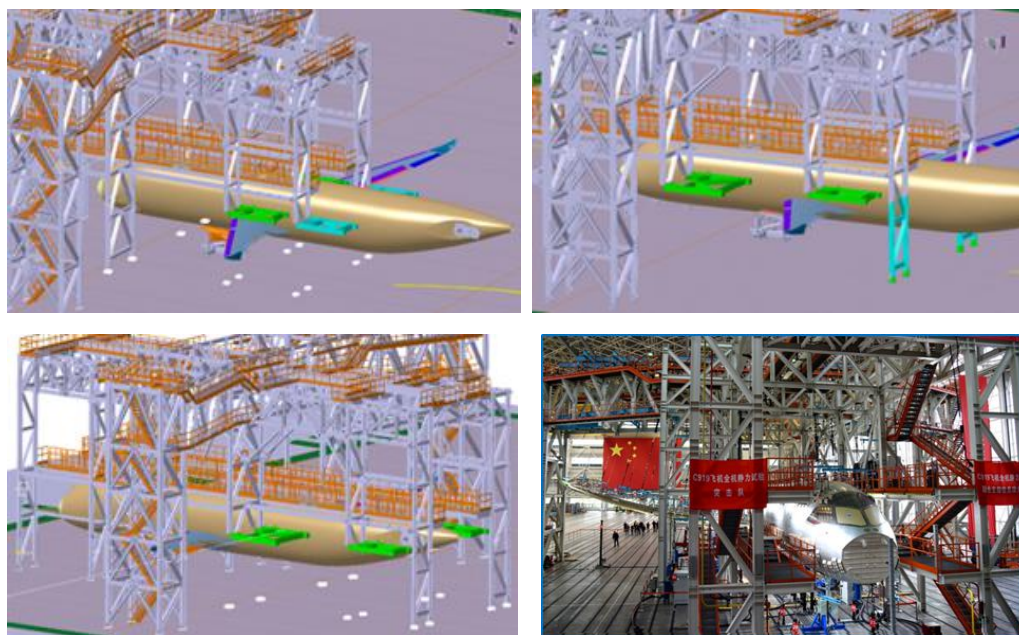


Figure 5-27 Schematic diagram of quick entry of test pieces

⁶⁸ AVIC Aircraft Strength Research Institute. LIU Wei: liuweifdu@126.com

Two-way statically determinate loading technology for fuselage double floor

In view of the complex load distribution of the fuselage and the various load conditions, a multi-type load parameterized model of the fuselage was established, and the load distribution and transmission law were analyzed and the load division equivalent method based on the passenger/commercial load ratio was proposed, and the multi-level partitioned load simulation technology has developed, the complex load design software for the fuselage is developed, which improved the efficiency and accuracy of load optimization. The C919 aircraft has a passenger and cargo double-layer fuselage structure. A double-floor-two-direction loading device with air tightness has been developed to solve the problem of coordinated and stable loading of the passenger cabin and cargo compartment and the weight of the fuselage. The double-floor loading system is shown in Figure 5-28.

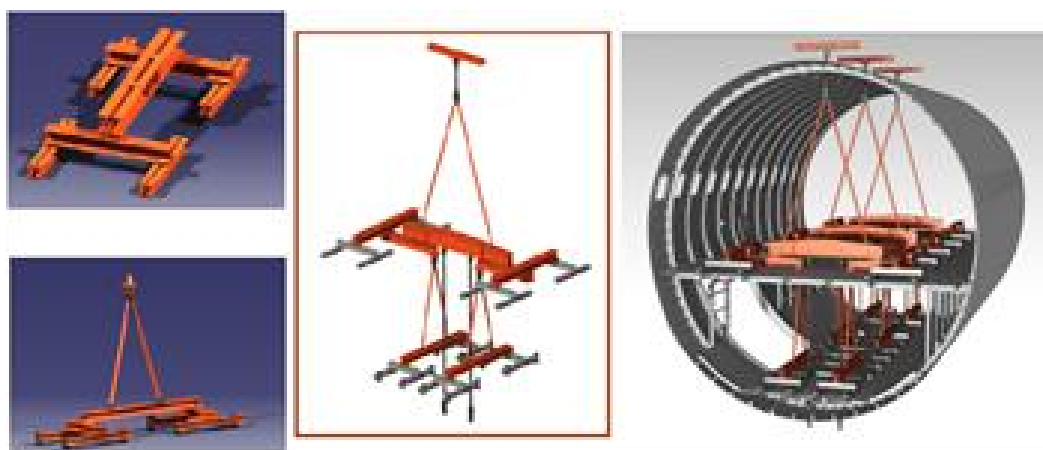


Figure 5-28 Schematic diagram of loading technology of double floor beams in engine room Large aspect ratio flexible wing load processing and application technology

Aiming at the problems of high wing loading density and frequent design and replacement, a mathematical model of the wing loading point was established, and a method of fitting the wing deformation quadratic curve was proposed, and the wing load partition design technology was developed, which achieved modular loading and multi-condition optimization reconstruction of loading points, and developed a wing unit loading module device as shown in Figure 5-29. It reduces the number of loading nodes and reduces the replacement time. Aiming at the difficulty of accurately applying the load caused by the iterative coupling of loading and deformation of the wing, a method based on the simulation analysis structure for fitting the deformation equation of the double-beam long straight wing and real-time simulation of the deformation curve is proposed, as shown in Figure 5-30. It broke through the large aspect ratio wing loading design based on the precise deformation curve, realized the accurate application of the load perpendicular to the wing chord plane during the deformation process, and formed the large deformation wing load design specification. The wing load equivalent similarity is more than 99%, and the load optimization efficiency is increased by 60%.

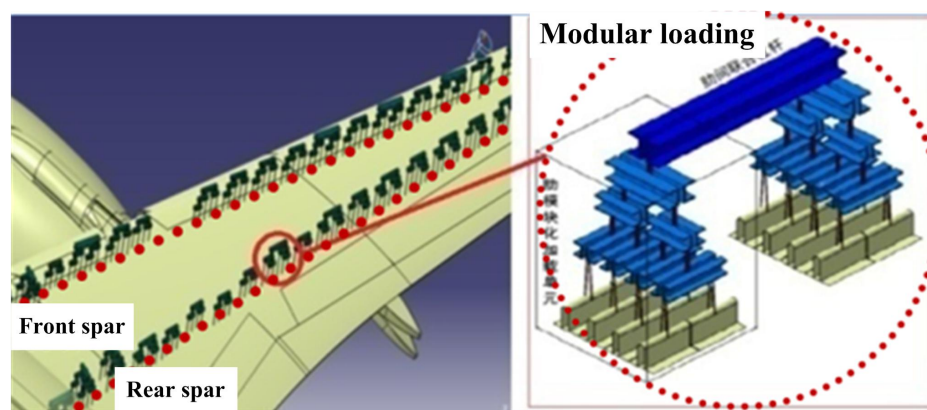


Figure 5-29 Schematic diagram of loading module of wing unit

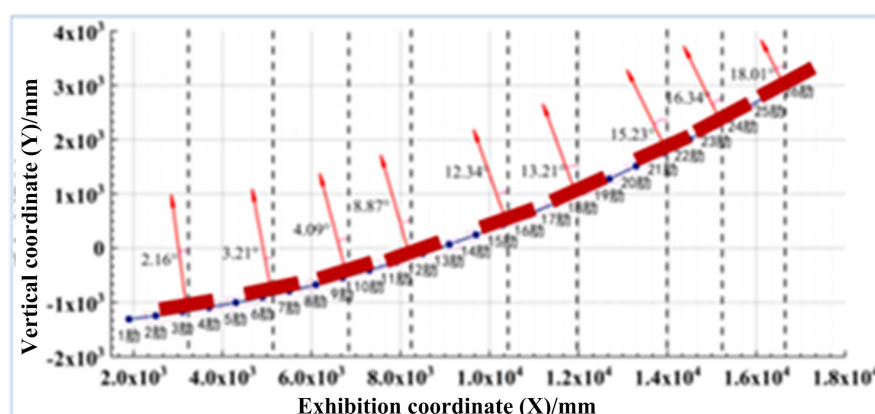


Figure 5-30 Schematic diagram of large wing deformation and loading direction

5.2.3 Static and Damage Tolerance Tests of Full-Scale Composite Fuselage Barrel Sections⁶⁹

The integrated authentication technology of full-scale wide-body composite fuselage straight section solves the problems of complex boundary conditions simulation of full-scale large-size composite parts, large load support system of test pieces, frequent replacement of static/fatigue test loading system, etc. It has been developed to provided suitable static and damage tolerance test device of full-scale fuselage straight section composite structure for civil aircraft, and provided a test forensics method for the civil aircraft composite fuselage structure.

Special boundary simulation of large diameter and large load fuselage

The loads outside the barrel section of the fuselage include the front fuselage and the middle and rear fuselage loads. In order to ensure the bearing capacity of the structural assessment section is true and accurate, the inertial load, aerodynamic load of the fuselage structure and the inertial load of passenger/cargo floor must be accurately transferred to the assessment section through the intermediate transition duct (ITD). The external load of ITD accumulates to the end faces of the front and rear ITD, which is equivalent to 6 free concentrated loads. The sealing cover is designed at the front and rear ITD, and a load box and multiple loading joints are set at the same time. The external load of the ITD realizes concentrated load and bending moment application through the sealing cover loading joints and is transmitted to the front and rear ITD. The special boundary simulation connection of the fuselage

⁶⁹ AVIC Aircraft Strength Research Institute. GUO Qiong: 310275545@qq.com

is shown in Figure 5-31.

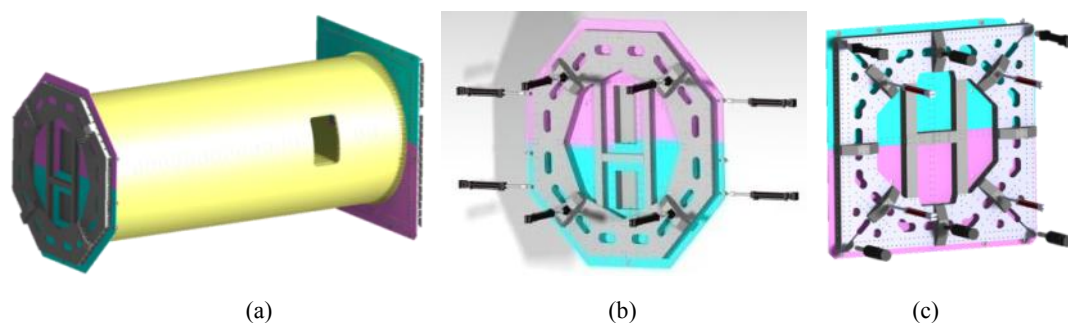


Figure 5-31 Special boundary simulation of the fuselage : (a) Joint diagram of sealing cover and fuselage; (b) Schematic diagram of the front sealing cover; (c) Schematic diagram of rear sealing cover

Strut-differential combined statically determinate support system

The static/fatigue test of full-scale aircraft structure inevitably involves the determination of the test constraint scheme. Reasonable constraint setting is the fundamental guarantee for the safety and smooth progress of the test. It's an important part of the test design process. There is no landing gear structure or other reinforced load-bearing structure in the full-scale composite fuselage barrel section test, so constraints must be set in the non-key assessment parts and the parts with large load-bearing capacity to meet the safe and stable operation of the test. Constraint points are set on the front and rear sealing covers to form a set of 6-DOF strut-differential combined support system, as shown in Figure 5-32. The front sealing cover is provided with a strut-type vertical constraint, and the rear sealing cover is equipped with two strut-type vertical constraint symmetrically to provide vertical, pitch, and roll constraints of the test system; Two groups of bi-directional differential soft constraints are formed by symmetrical uniaxial tensile constraints on the left and right sides of the front and rear sealing covers respectively, which are used to provide lateral and yaw constraints of the test system. A heading constraint is provided for the test system with a position-controlled actuating cylinder on the rear sealing cover.

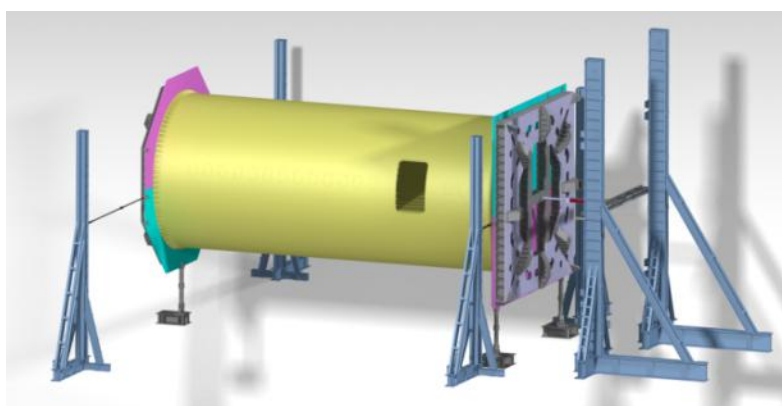


Figure 5-32 Schematic diagram of statically determinate support system

In order to accurately simulate the boundary load of the test specimen, a dynamic calculation program of passive load was written to realize the accurate application of boundary load through real-time monitoring of the errors of passive loading points in the test. The principle is shown in Fig. 6. The program introduces the error of passive loading point into the control system, which solves the problem that the passive load of constraint point needs to be monitored manually during the test process, and improves the efficiency test operation. The active loading point of a certain working condition test

meets the error requirements. The load application results at three vertical constraints are shown in Figure 5-33, the maximum error does not exceed 2%. The strain of the key parts of the structure is in accordance with the expectation, which indicates that the test boundary conditions can be accurately simulated by setting active and passive loading points on the front and rear sealing covers.

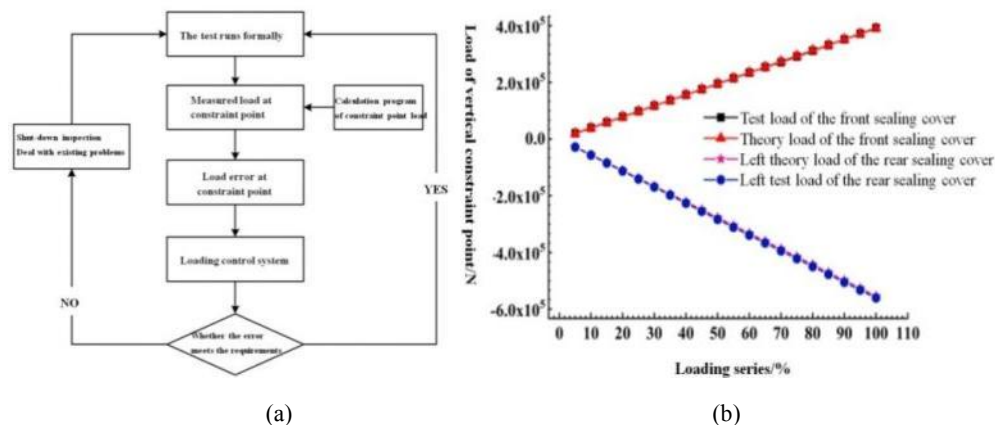


Figure 5-33 Principle of load error monitoring at constraint points and test results

(a) Principle of load error monitoring at constraint points; (b) Passive loading results of vertical constraint points

Double-deck bi-directional loading system

The composite fuselage barrel section has the remarkable characteristics of large size and large load. The test requires simultaneous loading of 8 slide rails in the passenger cabin and 4 slide rails in the cargo compartment. The number of final loading nodes on each frame station is 1.5 times that of C919 aircraft; At the same time, the space between the passenger and cargo compartments in the composite fuselage barrel section has increased from about 1.4 meters to about 2 meters, which makes it more difficult to coordinate the loading between layers. The design technology of loading device for floor beam of wide-body fuselage is proposed. The loading device for floor beam of composite fuselage barrel section is shown in Figure 5-34. This set of loading system includes two independent parts: upward loading/lifting mechanism and downward loading lever. It can deduct the dead weight of the loading device and the corresponding weight of the fuselage section structure at the same time and exert upward load on the fuselage structure. The downward loading lever can achieve the application of downward load on the fuselage structure, which accurately distribute the load to each frame and floor beam.

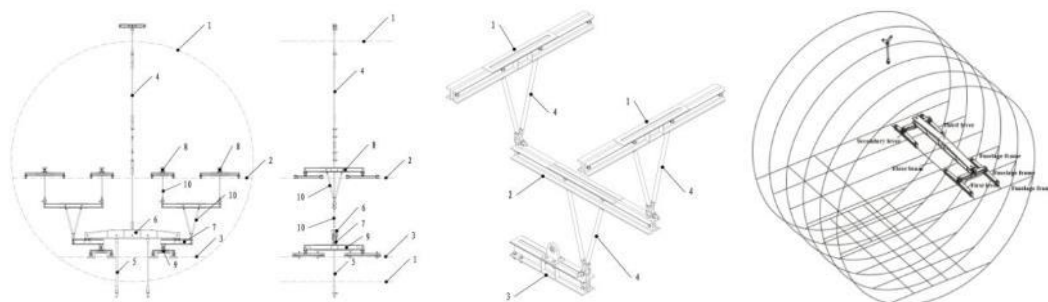


Figure 5-34 Schematic diagram of loading device for passenger cabin and cargo

5.2.4 New Method of Helicopter Large Structure Strength Test Based on Defect Tolerance⁷⁰

Strength performance shall be verified by full-scale structural tests in accordance with the requirements of articles such as CCAR29, § 571, etc. According to the airworthiness clause, this paper proposes the strength verification method of the tail section according to the structure form and load characteristics of a certain type of tail section, prefabricates the initial defects on the test piece, designs the installation, test load and loading mode of the test piece, and uses a test piece to verify the static strength, fatigue strength and defect tolerance characteristics.

The research includes four key parts: the verification test design technology of large tail structure, defect prefabrication and temperature environment simulation; fatigue life test spectrum design and static strength test load calculation; and fatigue strength and defect tolerance characteristics verification technology of large structure.

The main achievements of this study are as follows: a large-scale helicopter structural strength test method based on defect tolerance is established, including test environment, defect prefabrication, installation form, and test load, loading mode, calibration and test procedure. Among them, the test environment, conditions and prefabrication of initial defects should be consistent with or close to the actual use of the helicopter as far as possible; the static strength test load considers the maximum load condition in the life cycle of the model; the fatigue test load spectrum is determined by stress analysis, life calculation, damage equivalence and other methods according to the typical mission profile of the model, which conforms to the requirements of the model in the life cycle.

Strength test procedure of helicopter large structure based on defect tolerance

The test verification of helicopter tail structure is divided into seven stages:

Stage 1: manufacturing initial defects on full-scale tail test pieces, including possible process debonding and impact pits.

Stage 2: limited load static strength test under high temperature environment, including flight and landing load conditions.

Stage 3: fatigue life test of 20000 hours (one life cycle) of ground-air-ground load cycle.

Stage 4: static strength test under 1.1 times ultimate load in high temperature environment, including flight and landing load conditions.

Stage 5: after repairing part of the structure damage and adding some visual obvious detectable damage (CVID), the fatigue life test was carried out for 10000 hours.

Stage 6: static strength test under 1.2 times ultimate load in high temperature environment, including flight and landing conditions.

Stage 7: static strength test under high temperature until failure

Defect prefabrication and temperature environment simulation

The prefabrication of defects on the test pieces shall cover the manufacturing quality and service

⁷⁰China Helicopter Research and Development Institute. WANG Weiwei, LI Qingrong: 30440778@qq.com

conditions of the severity, mainly including the large stress area of the structure, the structural connection area and the area vulnerable to the impact of foreign objects, as shown in Figure 5-35.

The release position of the metal ball is determined by the calibration test to ensure the accuracy of the impact energy. The impact energy is determined by the impact test of small specimens with the same structure. After the impact, the test specimens are tested to identify the impact defect size.

The simulation of the temperature environment on board adopts the way of covering the outer surface of the tail section test piece with heating blanket. The temperature of the tail beam and the vertical tail heating blanket are controlled respectively, and the surface temperature of the test piece is ensured within the required error range through the temperature sensors arranged on the surface of the structure.

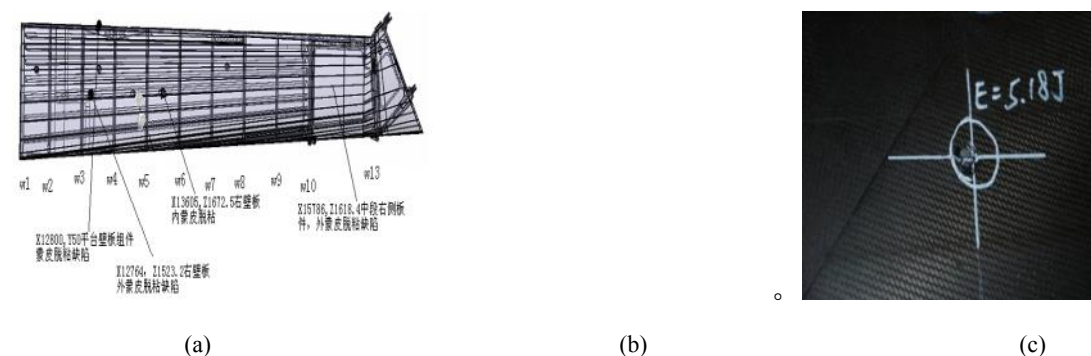


Figure 5-35 Defect prefabrication: (a) Schematic diagram of manufacturing defect location of tail beam, (b) Schematic diagram of manufacturing defects of panel assembly, (c) photos of impact at point A

Experimental design and verification

In order to simulate the real boundary as much as possible, the tail section test piece contains a part of transition section structure (for example, a certain type of aircraft is between 7 frames and 8 frames of helicopter body). The test installation and loading are shown in Figure 5-36.

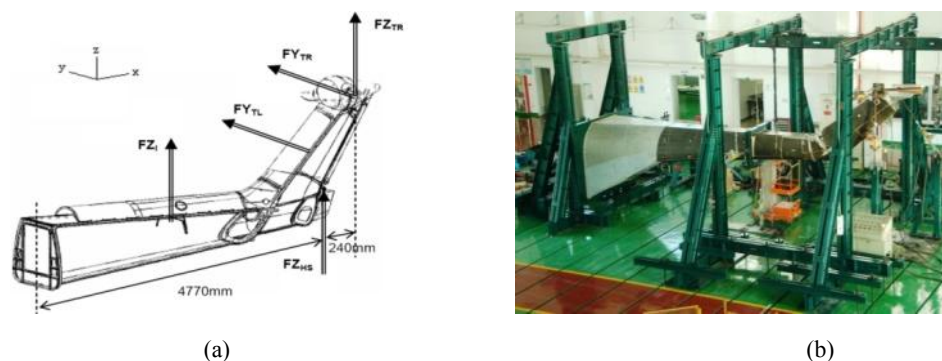


Figure 5-36 Test piece installation and loading point: (a) Installation of full size tail test piece, (b) Schematic diagram of test loading

Helicopter tail fatigue is a low cycle fatigue problem. Fatigue test spectrum is used to test. After that static strength test shall be conducted to verify that the helicopter structure can withstand all possible severe loads without failure during the whole life span. The typical test data are shown in Figure 5-37.

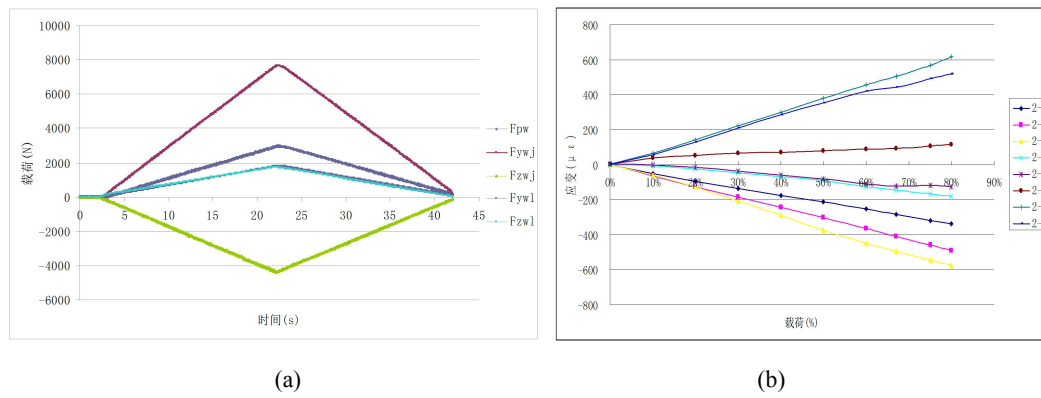


Figure 5-37 Typical test results: (a) load cycle of ground-air-ground,(b) Load-strain curves of typical measuring points